Degradation and Processes in Lithium Batteries



Euan McTurk

Linacre College

University of Oxford

A thesis submitted for the degree of

DPhil Materials

Michaelmas 2015

Acknowledgements

I came to the field of battery research from a Physics background, so the transition to the fields of Electrochemistry and Materials Science involved steep learning curves and a gamble from whoever took me on. Therefore, I must thank Professor Peter G. Bruce for giving me the chance to take the plunge and prove my capability within his research group.

In addition to Peter, there were many colleagues who provided invaluable assistance during my DPhil. I owe a great deal to the insight and professionalism of Dr Lee Johnson, who possesses an outstanding knowledge of electrochemistry and a meticulous eye for detail. The knowledge, support, encouragement and enthusiasm of Dr Kan-Hao Xue, Professor Alejandro Franco, Professor David A. Howey, Dr Matthew Roberts and Christoph Birkl has not gone unnoticed; it was a pleasure working alongside you on the multiple publications that have stemmed from our work. I am also indebted to Dr Andy Naylor, Dr Ola Hekselman and Dr Francis Kinyanjui for their invaluable advice during the writing of this thesis.

Keeping a lab running is a group effort. I must thank Dr Yuri Andreev and Dr Nuria Tapia for their assistance with, and upkeep of, XRD machinery, which is no small task. Likewise, Dr Krzysztof Maranski and John Hall must be thanked for their never-ending duties of maintaining the group's plethora of glove boxes, and for passing on their knowledge to me. I would also like to thank Dr Andy Naylor for his IT support, and Mrs Gabriella Chapman, Dr Felix Richter and Stefanie Zekoll for providing me with SEM training and assistance.

There are many staff behind the scenes who keep the entire University running smoothly and to whom we all owe a great deal. In no particular order, I must sincerely thank this huge group of people that includes Zsofia Szabo, Levi Dash, Robert Cathcart, Artur Czernik, Paul Sheard, Paul Warren, Ross Wackett, Howard Thomas, everyone on the Green Impact Committee, Les

Chorley, Brian Walker, Jane Foxall, Tim McAree and Barry Fellows for regularly going out of their way to keep the group going.

Morale and support were crucial during some of the testing times for the group, such as lab renovations and relocations. John Hall, Juliette Billaud, Chunmei Li, Zsofia Szabo, Levi Dash, Cassian Marriner-Edwards, Dr Felix Richter and Dr Filip Wormald were pivotal in this regard, and I must thank Dr Stefan Freunberger for always encouraging me to keep pushing with the project. Of course, I must thank my family and friends for their continued support and enthusiasm which spurred me on from afar. Special thanks go to my better half Diane for enduring a long-distance relationship (and many an expensive train journey), and to my parents for taking on most of my belongings from Dundee, including two cars!

As well as journal articles, there were many other highlights along the way, including celebrity visits and Departmental awards. I thank everyone on the Green Impact Committee for their award-winning efforts, and also thank Robert Llewellyn for stopping by; we had a great time.

I would like to thank the EPSRC for funding my DPhil, and Peter for kindly providing additional support for the final month of the project.

Finally, I would like to dedicate this thesis to the staff at JMBS (formerly Axeon), Dundee, many of whom are graduates of the Bruce group. I owe the people of this plucky and hugely successful enterprise a massive thanks for their help in procuring the batteries for my "vintage" Peugeot 106 Electric, which was expertly upgraded by the incredibly capable Evan Tuer. Alas, the company that bought them out barely three years ago, Johnson Matthey, has shut the factory in Dundee and is relocating it down south, against all logic and the will of its workforce. This action amounts to nothing but mindless centralisation for the sake of centralisation and has ripped the heart out of the electric vehicle revolution of Dundee, and Scotland. Rest assured that I am doing everything in my power to ensure that Axeon will live on and thrive in Dundee.

Degradation and Processes in Lithium Batteries

Euan McTurk, Linacre College
DPhil Materials
Michaelmas Term 2015

The automotive industry requires rapid advances in battery technology to fulfil the range and price criteria set by its consumer base. Lithium-ion cell chemistries are currently best-suited to this application, but are approaching their maximum practical energy density and have yet to exhibit lifespans that are equivalent to that of the vehicles that they power. Therefore, there is considerable interest in the next-generation lithium-air cell, which promises upwards of a five-fold increase in energy density over today's lithium-ion cells. However, there are many hurdles to overcome, the most important being limited cycle life.

Two new organic solvents, namely adiponitrile and glutaronitrile, were investigated as possible new electrolytes for non-aqueous lithium-air cells. Both electrolytes were found to be susceptible to nucleophilic attack by the intermediate $O_2^{\bullet-}$ radical species, resulting in rapid capacity loss upon cycling and the conversion of the discharge product, Li_2O_2, to LiOH. As such, these solvents have been ruled out for use in lithium-air applications.

Work then focussed on the parameterisation of lithium-air cells to assist the development of a multiscale model of the lithium-air discharge mechanism that incorporates the simultaneous formation of Li_2O_2 in solution and as a surface layer for the first time. Numerous analytical techniques were used to obtain the oxygen concentration and diffusion coefficient of multiple electrolytes, as well as details pertaining to the cathode structure of the cell. The model was shown to predict the discharge profile of a lithium-air cell with greater accuracy than previous models at low and medium current densities, and will thus be a useful tool for the rapid screening of new electrolyte solutions and cathode structures.

Finally, a new 3-electrode modification technique was developed for commercial lithium-ion pouch cells that allows potential profiles of each electrode to be obtained *in-situ* with no impact upon cell performance, as verified by cycling with unmodified cells and cathode/anode half-cells, and by post-mortem analysis. This technique has provided the data required to experimentally verify a parametric open circuit voltage model for lithium-ion cells that can model and predict electrode-specific decomposition mechanisms to within an accuracy of 10 mV RMSE. Ultimately, the model may be used to improve the effectiveness of a vehicular battery management system and extend the lifespan of the traction battery pack.

List of Abbreviations

BET	Brunauer-Emmett-Teller Analysis
BJH	Barrett-Joyner-Halenda Method
BMS	Battery Management System
CC	Constant Current (galvanostatic cycling)
CE	Counter Electrode
CP	Constant Potential (potentiostatic cycling)
CV	Cyclic Voltammetry
DMC	Dimethyl Carbonate
DMF	Dimethylformamide
DMSO	Dimethyl Sulfoxide
DoD	Depth of Discharge
EC	Ethylene Carbonate
EDX	Energy-Dispersive X-ray Spectroscopy
EMF	Electromotive Force
EV	Electric Vehicle
FTIR	Fourier Transform Infrared Spectroscopy
GITT	Galvanostatic Intermittent Titration Technique
ICE	Internal Combustion Engine
LCO	Lithium Cobalt Oxide
LFP	Lithium Iron Phosphate
LMO	Lithium Manganese Oxide
LNO	Lithium Nickel Oxide
LSV	Linear Sweep Voltammetry
LTO	Lithium Titanium Oxide
NCA	Lithium Nickel Cobalt Aluminium Oxide
NCO	Lithium Nickel Cobalt Oxide
NMC	Lithium Nickel Manganese Cobalt Oxide
NMP	N-Methyl-2-Pyrrolidone
OCV	Open Circuit Voltage
OER	Oxygen Evolution Reaction
ORR	Oxygen Reduction Reaction
PC	Propylene Carbonate
PSD	Pore Size Distribution
PTFE	Polytetrafluoroethylene
RDE	Rotating Disk Electrode
RE	Reference Electrode
RMSE	Root Mean Square Error
SEI	Solid Electrolyte Interphase
SEM	Scanning Electron Microscopy
SHE	Standard Hydrogen Electrode
SoC	State of Charge
SoH	State of Health
TEGDME	Tetraethylene Glycol Dimethyl Ether
TFSI	Bistrifluoromethanesulfonimidate (salt anion)
UME	Ultramicroelectrode
WE	Working Electrode
XRD	X-ray Diffraction

List of symbols

Symbol	Meaning	Units
a	Specific surface area	m^{-1}
A	Surface area	m^2
C	Concentration	mol m^{-3} (mM)
d	Distance between atoms in crystal structure	m
D	Diffusion coefficient	m^2 s^{-1}
E	Potential	V
E°	Standard electrode potential	V
F	Faraday constant	C mol^{-1}
ΔG	Gibbs free energy	kJ mol^{-1}
I	Current	A
j_{Far}	Faradic current density	A m^{-2}
k	Kinetic rate	$mol^{0.5}$ $m^{-0.5}$ s^{-1}
m	Gravimetric mass	g
M	Molar mass	g mol^{-1}
n	Number of electrons transferred per reactant molecule	-
N	Number of electrons transferred per mole	mol^{-1}
Q	Charge	C
Q_r	Reaction quotient	-
r	Radius	m
R	Universal gas constant	J mol^{-1} K^{-1}
s	Saturation	-
t	Time	s
T	Temperature	K
v	Sweep rate	V s^{-1}
ν_k	Kinematic viscosity	m^2 s^{-1}
V	Volume	m^3
z	Valence number of ion	-
α	Surface area distribution function	nm^{-1}
β	Charge transfer coefficient	-
Δx	Bin width	m
δ	Film thickness	nm
ε	Porosity	-
η	Butler-Volmer overpotential	V
θ	Angle of incidence	°
λ	Wavelength	m
ξ	Escape probability	-
ρ	Density	g m^{-3}
ϱ	Li_2O_2 resistivity	Ω m
χ	Escape function	-
ω	Angular velocity	rad s^{-1}

Contents

Chapter 1: Introduction 1

1.1 The need for electrochemical energy storage 1
1.2 Principles of energy storage 5
1.3 A history of automotive battery technology 9
1.4 Current generation: the lithium-ion battery 18
1.5 The lithium-air cell 26
1.6 Research objectives 38
1.7 References 41

Chapter 2: Experimental procedures 64

2.1 Cell assembly 64
2.1.1 Swagelok cell 64
2.1.2 Coin cell 65
2.1.3 Glass cell 66
2.2 Preparation of cell components 67
2.2.1 Anodes 68
2.2.2 Cathodes 68
2.2.3 Separators 69
2.3 Electrolyte purification 69
2.3.1 Distillation 70
2.3.2 Karl Fischer Titration (KFT) 71
2.3.3 Drying of salts 73
2.4 Cell cycling procedures 73
2.4.1 Galvanostatic cycling (CC) 74
2.4.2 Potentiostatic cycling (CP) 74
2.4.3 Galvanostatic intermittent titration technique (GITT) 75
2.5 Electrochemical techniques 76
2.5.1 Linear sweep voltammetry (LSV) and cyclic voltammetry (CV) 77
2.5.2 Obtaining the diffusion coefficient and concentration of reactants in an electrolyte 78
2.5.2.1 Determining the surface area of a planar electrode 79
2.5.2.2 Chronoamperometry and the Cottrell equation 80
2.5.2.3 Rotating disk electrode (RDE) and the Levich equation 81
2.5.2.4 The ultramicroelectrode (UME) 82
2.6 Materials characterisation and post-mortem analysis 83
2.6.1 Fourier transform infrared spectroscopy (FTIR) 83
2.6.2 X-ray diffraction (XRD) 85
2.6.3 Scanning electron microscopy (SEM) and energy-dispersive X-ray spectroscopy (EDX) 88
2.6.4 Brunauer-Emmett-Teller surface area analysis (BET) 92
2.7 References 94

Chapter 3: Instabilities of nitrile electrolytes for non-aqueous lithium-air cells 97

3.1 Introduction 97

3.1.1 The search for a stable lithium-air electrolyte *97*
3.1.2 Nitriles as an electrolyte for lithium-air cells *98*
3.2 Capacity retention of nitrile-based lithium-air cells *100*
3.2.1 Preparation of cell components *101*
3.2.2 Preparation of electrolyte solution *101*
3.2.3 Cell cycling procedure *101*
3.2.4 Results and analysis *102*
3.3 Chemical stability of nitriles in contact with intermediate and discharge species *106*
3.3.1 Chemical stability analysis procedure *108*
3.3.2 Results and analysis *108*
3.3.2.1 Stability of adiponitrile towards Li_2O_2 and KO_2 *108*
3.3.2.2 Stability of glutaronitrile towards Li_2O_2 and KO_2 *113*
3.4 Electrochemical stability of nitriles within potential limits of Li-air cell cycling *117*
3.4.1 Electrochemical stability analysis method *118*
3.4.2 Results and analysis *119*
3.5 Revised cycling procedures based on electrochemical stability of nitriles to enhance capacity retention *122*
3.6 Oxygen concentration and kinetics within nitrile electrolytes *123*
3.6.1 Determining oxygen concentration and diffusion coefficient in nitriles *124*
3.6.2 Results and analysis *125*
3.7 Conclusions and further work *128*
3.8 References *130*

Chapter 4: Experimental verification of novel lithium-air multiscale computerised model **135**

4.1 Introduction *135*
4.2 Description of multiscale model *137*
4.3 Discharging and parameterising real cells *145*
4.3.1 Cell cycling *145*
4.3.2 Experimentally obtaining the oxygen diffusion coefficient and bulk concentration in the electrolytes *146*
4.3.3 Obtaining the pore size distribution (PSD) *151*
4.4 Comparison of model and real cell cycling data *152*
4.5 Conclusions and further work *157*
4.6 References *159*

Chapter 5: Modification of commercial lithium ion pouch cells for long term degradation studies **164**

5.1 Introduction *164*
5.2 Experimental procedures *167*
5.2.1 Full cell preparation *167*
5.2.2 Half-cell fabrication *167*
5.2.3 "Patch" modification method *168*
5.2.4 "Wire" modification method *169*
5.2.5 Cell cycling *170*

5.2.6 Post-mortem analysis *171*
5.3 Results and analysis *171*
5.3.1 Capacity retention *171*
5.3.2 Post-mortem analysis *174*
5.3.3 Electrode potential verification *180*
5.4 Conclusions and further work *184*
5.5 References *186*

Chapter 6: Conclusions and outlook **189**

6.1 References *195*

Appendix A **199**

A.1 Calculation of air flow rate for Li-air automotive battery pack *199*
A.2 Calculation of onboard oxygen storage required for an oxygen-fed Li-O_2 automotive battery pack *202*
A.3 Calculation of quantity of soda lime required for an air-fed Li-air automotive battery pack *203*
A.4 References *203*

Appendix B **204**

B.1 Identification of pouch cell cathode chemistry *204*
B.2 Table of chemical composition of cathode samples as determined by EDX *206*
B.3 EDX colour maps of unmodified, cycled anode *206*
B.4 RMSE data for potential profiles obtained from half-cells and 3-electrode cells *207*
B.5 References *208*

1 Introduction

1.1 The need for electrochemical energy storage

Increasing global population, combined with rapid technological advances and increasing uptake of consumer electronics and personal transport in emerging markets, is driving an increase in energy demand. Globally, energy demand has almost doubled over the past forty years, from 54,335 terawatt hours (TWh, a unit that is equal to 3.6 petajoules) in 1973 to 104,426 TWh in 2012. Oil formed the highest proportion of this consumption at 40.7 % in 2012, of which 63.7 % was used to fuel the transport sector, mostly through its refinement to petroleum and diesel, which are then burned in internal combustion engines (ICEs) to provide traction to most of the vehicles on the road today [1]. However, this process produces a number of unwanted products that have a negative impact on local air quality and health. Examples include NO_X emissions, which cause acid rain, lung damage and cardiovascular problems, and carcinogenic nanoparticulate matter [2, 3, 4, 5]. These are particularly prevalent in diesel emissions and are therefore a major concern for countries like the UK, which has a heavy reliance on diesel for haulage, agriculture and public transport as well as privately owned vehicles; it is estimated that diesel emissions are responsible for 5,800 premature deaths in the UK per annum [6]. The recent VW emissions scandal, where the manufacturer rigged emissions tests of their diesel engines so that they passed when in reality they emitted 40 times the legal limit for nitrogen oxides (NO_X), has sparked concern over the continued use of the internal combustion engine, particularly the diesel engine, in the transport sector [6]. Additionally, the use of diesel-based vehicles in agriculture has been shown to negatively impact on insect-based pollination. NO_X emissions impair the ability of honeybees to detect oilseed rape which, as well as being an increasingly important food ingredient in the UK, is

ironically also a crop that may be used to produce biodiesel [7, 8]. Furthermore, the burning of fossil fuels produces CO_2, the artificially inflated atmospheric content of which is responsible for ocean acidification and anthropogenic climate change, which has far-reaching consequences for spread of disease, flood and drought prevention, biodiversity and the food chain [9, 10, 11]. Given that CO_2 emissions from oil increased by 41.6 % between 1973 and 2012, equating to an additional 3.3 billion tonnes of CO_2 emitted into the atmosphere in the latter year, there is a pressing need to decarbonise the global energy supply [12].

One of the most effective ways to decarbonise global energy consumption is to transition to an electrified transport infrastructure [9, 13, 14]. Electricity can be produced *via* renewable methods such as wind turbines, solar photovoltaic arrays and tidal generators, and therefore avoid the production of the harmful emissions outlined above. Even electricity produced from large thermal generators, such as gas-fired power plants, has the potential to be more environmentally friendly than vehicles powered directly by oil-derived fuels, due to the comparative ease of installing advanced emissions scrubbers, carbon capture and storage (CCS) or combined heat and power (CHP), whereby residual heat from the steam used to power the turbine is transferred to district heating schemes. Additionally, the efficiency of large thermal generators is superior to that of ICEs; combined cycle gas turbine (CCGT) power plants, which burn gas in a gas turbine and use the heat of the reaction to boil steam which powers a steam turbine, have combined cycle efficiencies approaching 60 %, compared to the < 40 % thermal efficiency of ICEs [15, 16]. Despite these environmental and economic advantages, electrified transport is still a global minority, to the extent that only 1.6 % of electricity was used to power the transport sector in 2012. When the total energy associated with global electricity and oil consumption for that year are compared, it can be seen that electricity provided only 1.1 % of the energy that oil did to the transport sector [1].

The automotive industry has a historic reliance on the ICE stretching back to the early 20th century, when oil-derived petroleum and diesel emerged as dominant fuel sources on account of their high energy density – approximately 13,000 watt hours per kilogram (Wh kg^{-1}) for petroleum - and the ability to rapidly refuel the vehicle, adding hundreds of miles of range in about five minutes. In comparison, commercially-available secondary (rechargeable) battery technology was limited to approximately 50 Wh kg^{-1} at a cell level for most of the 20th century, and recharging times were slow, thus hindering the range and performance of electric vehicles, as will be discussed later. However, the poor efficiency of the ICE at < 40 %, combined with further energy losses in the drivetrain, idling, braking, aerodynamic drag and providing power to auxiliary accessories culminates in a "pump-to-wheel" efficiency of *circa* 12.6 % for ICE-powered vehicles, giving a real-world specific energy of 1,638 Wh kg^{-1} for petroleum [16].

Recently, advances in secondary cell chemistries have vastly improved the viability of EVs. The 90 % efficiency of both electric motors and modern cell chemistries, plus the simplification of the drivetrain, absence of idling losses and the ability of an EV to recover energy under braking (regenerative braking), gives EVs a "battery-to-wheel" efficiency of *circa* 70 % [16, 17]. Another advantage of EVs is that their battery packs can be used as grid storage to store excess electricity when demand is low and reduce the peak demand on power stations; this is especially useful if a large percentage of generators connected to the grid are renewable, since the output from wind turbines and solar panels is intermittent [18, 19]. Furthermore, the real-world range of the latest EV models is upwards of 100 miles per charge, whilst Tesla have quoted a New European Driving Cycle (NEDC) maximum range of 346 miles for their Model S. This, combined with the standardisation and widespread distribution of rapid charging formats over the past decade, such as the CHAdeMO 50 kW DC format favoured by Nissan or the 125 kW Supercharger network from Tesla, has facilitated cross-country journeys and continental road trips under fully electric propulsion, with the ability to add as many as 170

miles of range to the vehicle within 30 minutes [20, 21]. As such, there are clear merits to the advancement of electric vehicles, in terms of decarbonisation, reduction in air and noise pollution and improvements in efficiency. Consequently, uptake of modern EVs has soared, which in turn has allowed battery production to be scaled up, with resultant reductions in cost per kWh capacity and thus increased affordability [22]. This is evident in UK sales figures showing that the Nissan LEAF, the most popular of the new generation of electric vehicles, is outselling the Toyota Prius, the first major hybrid car to enter the UK market, by 190 % from their respective launch dates [23].

Whilst substantial progress has undoubtedly been made in secondary cell technologies over the past twenty years, progress still falls short of the demands of the automotive industry. For example, the New Energy and Industrial Technology Development Organization of Japan (NEDO) has set a target of 700 Wh kg^{-1} for automotive traction battery packs to bring them sufficiently close to the overall specific energy of ICE-powered vehicles to compete on range [24]. Similarly, IBM's Battery 500 project aims to culminate in an electric vehicle with a range of 500 miles per charge [25]. Targets have also been set regarding capacity retention, for which the United States Advanced Battery Consortium aims to develop cell chemistries which lose no more than 30 Wh kg^{-1} of capacity within the first 10 years [26]. However, today's market-leading lithium-ion cells offer approximately 200 Wh kg^{-1} energy density with a capacity fade of 30 % or more within 8 years, equating to 60 Wh kg^{-1} for cells with the highest energy density. Improvements in capacity retention may be achieved either through the cell chemistry or refinement of the battery management system (BMS), which regulates the potential, current and temperature of cells in the pack. However, there is a need to develop new secondary cell chemistries that offer a step change in energy density. This work shall contribute towards the development of promising next-generation cell chemistries through gaining a greater understanding of the mechanisms that take place within them during cycling, before moving

on to supporting the development of advanced BMS algorithms that can extend the cycle lives of today's commercial lithium-ion cells.

1.2 Principles of energy storage

An electrochemical cell consists of two half-cells, each formed of an electrode (current collector and reaction site) in an electrolyte (which facilitates ionic transport between the two electrodes). In the vast majority of modern secondary cells, the electrolyte is shared between the two half-cells, and consists of either salt dissolved in solvent(s), or an ionically conductive polymer or glass-ceramic.

In an electrochemical cell, one of the electrodes will form the anode, or negative electrode, which is where oxidation (loss of electrons) occurs during discharge, whilst the other forms the cathode, or positive electrode, where reduction (gain of electrons) occurs during discharge. These redox (reduction and oxidation) reactions convert chemical energy stored in the anode to electrical energy that can be used to perform work in the external circuit. The maximum amount of energy available to do this work is referred to as Gibbs free energy, ΔG, and has the corresponding equation (1):

$$\Delta G = \Delta G^{\circ} + \frac{RT}{NF} \ln Q_r \tag{1}$$

where R is the universal gas constant, which relates the energy of a mole of reactants to its temperature (8.314 J mol^{-1} K^{-1}); T is the temperature in K; N is the number of electrons transferred in moles, F is the Faraday constant, which expresses the magnitude of charge contained by one mole of electrons (96485.333 C mol^{-1}), and Q_r is the reaction quotient. The latter is the ratio of the molar quantities of reactants and products such that, in a reaction where:

$$aA + bB \rightleftharpoons yY + zZ \quad (2)$$

where lowercase letters represent the number of moles of the reactant or product denoted by the equivalent capital letter, then the reaction quotient Q_r is:

$$Q_r = \frac{[Y]^y[Z]^z}{[A]^a[B]^b} \quad (3)$$

where bracketed capital letters denote the activity of the respective reactant or product at a given time. The Gibbs free energy may also be expressed with regards to the potential of the cell using equation (4):

$$\Delta G = -\Delta ENF \quad (4)$$

where ΔE is the potential difference, or electromotive force (EMF), between the electrodes. During discharge, the potential of the cathode, or working electrode (WE, so-called because the reaction of interest takes place upon or within it), decreases whilst that of the anode, or counter electrode (CE, which completes the cell and allows electrical and ionic current to flow), increases. The process is terminated when equilibrium is reached between the chemical potential of the cathode and anode.

It is imperative from equation (4) that the two electrodes must have a different standard electrode potential, or E°, in order for there to be a potential difference between the electrodes, thus allowing the discharge reaction to occur. The potential of each electrode cannot be measured in isolation. Therefore, E° is determined using a standard hydrogen electrode (SHE), which is a platinum wire bubbled with hydrogen gas at 1 atmosphere of pressure, in 1 molar (M) concentration of acidic solution, at 25 °C. The standard potential of the SHE is assigned the relative value of 0 V. The electrode of unknown E° is placed in an electrolyte with 1 M

concentration of its own ions, and connected to the electrolyte of the SHE *via* a salt bridge. No external potential is applied, so as to measure the true EMF between the electrodes. Ideally, there should be infinite resistance in the external circuit to prevent current flow, which would result in electrons flowing from the relatively negative electrode to the relatively positive electrode and thus lowering the potential difference between them. Since E° of the SHE is 0 V, E° of the electrode of interest corresponds to E_{cell}. Looking at E° in isolation, i.e. ignoring factors such as the gravimetric density of electrode materials, it is desirable to pick two electrode materials that have the greatest difference between their standard electrode potentials. This will provide the largest cell voltage, which is proportional to specific energy since the energy stored or provided by a cell is equal to the area under an *I*/*E* (current *vs.* potential) curve of a cell that has been charged or discharged over a given period of time. Therefore, a higher cell voltage allows a greater amount of energy to be stored in the cell per unit mass.

In real-world cell operation, parameters such as temperature and concentration of anions and cations in the electrolyte solution can vary. Therefore, cell potentials will not always equate to $E^{\circ}_{\text{cell}} = E^{\circ}_{\text{cathode}} - E^{\circ}_{\text{anode}}$. The Nernst equation (5) is used to factor in variable parameters and obtain the true potential of the cell:

$$E_{cell} = E^{\circ}_{cell} - \frac{RT}{NF} \ln Q_r \tag{5}$$

which is related to equation (1) by equation (4).

The capacity of the cell is defined as the current transferred over the time that it takes to completely discharge the cell from 100 % State of Charge (SoC) to 0 % SoC, i.e. the charge transferred. This may also be expressed by Faraday's law (6):

$$Q = zF\frac{m}{M} \quad (6)$$

Where Q is the charge in Coulombs; z is the valence of the active material, i.e. the number of electrons transferred per ion; F is Faraday's constant; and m and M are the gravimetric and molar masses of the active electrode material, respectively. It is worth noting that Ampere hours (Ah) are the preferred unit for storage cells; since one Coulomb is one Ampere of current passed in one second, the capacity of the cell in Ah is Q/3600.

From Equation (6), it can be seen that electrode structures with heavy molar masses reduce the ratio of charge transferred for a given gravimetric mass of reactants. Ergo, lightweight electrode materials are favoured in order to improve the specific capacity of the cell, i.e. its capacity per unit mass (typically mAh g^{-1} for cells or Ah kg^{-1} for battery packs), especially for mobile applications such as automotive traction batteries. Another important consideration for automotive applications is the volumetric capacity, i.e. the capacity of the cell per unit volume (mAh cm^{-3} and Ah l^{-3} for cells and battery packs, respectively), which impacts on how much battery capacity can be accommodated in a limited space. The gravimetric and volumetric energy density can be obtained by multiplying the specific or volumetric capacity respectively by the nominal voltage, i.e. the typical discharge potential of the cell or battery pack, which may be obtained from the Nernst equation (Equation (5)).

The maximum rate at which a cell can charge or discharge is also an important consideration when designing an automotive battery pack; the pack must be able to deliver the maximum power rating of the motor(s) and accept the maximum power of the charging equipment that the vehicle is designed to be compatible with, e.g. a rapid charger. Conventionally, the rate at which a cell is charging or discharging is expressed as the C-rate, which is inversely proportional to the time required to reach 0 % SoC from 100 % SoC (or vice versa for charging)

at a given current. As such, a cell discharging at 1 C would take one hour to fully discharge from 100 % SoC; a cell discharging at 0.1 C would take ten hours; and a cell discharging at 10 C would take six minutes. The maximum C-rate may be limited by mass transport, electron transfer kinetics or the internal resistance of the cell.

1.3 A history of automotive battery technology

In the early days of personal automotive transport, when both secondary batteries and internal combustion engines (ICEs) were in their infancy, electric vehicles (EVs) commanded a sizeable market share by virtue of their superior comfort and ease of use, especially when considering the dangerous crank handle starting procedure and complex gear shifting required on the first generation of ICE-powered vehicles. Lead-acid batteries, invented by Gaston Planté in 1859 and commercialised by Henri Tudor in 1886, were the only variant of secondary cell available at the time, having superseded the voltaic pile primary (single use) cells used in the first crude electric carriage developed by Robert Anderson in the 1830s [27]. Lead-acid batteries are comprised of a series of cells with stacks of alternating lead anode plates and lead oxide (PbO_2) cathode plates, immersed in a solution of sulfuric acid (H_2SO_4). On discharge, the hydrogen sulfate anion (HSO_4^-) participates in reactions to form lead sulfate ($PbSO_4$) at both electrodes, through oxidation with lead at the anode and reduction with PbO_2 and three H^+ cations at the cathode; the latter also forms two water molecules. The discharge reaction is depicted in Figure 1(a) and may be written thus for the full cell [28]:

$$PbO_2 + Pb + 2H_2SO_4 \rightarrow 2PbSO_4 + 2H_2O \qquad E_{OC} = 2.0 \text{ V}$$

Due to the weight of their components, lead-acid cells have a specific energy in the range of 25 - 35 Wh kg^{-1}. To put that into perspective, the energy contained in a fully charged 1 kg

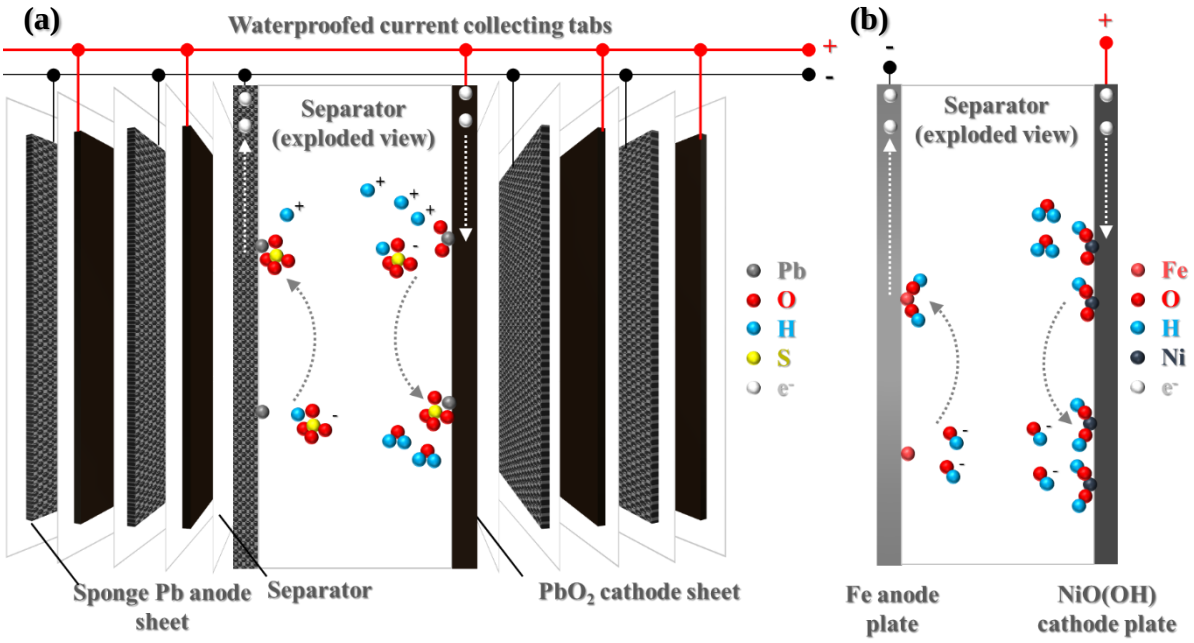

Figure 1: Exploded diagram of a lead-acid cell, depicting the discharge mechanism (a). The NiFe cell discharge mechanism is shown in (b); the layout of the NiFe cell is similar to the full lead-acid diagram in (a).

lead-acid battery would only satisfy the peak power demand of an 80 kW Nissan LEAF traction motor for 1.125 seconds. Therefore, EVs that used these cells were hindered by considerable kerb weight; a prime example is the 500 kg Tudor battery pack which comprised 37 % of the kerb weight of the Egger-Lohner C.2 electric vehicle, which was technically the first Porsche ever made [29]. Additionally, side reactions during charging lead to the evolution of oxygen and hydrogen, known as "gassing," and result in the incomplete removal of $PbSO_4$ from the electrodes, thus leading to their passivation and eventual cell failure [28]. Nonetheless, lead-acid cells were used to power the Jamais Contente past the 100 km h^{-1} barrier in 1899, setting a world vehicle speed record in the process [30]. They also featured in New York's Electric Vehicle Company taxi fleet in the late 19th century, in conjunction with battery swapping stations a century before Renault and Tesla announced their own plans for such infrastructure [31, 32, 33].

The first commercial challenge to lead-acid cells was unveiled by Waldemar Jungner and Thomas Edison in 1901 in the form of the nickel-iron (NiFe) battery. NiFe cells use abundant and relatively nontoxic electrode materials in the form of nickel hydroxide (NiO(OH)) cathodes and iron anodes, and an alkaline electrolyte solution of 30 wt. % potassium hydroxide (KOH), producing the following full cell discharge reaction (Figure 1(b)):

$$Fe + 2NiO(OH) + 2H_2O \rightarrow Fe(OH)_2 + 2Ni(OH)_2 \qquad E_{OC} = 1.2\ V$$

The addition of 50g l^{-1} LiOH has been shown to increase the calendar life of the cell and the discharge capacity of the cathode. NiFe cell chemistry is tolerant of overcharging, overdischarging and long-term storage, and has been demonstrated to have a calendar life spanning decades, thus making it far more robust than lead-acid cells, which by the advent of NiFe technology had started to fail en masse in the Electric Vehicle Company's taxi fleet amidst the hastened expansion of their business [31, 34]. However, NiFe cells suffer from high rates of self-discharge, losing *circa* 15 % of their capacity per week at 298 K, due to the close proximities of the potentials of the anode and the hydrogen evolution reaction, resulting in hydrogen evolution throughout the cycling procedure and when the cell is not in use. This is despite the addition of LiOH mitigating the impact of the oxides and hydroxides of anode impurities, such as magnesium, which lower the oxygen overpotential of the cathode. The problem increases five-fold at 313 K, thus proving to be an issue for use in vehicles in hotter climates, but is alleviated somewhat at lower temperatures. However, running in sub-zero temperatures is also problematic due to the passivation of the iron anode. Furthermore, NiFe cells suffer from a low energy efficiency, ranging from 50 % - 70 % [35, 36, 37]. Consequently, lead-acid traction batteries were the most common variant throughout most of the 20th century, appearing in vehicles such as the Detroit Electric range (with optional $600 NiFe upgrade, which saved 147 kg of kerb weight), of which several examples were purchased by Henry Ford.

By the 1930s, the proliferation of petrol and diesel refuelling infrastructure, and falling price and increasing practicality of ICE-powered vehicles, had relegated EVs to niche markets [38, 39]. When EVs were briefly revived to tackle local emissions and the oil crisis the 1960s and 1970s, it was lead-acid battery packs that were installed in leading examples, such as the Enfield 8000 and Sebring-Vanguard Citicar [27, 40, 41].

A more sustained wave of EV marketing and manufacturing began in the 1990s. During this period, automotive manufacturers moved away from lead-acid battery packs towards rival secondary cell chemistries for the first time, with sodium-sulfur (NaS) being one of the first such alternative cell chemistries to be trialled in EVs. The NaS cell chemistry, originally developed by Ford in the 1960s [42], is based on the oxidation of molten sodium to Na^+, which traverses a ceramic beta alumina solid electrolyte (BASE) to a chamber of molten sulfur. The solid electrolyte contains Na^+ mobile ions and facilitates rapid ionic conductivity of Na^+ whilst prohibiting electronic conductivity. Therefore, electrons from the Na^+ ions must traverse the external circuit to the chamber of molten sulfur, resulting in the formation of polysulfide. The poor electronic conductivity of the BASE material ensures low rates of self-discharge and a typical coulombic efficiency of 89 %. The full cell reaction (Figure 2(a)) may be written as:

$$2Na + xS + \rightarrow Na_2S_x$$

where $3 < x < 5$, giving a corresponding E_{OC} range of 1.78 V – 2.208 V [43].

NaS battery packs offer a specific energy of 110 Wh kg^{-1}, a step change in comparison to the cell chemistries that preceded them. Additionally, they can provide 150 W kg^{-1} of power and endure 1,000 cycles to high Depth of Discharge (DoD) [44]. Consequently, they were trialled in the Ford Ecostar van and BMW E1 of the early 90s, giving them a range of 100 miles and 125 miles per charge, respectively [41, 45]. However, these were not as straightforward to

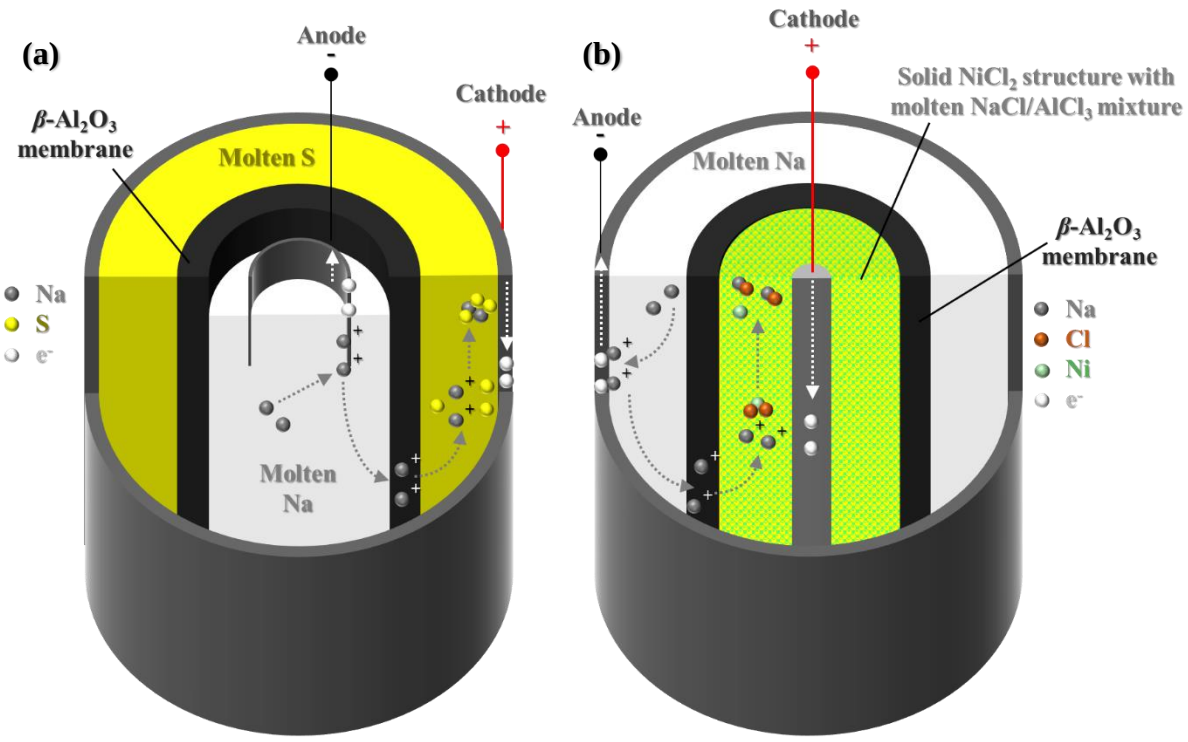

Figure 2: Schematics and discharge mechanisms of NaS (a) and ZEBRA (b) molten salt cells.

implement as lead-acid cells since, being molten salt batteries, they required operating temperatures of 300 – 350 °C. Whilst this was achievable, the corrosive nature of sodium polysulfides at high temperatures, combined with the flammability of sodium in contact with air, resulted in two Ecostar battery fires whilst the vehicles were recharging, and the project was halted [44, 46].

Improvements to molten-salt battery technology were achieved by the Zeolite Battery Research Africa (ZEBRA) project, which resulted in the eponymous cell based on sodium nickel-chloride chemistry. In a ZEBRA cell, the molten sulfur cathode is replaced with a solid porous $NiCl_2$ structure containing a molten $NaAlCl_4$ secondary electrolyte, resulting in the following full cell discharge reaction (Figure 2(b)) [47]:

$$2Na + NiCl_2 \rightarrow Ni + 2NaCl \qquad E_{OC} = 2.58\ V$$

Transport for the Na^+ ions is provided by the eutectic mixture of NaCl and $AlCl_3$, i.e. a mixture with a ratio that yields the lowest melting point for the two components of the electrolyte by impeding each component's crystallisation. The ZEBRA cell has similar energy and power densities to NaS cells, but is inherently safer due to its use of solid state cathode materials, thus reducing the likelihood of corrosion; the stability of the electrolyte when in contact with sodium metal; and the ability to be assembled in the discharged state [43, 44, 48]. Additional advantages include an energy efficiency of up to 90 % and the ability to overcharge by the equivalent of 5 % of the cell's capacity *via* a reversible reaction in the secondary electrolyte:

$$2NaAlCl_4 + Ni_4 \leftrightarrow 2Na + Ni(AlCl_4)_2$$

The latter is advantageous in automotive applications since it allows a fully-charged EV to drive downhill without any impact on regenerative braking performance. However, the battery packs require heating elements to maintain operating temperature even when not in use, consuming up to 14 % of the pack's capacity per day in the process [49]. BMW trialled the ZEBRA cell in its E2, but concluded that energy storage technologies were not yet mature enough for commercialisation [45]. ZEBRA cells would later be revived as a battery option for Modec vans in the mid-to-late 2000s before the company entered administration. Examples with ZEBRA battery packs are still running today, but encounter difficulties in recouping their maximum range if left unplugged for prolonged periods of time, thus allowing the electrolyte to solidify.

Nickel cadmium (NiCd) cells, which offer a doubling of energy density over lead-acid, were most prominently used in PSA Peugeot-Citroen's range of EVs from 1995-2005, including the Peugeot 106 Electric and Citroen Berlingo Electric [44]. The Saft STM 5-100MRE prismatic cells in question (Figure 3(a)) were comprised of alternating sheets of nickel(III) oxide-

hydroxide (NiO(OH)) cathodes and cadmium anodes with separators in-between, with an electrolyte of potassium hydroxide (KOH) in deionised water. The discharge reaction is thus:

$$Cd + 2NiO(OH) + 2H_2O \rightarrow Cd(OH)_2 + 2Ni(OH)_2 \quad E_{OC} = 1.2\ V$$

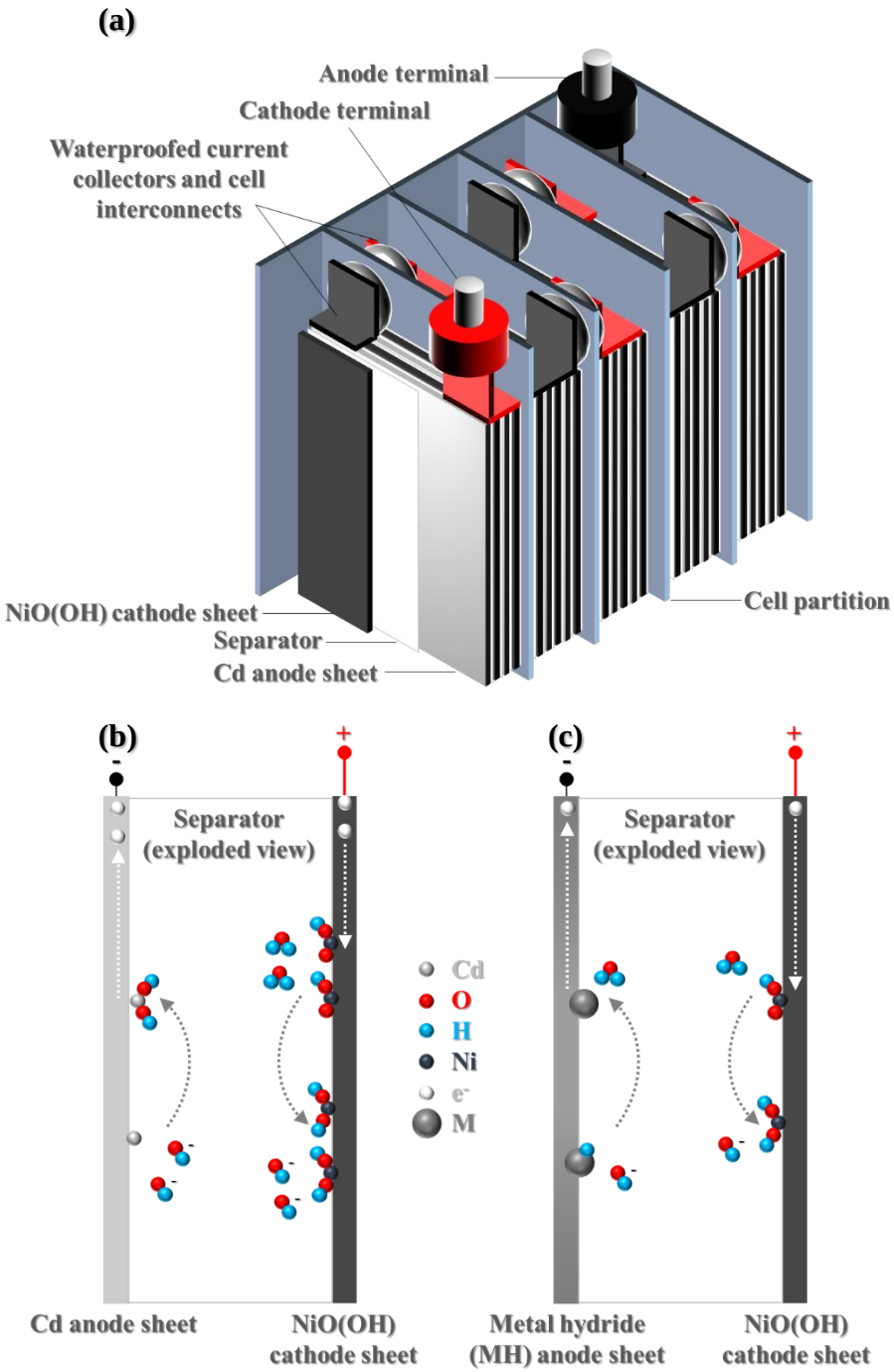

Figure 3: Cutaway diagram of a Saft STM 5-100MRE NiCd cell as used by Peugeot-Citroen between 1995 and 2005 (a), with the NiCd discharge mechanism (b). The NiMH discharge mechanism is shown in (c).

PSA achieved a range of 50 miles per charge in their vehicles, although this was by incorporating at least 264 kg of batteries, using deliberately low-power traction motors (20 kW for the 106 Electric), electronically limiting the top speed to 60 mph and heating the cabin using a Webasto oil-burning heater in order to conserve energy [50]. Additionally, NiCd cells undergo gassing of the electrolyte when overcharged, so the battery packs in PSA Peugeot-Citroen EVs consequently required an authorised dealer to occasionally top up their electrolyte with deionised water through the vehicle's inbuilt plumbing. NiCd cells suffer from "memory effect" whereby, upon being consistently charged from the same mid-point SoC rather than being fully discharged first, the cell potential drops at said SoC, thus giving the impression that the cell's charge has been fully depleted when it has not [51]. This has to be factored into the EV's drive cycle in order to preserve the health of the battery pack and prevent a pronounced loss of peak power with several percent SoC remaining. Whilst the performance characteristics of the vehicles were still respectable at the time and represented a marked improvement over previous generations of EVs, the cells, built by Saft, suffered from separator defects that resulted in the dendritic growth of cadmium from the anode, which reached the cathode and internally shorted the cell. As a result, some battery packs lasted only a fifth of their expected 100,000 km lifespan [52]. Whilst this was remedied by Saft in battery packs made after the year 2000, their use in automotive applications was ultimately banned under EU law due to their use of toxic heavy metals [53].

The biggest breakthrough in traction battery technology in the 1990s was the nickel metal hydride (NiMH) cell. Advanced versions of these cells provide up to 40 % greater specific energy than NiCd cells; an operating temperature range of -30 °C → 70 °C; a cell chemistry free from toxic heavy metals; tolerance to overcharge and overdischarge due to gas recombination reactions which prevent a build-up in pressure; a cycle life in excess of 1,000 cycles at high DoD; rapid charge capability on account of their > 1000 W kg^{-1} power

density; and a calendar life comparable to that of the car that it powers [44, 54, 55, 56, 57]. Pricing at the time was considered competitive, although their value of $500-$600 per kWh is considered expensive today [58]. The NiMH cell chemistry differs from NiCd in that the cadmium anode is replaced with a metal alloy, denoted as M, which is able to store hydrogen (hence MH). Consequently, the two-electron Cd process from NiCd cells is replaced with a one-electron process surrounding M, such that upon discharge, M is dehydrogenated, with the hydrogen subsequently reacting with OH^- in the electrolyte to form water (Figure 3(c)). The full cell reaction is [55]:

$$MH + NiO(OH) \rightarrow M + Ni(OH)_2 \qquad E_{OC} = 1.2\ V$$

The 63 Wh kg^{-1} specific energy of Panasonic's EV-95 NiMH cells allowed some automotive manufacturers to produce EVs capable of exceeding 100 miles per charge, such as the GM EV1 and the Toyota RAV4 EV, both of which were available by fixed-term lease only [59, 60, 61]. These cells performed reliably, with the only major drawback being the high rate of self-discharge, ranging from 15 % to 60 % per month [57, 59]. Alas, the use of NiMH cells in EV battery packs was curtailed when Chevron bought the patent to this technology and threatened to sue Panasonic, if it continued to produce its EV-95 (95 Ah) NiMH battery [62, 63]. NiMH cells were restricted to use in small-capacity battery packs in hybrid vehicles such as the Toyota Prius and Honda Insight, and the widespread uptake of EVs was delayed by about a decade [64]. The majority of NiMH-powered EVs were repatriated and crushed at the end of their leases, with only a handful of deactivated EV1s and 328 functioning RAV4 EVs surviving after considerable public pressure to save the vehicles [65]. Many of the latter are still running on their original battery packs, which still yield upwards of 70 % of their original capacity [60]. They also retained their market value during the 2000s until the advent of a new wave of EVs powered by the latest development in battery technology: lithium-ion.

1.4 Current generation: the lithium-ion battery

It was only when lithium-ion cells started to reach maturity that electric vehicles started to become mainstream for the first time in over a century. These cells operate by a markedly different mechanism from their predecessors, relying on the intercalation and deintercalation of lithium ions moving between the anode, which is usually a variant of carbon such as graphite, and a heavy metal oxide cathode, rather than forming new discharge products (Figure 4). Upon the introduction of the first Li-ion cell by Sony in the early 1990s, Nissan quickly partnered with Sony to produce the first generation of Li-ion powered electric vehicles, namely the Prairie Joy EV and Altra EV of 1996 and 1997, respectively [66]. The battery pack was based on the lithium cobalt oxide (Li_XCoO_2, or LCO) cathode chemistry and yielded a specific energy of

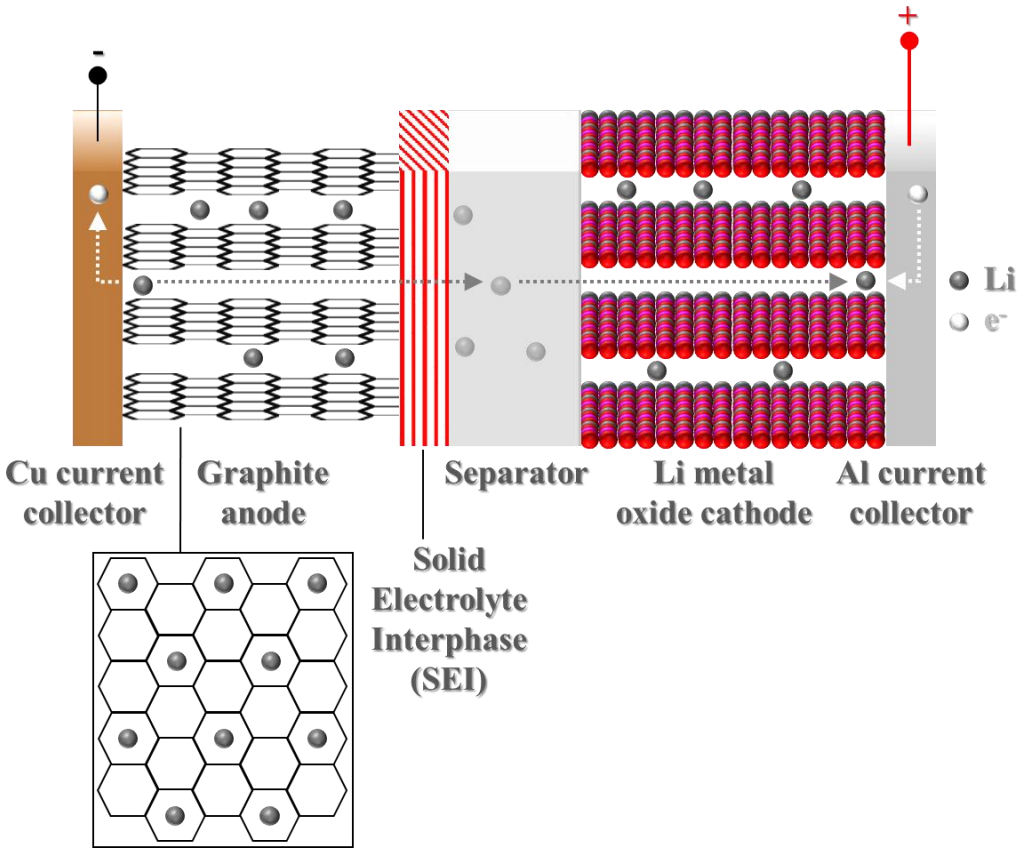

Figure 4: Schematic of a lithium-ion cell, depicting the discharge mechanism and the ordering of Li^+ ions in the anode in the charged state, which is limited to one Li^+ ion per six C atoms (inset).

90 Wh kg^{-1} [67]. However, cobalt is a toxic and expensive heavy metal, and LCO is chemically unstable due to the high reactivity of the cathode material in the delithiated state [68]. Both of these issues have been addressed by the development of alternative cathode materials such as lithium iron phosphate ($LiFePO_4$, or LFP), as used by Chinese EV manufacturer BYD, and lithium manganese oxide (LMO) and lithium nickel oxide (LNO) [69]. Unfortunately, LFP has been shown to exhibit a memory effect, specifically under irregular cycling patterns such as EV drive cycles, whilst LMO and LNO have poor cycling and thermal stability, respectively [70, 71, 72]. The latter has resulted in some manufacturers blending LMO with other metal oxides to improve stability and maximum current delivery, which has resulted in a return to chemistries that contain heavy metals. One such example is the lithium nickel cobalt aluminium oxide (NCA)-LMO blend used in the Nissan LEAF [73, 74].

In recent years, new cathode chemistries comprised of cobalt-containing lithium oxides have been developed that offer distinct performance advantages over the original LCO. This has resulted in some automotive manufacturers opting for cell chemistries that do not contain any cobalt-free lithium oxides. For example, Tesla favours NCA for its market-leading energy density, whilst lithium nickel manganese cobalt oxide ($Li_XNi_{1/3}Mn_{1/3}Co_{1/3}O_2$, or NMC), which has high thermal stability and excellent capacity retention, features in the Toshiba SCiB cells offered in the Mitsubishi i-MiEV and Honda Fit EV [69, 72, 75, 76, 77]. The cobalt content of cells containing NMC can be reduced through layering or blending with LMO, which in turn increases the specific energy; this is used in the Renault Zoe and Fiat 500e [74, 78].

The solvents used in the electrolyte of Li-ion cells have a reduction potential that is higher than that of the graphite anode process. Thus, the electrolyte decomposes during the first few cycles of a Li-ion cell. However, the decomposition process forms a layer of electrolyte decomposition products on the anode. The layer, known as the solid electrolyte interphase (SEI), is passivating against further decomposition and is Li^+ selective, thus allowing the cell

to continue operation for hundreds, or thousands, of cycles with a vastly reduced rate of decomposition in comparison to the first few cycles, as well as protecting against lithium plating under normal operating conditions [79, 80, 81, 82]. The SEI formed in Li-ion cells is unique amongst alkali metals in that it is completely insoluble and therefore permanent. Lithium is irreversibly consumed during the formation of the SEI. Therefore, it is common practice to manufacture cells with an excess of lithium in the cathode to compensate for this. Since the cell is built in the discharged state, and therefore initially contains no lithium in the carbon anode, the lithium content of the cathode determines the capacity of the cell, i.e. it is cathode-limited [83, 84].

The development of Li-ion cell chemistries has resulted in the specific energy of market-leading cells reaching 150 – 200 Wh kg^{-1} [73]. However, this has been achieved in part by loading greater amounts of active material into the cell, which increases pressure on the separators and jeopardises safety [81]. Pure lithium could theoretically be used as the anode material, but this presents excessive risk given its instability towards many organic electrolytes, air and water [79]. Nonetheless, Tadiran commercialised a Li metal *vs.* $LiMnO_2$ cell in the mid-1990s, with the notable safety mechanism of a liquid electrolyte that polymerises when the cell is shorted or overheated [85]. The polymerisation process increases the internal resistance of the cell, preventing thermal runaway, i.e. the energy (heat) produced by the reaction exceeding the point where it becomes self-sustaining, leading to explosion. However, no Li-ion cells with pure Li anodes have been used in mainstream automotive traction applications.

The most common anode design for Li-ion cells features a variant of carbon, such as graphite, intercalated with lithium ions. The intercalation mechanism favours the formation of the minimum number of Li^+ layers possible, since this is the path of least resistance owing to the energy required to expand the van der Waals gap between graphene layers in the graphite and

to overcome the repulsive force between layers of intercalated Li^+ ions. Consequently, a charged carbon anode has densely populated, highly organised Li^+ layers (Figure 5). The carbon-based anode improves safety over Li metal by reducing the likelihood of dendritic Li deposition upon charge or the reaction of metallic Li with the electrolyte. However, it reduces the energy density of the anode since graphite can only accommodate one lithium ion for every six carbon atoms (Figure 4) [80]. Furthermore, safety may still be impaired by manufacturing defects such as metal particulate ingress during the crimping of cylindrical cell housing (e.g. 18650 format). These can form dendrites on the anode, which puncture the membrane and short-circuit the cell, leading to thermal runaway [86].

Recently, anodes have been developed that are formed of lithium titanate oxide ($Li_4Ti_5O_{12}$, or LTO), a material that has a much greater surface area than carbon. As a result, lithium can intercalate and deintercalate much quicker and easier than in carbon, boosting the maximum current rates upon charge and discharge and improving the reversibility of the discharge mechanism, despite having poor conductivity [87, 88, 89]. Furthermore, LTO anodes do not undergo structural change during the intercalation and deintercalation of lithium ions [87, 90]. LTO-based cells are therefore capable of achieving exceptional cycle lives, such as the

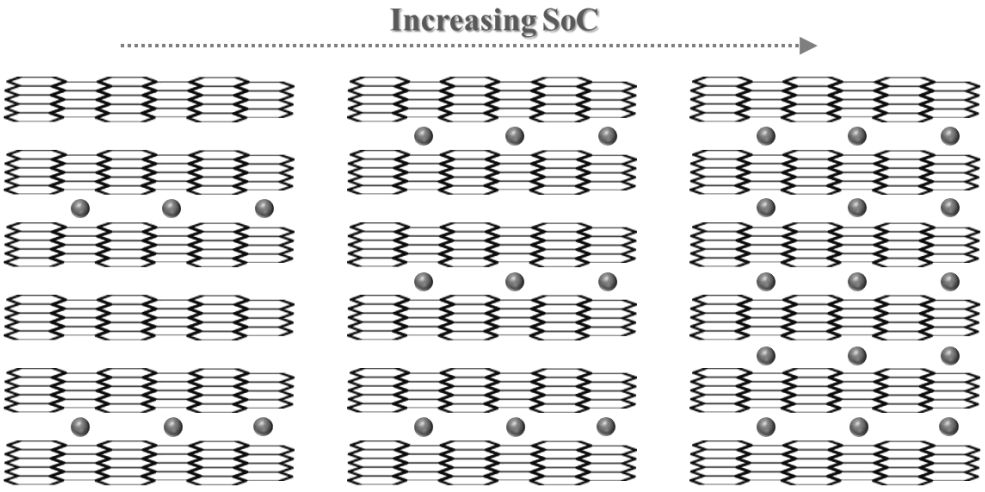

Figure 5: Illustration of the change to the ordering of Li^+ ions between layers of graphene in the anode of a lithium-ion cell with increasing State of Charge (derived from [80]).

>10,000 cycle rating of Toshiba SCiB cells [91]. Despite being able to accommodate more lithium ions than graphite, the higher anodic potential (and thus lower potential difference for the full cell) and higher gravimetric density of LTO results in a decrease in specific capacity *vs*. graphite anodes, with a theoretical maximum of 175 mAh g^{-1} compared to 372 mAh g^{-1} for graphite anodes [92]. Due to having an anodic potential above the decomposition potential of typical electrolyte solvents (1.5 V as opposed to ≈ 0.8 V, *vs*. Li/Li^+), it was previously believed that LTO anodes did not undergo SEI formation [81, 93]. However, this has been latterly disproven [94]. Table 1 summarises the performance characteristics of the most commonly used electrode materials.

Li-ion cells are particularly sensitive to operating outwith their manufacturer-determined potential operating windows. Overdischarge leads to the continuous reduction of the electrolyte due to the absence of a cathode SEI, with the subsequent release of flammable gases; the irreversible structural change of the anode due to excessive loss of lithium, with subsequent loss of anode active material; and the oxidation and decomposition of the copper anode current collector, which then forms dendritic growths upon charging, leading to internal short circuits [69, 80, 81, 84, 95].

During overcharge, oxygen is removed from the cathode active material, rendering it inert and thus resulting in irreversible capacity loss. Common electrolytes typically oxidise at potentials greater than 4.5 V *vs*. Li/Li^+, releasing flammable gases and producing insoluble decomposition products that can block the porous electrode structures [84, 96]. When the anode potential falls below 0 V *vs*. Li/Li^+, lithium is prevented from intercalating into the active material, resulting in anodic lithium plating. This has a number of consequences, including reactivity towards, and decomposition of, liquid electrolytes; mechanical stress upon cell components, with the risk of damage to the SEI upon reversal; loss of a conductive pathway to the anode material caused by porous structures in the lithium, thus irreversibly reducing its capacity; and

Material	Theoretical specific capacity of material	Advantages	Disadvantages
Cathodes			
Lithium cobalt oxide	140 mAh g^{-1} [81]	Easy to fabricate; stable cycling if lithium utilisation is less than 50 % [97]	Cobalt is toxic, expensive heavy metal; not suited to rapid charging; poor thermal stability with standard electrolytes [71, 75, 76, 96, 98]
Lithium iron phosphate	170 mAh g^{-1} [81]	Low cost; non-toxic; high safety [81]	Low conductivity, which requires carbon coating which lowers specific capacity; memory effect [70, 81]
Lithium nickel oxide	275 mAh g^{-1} [72]	High energy density; low cost *vs*. cobalt	Poor thermal stability; Ni^{3+} more easily reduced than Co^{3+}; Ni^{2+} blocks Li^{+} diffusion pathways [71]
Lithium manganese oxide	240 mAh g^{-1} [97]	Electrical and thermal stability [84, 71]	Poor cycling stability: Mn^{3+} disproportionates to Mn^{2+} and Mn^{4+}, which is removed from the cathode structure and decomposes the anode SEI [72]
Lithium nickel cobalt aluminium oxide	200 mAh g^{-1} [72]	High practical specific energy	Elevated capacity fade at temperatures > 40 °C [72]; reactive materials
Lithium nickel manganese cobalt oxide	160 – 170 mAh g^{-1} [81]; 195 mAh g^{-1} for macroporous versions [77]	Excellent thermal stability with standard electrolytes; good capacity retention even at high temperatures [75, 76, 77]	Cobalt is a toxic heavy metal
Anodes			
Graphite	372 mAh g^{-1} [79]	Low cost, good cyclability, stability at ambient temperatures [79]	Low solid diffusion coefficient; expands upon charging; low onset temperatures for decomposition reactions in the charged state, leading to thermal runaway (as little as 80 °C) [71, 99, 100, 101]
Lithium titanium oxide	175 mAh g^{-1} [92]	Minimal volume change during cycling; long cycle life; superior thermal stability with common electrolytes [99]	Low specific capacity

Table 1: Summary of commercial lithium-ion electrode materials, their advantages and disadvantages.

increasing difficulty for lithium intercalation and deintercalation under normal operating conditions, which in turn accelerates the lithium plating process [79, 95]. Consequently, Li-ion battery manufacture incorporates a number of safety mechanisms to protect the cell when it is overcharged or overdischarged, including low lithium content in graphite anodes to reduce the likelihood of lithium plating, albeit at the expense of specific capacity, and the use of polymer separators with melting points of between 130 °C and 160 °C to prevent thermal runaway by blocking the ionic current pathway [84]. LTO anodes also help to prevent lithium plating due to their higher potential than graphite anodes. Additionally, LTO anodes undergo a pronounced dip in potential upon overcharge, making the process easier to identify from the full cell potential profile than with graphite anodes due to the latter's flat potential profile that operates close to 0 V *vs*. Li/Li^+ upon charge [87, 89].

Li-ion cells are also sensitive to operating temperature. Lithium plating of the anode is the dominant failure mechanism when Li-ion cells are operated below the optimum temperature of 25 °C [96, 102, 103]. This is reflected in an increase in internal resistance caused by poor reaction kinetics [104]. Some of the plated lithium is able to diffuse into the anode if the cell is allowed to return to ambient temperatures under rest, since the solid diffusion coefficient of the anode, which is rate-limiting at low temperatures, increases sufficiently to allow lithium diffusion to proceed [105].

At temperatures above 25 °C, the dominant failure mechanisms are loss of lithium from the cathode structure and decomposition of the electrolyte, resulting in capacity loss. Lithium and other constituent elements from the cathode and electrolyte then proceed to thicken the anode SEI layer, which increases internal resistance [103, 104]. This impedance may be worked around by reducing the charge and discharge rates, particularly upon approaching the maximum and minimum SoC respectively, which allows the original capacity of the cell to be attained; this is partly why modern EV rapid chargers taper off current delivery to an EV as the

SoC nears 100 %. However, this has obvious disadvantages concerning automotive applications since it implies limiting power delivery or increasing charging time in order to conserve the State of Health (SoH) of the pack [106]. At even greater temperatures, the SEI breaks down, allowing lithium intercalated into the anode to decompose the electrolyte, leading to thermal runaway; this occurs at 80 °C in carbon anodes when used with standard electrolyte solutions such as an ethylene carbonate/diethyl carbonate mixture with $LiPF_6$ salt [101].

Self-discharge is also temperature dependent, ranging from the comparatively low rate of *circa* 3 % per month at 25 °C to > 10 % per month at 55 °C [84, 107, 108]. This process involves the oxidation of the electrolyte at, and insertion of lithium into, the cathode structure, whilst the anode retains its original lithium content. Consequently, the electrodes become unbalanced, increasing the likelihood of lithium plating [84]. Dissolution of the transition metal component of the cathode structure, instigated by electrolyte impurities such as hydrogen fluoride (HF) and water, is also observed at elevated temperatures, even when the cell is not in use [107].

The above sensitivities of Li-ion cells present issues in automotive applications, due to the likelihood of operating in temperature extremes, such as winter driving, and the high current densities arising from harsh acceleration, regenerative braking and rapid charging [79]. Therefore, complex battery management systems (BMS) have been developed that monitor the temperature and potential of each string of cells in the battery pack to prevent them from overheating or straying beyond their manufacturer-specified potential window, thus preventing thermal runaway and subsequent explosion. Some systems also feature battery heaters to prevent lithium plating when charging in cold weather, such as on the Nissan LEAF. The use of highly sensitive thermocouples to detect the temperature inflection point that indicates onset of lithium plating during charging has also been suggested [109]. Thanks to well-designed BMS algorithms and improvements in battery manufacturing and pack layout, these battery packs are lasting longer than many critics had predicted [110, 111].

The lithium intercalation mechanism of graphite has a theoretical specific capacity of 372 mAh g^{-1} [79]. Taking typical Li-ion cell potentials into account, this translates into an anode specific energy of 1190 – 1380 Wh kg^{-1} which, in conjunction with similarly energy-dense cathode materials and lightweight components such as separators and casing, could exceed the 700 Wh kg^{-1} target for automotive traction batteries set by the New Energy and Industrial Technology Development Organization (NEDO) of Japan [24]. However, in reality, modern Li-ion cells are limited to a specific energy of *circa* 200 Wh kg^{-1} at best. This is due to the mass of the separator and cell housing, coupled with the inferior specific capacities of metal oxide cathode materials that are typically limited to *circa* 200 mAh g^{-1} [112]. Therefore, a step change in cell chemistry is required to meet the targets of the automotive industry.

1.5 The lithium-air cell

The metal-air family of cell chemistries, which typically consist of a pure metal anode and porous cathode, react with oxygen from the air to produce metal oxides in the cathode structure. By virtue of not containing all of their constituent components, they are lightweight, have high specific capacities and are intrinsically protected against thermal runaway since the maximum reaction rate is determined by the oxygen concentration in, and the oxygen diffusion coefficient of, the electrolyte, which will likely be insufficient to facilitate an explosion [113]. As such, these cells have been of considerable interest to the automotive industry since the 1960s, when Scottish Aviation were closely following the development of the zinc-air cell with the hope of using it in their Scamp electric car [114]. Alas, today, the only commercial variant of the metal-air cell is the low-current zinc-air primary cell commonly used in hearing aids [115]. Whilst metal-air cells based on numerous metals have been investigated by the automotive industry in recent years, a significant amount of attention has been devoted to the lithium-air cell, in both aqueous and non-aqueous forms; in this work, only the latter is considered.

The first non-aqueous Li-air cell was introduced by Abraham and Jiang in 1996 [116]. It represented a radical departure from conventional Li-ion cells, with pure lithium foil used as an anode, the carbon active material moved to the cathode and heavy metal oxide materials removed completely. These cells utilise the lightest metal in the periodic table, undergoing a two electron reduction mechanism at the cathode to form lithium peroxide, Li_2O_2:

$$2Li^+ + 2e^- + O_2 \rightarrow Li_2O_2 \qquad E_{OC} = 2.96 \text{ V } \textit{vs.} \text{ Li/Li}^+$$

This reaction yields a theoretical maximum specific energy of 3,505 Wh kg^{-1} for the cathode, including the mass of oxygen [116, 117, 118]. Admittedly, any commercially-developed Li-air cells would not reach this specific capacity due to the mass of the separators, counter electrode, electrolyte and cell casing. However, a cell specific energy in excess of the 1,638 Wh kg^{-1} tank-to-wheel efficiency of an ICE could be achievable [25]. Consequently, Li-air cells have become the subject of a global research effort, which intensified upon the discovery that reversible cell chemistries could be fabricated [119].

During the lithium-air discharge reaction, oxygen (O_2) molecules from the atmosphere enter the porous network of the cathode, where they are reduced to form $O_2^{\bullet-}$ radicals on the pore walls:

$$O_2 + e^- \rightarrow O_2^{\bullet-}$$

Lithium ions traverse the non-aqueous electrolyte to the cathode, where each $O_2^{\bullet-}$ radical takes on one Li^+ ion to form lithium superoxide, LiO_2, followed by a second Li^+ ion and electron to form the final discharge product lithium peroxide, Li_2O_2:

$$O_2^{\bullet-} + Li^+ \rightarrow LiO_2$$

$$LiO_2 + Li^+ + e^- \rightarrow Li_2O_2$$

Li_2O_2 is insulating and insoluble in organic electrolyte, and thus forms a passivating film over the reaction sites (i.e. the cathode pore walls), which terminates the reaction. It is therefore advantageous to use a cathode structure with a high surface area since this will deliver a higher discharge capacity by providing more reaction sites and thus taking longer to passivate [116]. Whilst Li_2O_2 is insoluble in the non-aqueous Li-air cell, the reaction is reversible, so the Li_2O_2 layer is oxidised back to Li^+ and O_2 upon charging the cell, with the oxygen returning to the atmosphere.

Until recently, it was assumed that Li_2O_2 only forms on the surface of cathode pores. However, Johnson *et al.* have suggested that the solution-phase nucleation and growth of Li_2O_2 crystals may take place in Li-air cells [120]. In this process, $O_2^{\bullet-}$ radicals drift away from the pore walls into the electrolyte within the pore structure, where they form LiO_2. Then, two neighbouring LiO_2 particles undergo disproportionation, i.e. the simultaneous oxidation and reduction of species to create two different products, during which Li_2O_2 and O_2 are formed. The propensity for Li_2O_2 to form a surface layer or nucleate in solution is governed by the donor number of the solvent, illustrated in Figure 6, which relates to the binding strength with which the solvent

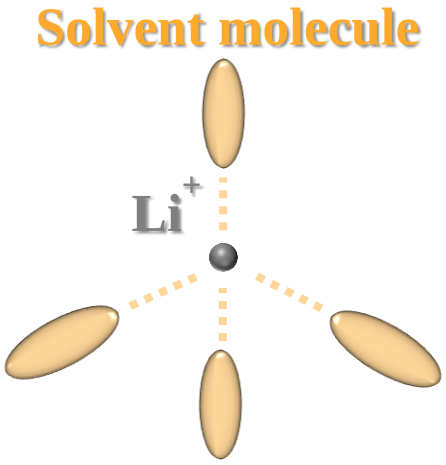

Figure 6: Illustration of how a solvent with a high donor number keeps Li^+ cations in solvation, thus encouraging solution-phase formation of Li_2O_2

is able to solvate the Li^+ cation. This value is the negative enthalpy (kJ mol^{-1}) arising from the addition of the solvent to an equal molar quantity of $SbCl_5$ in 1,2-dichloroethane. Solvents with higher donor numbers are able to keep more Li^+ cations in solvation than solvents with low donor numbers.

Should the proposed solution-phase Li_2O_2 growth mechanism happen in real cells, the result will be a three-fold increase in specific capacity *vs*. surface-based reactions due to the continuous vacation, rather than passivation, of reaction sites [120]. The surface layer growth and solution phase discharge mechanisms are illustrated in Figure 7.

The foremost limitation that has thus far prevented lithium-air cells from reaching commercial viability is their limited cycle life. Bruce *et al.* were the first to demonstrate a secondary Li-air cell in 2006, but over the intervening decade, Li-air cells have rarely achieved more than fifty cycles before failure; often considerably less [113, 119, 121, 122, 123, 124, 125, 126, 127, 128]. One major contributor to the premature failure of Li-air cells is the instability of the electrolyte when exposed to $O_2^{\bullet-}$ radicals [119]. A prime example of the former is the propylene carbonate (PC) solvent favoured in many earlier studies [64, 113, 119, 121, 122, 123, 126]. The tertiary carbon group in PC is comparatively electropositive due the presence of an adjacent oxygen atom in the structure. As such, during the discharge reaction, it is attacked by $O_2^{\bullet-}$ radicals to form intermediate decomposition species which, through further oxidative decomposition, form the decomposition salts lithium carbonate, formate and acetate [129]. $O_2^{\bullet-}$ radical-led decomposition was confirmed experimentally through post-mortem analysis of cells after a certain number of discharges and cycles by Fourier transform infrared spectroscopy (FTIR), nuclear magnetic resonance spectroscopy (NMR) and mass spectrometry. These revealed the presence of the aforementioned decomposition products and their intermediate species as detailed in the proposed oxidative decomposition mechanism in [129] and outlined

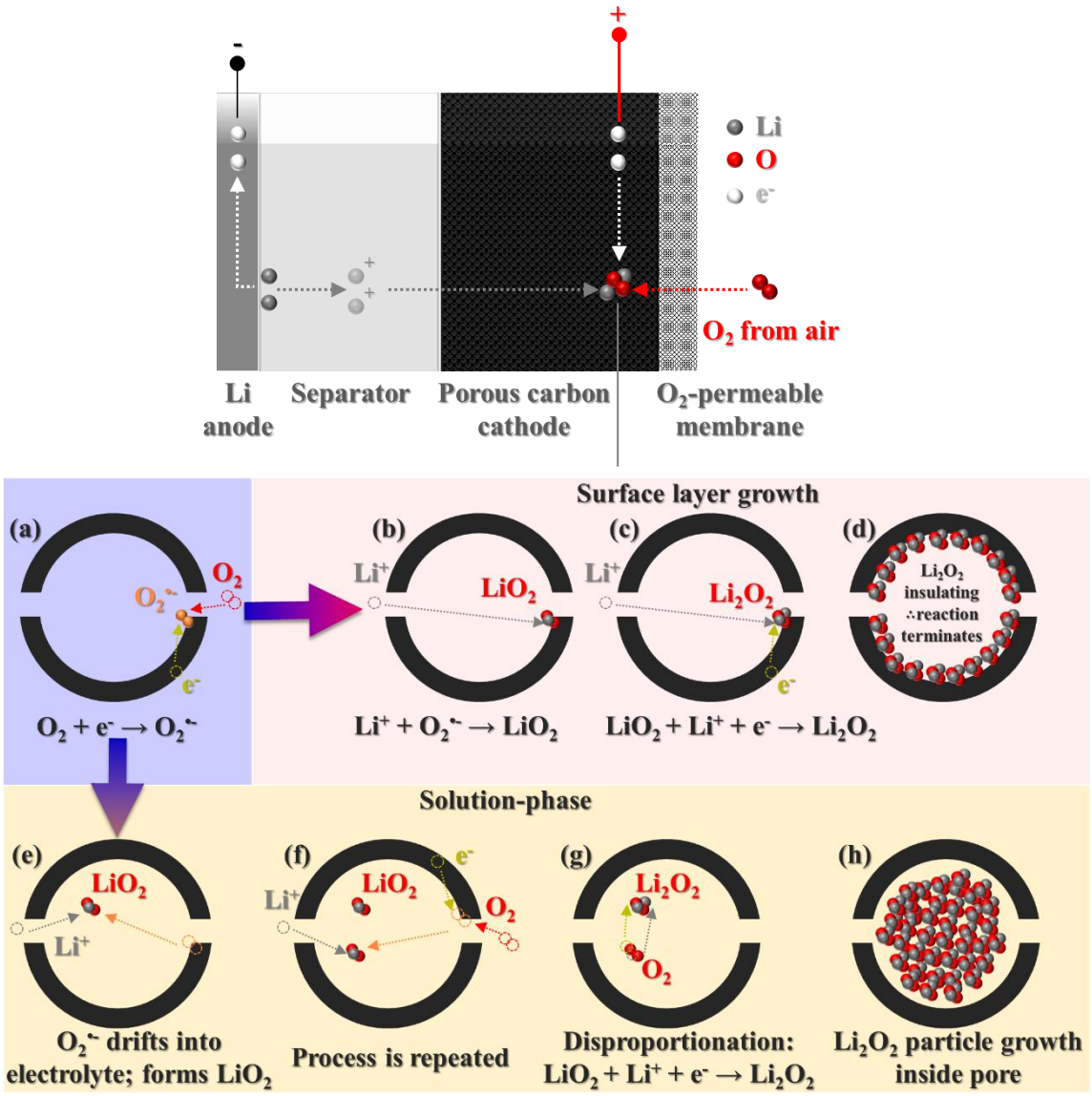

Figure 7: Schematic of a Li-air cell, showing the reduction of O_2 to the $O_2^{\bullet-}$ radical (a) followed by the surface layer (b-d) or solution-phase (e-h) Li_2O_2 formation mechanisms.

in Figure 8. Bryanstev and Blanco verified the mechanism theoretically using quantum chemical computations [130].

Whilst the formation of the desired Li_2O_2 discharge product is reversible, the decomposition salts are irreversible due to their high oxidation potentials and thus form a passivating layer on the cathode reaction sites over subsequent cycles, eventually leading to cell failure. Additionally, cyclic voltammetry revealed that the rate of this reaction is moderately fast; the lack of an oxygen evolution peak during the anodic sweep with oxygen-bubbled PC at sweep

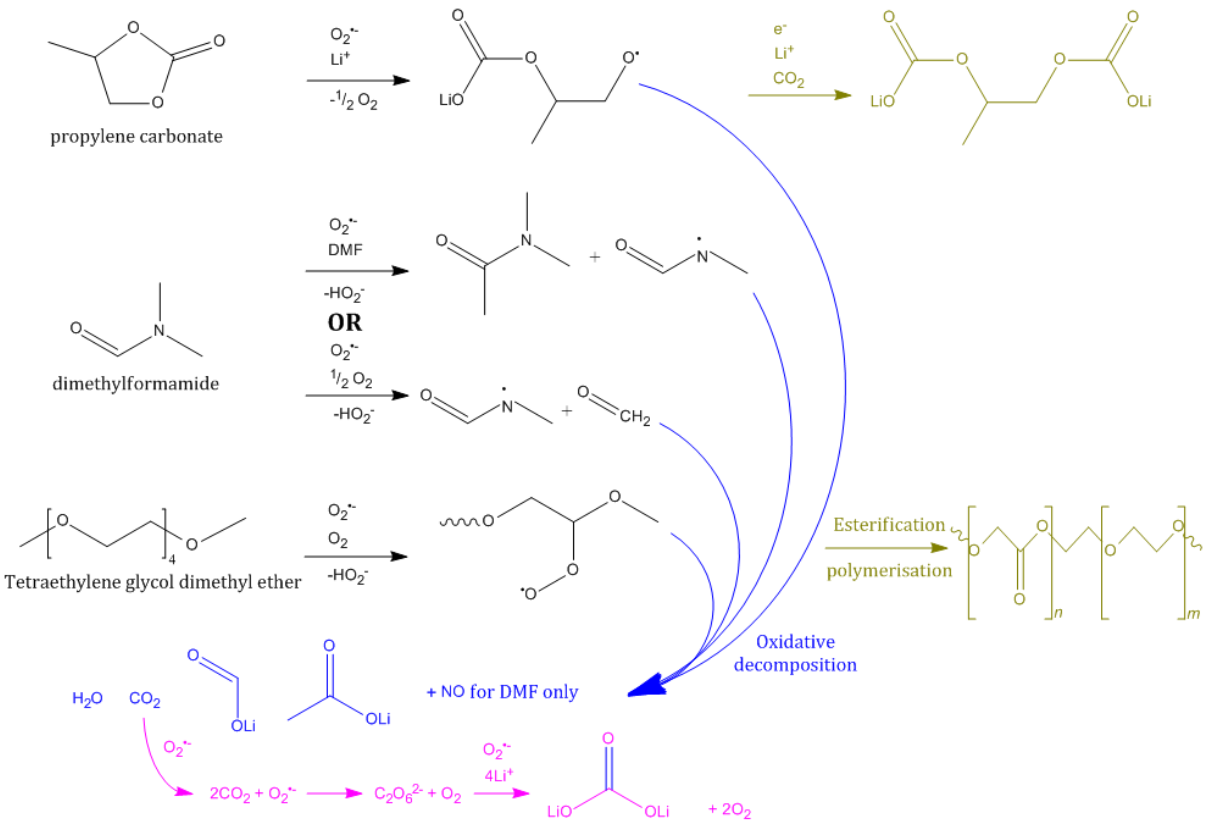

Figure 8: Decomposition mechanisms for PC, DMF and TEGDME during discharge in Li-air cells.

rates of 50 mV s^{-1} or less indicates the rapid consumption of $O_2^{\bullet-}$ radicals through the decomposition process [131].

Given the lack of stability of organic carbonates towards the intermediate species of the discharge reaction of the Li-air cell, attention turned to alternative aprotic electrolytes. Ethers, such as tetraethylene glycol dimethyl ether (TEGDME), were seen as promising candidates on account of their stability at the high potentials required to oxidise Li_2O_2 during charging, stability when used with pure Li anodes, low cost, relative safety, high dielectric constant (and thus ability to dissolve salt) and low volatility [125, 127, 132]. The latter is particularly crucial for real-world applications, where the cell sources oxygen from the atmosphere and is thus not a sealed system; a volatile electrolyte would be able to evaporate at a higher rate under such conditions. Studies of TEGDME electrolyte showed that the desired discharge product, Li_2O_2,

formed upon the first discharge, and thus that the solvent is more stable in the presence of $O_2^{\bullet-}$ radicals than organic carbonates. However, electrolyte decomposition was still observed, with lithium carbonate, formate and acetate also forming upon discharge, and the cells showing no sign of Li_2O_2 after the fifth discharge [127]. The proposed decomposition reaction for TEGDME, leading to the aforementioned Li salts, is shown in Figure 8. The solvent was also found to react with pure Li anodes [125]. Studies of dimethoxyethane (DME) showed that the electrolyte reacts with Li_2O_2 upon both discharge and charge [133, 134]. The latter results in the formation of a passivating layer of lithium carbonate over the Li_2O_2 layer to the point that the cell is no longer able to cycle. The study also indicated that CO_2 is evolved from DME-based cells upon charge due to the oxidation of lithium carbonate at high potentials [133]. Cathodes made of carbon nanotubes have been found to help improve the cyclability of DME, but Li_2O_2 is still not fully oxidised upon charge, thus leaving the reaction sites passivated [135]. Cyclic ethers 1,3-dioxolane and 2-methyl-THF have also been investigated, but they exhibit electrolyte decomposition during cycling as well, thus ruling out the suitability of ethers for application in a commercial Li-air secondary cell [127]. Further studies of ether electrolytes found that many are unstable in contact with Li_2O_2, decomposing to form carboxylates. The resultant decomposition mechanism can lead to the decomposition of the carbon cathode if it uses Kynar binder [136].

Amides, such as dimethylformamide (DMF), were assessed for suitability in Li-air systems on account of their stability towards $O_2^{\bullet-}$ radicals when used with molecular cations such as TBA^+ or quaternary ammonium [137]. Whilst DMF is reactive towards Li metal, it may be used in a Li-air cell in conjunction with a lithium anode with a preformed solid electrolyte interphase that is passivating against the solvent [138]. When DMF was used in a Li-air cell with $LiClO_4$ salt, post-mortem analysis of cathodes after the first discharge and cycle revealed that Li_2O_2 was formed and removed as hoped. Alas, successive cycles revealed the accumulation of

irreversible decomposition products, namely lithium carbonate, formate and acetate, on the cathode active sites, as well as the formation of NO, H_2O and CO_2. This resulted in cells losing two thirds of their original discharge capacity within ten cycles, thus indicating that the solvent is unsuitable for Li-air cells. Dimethylacetamide (DMA) and *N*-methyl-2-pyrrolidone (NMP) were also tested but found to encounter similar or heightened degradation during cycling [139]. The decomposition mechanism for DMF proposed in [139] is also shown in Figure 8.

Dimethyl sulfoxide (DMSO) gained interest as a Li-air electrolyte solvent after it was found to improve the stability of oxygen reduction intermediates, such as $O_2^{\bullet-}$ radicals, in a Li-air cell [140]. One notable drawback is that DMSO reacts with pure Li anodes due to the lack of formation of a stable SEI [141]. However, this can be mitigated by soaking the anodes in a solution of PC with the desired electrolyte salt for several days, then rinsing with pure DMSO prior to assembly. Studies of DMSO electrolyte found that it is able to form a stable, reversible cell in conjunction with a nanoporous gold cathode; the same was attempted with DME, but this was found to decompose rapidly [142]. However, given the cost of gold and its gravimetric density (which limited the DMSO cell to a cathodic specific capacity of 300 mAh g^{-1}), this electrode is commercially impractical. DMSO was found to decompose through nucleophilic attack by Li_2O_2 and $O_2^{\bullet-}$ radicals when used with a conventional carbon cathode, a carbon cathode coated with gold nanoparticles or a carbon cathode with α-MnO_2 nanowires. The latter resulted in the formation of LiOH due to the presence of –OH groups on the surface of the α-MnO_2 nanowires [142, 143]. Other studies suggested that DMSO can be decomposed by Li_2O_2 within time periods ranging from two to twenty days, thus hindering its practicality within real-world applications where the battery pack may be left in a partially-discharged state for prolonged periods of time [144, 145]. Later work refuted this, having observed no change to DMSO aged with Li_2O_2 for two months, but encountered decomposition of DMSO to $DMSO_2$ by $O_2^{\bullet-}$ radicals within the same period [146]. Recent work has also demonstrated that

DMSO is stable in contact with Li_2O_2 for periods of upwards of two months, and that long-term cyclability can be achieved when a platinum-catalysed carbon nanotube cathode is used [147].

Other variants of non-aqueous electrolytes have been studied as possible candidates for use in Li-air cells. One such class of electrolytes is ionic liquids, which are salts that are molten at room temperature. These have the advantages of being non-flammable and non-toxic, and are thus safer to dispose of. Additionally, some are hydrophobic, which helps to prevent water ingress. Alas, some, such as 1-ethyl-3-methylimidazolium bis(trifluoromethylsulfonylimide) (EMITFSI) and diethylmethyl(2-methoxyethyl)ammonium bis(trifluoromethylsulfonylimide), have proven to be unstable towards Li anodes or Li_2O_2. Others have exhibited performance in Li-air cells that has been far from satisfactory. One such salt, *N*-methyl-*N*-propylpiperidinium bis(trifluoromethylsulfonyl)imide, was found to produce volumes of hydrogen, carbon dioxide and water that equated to 45 % of the oxygen absorbed by the cell during the reduction reaction. Further evidence of decomposition reactions taking place was observed by the ratio of electrons to O_2 molecules consumed being greater than two, despite O_2 reduction in the Li-air cell being a two-electron process [148]. However, one Li-air cell that used EMITFSI was reported to operate for a period of 56 days in air, indicating that this category of electrolytes could still represent a promising avenue of research [149].

Li-air cells with solid-state electrolytes made from polymer-ceramics and glass-ceramics (GC) have demonstrated excellent cyclability. Additionally, the solid-state nature of the cell removes the issue of solvent evaporation during use. However, these cells tend to suffer from low maximum current densities and usually require elevated operating temperatures (30 – 105 °C), which hinders their suitability for automotive applications [150]. Furthermore, little is known about the exact nature of their discharge and charge mechanisms, and the formation of decomposition products upon cycling, if any. Experiences with non-aqueous

liquid electrolytes have demonstrated that this must be properly investigated prior to committing to the use of solid-state electrolytes in Li-air cells [118].

Whilst the search for a stable electrolyte remains a top priority in Li-air research, another contributor to premature cell failure is the instability of cathode materials, either in contact with the Li_2O_2 discharge product or at the high potentials encountered during charging. Carbon cathodes prepared using the conventional polyvinylidene fluoride (PVDF) binder and NMP, a solvent used for the preparation of Li-ion carbon anodes, were found to be particularly sensitive to Li_2O_2, which is a strong Lewis base [126]. During discharge, carbon cathodes have also been demonstrated to form lithium carbonate, Li_2O and O_2 at the carbon-Li_2O_2 interface, through a reaction between Li_2O_2 and carbon. When the cells are charged at potentials above 4 V, as is often necessary to oxidise Li_2O_2 completely, CO_2 is evolved from the oxidation of the lithium carbonate. Evidence of such decomposition may be obtained through *in-situ* differential electrochemical mass spectrometry (DEMS), whereupon the detection of CO_2 during charging is indicative of the decomposition of the electrolyte or carbon in the cathode structure. The origin of the carbon in the CO_2 evolved at potentials > 4 V has been proven to be approximately 1:1 cathode:electrolyte decomposition through the use of ^{13}C isotopes in the cathode structure, thus differentiating it from the ^{12}C most likely found in the solvent [133].

Li-air cells presently suffer from a large potential hysteresis during cycling, which leads to poor cyclic efficiency. This is due to the high overpotential required to oxidise Li_2O_2 upon charging, which can result in charge potential plateaus of upwards of 4.2 V [124]. As well as poor cyclic efficiency, this high charge potential can also contribute towards the decomposition of some organic electrolytes [126, 151]. Use in conjunction with highly porous carbon cathodes only serves to exacerbate the degradation of these electrolytes due to the increased number of reaction sites [128]. Therefore, unless a method can be devised to minimise the hysteresis of Li-air cells, there is still a need to identify a solvent that is stable in the presence

of $O_2^{\bullet-}$ radicals, does not react with pure Li anodes and has both a lower reduction potential than O_2 and a higher oxidation potential than Li_2O_2 to ensure stability within a Li-air cell.

Integrating a Li-air battery pack into a vehicle will present new challenges. Oxygen must be delivered to the cells in a suitable purity and quantity to sustain the discharge reaction and meet the power demand of the vehicle without resulting in cell degradation. As shown in Appendix A, a Li-air vehicle based on the Nissan LEAF will require a nominal air flow rate of 8.79 litres per second and a peak air flow rate of 93.71 litres per second. Both flow rates can be readily provided *via* air intakes when the vehicle is in motion, but for low speed and stationary scenarios, the peak air flow could be provided by small, lightweight fans powered by the vehicle's auxiliary circuit. For example, the peak air flow rate could be provided by six Orion ODB600PT-12HB blowers, representing a total power drain of 43.2 watts [152].

Numerous options exist to remove atmospheric impurities, such as water vapour and CO_2, from the air flow to Li-air cells. Oxygen-selective membranes are the most preferable option because they are lightweight, thin and easily built into the outer cathode of the cell, thus having minimal impact on gravimetric and volumetric energy density. Unfortunately, such a membrane has yet to be identified that doesn't also reduce the rate of oxygen permeation into the cell and therefore limit its maximum discharge current [153]. Water could be removed using a condenser, but this would increase auxiliary power consumption and add an additional serviceable component at the expense of gravimetric and volumetric energy density. Molecular sieves could be used for the same purpose, but these would need to be dried periodically, perhaps using an integrated heating device that is powered by mains electricity when the car is charging so as not to add further auxiliary load to the vehicle. CO_2 could be removed using soda lime housed within an absorber chamber, which would also retain water as part of the reaction process [154]. However, approximately 13.35 kg of soda lime would be required to scrub CO_2 from the total volume of air required for a full discharge in the vehicle example

provided in Appendix A, and soda lime is not regenerable [155]. These factors combine to negatively impact on both volumetric and gravimetric energy density if the soda lime supply is to be sufficient for several cycles, whilst the latter implies additional expense associated with soda lime replacement and also requires the widespread implementation of additional infrastructure for soda lime replacement and disposal. Another option to remove CO_2 is pressure swing adsorption, whereby air flows into a high pressure chamber containing a CO_2 adsorbent, such as zeolite, until the concentration of the working gas approaches equilibrium, following which the adsorbent is regenerated by reducing the pressure in the chamber. An additional advantage of the system is that it further purifies the air flow to the Li-air battery pack by removing nitrogen [156]. However, pressure swing adsorption requires two chambers to be fitted to the vehicle, which would alternate between adsorbing CO_2 and being regenerated, plus a compressor and vacuum pump to regulate the pressure of the working chamber. This would add considerable weight, complexity and power drain to the battery system at the expense of energy density.

An alternative approach to the air purity concern would be to use an onboard compressed oxygen tank to provide pure oxygen. Alas, for mid-sized cars such as the example in Appendix A, the volume of oxygen required for a full discharge is 110.43 m^3 at atmospheric pressure and a temperature of 15 °C. The largest 230 bar oxygen cylinders typically contain the equivalent of 11.09 m^3 of oxygen at atmospheric pressure, measure 1.46 m tall by 23 cm wide and weigh 80 kg when full [157]. Ten such cylinders would be required to be carried by the vehicle, rendering this approach unfeasible since the additional weight and volume will negate the improvements in energy density offered by Li-air over Li-ion at cell level. However, it must be remembered that Li-air cells are still at the early stages of research and development, so the exact nature of their sensitivity to atmospheric impurities is as yet unknown; H_2O and CO_2 content in air may have negligible impact on the performance of commercial Li-air battery

packs. Given the air flow rate requirement of a Li-air battery pack and the subsequent blower specification, a Li-air-powered vehicle could be created with minimal impact on cost and energy density due to additional components, provided that a suitable O_2-selective membrane is developed.

Table 2 compares the key operational characteristics of all of the automotive secondary cell chemistries considered above, to those of Li-air.

1.6 Research objectives

A solvent has yet to be discovered that acts as a stable electrolyte in a Li-air cell. This work shall study alternative electrolyte solutions with the aim of finding a solvent that meets all of the criteria for the reversible and sustainable operation of a Li-air cell, including stability within the oxygen reduction and evolution window, compatibility with conventional electrode materials and resistance to attack from $O_2^{\bullet-}$ radicals. In the event that the solvents do not satisfy these conditions, the failure mechanisms shall be investigated in order to gain greater understanding of what makes a solvent a successful or unsuccessful candidate for the Li-air cell.

A number of computational models have been developed that aim to predict the discharge characteristics of a fully parameterised Li-air cell with a given electrolyte, which is useful for screening solvents to find potential candidates for highly reversible Li-air cells [158, 159, 160]. Recently, understanding of the characteristics of Li-air electrolytes has been pursued in the lab at a fundamental electrochemical level [120]. However, the latest advancements in practical knowledge of electrolyte behaviour have yet to be incorporated into a computational model, thus compromising their accuracy. As such, work shall be undertaken to support the

Cell chemistry	**Cell voltage (V)**	**Specific energy (Wh kg^{-1})**	**Energy density (Wh l^{-1})**	**Specific power (W kg^{-1})**	**Calendar life (years)**	**Cycle life (cycles)**	**Operating temperature (°C)**
Pb-acid	2.0	20 – 30	80	150	3 – 5	300 – 500	-10 – 40
Ni-Fe	1.2	23 – 50	115	100 – 170	7 – 25; over a century reported [34]	> 1000	0 – 60
NaS [161]	1.8	110	120	150	15	2500	300 – 350
ZEBRA [47]	2.5	120	150	180	> 10	3500	270 – 350
NiCd	1.2	45 – 60	120	250	> 15	2000	-20 – 45
NiMH	1.2	50 – 80	150 – 300	200 – 1200 [55]	> 15	> 1000	-20 – 40
Li-ion	3.2 – 3.7	80 – 200	250 – 700	250 – 350	3 (portable electronics); 8 (EVs)	> 1000	-20 – 60
Li-air [118]	2.96	3,505 (cathode, including mass of O_2)	3,436 (cathode, theoretical, factoring in Li and Li_2O_2)	≈ 175 in tests so far	N/A	< 100 cycles thus far	room temperature so far

Table 2: Comparison of the operational characteristics of the automotive secondary cell chemistries considered in this chapter [59].

development of a new comprehensive computational model that factors in this latest information on the mechanisms encountered in a Li-air cell with a given electrolyte. This will allow rapid prediction of optimum electrolyte and cathode properties in the search for highly reversible Li-air cells.

Until Li-air reaches commercial viability, the automotive industry will remain reliant on Li-ion cells. However, BMS algorithms have yet to advance to the stage where they can detect and prevent electrode-specific failure mechanisms that reduce the cycle and calendar life of the cell. One major problem faced when trying to resolve this is that commercial Li-ion cells are two-electrode systems. As such, the separate potential profiles of the WE and CE, which can indicate failure mechanisms taking place at each electrode, are not readily available. Therefore, the only potential-based information available to the BMS is the full-cell potential profile, which is the difference between the potentials of each electrode, and thus cannot be used on its own to accurately predict, detect or mitigate the failure mechanisms for each electrode individually. However, electrode-specific potential profiles could be obtained if a reference electrode (RE) was inserted into the cell, the stable potential of which could then be used to measure the potential of the WE and CE individually. The only such work on commercial cells has involved invasive procedures on 18650 cylindrical cells, which are generally not favoured by the automotive industry. Additionally, the modification procedures have altered the characteristics of the cells, such as internal resistance and capacity retention, and therefore do not accurately reflect their real-life operational characteristics [162, 163, 164, 165]. Here, a minimally-invasive RE insertion procedure shall be developed for a commercial pouch cell for the first time, allowing WE and CE potential profiles to be obtained *in-situ*. The profiles will be verified using half-cells created from material recovered from pristine pouch cells, and the capacity retention of the modified cells compared to that of unmodified cells to ensure that the procedure has not impacted on the performance of the cells. The WE and CE profiles will be

applied to a computational model that predicts the onset of failure mechanisms for Li-ion cells, which can be deployed in a BMS to increase the cycle life of a battery pack.

1.7 References

[1] International Energy Agency, "Consumption," in *Key World Energy Statistics*, Paris, OECD/IEA, 2014, pp. 28 - 34.

[2] I. C. Mills, R. W. Atkinson, S. Kang, H. Walton and H. R. Anderson, "Quantitative Systematic Review of the Associations Between Short-Term Exposure to Nitrogen Dioxide and Mortality and Hospital Admissions," *BMJ Open,* vol. 5, pp. 1 - 8, 2015.

[3] International Agency for Research on Cancer, World Health Organisation. (12 June 2012). *IARC: Diesel Engine Exhaust Carcinogenic*. [Online]. Available: http:// www.iarc.fr/en/media-centre/pr/2012/pdfs/pr213_E.pdf. [Accessed 06 October 2015].

[4] L. Benbrahim-Tallaa, R. A. Baan, Y. Grosse, B. Lauby-Secretan, F. E. Ghissassi, V. Bouvard, N. Guha, D. Loomis and K. Straif, "Carcinogenicity of Diesel-Engine and Gasoline-Engine Exhausts and Some Nitroarenes," *Lancet. Oncol.,* vol. 13, pp. 663 – 664, 2012.

[5] B. Ostro, J. Hu, D. Goldberg, P. Reynolds, A. Hertz, L. Bernstein and M. J. Kleeman, "Associations of Mortality with Long-Term Exposures to Fine and Ultrafine Particles, Species and Sources: Results from the California Teachers Study Cohort," *Environ. Health Perspect.*, vol. 123, no. 6, pp. 549 - 556, 2015.

[6] K. Mathiesen and A. Neslen, The Guardian. (23 September 2015). *VW Scandal Caused Nearly 1m Tonnes of Extra Pollution, Analysis Shows*. [Online]. Available: https://

www.theguardian.com/business/2015/sep/22/vw-scandal-caused-nearly-1m-tonnes-of-extra-pollution-analysis-shows. [Accessed 13 May 2016].

[7] R. D. Girling, I. Lusebrink, E. Farthing, T. A. Newman and G. M. Poppy, “Diesel Exhaust Rapidly Degrades Floral Odours used by Honeybees,” *Scientific Reports*, vol. 3, Rep. srep02779, 2013.

[8] A. Stephenson, J. Dennis and S. Scott, “Improving the Sustainability of the Production of Biodiesel from Oilseed Rape in the UK,” *Process Saf. Environ.*, vol. 86, no. 6, pp. 427 – 440, 2008.

[9] B. Scrosati, J. Hassoun and Y.-K. Sun, “Lithium-Ion Batteries. A Look Into the Future,” *Energy Environ. Sci.*, vol. 4, pp. 3287 - 3295, 2011.

[10] M. Rhein, S. Rintoul, S. Aoki, E. Campos, D. Chambers, R. Feely, S. Gulev, G. Johnson, S. Josey, A. Kostianoy, C. Mauritzen, D. Roemmich, L. Talley and F. Wang, “Observations: Ocean," in *Climate Change 2013: The Physical Science Basis. Contribution of Working Group I to the Fifth Assessment Report of the Intergovernmental Panel on Climate Change*, Cambridge University Press, Cambridge, 2013, p. 259.

[11] B. Kirtman, S. Power, J. Adedoyin, G. Boer, R. Bojariu, I. Camilloni, F. Doblas-Reyes, A. Fiore, M. Kimoto, G. Meehl, M. Prather, A. Sarr, C. Schär, R. Sutton, G. v. Oldenborgh, G. Vecchi and H. Wang, “Near-Term Climate Change: Projections and Predictability," in *Climate Change 2013: The Physical Science Basis. Contribution of Working Group I to the Fifth Assessment Report of the Intergovernmental Panel on Climate Change*, Cambridge University Press, Cambridge, 2013, pp. 955 - 957.

[12] International Energy Agency, “Emissions,” in *Key World Energy Statistics*, Paris, OECD/IEA, 2014, p. 44.

[13] J. B. Goodenough and K.-S. Park, “The Li-Ion Rechargeable Battery: A Perspective,” *J. Am. Chem. Soc.*, vol. 135, no. 4, pp. 1167 – 1176, 2013.

[14] G. A. Elia and J. Hassoun, “A Polymer Lithium-Oxygen Battery,” *Scientific Reports*, Rep. srep12307, 2015.

[15] H. S. Leff, “Thermodynamics of Combined-Cycle Electric Power Plants,” *Am. J. Phys.*, vol. 80, no. 6, pp. 515 - 518, 2012.

[16] B. Richter, D. Goldston, G. Crabtree, L. Glicksman, D. Goldstein, D. Greene, D. Kammen, M. D. Levine, M. L. M. Savitz, D. Sperling, F. Schlachter and J. H. Scofield, *Energy Future: Think Efficiency*, American Physical Society, 2008, pp. 44 - 45.

[17] N. Green, “Future Energy Systems for Road Transport,” presented at the CATAPULT Energy Storage Conf., University of Warwick, 2013.

[18] Nissan Newsroom Europe. (03 March 2015). *Power to Spare - Nissan and Endesa Sign Pledge to Promote Europe's First Mass Market Vehicle to Grid System*. [Online]. Available: http://newsroom.nissan-europe.com/EU/en-gb/Media/Media.aspx?mediaid=130188. [Accessed 06 October 2015].

[19] Y. Tang, J. Yang, J. Yan and H. He, “Intelligent Load Frequency Controller Using GrADP for Island Smart Grid with Electric Vehicles and Renewable Resources,” *Neurocomputing*, vol. 170, pp. 406 – 416, 2015.

[20] S. Brown, DriveEV. (26 April 2016). *Plug In Adventures Completes North Coast 500 - a 516-Mile Journey in an EV*. [Online]. Available: https://driveev.net/2016/04/26/plug-in-adventures-completes-north-coast-500-a-516-mile-journey-in-an-ev/. [Accessed 11 May 2016].

[21] Tesla Motors. (2015). *Supercharger*. [Online]. Available: http://www.teslamotors.com/en_GB/supercharger. [Accessed 06 October 2015].

[22] Tesla Motors. (2015). *Tesla Gigafactory*. [Online]. Available: http://www.teslamotors.com/en_GB/gigafactory. [Accessed 06 October 2015].

[23] Department for Transport. (10 September 2015). *Table VEH0120: Licensed Vehicles by Make and Model, Great Britain, Quarterly from 1994*. [Online]. Available: https://www.gov.uk/government/statistical-data-sets/veh01-vehicles-registered-for-the-first-time. [Accessed 06 October 2015].

[24] T. Zhang, N. Imanishi, S. Hasegawa, A. Hirano, J. Xie, Y. Takeda, O. Yamamoto and N. Sammes, "Li/Polymer Electrolyte/Water Stable Lithium-Conducting Glass Ceramics Composite for Lithium-Air Secondary Batteries with an Aqueous Electrolyte," *J. Electrochem. Soc.,* vol. 155, no. 12, pp. A965 - A969, 2008.

[25] G. Girishkumar, B. McCloskey, A. C. Luntz, S. Swanson and W. Wilcke, "Lithium−Air Battery: Promise and Challenges," *J. Phys. Chem. Lett.,* vol. 1, no. 14, pp. 2193–2203, 2010.

[26] S. Santhanagopalan, J. Stockel and R. E. White, "Secondary Batteries - Lithium Rechargeable Systems - Lithium-Ion | Lifetime Prediction," in *Encyclopedia of Electrochemical Power Sources*, vol. 5, Amsterdam, Elsevier, 2009, pp. 418 - 437.

[27] E. J. Cairns and P. Albertus, “Batteries for Electric and Hybrid-Electric Vehicles,” *Annu. Rev. Chem. Biomol. Eng.,* vol. 1, pp. 299 - 320, 2010.

[28] B. Zhang, J. Zhong, W. Li, Z. Dai, B. Zhang and Z. Cheng, “Transformation of Inert $PbSO_4$ Deposit on the Negative Electrode of a Lead-Acid Battery into its Active State,” *J. Power Sources,* vol. 195, pp. 4338 - 4343, 2010.

[29] Porsche Cars North America, Inc. (27 January 2014). *The First Porsche in the World - the Return of the "P1"*. [Online]. Available: http://press.porsche.com/news/release.php?id=842. [Accessed 25 May 2015].

[30] M. Armand and J. M. Tarascon, “Building Better Batteries,” *Nature,* vol. 451, pp. 652 - 657, 2008.

[31] A. Madrigal, “The National Electric Transportation System That Almost Was,” in *Powering the Dream: The History and Promise of Green Technology*, Cambridge, MA: Da Capo Press, 2011, pp. 71 - 83.

[32] Renault Press. (20 June 2011). *Renault and Better Place Partner in Australia to Launch Fluence Z.E. in 2012*. [Online]. Available: http://media.renault.com/global/en-gb/renaultgroup/Media/PressRelease.aspx?mediaid=28864. [Accessed 25 May 2015].

[33] The Tesla Motors Team. (19 December 2014). *Battery Swap Pilot Program*. [Online]. Available: http://www.teslamotors.com/en_GB/blog/battery-swap-pilot-program. [Accessed 25 May 2015].

[34] D. Ford, The New York Times. (5 August 2007). *Back to the Future in a 98-Year-Old Electric Car*. [Online]. Available: http://www.nytimes.com/2007/08/05/automobiles/05BAKER.html?_r=0 [Accessed 14 May 2016].

[35] C. Chakkaravarthy, P. Periasamy, S. Jegannathan and K. I. Vasu, “The Nickel/Iron Battery,” *J. Power Sources,* vol. 35, no. 1, pp. 21 - 35, 1991.

[36] G. Hapert, “Past Developments and the Future of Nickel Electrode Cell Technology,” *J. Power Sources,* vol. 12, no. 3 - 4, pp. 177 - 192, 1984.

[37] H. Wang, Y. Liang, M. Gong, Y. Li , W. Chang, T. Mefford, J. Zhou, J. Wang, T. Regier, F. Wei and H. Dai, “An Ultrafast Nickel–Iron Battery from Strongly Coupled Inorganic Nanoparticle/Nanocarbon Hybrid Materials,” *Nature Communications,* vol. 3, Rep. ncomms1921, 2012.

[38] C. D. Anderson and J. Anderson, “The Evolution of the Electric Vehicle,” in *Electric and Hybrid Cars: A History, 2d ed.*, McFarland & Co Inc., 2009, pp. 17 - 52.

[39] F. R. Bryan, “Ford-Edison Electric Car,” in *Friends, Families and Forays: Scenes from the Life and Times of Henry Ford*, Wayne State University Press, 2002, pp. 153 - 161.

[40] F. J . Stenger, J. M. Bozek. and R. F. Soltis, “Results of Baseline Tests of the EVA Metro Sedan, Citi-Car, Jet Industries Electra-Van, CDA Town Car, and Otis P-500 Van,” National Aeronautics and Space Administration, Lewis Research Center, Cleveland, OH, Rep. NASA TM X-73638, October 1976.

[41] W. A. Adams, “Exploratory Research and Development of Batteries and Supercapacitors for Electric/Hybrid Vehicle Applications,” in *Proceedings of the Symposium on Exploratory Research and Development of Batteries for Electric and Hybrid Vehicles,* San Antonio, TX. 1996, pp. 1 - 15

[42] J. T. Kummer and N. Weber, “Battery Having a Molten Alkali Metal Anode and a Molten Sulfur Cathode”. U.S. Patent US3413150 A, 26 November 1968.

[43] Z. Yang, J. Zhang, M. C. W. Kintner-Meyer, X. Lu, D. Choi, J. P. Lemmon and J. Liu, “Electrochemical Energy Storage for Green Grid,” *Chem. Rev.,* vol. 111, pp. 3577-3613, 2011.

[44] M. H. Westbrook, “Energy Sources 1: Storage Batteries,” in *The Electric Car: Development and Future of Battery, Hybrid and Fuel Cell Cars*, The Institution of Electrical Engineers, 2005, pp. 65 - 87.

[45] BMW Group. (25 March 2010). *25 Years of BMW (Forschung und) Technik GmbH.* [Online]. Available: https://www.press.bmwgroup.com/global/pressDetail.html?title=25-years-of-bmw-forschung-und-technik-gmbh&outputChannelId=6&id=T0078527EN&left_menu_item=node__4097. [Accessed 26 May 2015].

[46] L. J. B. Jr. and R. H. Munson. (21 October 1994). *Correspondence Relating to: Recall 94V-175: 1993 Ford Ecostar Battery Fires*. [Online]. Available: http://www.autosafety.org/sites/default/files/imce_staff_uploads/94V175%20Part%20573%20Ford%20Ecostar.pdf. [Accessed 06 October 2015].

[47] C.-H. Dustmann, “Advances in ZEBRA Batteries,” *J. Power Sources,* vol. 127, pp. 85 - 92, 2004.

[48] B. L. Ellis, L. F. Nazar, “Sodium and Sodium-Ion Energy Storage Batteries,” *Current Opinion in Solid State and Materials Science,* vol. 16, no. 4, pp. 168-177, 2012.

[49] K. B. Hueso, M. Armand and T. Rojo, “High Temperature Sodium Batteries: Status, Challenges and Future Trends,” *Energy Environ. Sci.,* vol. 6, pp. 734-749, 2013.

[50] Saft. (2007). *Nickel-Cadmium (Ni-Cd) - STM - High Energy Module for Traction*. [Online]. Available: http://aircraft.saftbatteries.com/tabid/150/Language/en-US/tabid/293/TypeControl/Produit/ProduitId/44/Default.aspx. [Accessed 26 May 2015].

[51] A. A. Hussein and A. A. Fardoun, "Design Considerations and Performance Evaluation of Outdoor PV Battery Chargers," *Renewable Energy,* vol. 82, pp. 85 – 91, 2015.

[52] Per Jørgensen Møller, Danish EV Committee. (2003). *Investigation of Breakdown of the SAFT STM5-100 Battery*. [Online]. Available: http://www.evdl.org/docs/saft-failures.pdf. [Accessed 14 May 2016].

[53] A. Shukla, S. Venugopalan and B. Hariprakash, "Secondary Batteries - Nickel Systems | Nickel–Cadmium: Overview," in *Encyclopedia of Electrochemical Power Sources*, vol. 4, Amsterdam, Elsevier, 2009, pp. 452 - 458.

[54] F. Feng, M. Geng and D. Northwood, "Electrochemical Behaviour of Intermetallic-Based Metal Hydrides used in Ni/Metal Hydride (MH) Batteries: A Review," *Int. J. Hydrogen. Energ.,* vol. 26, pp. 725 - 734, 2001.

[55] Y. Liu, H. Pan, M. Gao and Q. Wang, "Advanced Hydrogen Storage Alloys for Ni/MH Rechargeable Batteries," *J. Mater. Chem.,* vol. 21, pp. 4743 - 4755, 2011.

[56] BASF. *Stationary Battery (NiMH)*. [Online]. Available: http://www.catalysts.basf.com/p02/USWeb-Internet/catalysts/en/content/microsites/catalysts/prods-inds/batt-mats/stationary-battery. [Accessed 07 October 2015].

[57] John J. C. Kopera, Cobasys. (25 June 2004). *Inside the Nickel Metal Hydride Battery*. [Online]. Available: http://www.cobasys.com/pdf/tutorial/inside_nimh_battery_technology.pdf. [Accessed 07 October 2015].

[58] W.-K. Hu, R. V. Denys, C. C. Nwakwuo, T. Holm, J. P. Maehlen, J. K. Solberg and V. A. Yartys, "Annealing Effect on Phase Composition and Electrochemical Properties of the Co-Free La_2MgNi_9 Anode for Ni-Metal Hydride Batteries," *Electrochim. Acta*, vol. 96, pp. 27 - 33, 2013.

[59] I. Uehara, T. Sakai and H. Ishikawa, "The State of Research and Development for Applications of Metal Hydrides in Japan," *J. Alloy. Compd.*, vol. 253 – 254, pp. 635 – 641, 1997.

[60] B. Zimmermann, H. Dura and M. Weil, "Towards Time-Resolved LCA of Electric Vehicles in Germany," *Metall. Res. Technol.*, vol. 111, pp. 169 – 178, 2014.

[61] Panasonic EV Energy Co., Ltd. (1998). *PEV Battery for Pure Electric Vehicles*. [Online]. Available: http://www.evnut.com/rav_battery_data_sheet.html. [Accessed 13 August 2015].

[62] United States Securities and Exchange Commission. (07 July 2004). *Form 8-K Patent Infringement Settlement*. [Online]. Available: https://web.archive.org/web/20040717233048/http://www.ovonic.com/PDFs/Financial_Reports/form_8k/8k_mbi_patent_infringe_settlement_7july04.pdf. [Accessed 07 October 2015].

[63] S. Ovshinsky, Interviewee. (14 October 2008). *The Edison of our Age: Stan Ovshinsky and the Future of Energy*. [Interview, Online]. Available: http://

www.theenergyroadmap.com/futureblogger/show/1030-stanford-ovshinsky-and-the-future-of-energy-interview-part-1. [Accessed 14 May 2016].

[64] F. Mizuno, S. Nakanishi, Y. Kotani, S. Yokoishi and H. Iba, "Rechargeable Li-Air Batteries with Carbonate-Based Liquid Electrolytes," *Electrochemistry,* vol. 78, no. 5, pp. 403 - 405, 2010.

[65] C. Paine, Director. *Who Killed the Electric Car?* [Film]. USA: Electric Entertainment, 2006.

[66] Nissan Motor Corporation. (2 August 2009). *Nissan's Pursuit for Zero Emission Mobility: The Unplugged Story*. [Online]. Available: http://www.nissan-global.com/EN/NEWS/2009/_STORY/090802-03-e.html. [Accessed 28 May 2015].

[67] C. Madrid, J. Argueta and J. Smith. Southern California Edison. (September 1999). *Performance Characterization - 1999 Nissan Altra-EV with Lithium-Ion Battery*. [Online]. Available: https://avt.inl.gov/sites/default/files/pdf/fsev/altra_report.pdf. [Accessed 13 May 2016].

[68] M. M. Thackeray, S.-H. Kang, C. S. Johnson, J. T. Vaughey, R. Benedek and S. A. Hackney, "Li_2MnO_3-Stabilized $LiMO_2$ (M = Mn, Ni, Co) Electrodes for Lithium-Ion Batteries," *J. Mater. Chem.,* vol. 17, pp. 3112 - 3125, 2007.

[69] L. Lu, X. Han, J. Li, J. Hua and M. Ouyang, "A Review on the Key Issues for Lithium-Ion Battery Management in Electric Vehicles," *J. Power Sources,* vol. 226, pp. 272 - 288, 2013.

[70] T. Sasaki, Y. Ukyo and P. Novák, "Memory Effect in a Lithium-Ion Battery," *Nat. Mater.,* vol. 12, pp. 569-575, 2013.

[71] P. G. Balakrishnan, R. Ramesh and T. P. Kumar, “Safety Mechanisms in Lithium-Ion Batteries,” *J. Power Sources*, vol. 155, no. 2, pp. 401 – 414, 2006.

[72] N. Nitta, F. Wu, J. T. Lee and G. Yushin, “Li-Ion Battery Materials: Present and Future,” *Materials Today*, vol. 18, no. 5, pp. 252 - 264, 2015.

[73] Automotive Energy Supply Corporation. (2013). *Cell, Module, and Pack for EV Applications*. [Online]. Available: http://www.eco-aesc-lb.com/en/product/liion_ev/. [Accessed 28 May 2015].

[74] B. Scrosati, J. Garche and W. Tillmetz, “State-of-the-Art Vehicles,” in *Advances in Battery Technologies for Electric Vehicles*, Cambridge, Woodhead Publishing, 2015, p. 132.

[75] J. Jiang, T. Buhrmester, K. Eberman, L. J. Krause and J. R. Dahn, “Electrochemical and Thermal Comparisons of $Li[Ni_{0.1}Co_{0.8}Mn_{0.1}]O_2$ Synthesized at Different Temperatures (900, 1000, and 1100 Degrees C),” *J. Electrochem. Soc.*, vol. 152, no. 1, pp. A19 - A22, 2005.

[76] J. Jiang, K. W. Eberman, L. J. Krause and J. R. Dahn, “Structure, Electrochemical Properties, and Thermal Stability Studies of $Li[Ni_{0.2}Co_{0.6}Mn_{0.2}]O_2$ - Effect of Synthesis Route,” *J. Electrochem. Soc.*, vol. 152, no. 9, pp. A1874 - A1878, 2005.

[77] K. M. Shaju and P. G. Bruce, “Macroporous $Li(Ni_{1/3}Co_{1/3}Mn_{1/3})O_2$: A High-Power and High-Energy Cathode for Rechargeable Lithium Batteries,” *Adv. Mater.*, vol. 18, pp. 2330 – 2334, 2006.

[78] D. Larcher and J-M. Tarascon, “Towards Greener and More Sustainable Batteries for Electrical Energy Storage,” *Nat. Chem.*, vol. 7, pp. 19 - 29, 2015.

[79] W. Lu, C. M. López, N. Liu, J. T. Vaughey, A. Jansen and D. W. Dees, "Overcharge Effect on Morphology and Structure of Carbon Electrodes for Lithium-Ion Batteries," *J. Electrochem. Soc.,* vol. 159, no. 5, pp. A566 - A570, 2012.

[80] M. Winter, J. O. Besenhard, M. E. Spahr and P. Novák, "Insertion Electrode Materials for Rechargeable Lithium Batteries," *Adv. Mater.,* vol. 10, no. 10, pp. 725 - 763, 1998.

[81] B. Scrosati and J. Garche, "Lithium Batteries: Status, Prospects and Future," *J. Power Sources,* vol. 195, pp. 2419 - 2430, 2010.

[82] V. A. Agubra and J. W. Fergus, "The Formation and Stability of the Solid Electrolyte Interface on the Graphite Anode," *J. Power Sources,* vol. 268, pp. 153 - 162, 2014.

[83] J. Christensen and J. Newman, "Cyclable Lithium and Capacity Loss in Li-Ion Cells," *J. Electrochem. Soc.,* vol. 152, no. 4, pp. A818 - A829, 2005.

[84] P. Arora, R. E. White and M. Doyle, "Capacity Fade Mechanisms and Side Reactions in Lithium-Ion Batteries," *J. Electrochem. Soc,* vol. 145, no. 10, pp. 3647 - 3667, 1998.

[85] P. Dan, E. Mengeritsky, D. Aurbach, I. Weissman and E. Zinigrad, "More Details on the New $LiMnO_2$ Rechargeable Battery Technology Developed at Tadiran," *J. Power Sources,* vol. 68, pp. 443 - 447, 1997.

[86] A. H. Tullo, "Dell Recalls Lithium Batteries," *Chemical & Engineering News,* vol. 84, no. 34, p. 11, 21 August 2006.

[87] H. Yoshida, Y. Kobayashi, Y. Mita and H. Miyashiro, "Quantitative Evaluation of Charge-Discharge Cycle Test and Storage Test in Commercially Available Lithium-Ion Batteries," presented at 227th ECS Meeting, Chicago, IL, 2015.

[88] L. Kavan and M. Grätzel, “Facile Synthesis of Nanocrystalline $Li_4Ti_5O_{12}$ (Spinel) Exhibiting Fast Li Insertion,” *Electrochem. Solid St.*, vol. 5, no. 2, pp. A39 - A42, 2002.

[89] J. Morales, R. Trócoli, S. Franger and J. Santos-Peña, “Cycling-Induced Stress in Lithium Ion Negative Electrodes: LiAl/$LiFePO_4$ and $Li_4Ti_5O_{12}$/$LiFePO_4$ Cells,” *Electrochim. Acta,* vol. 55, no. 9, pp. 3075 - 3082, 2010.

[90] C. P. Sandhya, B. John and C. Gouri, “Lithium Titanate as Anode Material for Lithium-Ion Cells: A Review,” *Ionics,* vol. 20, no. 5, pp. 601 - 620, 2014.

[91] Toshiba Corporation. (2009). *Toshiba SCiB website*. [Online]. Available: http:// www.scib.jp/en/index.htm. [Accessed 03 June 2015].

[92] T. Ohzuku, A. Ueda and N. Yamamoto, “Zero-Strain Insertion Material of Li[$Li_{1/3}Ti_{5/3}$]O_4 for Rechargeable Lithium Cells,” *J. Electrochem. Soc,* vol. 142, no. 5, pp. 1431 - 1435, 1995.

[93] J. L. Allen, T. R. Jow and J. Wolfenstine, “Low Temperature Performance of Nanophase $Li_4Ti_5O_{12}$,” *J. Power Sources,* vol. 159, pp. 1340 - 1345, 2006.

[94] Y.-B. He, M. Liu, Z.-D. Huang, B. Zhang, Y. Yu, B. Li, F. Kang and J.-K. Kim, “Effect of Solid Electrolyte Interface (SEI) Film on Cyclic Performance of $Li_4Ti_5O_{12}$ Anodes for Li Ion Batteries,” *J. Power Sources,* vol. 239, pp. 269 - 276, 2013.

[95] S. F. Schuster, T. Bach, E. Fleder, J. Müller, M. Brand, G. Sextl and A. Jossen, “Nonlinear Aging Characteristics of Lithium-Ion Cells Under Different Operational Conditions,” *J. Energy Storage,* vol. 1, pp. 44 – 53, 2015.

[96] S. S. Zhang, K. Xu and T. R. Jow, “Study of the Charging Process of a $LiCoO_2$-Based Li-Ion Battery,” *J. Power Sources,* vol. 160, pp. 1349 – 1354, 2006.

[97] N.-S. Choi, Z. Chen, S. A. Freunberger, X. Ji, Y.-K. Sun, K. Amine, G. Yushin, L. F. Nazar, J. Cho and P. G. Bruce, “Challenges Facing Lithium Batteries and Electrical Double-Layer Capacitors,” *Angew. Chem. Int. Ed.,* vol. 51, no. 40, pp. 9994 – 10024, 2012.

[98] S. S. Choi and H. S. Lim, “Factors that Affect Cycle-Life and Possible Degradation Mechanisms of a Li-Ion Cell Based on $LiCoO_2$,” *J. Power Sources,* vol. 111, no. 1, pp. 130 - 136, 2002.

[99] J. Jiang, J. Chen and J. R. Dahn, “Comparison of the Reactions Between $Li_{7/3}Ti_{5/3}O_4$ or LiC_6 and Nonaqueous Solvents or Electrolytes Using Accelerating Rate Calorimetry,” *J. Electrochem. Soc.,* vol. 151, no. 12, pp. A2082 - A2087, 2004.

[100] M. N. Richard and J. R. Dahn, “Accelerating Rate Calorimetry Study on the Thermal Stability of Lithium Intercalated Graphite in Electrolyte,” *J. Electrochem. Soc,* vol. 146, no. 6, pp. 2068 - 2077 , 1999.

[101] D. D. MacNeil, D. Larcher and J. R. Dahn, “Comparison of the Reactivity of Various Carbon Electrode Materials with Electrolyte at Elevated Temperature,” *J. Electrochem. Soc.,* vol. 146, no. 10, pp. 3596 - 3602, 1999.

[102] H.-p. Lin, D. Chua, M. Salomon, H-C. Shiao, M. Hendrickson, E. Plichta and S. Slane, “Low-Temperature Behavior of Li-Ion Cells,” *Electrochem. Solid. St.,* vol. 4, no. 6, pp. A71 - A73, 2001.

[103] T. Waldmann, M. Wilka, M. Kasper, M. Fleischhammer, M. Wohlfahrt-Mehrens, "Temperature Dependent Ageing Mechanisms in Lithium-Ion Batteries - A Post-Mortem Study," *J. Power Sources,* vol. 262, pp. 129 - 135, 2014.

[104] S. S. Zhang, K. Xu and T. R. Jow, "Charge and Discharge Characteristics of a Commercial $LiCoO_2$-Based 18650 Li-Ion Battery," *J. Power Sources,* vol. 160, pp. 1403 – 1409, 2006.

[105] J. Fan and S. Tan, "Studies on Charging Lithium-Ion Cells at Low Temperatures," *J. Electrochem. Soc.,* vol. 153, no. 6, pp. A1081 - A1092, 2006.

[106] J. Christensen and J. Newman, "Effect of Anode Film Resistance on the Charge/Discharge Capacity of a Lithium-Ion Battery," *J. Electrochem. Soc.,* vol. 150, no. 11, pp. A1416 - A1420, 2003.

[107] A. Blyr, C. Sigala, G. Amatucci, D. Guyornard, Y. Chabre and J-M. Tarascon, "Self-Discharge of $LiMn_2O_4$/C Li-Ion Cells in Their Discharged State - Understanding by Means of Three-Electrode Measurements," *J. Electrochem. Soc.,* vol. 145, no. 1, pp. 194 - 209, 1998.

[108] B. A. Johnson and R. E. White, "Characterization of Commercially Available Lithium-Ion Batteries," *J. Power Sources,* vol. 70, no. 1, pp. 48 - 54, 1998.

[109] L. E. Downie, L. J. Krause, J. C. Burns, L. D. Jensen, V. L. Chevrier and J. R. Dahn, "In Situ Detection of Lithium Plating on Graphite Electrodes by Electrochemical Calorimetry," *J. Electrochem. Soc,* vol. 160, no. 4, pp. A588 - A594, 2013.

[110] Nissan Europe. (23 March 2015). *Nissan LEAF Battery Reliably Outperforms Cynics, Critics and Alternatives*. [Online]. Available: http://www.newsroom.nissan-europe.com/uk/en-gb/Media/Media.aspx?mediaid=131212. [Accessed 28 May 2015].

[111] M. Kane. (June 2015). *Nissan LEAF Taxi Hits 100,000 Miles – Still Has All Battery Bars*. [Online]. Available: http://insideevs.com/nissan-leaf-taxi-hits-100000-miles-still-battery-bars/.

[112] M. Mirzaeian and P. J. Hall, "Preparation of Controlled Porosity Carbon Aerogels for Energy Storage in Rechargeable Lithium Oxygen Batteries," *Electrochimica Acta,* vol. 54, no. 28, pp. 7444 – 7451, 2009.

[113] H. Cheng and K. Scott, "Carbon-Supported Manganese Oxide Nanocatalysts for Rechargeable Lithium–Air Batteries," *J. Power Sources,* vol. 195, no. 5, pp. 1370 – 1374, 2010.

[114] R. Carr, "In Search of the Town Car," *Design,* vol. 211, pp. 29 - 37, 1966.

[115] R. Padbury and X. Zhang, "Lithium–Oxygen Batteries—Limiting Factors That Affect Performance," *J. Power Sources,* vol. 196, no. 10, pp. 4436 – 4444, 2011.

[116] K. M. Abraham and Z. Jiang, "A Polymer Electrolyte-Based Rechargeable Lithium/Oxygen Battery," *J. Electrochem. Soc,* vol. 143, no. 1, pp. 1 - 5, 1996.

[117] Y. Shao, S. Park, J. Xiao, J.-G. Zhang, Y. Wang and J. Liu, "Electrocatalysts for Nonaqueous Lithium–Air Batteries: Status, Challenges, and Perspective," *ACS Catal.,* vol. 2, no. 5, pp. 844 – 857, 2012.

[118] P. G. Bruce, S. A. Freunberger, L. J. Hardwick and J.-M. Tarascon, "Li–O_2 and Li–S Batteries with High Energy Storage," *Nature Mat.,* vol. 11, pp. 19 – 29, 2012.

[119] T. Ogasawara, A. Débart, M. Holzapfel, P. Novák and P. G. Bruce, "Rechargeable Li_2O_2 Electrode for Lithium Batteries," *J. Am. Chem. Soc.,* vol. 128, no. 4, pp. 1390 - 1393, 2006.

[120] L. Johnson, C. Li, Z. Liu, Y. Chen, S. A. Freunberger, P. C. Ashok, B. B. Praveen, K. Dholakia, J.-M. Tarascon and P. G. Bruce, "The Role of LiO_2 Solubility in O_2 Reduction in Aprotic Solvents and its Consequences for Li–O_2 Batteries," *Nature Chemistry,* vol. 6, pp. 1091 – 1099, 2014.

[121] J. Read, "Characterization of the Lithium/Oxygen Organic Electrolyte Battery," *J. Electrochem. Soc.,* vol. 149, no. 9, pp. A1190 - A1195, 2002.

[122] A. Débart, J. Bao, G. Armstrong and P. G. Bruce, "An O_2 Cathode for Rechargeable Lithium Batteries: The Effect of a Catalyst," *J. Power Sources,* vol. 174, no. 2, pp. 1177 – 1182, 2007.

[123] A. Débart, A. P. J. Bao and P. Bruce, "α-MnO2 Nanowires: A Catalyst for the O_2 Electrode in Rechargeable Lithium Batteries," *Angew. Chem. Int. Edit.,* vol. 47, no. 24, pp. 4521 – 4524, 2008.

[124] D. Zhang, Z. Fu, Z. Wei, T. Huang and A. Yu, "Polarization of Oxygen Electrode in Rechargeable Lithium Oxygen Batteries," *J. Electrochem. Soc.,* vol. 157, no. 3, pp. A362 - A365, 2010.

[125] C. Ó. Laoire, S. Mukerjee, E. J. Plichta, M. A. Hendrickson and K. M. Abraham, "Rechargeable Lithium/TEGDME-$LiPF_6$/O_2 Battery," *J. Electrochem. Soc.*, vol. 158, no. 3, pp. A302 - A308, 2011.

[126] W. Xu, V. V. Viswanathan, D. W. S. A. Towne, J. Xiao, Z. Nie, D. Hu and J.-G. Zhang, "Investigation on the Charging Process of Li_2O_2-Based Air Electrodes in Li–O_2 Batteries with Organic Carbonate Electrolytes," *J. Power Sources*, vol. 196, no. 8, pp. 3894 - 3899, 2011.

[127] S. A. Freunberger, Y. Chen, N. E. Drewett, L. J. Hardwick, F. Bardé and P. G. Bruce, "The Lithium–Oxygen Battery with Ether-Based Electrolytes," *Angew. Chem. Int. Ed.*, vol. 50, no. 37, pp. 8609 – 8613, 2011.

[128] J. Xiao, J. Hu, D. Wang, D. Hu, W. Xu, G. L. Graff, Z. Nie, J. Li and J.-G. Zhang, "Investigation of the Rechargeability of Li–O_2 Batteries in Non-Aqueous Electrolyte," *J. Power Sources*, vol. 196, no. 13, pp. 5674 – 5678, 2011.

[129] S. A. Freunberger, Y. Chen, Z. Peng, J. M. Griffin, L. J. Hardwick, F. Bardé, P. Novák and P. G. Bruce, "Reactions in the Rechargeable Lithium–O_2 Battery with Alkyl Carbonate Electrolytes," *J. Am. Chem. Soc.*, vol. 133, no. 20, pp. 8040 – 8047, 2011.

[130] V. S. Bryantsev and M. Blanco, "Computational Study of the Mechanisms of Superoxide-Induced Decomposition of Organic Carbonate-Based Electrolytes," *J. Phys. Chem. Lett.*, vol. 2, no. 5, pp. 379 – 383, 2011.

[131] J. Herranz, A. Garsuch and H. A. Gasteiger, "Using Rotating Ring Disc Electrode Voltammetry to Quantify the Superoxide Radical Stability of Aprotic Li–Air Battery Electrolytes," *J. Phys. Chem. C*, vol. 116, no. 36, pp. 19084 – 19094, 2012.

[132] J. Read, “Ether-Based Electrolytes for the Lithium/Oxygen Organic Electrolyte Battery,” *J. Electrochem. Soc.,* vol. 153, no. 1, pp. A96 - A100, 2006.

[133] B. D. McCloskey, A. Speidel, R. Scheffler, D. C. Miller, V. Viswanathan, J. S. Hummelshøj, J. K. Nørskov and A. C. Luntz, “Twin Problems of Interfacial Carbonate Formation in Nonaqueous Li–O_2 Batteries,” *J. Phys. Chem. Lett.,* vol. 3, no. 8, pp. 997 – 1001, 2012.

[134] B. D. McCloskey, D. S. Bethune, R. M. Shelby, G. Girishkumar and A. C. Luntz, “Solvents’ Critical Role in Nonaqueous Lithium–Oxygen Battery Electrochemistry,” *J. Phys. Chem. Lett.,* vol. 2, no. 10, pp. 1161 – 1166, 2011.

[135] R. R. Mitchell, B. M. Gallant, C. V. Thompson and Y. Shao-Horn, “All-Carbon-Nanofiber Electrodes for High-Energy Rechargeable Li–O_2 Batteries,” *Energy Environ. Sci.,* vol. 4, pp. 2952 - 2958, 2011.

[136] R. Younesi, M. Hahlin, F. Björefors, P. Johansson and K. Edström, “Li–O_2 Battery Degradation by Lithium Peroxide (Li_2O_2): A Model Study,” *Chem. Mater.,* vol. 25, no. 1, pp. 77 – 84, 2013.

[137] V. S. Bryantsev, J. Uddin, V. Giordani, W. Walker, D. Addison and G. V. Chase, “The Identification of Stable Solvents for Nonaqueous Rechargeable Li-Air Batteries,” *J. Electrochem. Soc,* vol. 160, no. 1, pp. A160 - A171, 2013.

[138] V. Y. Nimon, S. J. Visco, L. C. D. Jonghe, Y. M. Volfkovich and D. A. Bograchev, “Modeling and Experimental Study of Porous Carbon Cathodes in Li-O_2 Cells with Non-Aqueous Electrolyte,” *ECS Electrochem. Lett.,* vol. 2, no. 4, pp. A33 - A35, 2013.

[139] Y. Chen, S. A. Freunberger, Z. Peng, F. Bardé and P. G. Bruce, "Li−O_2 Battery with a Dimethylformamide Electrolyte," *J. Am. Chem. Soc.*, vol. 134, no. 18, pp. 7952 - 7957, 2012.

[140] C. O. Laoire, S. Mukerjee, K. M. Abraham, E. J. Plichta and M. A. Hendrickson, "Influence of Nonaqueous Solvents on the Electrochemistry of Oxygen in the Rechargeable Lithium-Air Battery," *J. Phys. Chem. C.*, vol. 114, no. 19, pp. 9178 - 9186, 2010.

[141] M. Roberts, R. Younesi, W. Richardson, J. Liu, T. Gustafsson, J. Zhu and K. Edström, "Increased Cycling Efficiency of Lithium Anodes in Dimethyl Sulfoxide Electrolytes For Use in Li-O_2 Batteries," *ECS Electrochem. Lett.*, vol. 3, no. 6, pp. A62 - A65, 2014.

[142] Z. Peng, S. A. Freunberger, Y. Chen and P. G. Bruce, "A Reversible and Higher-Rate Li-O_2 Battery," *Science,* vol. 337, pp. 563 - 566, 2012.

[143] D. Sharon, M. Afri, M. Noked, A. Garsuch, A. A. Frimer and D. Aurbach, "Oxidation of Dimethyl Sulfoxide Solutions by Electrochemical Reduction of Oxygen," *J. Phys. Chem. Lett.*, vol. 4, no. 18, pp. 3115 – 3119, 2013.

[144] R. Younesi, P. Norby and T. Vegge, "A New Look at the Stability of Dimethyl Sulfoxide and Acetonitrile in Li-O_2 Batteries," *ECS Electrochem. Lett.*, vol. 3, no. 3, pp. A15 - A18, 2014.

[145] D. G. Kwabi, T. P. Batcho, C. V. Amanchukwu, N. Ortiz-Vitoriano, P. Hammond, C. V. Thompson and Y. Shao-Horn, "Chemical Instability of Dimethyl Sulfoxide in Lithium−Air Batteries," *J. Phys. Chem. Lett.*, vol. 5, pp. 2850 - 2856, 2014.

[146] N. Mozhzhukhina, L. P. M. D. Leo and E. J. Calvo, “Infrared Spectroscopy Studies on Stability of Dimethyl Sulfoxide for Application in a Li–Air Battery,” *J. Phys. Chem. C*, vol. 117, no. 36, pp. 18375 – 18380, 2013.

[147] M. A. Schroeder, N. Kumar, A. J. Pearse, C. Liu, S. B. Lee, G. W. Rubloff, K. Leung and M. Noked, “DMSO–Li_2O_2 Interface in the Rechargeable Li–O_2 Battery Cathode: Theoretical and Experimental Perspectives on Stability,” *ACS Appl. Mater. Interfaces,* vol. 7, no. 21, pp. 11402 – 11411, 2015.

[148] B. D. McCloskey, D. S. Bethune, R. M. Shelby, T. Mori, R. Scheffler, A. Speidel, M. Sherwood and A. C. Luntz, “Limitations in Rechargeability of Li-O_2 Batteries and Possible Origins,” *J. Phys. Chem. Lett.,* vol. 3, no. 20, pp. 3043 - 3047, 2012.

[149] T. Kuboki, T. Okuyama, T. Ohsaki and N. Takami, “Lithium-Air Batteries using Hydrophobic Room Temperature Ionic Liquid Electrolyte,” *J. Power Sources,* vol. 146, no. 1 - 2, pp. 766 – 769, 2005.

[150] B. Kumar, J. Kumar, R. Leese, J. P. Fellnerb, S. J. Rodrigues and K. M. Abraham, “A Solid-State, Rechargeable, Long Cycle Life Lithium–Air Battery,” *J. Electrochem. Soc.,* vol. 157, no. 1, pp. A50 - A54, 2010.

[151] S. Wu, J. Tang, F. Li, X. Liu and H. Zhou, “Low Charge Overpotentials in Lithium–Oxygen Batteries Based on Tetraglyme Electrolytes with a Limited Amount of Water,” *Chem. Commun.,* vol. 51, pp. 16860 - 16863, 2015.

[152] Orion Fans. *ODB600PT Blower Series*. [Online]. Available: http://orionfans.com/products/dc-fans/item/odb600pt.html. [Accessed 13 May 2016].

[153] O. Crowther and M. Salomon, “Oxygen Selective Membranes for Li-Air (O_2) Batteries,” *Membranes,* vol. 2, pp. 216 -227, 2012.

[154] Molecular Products Ltd. (28 May 2009). *An Introduction to Sofnolime*. [Online]. Available: http://www.molecularproducts.com/pdf/technical-library/An%20 Introduction%20to%20Sofnolime%20Technical%20Article.pdf. [Accessed 12 May 2016].

[155] V. Ahuja, "CO_2 Removal from Air for Alkaline Fuel Cells Operating with Liquid Hydrogen," Ph.D. thesis, Dept. Mech. Eng., Univ. Canterbury, Christchurch, New Zealand, 1996, p. 10.

[156] L. Riboldi and O. Bolland, “Evaluating Pressure Swing Adsorption as a CO_2 Separation Technique in Coal-Fired Power Plants,” *International Journal of Greenhouse Gas Control,* vol. 39, pp. 1 – 16, 2015.

[157] BOC Ltd. (2012). *Oxygen Factsheet*. [Online]. Available: http:// www.boconline.co.uk/internet.lg.lg.gbr/en/images/Oxygen-factsheet410_54571.pdf?_ga=1.40168039.492724055.1462978313. [Accessed 13 May 2016].

[158] V. Bevara and P. Andrei, “Changing the Cathode Microstructure to Improve the Capacity of Li-Air Batteries: Theoretical Predictions,” *J. Electrochem. Soc.*, vol. 161, no. 14, pp. A2068 - A2079, 2014.

[159] C. Y. Jung, T. S. Zhao and L. An, “Modeling of Lithium-Oxygen Batteries with the Discharge Product Treated as a Discontinuous Deposit Layer,” *J. Power Sources,* vol. 273, pp. 440 - 447, 2015.

[160] K.-H. Xue, T.-K. Nguyen and A. A. Franco, “Impact of the Cathode Microstructure on the Discharge Performance of Lithium Air Batteries: A Multiscale Model,” *J. Electrochem. Soc.,* vol. 161, no. 8, pp. E3028 - E3035, 2014.

[161] C. H. Dustmann and A. Bito., “Secondary Batteries - High Temperature Systems | Safety,” in *Encyclopedia of Electrochemical Power Sources*, vol. 4, Amsterdam, Elsevier, 2009, pp. 324 - 334.

[162] J. R. Belt, D. M. Bernardi and V. Utgikar, “Development and Use of a Lithium-Metal Reference Electrode in Aging Studies of Lithium-Ion Batteries,” *J. Electrochem. Soc.,* vol. 161, no. 6, pp. A1116 - A1126, 2014.

[163] P. Liu, J. Wang, J. Hicks-Garner, E. Sherman, S. Soukiazian, M. Verbrugge, H. Tataria, J. Musser and P. Finamore, “Aging Mechanisms of $LiFePO_4$ Batteries Deduced by Electrochemical and Structural Analyses,” *J. Electrochem. Soc.*, vol. 157, no. 4, pp. A499 - A507, 2010.

[164] W. Fang, O. J. Kwon and C.-Y. Wang, “Electrochemical-Thermal Modeling of Automotive Li-Ion Batteries and Experimental Validation using a Three-Electrode Cell,” *Int. J. Energy Res.,* vol. 34, no. 2, pp. 107 - 15, 2010.

[165] G. Nagasubramanian, “Two- and Three-Electrode Impedance Studies on 18650 Li-Ion Cells,” *J. Power Sources,* vol. 87, no. 1 - 2, pp. 226 - 229, 2000.

2 Experimental procedures

2.1 Cell assembly

Three main types of cell were used in this work. Each type is tailored towards a specific application.

2.1.1 Swagelok cell

The Swagelok cell is a two-electrode system based on standard Swagelok brand plumbing components. This cell type may be configured to allow gases to penetrate the cell. As such, it is well suited to Li-air applications. An exploded view of this cell shown in Figure 1. The stainless steel cell structure consists of two rods, which act as the anode and cathode current collectors, inserted into the hollow cell housing and held in place with nuts and ferrules. A sheet of Mylar insulating polymer film is wrapped around the inside of the cell housing prior to inserting the rods in order to prevent short circuits. The cathode current collector is hollow to allow oxygen to enter the cell, whilst the anode current collector is solid. If the cathode active material requires mounting on a substrate due to a lack of rigidity (such as Super P carbon electrodes), then a stainless steel mesh is used in order to allow the free flow of gas to the cell. Separators wetted with electrolyte are placed between the anode and cathode during assembly. The atmosphere of this cell may be controlled by inserting it into a custom-built glass Swagelok case and purging it with the desired gas; for Li-air work in this thesis, this was pure O_2. Swagelok cells with a ½" inner diameter were used throughout this work.

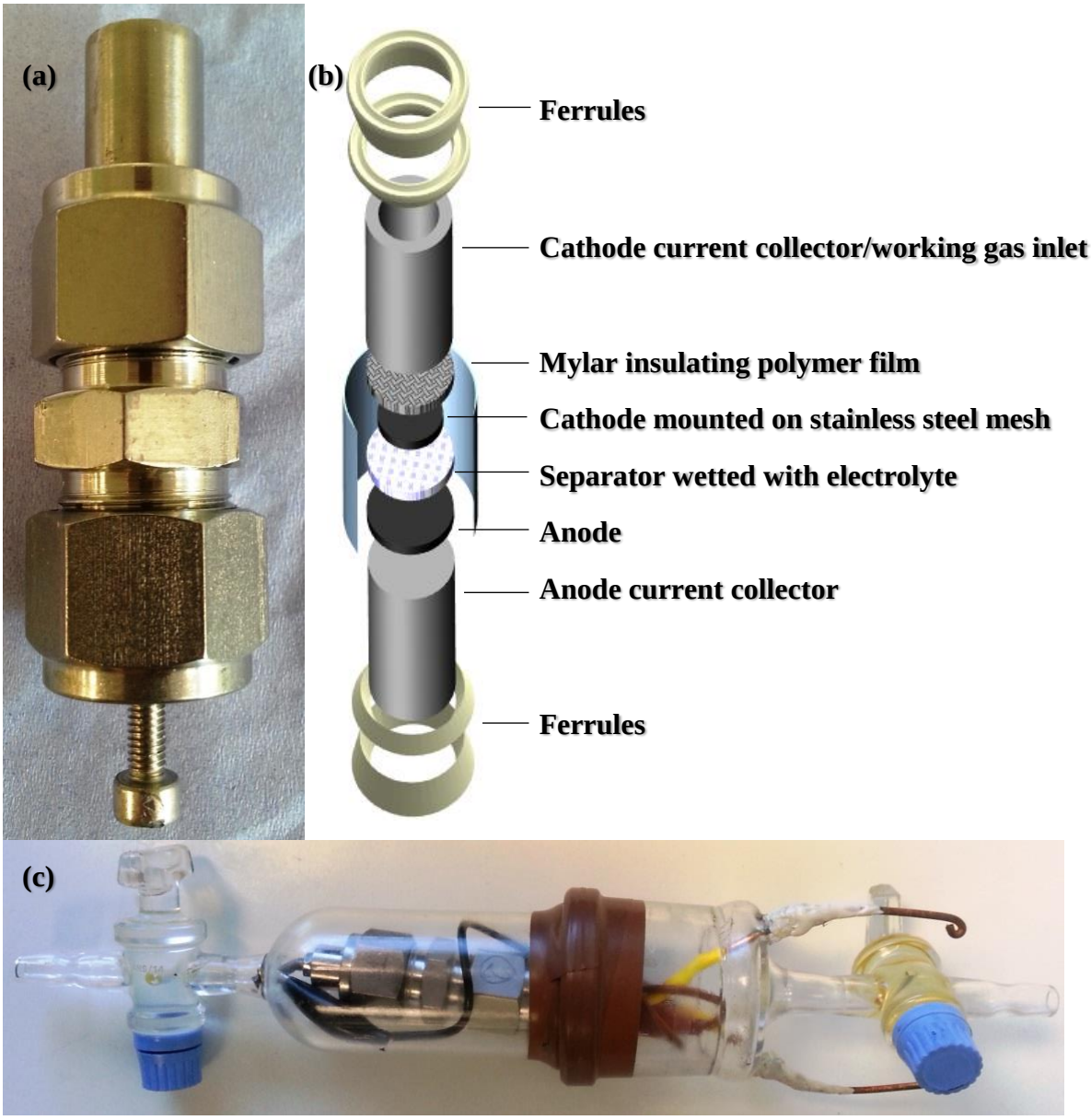

Figure 1: The Swagelok cell. (a) Photograph of a Swagelok cell. (b) Exploded diagram of the internal components. (c) Photograph of a complete assembly inside a glass Swagelok case.

2.1.2 Coin cell

Coin cells are sealed two-electrode cells that prevent atmospheric ingress and electrolyte evaporation. Coin cell cases of the 2325 format were used in this work to build half-cells based on commercial lithium-ion electrode materials. An exploded schematic of this cell is shown in Figure 2.

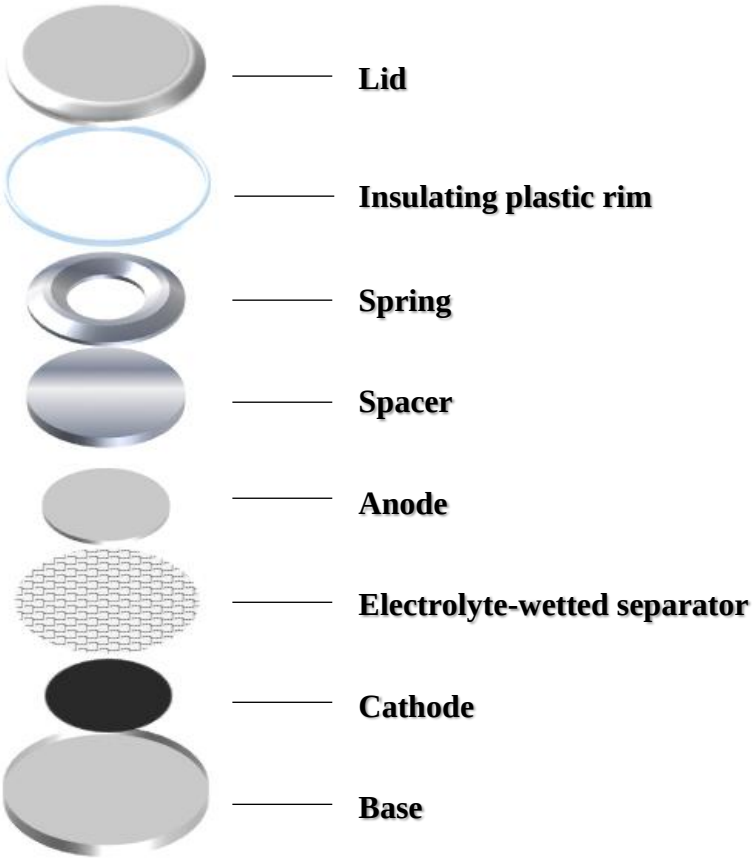

Figure 2: Exploded schematic of a coin cell.

The cell is comprised of a base and lid with an insulating plastic rim to join them together whilst preventing short circuits. Inside, the cathode, electrolyte-wetted separator and anode are placed on top of each other, followed by a spacer and spring to improve electrical contact with the lid. The cell is then pressed together in a pneumatic press.

2.1.3 Glass cell

Glass cells, or flooded cells, are versatile cells that can be configured as multi-electrode systems that are either airtight or facilitate purging with a working gas of choice. As such, these cells were heavily used for electrochemistry work, typically as three-electrode systems with N_2 or O_2 working gas. Electrodes used for this type of cell are typically polished stick electrodes, i.e. smooth disks of active material at the end of a rod, or wires made of the material

of choice. Strip-shaped electrodes were occasionally used in this work; these were inserted into the cell on the end of a stainless steel crocodile clip.

Figure 3 shows a typical three-electrode glass cell with gas purging capability. The cell consists of the working (WE), counter (CE) and reference (RE) electrodes of choice, plus gas in and gas out glassware, inserted into the necks of the glass cell. Enough electrolyte is injected into the glass cell to immerse the ends of the electrodes, taking care to avoid adding an excessive amount as this could directly contact the electrode holders, such as the crocodile clips, and thus alter the electrochemistry taking place in the system.

2.2 Preparation of cell components

Whilst commercially available electrodes feature in some of this work, most notably the stick, rotating disk and ultramicroelectrodes used for electrochemical studies, many of the cells

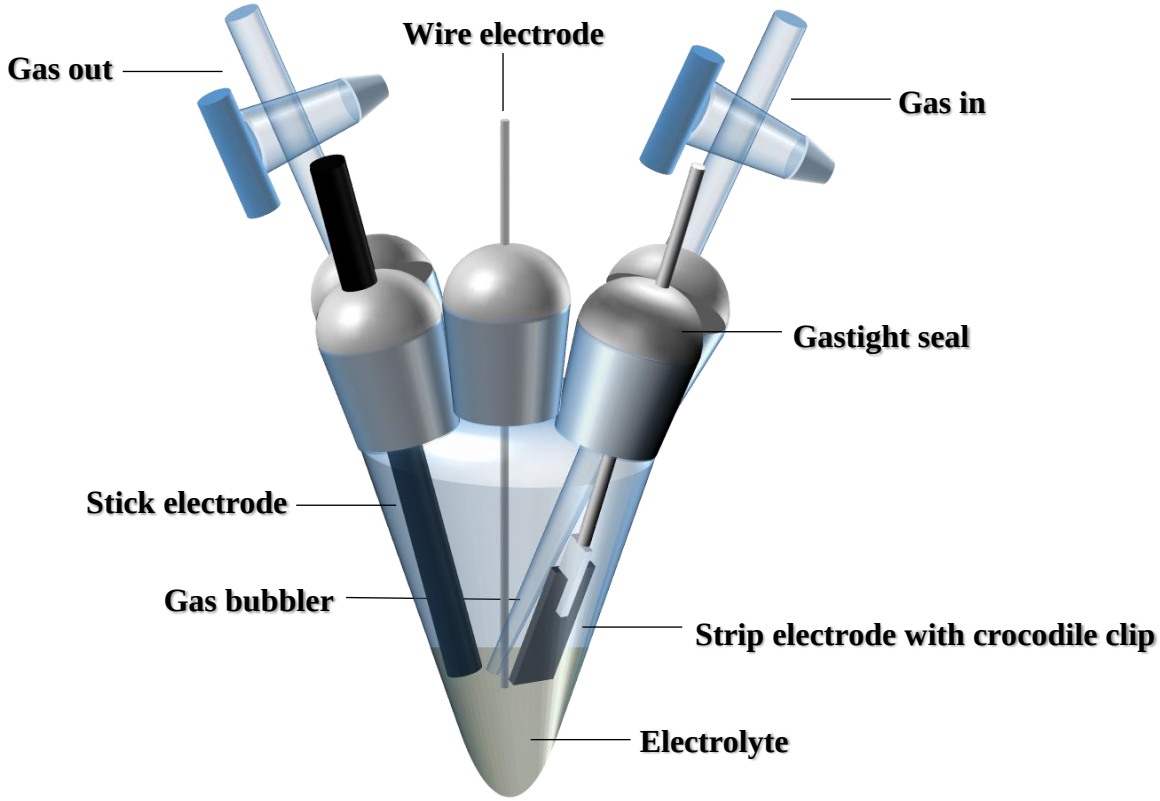

Figure 3: Schematic of a typical three-electrode glass cell with gas purging capability.

discussed later featured electrodes that were fabricated in the lab. Here, the in-lab preparation of standard cell components is explained in detail.

2.2.1 Anodes

Cells in the Li-air studies used chemically-precharged lithium iron phosphate (LFP) anodes. These are favoured over pure lithium foil due to their stability in contact with water, air and electrolyte; conversely, lithium foil can be powdered by some electrolytes such as DMSO due to the lack of formation of a stable SEI layer [1].

LFP anodes were fabricated by mixing LFP powder (MTI Corporation), Super P Li carbon black (TIMCAL) and polytetrafluoroethylene (PTFE) preparation (Aldrich) diluted to 10 wt. % suspension in distilled water in a ratio of 8:0.5<X<1:1. The mixture was wetted with isopropanol (Sigma Aldrich) to form a slurry, which was mixed into a ball and cut into equal portions containing 30 mg active material. The portions were pressed into disks and soaked in a solution containing a 1:1 ratio of ethanol and distilled water for 30 minutes to remove the surfactant in the PTFE solution before chemically precharging them in a solution of 250 ml distilled water with 3.6 ml hydrogen peroxide (Fisher Chemical) and 1.5 ml acetic acid (Sigma Aldrich). The anodes were then rinsed in 1:1 ethanol/H_2O solution again and dried under vacuum at 120 °C overnight in a Buchi oven. This method is similar to the anode preparation method employed for previous Li-air studies [2].

2.2.2 Cathodes

Super P Li was chosen as the carbon material due to its high surface area of 62 $m^2 g^{-1}$. A slurry of Super P Li and 10 wt. % PTFE in suspension in distilled water was created in a ratio of 9:1. This was mixed into a ball and divided into equal portions containing 1.5 mg active material.

Each portion was spread onto a ½" diameter disk of 180 mesh stainless steel current collector (Advent Research Materials). The cells were then rinsed and dried in the same manner as the anodes. This method is based on that used in a number of previous studies [2, 3].

2.2.3 Separators

Whatman glass microfiber separators were used in the Swagelok and coin cells in this study. These have the advantage of being non-flammable and highly absorbent, allowing them to be soaked in electrolyte solution; additionally, adiponitrile (Chapter 3) was found to have difficulty permeating Celgard polymer separators.

Appropriately sized disks were cut from the large, as-supplied disks using hole punches. The separators were then sonicated in acetone for 15 minutes and dried under vacuum at 300 °C overnight.

2.3 Electrolyte purification

Commercial cell electrolytes, such as LP30, are readily available from chemical suppliers. These have a known purity and quantity of solvent and salt in their composition, and are thus ready to use straight from their containers. However, solvents used in the preparation of novel electrolytes are typically between 97 % and 99 % pure. This means that they contain a combination of water and lighter and heavier solvents which could impact on the performance and cycle life of a cell due to unexpected side reactions with the salt, electrodes or discharge products. Salts used may also contain water if they have not been packaged in an inert atmosphere. Therefore, solvents must be purified, and salts dried, prior to use.

2.3.1 Distillation

A solvent and the impurities that it contains have different boiling points. When heat is applied to the solvent mixture, and the liquid with the lowest boiling point, i.e. the most volatile solvent, starts to boil, the temperature of the solvent mixture does not increase until said liquid has completely boiled. Once this has happened, the temperature will increase until it reaches the next most volatile liquid's boiling point and so on. Distillation exploits this by boiling off lighter impurities before collecting the pure solvent, leaving heavier impurities behind.

Distillation equipment consists of a starting flask with heating element situated beneath an insulated vertical column that is water-cooled at the top. A valve at the top of the column controls the flow of solvent to a collection flask. The impure solvent is placed in the starting flask with a magnetic stirring bar to improve heat transfer through the solvent. Additionally, anti-bumping granules are added to prevent flash boiling, whereby the solvent aggressively vaporises and shoots up the column. In order to prevent water from the atmosphere from becoming absorbed by the purified solvent, an inert gas, such as argon, is flowed from the starting flask through the column to a valve just before the collection flask. For heavier solvents, a vacuum is applied to the valve near the collection flask, in place of the inert gas flow, thus reducing the boiling point of the solvent and requiring less energy for the process to proceed. Readings from temperature probes in the starting flask and at the top of the column allow the boiling point of the solvent to be determined, as well as whether or not the system is currently distilling the desired solvent or its lighter, or heavier, impurities.

Heat is applied to the starting flask, increasing gradually until the solvent starts to boil. The vapour slowly rises up the column before condensing at the top and running back down the column. This process is known as refluxing and helps to establish thermal equilibrium between the liquid and vapour throughout the column, with lighter solvents condensing towards the top

and heavier solvents towards the bottom. Therefore, after sufficient refluxing, only the most volatile solvent is present at the top of the column, which is then tapped off into the collection flask. The flask is then replaced whilst maintaining an inert atmosphere by shutting a valve just before the collection flask. The pure solvent is then distilled into the new collection flask, ensuring that the starting flask is not allowed to boil dry and thus boil off heavier impurities into the collection flask, ruining the purity of the distilled solvent.

Solvents used in this work have been distilled on a Fischer Labodest HMS 500 C column. Table 1 gives the distillation parameters used for the distillation of each solvent. Typically, solvents were distilled with starting volumes of between 300 ml and 1 litre, out of which approximately 60 % would be collected as pure solvent, with the remaining 40 % split evenly between the discarded first fraction and the heavier solvent left in the starting flask. Pure solvents were then transferred to an MBraun glove box with argon atmosphere (O_2 < 0.1 ppm; H_2O < 0.1 ppm), where they were decanted into Schott DURAN bottles and dried with freshly dried molecular sieves for several days prior to use, so as to remove any remaining moisture and prevent further H_2O ingress.

2.3.2 Karl Fischer titration (KFT)

The water content of distilled solvents must be checked to ensure that the distillation and drying procedures were successful. This is achieved using a Karl Fischer titrator, in which the water

Solvent	Atmosphere	Bath temperature (°C)	Mantle temperature (°C)
Acetonitrile	Argon	82	Unheated
Adiponitrile	Vacuum	160	90
Glutaronitrile	Vacuum	145	90
DMSO	Vacuum	74	62
TEGDME	Vacuum	147	90

Table 1: Distillation parameters for the solvents used throughout this study.

present in the electrolyte reacts with a known volume and concentration of titrant (reagent) until it is neutralised. The water concentration can be determined from the resultant current.

A diaphragm-less Karl Fischer titrator consists of a sealed flask containing a double-pin platinum reference electrode and liquid reagent formed of an alcohol, a base, sulfur dioxide and iodine ions (I^-). A current generator module containing a slender cathode wire and a large anode rim is immersed in the reagent. The assembly sits on top of a magnetic stirrer [4, 5].

The KFT process centres on the reaction of iodine (I_2) with water. In cases where the water concentration is high, iodine is added to the solvent to be analysed (i.e. the analyte), in a process known as volumetric titration. However, in this study, coulometric titration is used, since the water content of the analyte is sufficiently low to allow the reaction to complete *via* the electrochemical formation of I_2 from I^- already present in the reagent.

During coulometric titration, a known mass of analyte, typically the equivalent of *circa* 1 ml volume, is injected into the cell *via* an airtight silicon septum. As the solution is stirred, iodine ions are oxidised to I_2 at the anode; the large surface area of the anode rim at the edge of the generator module, coupled with the magnetic stirrer, ensures that the I_2 is dispersed in the solution before it can be reduced to I^- at the cathode. When I_2 comes into contact with water, the following titration reaction occurs:

$$ROH + SO_2 + RN \rightarrow (RNH)\cdot SO_3R$$

$$(RNH)\cdot SO_3R + 2RN + I_2 + H_2O \rightarrow (RNH)\cdot SO_4R + 2(RNH)I$$

Where ROH denotes the alcohol in the reagent. It can be seen from this that two I^- are required to produce I_2 which then subsequently reacts with a single H_2O molecule, and so two electrons are released per water molecule. The resultant current allows the number of water molecules present in the analyte to be determined and converted into H_2O concentration in parts per million (ppm) using the known mass of analyte added to the solution [6]. The cell can be

calibrated using a water standard, which is a solvent containing a pre-determined H_2O concentration.

All Karl-Fischer titration work discussed in later chapters was performed on a Mettler-Toledo C30 Coulometric diaphragm-less KF Titrator with Sigma-Aldrich HYDRANAL Coulomat AG reagent, which contains methanol (alcohol), and diethanolamine and imidazole (bases). The KFT was kept in an argon glove box to limit H_2O and CO_2 ingress from the atmosphere.

2.3.3 Drying of salts

Salts used in this work were dried under heat and vacuum for a prolonged period of time ranging from overnight to a period of several days. This was achieved either using a Buchi oven or the heated antechamber of a glove box. Care must be paid to the drying temperature used so as to drive off moisture without decomposing the salt. As such, it is preferable to dry the salt at 80 °C for several days than to dry it at 200 °C or more overnight.

2.4 Cell cycling procedures

A number of cycling procedures are available to characterise the performance of a cell. However, much can be learned from the open circuit voltage (OCV) or rest period, during which no external influence, such as current or potential, is applied, i.e. the cell is not cycled. During OCV, the potential of the cell may be measured, which can help to determine its approximate State of Charge (SoC); observe the electrodes reaching their equilibrium potential after cell assembly or cycling; or detect short circuits, which are identifiable by the cell potential decreasing despite no load being attached to the circuit. This technique may be used to allow cells to reach the temperature of the thermal chamber during temperature-controlled tests, and to rest cells after harsh cycling conditions before commencing the next procedure.

2.4.1 Galvanostatic cycling (CC)

In galvanostatic, or constant current (CC) cycling, a current of a fixed value is applied to the WE, thus initiating cycling. Conventionally, the polarity of the current is negative when discharging and positive when charging (denoted with respect to the cathode). The resultant potential is plotted against capacity or time, as shown in Figure 4. Cycle segments are typically specified to terminate upon the cell attaining a given capacity or reaching a predefined minimum or maximum potential.

The bulk of cell cycling featured in this work is CC cycling, and the results are commonly expressed as potential *vs.* time.

2.4.2 Potentiostatic cycling (CP)

When a cell undergoes potentiostatic, or constant potential (CP) cycling, the WE is held at a constant voltage. Consequently, the cell current becomes the variable parameter, gradually

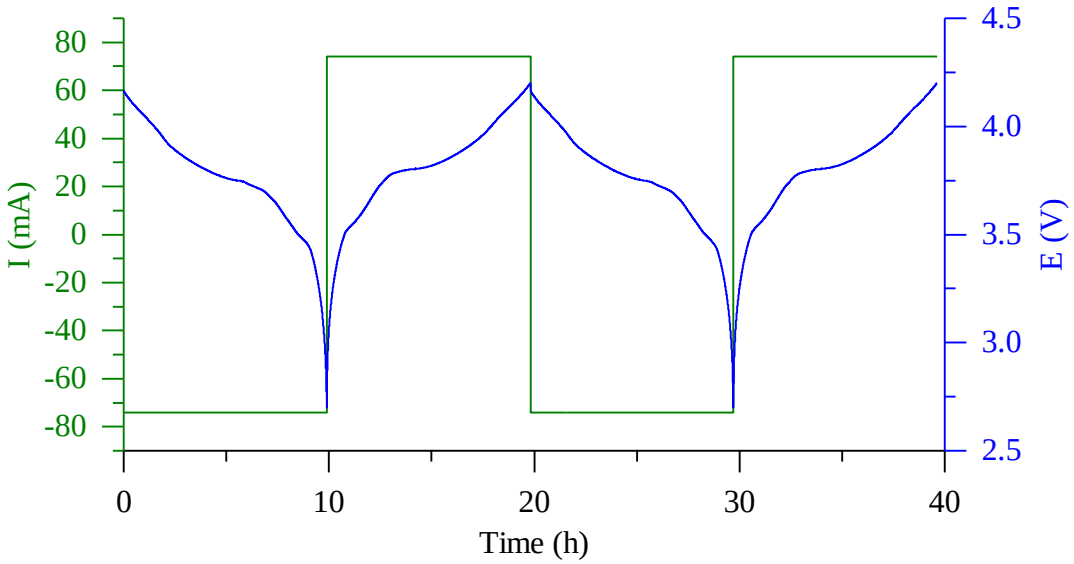

Figure 4: Example of galvanostatic cycling, whereby a constant current is applied, causing the potential to vary. The opposite occurs during potentiostatic cycling (CP).

tapering off until equilibrium between the electrodes is achieved at the fixed potential. Such cycling is particularly useful for ensuring that a cell is fully charged ahead of cycling, or fully discharged ahead of disassembly.

In this work, CP cycling is terminated when a specified minimum current value is reached.

2.4.3 Galvanostatic intermittent titration technique (GITT)

It is not possible to determine the OCV of a cell mid-cycle when a load is applied. However, this information is particularly important when designing battery management systems (BMS) to be used in real-world applications, such as automotive traction batteries, where the cycle patterns of cells are random. For Li-ion cells, GITT is a technique that allows the OCV of an electrode to be determined as a function of its lithium content, and also allows the diffusion coefficient of lithium within an electrode to be calculated [7]. However, the cycling procedure of the technique may be used to plot OCV as a function of SoC; GITT is used solely for this purpose in this work. Data is gathered by applying short bursts of constant current (CC) cycling at low C-rates (e.g. C/10), interspersed by pre-defined OCV periods. The duration of the CC segments may be determined as a fraction of the overall cell capacity, e.g. $1/50^{th}$. The OCV over various SoC may be obtained at the end of each rest period, during which the potential of the cell gradually stabilises as the WE and CE reach equilibrium following the CC cycling. Rest periods are typically one hour to allow equilibrium to be reached, with the condition that the time shall be increased if the potential is still shifting by more than a predetermined rate (typically in the range of millivolts per hour) by the end of the rest period. From this, a profile of OCV values at a large number of SoC is gradually built up (Figure 5); the smaller the fraction of cell capacity attributed to each CC segment, the greater the accuracy of the OCV profile.

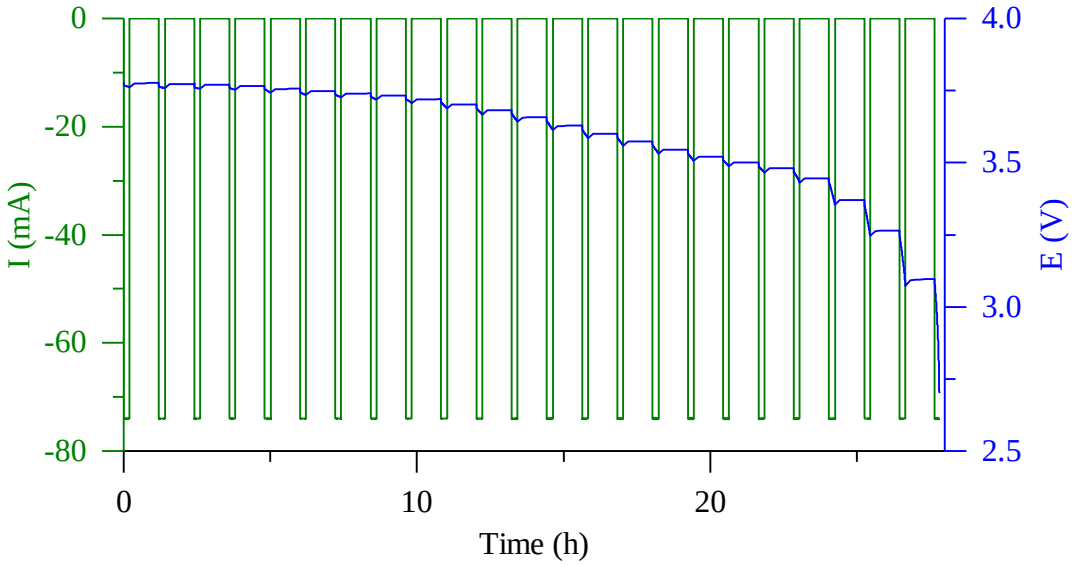

Figure 5: Example of GITT cycling. Short, galvanostatic pulses of current applied to the cell, followed by rests of approximately 1 hour, allow the OCV profile of the cell to be obtained throughout its SoC.

2.5 Electrochemical techniques

In addition to the cycling of full cells, crucial information can be obtained by applying electrochemical techniques to 3-electrode cells containing standardised components of known electrochemical performance, plus one novel cell component, e.g. the electrolyte. Typical components of such a cell include a nonporous stick WE made of gold or glassy carbon; a platinum wire CE; gas bubblers for the study of cell behaviour in a given atmosphere; and a RE. The RE has no external potential or current applied to it and, as such, does not participate in any reactions within the cell. Instead, the potential of the WE and CE may be measured individually against its pre-determined, constant standard potential. Stick electrodes are always polished prior to use, using alumina powder on a piece of fine grain polishing pad wetted with ethanol, so as to remove any impurities that may have accumulated on the surface during previous cycling.

The RE used in some later work is precharged lithium iron phosphate (LFP) in a fritted vessel containing dimethyl sulfoxide (DMSO) with a mixture of 0.1 M lithium perchlorate ($LiClO_4$) and 1 M tetrabutylammonium perchlorate ($TBAClO_4$). The glass frit prevents cross contamination of the RE and cell electrolytes whilst facilitating ionic conductivity, thus allowing the RE to function. The conductivity of the glass frit is low, but since no notable current flows through the RE, the voltage loss is negligible.

The potential of the fritted RE can be calibrated by placing a piece of lithium foil in the cell as the WE, and connecting the RE as the CE in a 2-electrode setup. The resulting OCV gives the potential of the RE *vs*. Li/Li^+ in that solvent, which can be used to standardise the potentials of all experiments.

2.5.1 Linear sweep voltammetry (LSV) and cyclic voltammetry (CV)

Linear sweep voltammetry (LSV) involves the application of a potential, that is either increasing (anodic sweep) or decreasing (cathodic sweep) at a constant rate expressed in volts per second ($V\ s^{-1}$), to a half-cell. Typically, this process will be started from a potential that lies before the oxidation or reduction potential, and then swept through said potential window in order to observe the peak current of the process, the total charge transferred and the potentials at which each step of the reaction takes place. Cyclic voltammetry (CV) is an extension of this method in which, when the potential limit (E_{max} or E_{min}) is reached, the sweep is reversed until the opposite potential limit is reached and so on (Figure 6) [8, 9]. The chemical reversibility of a reaction can be determined by comparing the charge transferred during the reduction and oxidation reactions.

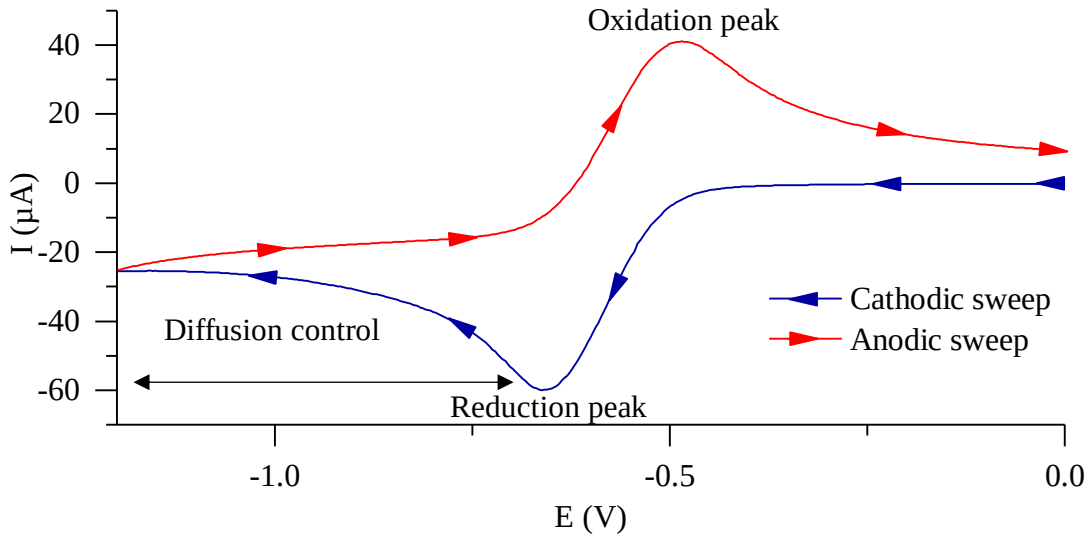

Figure 6: An example of cyclic voltammetry (CV) for O_2 reduction and oxidation in DMSO (see Figure 4(a), Chapter 4), showing the cathodic (blue) and anodic (red) sweeps, plus the direction in which their potentials are swept. The reduction peak, oxidation peak and region of diffusion control are indicated.

CV has been employed in this work to identify the potentials associated with the reduction and oxidation (redox) peaks of oxygen in a given solvent, which indicates whether or not these crucial steps occur within the operating window of a typical Li-air cell. It has also been used to obtain physico-chemical properties of electrolytes. In Figure 6, CV has been used to determine the region of diffusion control for the reduction of O_2 to O_2^- in DMSO, whereby the current is limited by the flux of O_2 to the working electrode. LSV has been used in this work to activate nucleation sites on copper wire ahead of electroplating with lithium.

2.5.2 Obtaining the diffusion coefficient and concentration of reactants in an electrolyte

The diffusion coefficient, *D*, of active species in an electrolyte dictates the current that can be achieved by a cell at a potential at which the current is diffusion-limited. By extension, the concentration, *C*, governs the quantity of available reactants per unit volume of electrolyte that can be transported to the surface of the WE. In practical terms, low values for either of these

parameters will negatively impact upon cell performance by limiting the maximum current and capacity, especially at high C-rates. Therefore, when screening solvents and modelling cell behaviour, it is imperative to know the values of these two parameters. Here, a number of techniques for determining *C* and *D* of reactants in an electrolyte are outlined.

2.5.2.1 Determining the surface area of a planar electrode

An accurate value for the surface area of a planar WE, and thus the area of the active surface upon which redox reactions take place, is essential when calculating the diffusion coefficient and concentration of reactants in an electrolyte, since this parameter forms an integral part of all equations that can be used to calculate these values. To find the surface area of a WE, the electrode is placed in a cell with an electrolyte of known values of *C* and *D*, and that is known to have a reversible redox reaction. The cell is then subjected to CV in an inert atmosphere. The peak reduction current from the resultant data is then inserted into the Randles-Sevcik equation (1), which considers the influence of the CV sweep rate on the peak current, I_p, obtained at room temperature [9]:

$$I_P = 2.69 \times 10^5 n^{\frac{3}{2}} C D^{\frac{1}{2}} v^{\frac{1}{2}} A \quad (1)$$

Here, *n* is the number of electrons transferred to reduce or oxidise the reactants; *C* is the concentration of the reactant in the electrolyte, in mol m^{-3} (mM); *D* is the diffusion coefficient of the reactant in the electrolyte, in m^2 s^{-1}; *v* is the sweep rate in V s^{-1} and *A* is the electrode surface area in m^2. By inserting the known values of *C* and *D* for the electrolyte and rearranging the equation, the surface area of the electrode may be determined.

An electrolyte consisting of 1 mM ferrocene methanol and 0.1 M sodium chloride in distilled water was used to determine the diameter of WEs used in this work. A value of $D = 7.8 \times 10^{-10}$ m^2 s^{-1} for this solvent was obtained from the literature [10].

2.5.2.2 Chronoamperometry and the Cottrell equation

Chronoamperometry, in conjunction with the Cottrell equation, may be used to study the change in current over time arising from a stepped change to the potential applied to a cell [11]. An example of this is found in Chapter 4 when the diffusion coefficient, *D*, and concentration, *C*, of the reactant (in this case oxygen) in an electrolyte are determined. First, CV is used to identify the potential range in which mass transport is the limiting factor, i.e. the reaction is under diffusion control; this corresponds to the region beyond the reduction peak during the cathodic sweep. The cell is then held at the corresponding potential for diffusion control for a period of twenty seconds, during which the current tapers off. This decrease in current arises from the limited supply of the reactant to the WE to participate in the reduction reaction as governed by the diffusion coefficient of the reactant in that electrolyte. A plot of the current *vs.* the inverse square root of time yields a straight line, the gradient of which can be inserted into a rearranged form of the Cottrell equation for the time-dependent current, I_t (2):

$$I_t = \frac{nFC\sqrt{D}A}{\sqrt{\pi t}} \tag{2}$$

where, in addition to the parameters that have previously been defined, *t* in the time in s. Since the values of both *C* and *D* are unknown, a second equation must be solved simultaneously with the Cottrell equation in order to obtain these values.

2.5.2.3 Rotating disk electrode (RDE) and the Levich equation

The rotating disk electrode is a WE that is typically made of a polished planar conductive material, such as gold or glassy carbon, embedded within an insulating outer material, as per a conventional stick WE. However, the RDE can spin at several hundred revs per minute (rpm), with the user having precise control over its angular velocity. Rotation helps to mitigate the deposition of insoluble salts during reduction and also serves to improve transport of the reactants to the active surface of the electrode. This is achieved by repelling the solvent and salt on the surface of the electrode through centrifugal force, which in turn draws more electrolyte (and thus reactants) from directly underneath the electrode towards its surface to fill the void [12].

When an electrochemical cell featuring a RDE WE undergoes CV, the current increases in a sigmoidal (S-shaped) fashion until it reaches a plateau that is determined by the rotation of the RDE and the resultant transport of reactants to the electrode surface. The current plateau is the Levich current, I_L, which has the corresponding Levich equation (3):

$$I_L = 0.62nFAD^{\frac{2}{3}}\omega^{\frac{1}{2}}{v_k}^{-\frac{1}{6}}C \quad (3)$$

where, in addition to the parameters that have previously been defined, ω is the angular velocity of the RDE in rad s^{-1} and v_k is the kinematic viscosity of the solvent in m^2 s^{-1}. The Levich equation may be solved simultaneously with the Cottrell equation to obtain the values of C and D for the reactants in that particular electrolyte.

All RDE work in this thesis used a glassy carbon RDE with a surface area of 1.96×10^{-5} m^2, spun at 600 rpm.

2.5.2.4 The ultramicroelectrode (UME)

The ultramicroelectrode (UME) is an electrode with a diameter in the region of a few micrometres. This small diameter minimises the current through, and voltage drop across, the electrode, which is advantageous when performing electrochemistry on organic solvents due to their high resistance. In theory, this allows the steady-state current to be achieved at high scan rates without distorting the data. The diffusion layer of UMEs, i.e. the region near the electrode where the concentration of the electroactive species is different to that of the bulk solution, is larger with respect to the standard-dimension electrodes used for the chronoamperometry studies outlined above.

Upon undergoing voltammetry, the magnitude of the current of a UME increases in a sigmoidal fashion until it reaches the steady-state current, I_{SS}. The UME equation for I_{SS} factors in the radial diffusion that occurs with a disk-shaped UME, which results in current density being stronger at the edge of the UME than in the centre:

$$I_{SS} = 4nFDCr \tag{4}$$

where, in addition to the parameters defined above, r is the radius of the UME in m.

Equation (4) may also be used to calculate the radius of a UME when the cell undergoes a potential sweep in an electrolyte with known concentration C and diffusion coefficient D for the reactant, such as the electrolyte containing ferrocene methanol described in Section 2.5.2.1. In this work, the radius of the UME was calculated using 1 mM ferrocene methanol and 0.1 M sodium chloride in distilled water as for macro-sized WEs.

2.6 Materials characterisation and post-mortem analysis

Upon completion of cycling, or cell failure, it is often useful to disassemble a cell and analyse the structure and/or chemical content of its electrodes and electrolyte. This provides information on the exact cause of the deterioration in a cell's State of Health (SoH), which is signalled by a decrease in capacity retention and an increase in potential hysteresis (the gap between the discharge and charge potential profiles). Numerous post-mortem analytical techniques may be employed on the same sample to reinforce the findings of each procedure. Such methods may also be applied to pristine, uncycled cell components to provide a before-and-after comparison of the composition of the materials used; any changes to the materials after cycling which do not correspond to the anticipated discharge products are a clear indication of cell degradation.

Additionally, when attempting to correlate cell performance to the characteristics of its components, or create electrode materials of a particular specification e.g. pore size, it is imperative to conduct material characterisation prior to cell assembly so that the parameters of the cell components are accurately known.

2.6.1 Fourier transform infrared spectroscopy (FTIR)

In electrode materials and reaction products, vibrations are encountered in the atomic bonds of the structure, which vary in frequency depending on chemical composition and structural formation. Materials will absorb radiation that corresponds to the vibration frequencies of their atomic bonds. These frequencies lie within the mid-infrared spectrum, ranging from 4000 cm^{-1} – 250 cm^{-1} (*circa* 2.5 μm – 40 μm; 120 THz – 7.5 THz). The unique atomic structure

of different materials results in each having its own signature of absorption frequencies. Fourier transform infrared spectroscopy (FTIR) allows these frequencies to be rapidly identified for a particular material.

A Fourier transform infrared spectroscope features two radiation sources: a halogen lamp that provides a wide range of infrared radiation wavelengths, and a HeNe laser that produces monochromatic light, i.e. light of only one wavelength, which is used for calibration. Light from the halogen lamp is fired into an interferometer that "encodes" a set of multiple wavelengths, known as an interferogram, into the signal using a beam splitter, a system of swivelling mirrors that can selectively block wavelengths of light from the halogen lamp's spectrum. The manipulated light travels onwards to the sample through a system of static mirrors. The radiation then passes through, or is absorbed by, the sample, with the transmitted radiation being aimed at a detector. The wavelengths of light present in the interferogram are changed by the interferometer and the process is repeated. The resultant signals from the detector, complete with data regarding the wavelengths present in each interferogram, are sent to a computer, where the Fourier transform mathematical method is used to interpret the transmittance of light at each wavelength, with the results then being plotted on a graph. By periodically adjusting the wavelengths present in the interferogram, the full wavelength spectrum of the halogen lamp is delivered to the sample much faster than by firing only one wavelength at the sample at a time [13]. A schematic of this process is provided in Figure 7.

Prior to running FTIR on a sample, it is good practice to take a background reading that may be subtracted from the sample spectrum using analytical software on a computer. Once the reading has been taken, a small sample of the material to be analysed is ground with some caesium iodide (CsI) using a pestle and mortar. The resultant powder is pressed into a pellet using a die set and hand press. The pellet is loaded into the sample holder of the spectrometer, where it undergoes FTIR. Differences between the spectra of pristine and cycled electrode

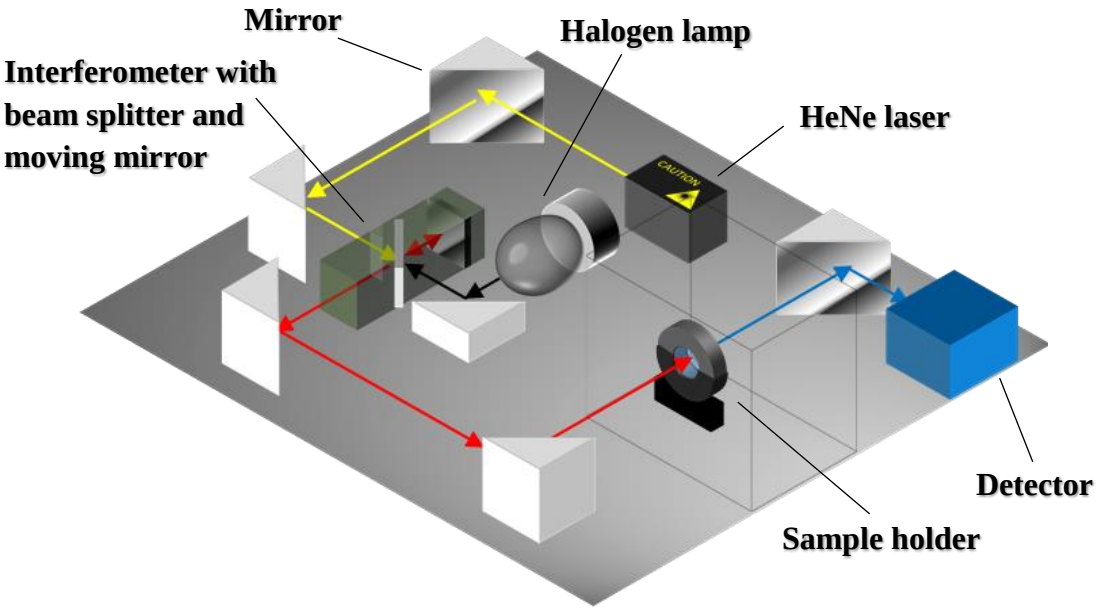

Figure 7: Schematic of the internal components and operational method of an FTIR configured in transmission mode. The path taken by light from the halogen lamp (black) and HeNe laser (yellow) through the interferometer (red) and sample (blue) to the detector is shown. The wire frame around the sample holder denotes the area of the FTIR that is open to the user.

materials may indicate the presence of discharge or decomposition products, which may be identified by comparing the latter spectrum with the spectra of known materials, i.e "standards."

FTIR performed in this work was conducted on a Thermo-Scientific Nicolet 6700 spectrometer housed in a nitrogen glove box to prevent H_2O and CO_2 ingress. Electrode materials were cleaned with distilled acetonitrile and dried under vacuum prior to undergoing FTIR to remove any residual electrolyte from their pores.

2.6.2 X-ray diffraction (XRD)

The atomic structure of a material's crystal lattice may be used to identify the material using X-ray diffraction. Having wavelengths of an order of magnitude similar to the spacing between atoms in a crystal structure (*circa* 10^{-10} m), X-rays are diffracted by such structures when fired

at them. Variations in the intensity and angle of the diffracted X-rays can be used to identify the crystal structures, and thus materials, present in a sample.

X-rays are produced by the X-ray diffractometer by firing electrons at a metal target, most commonly copper or iron. Target atoms undergo a 2p → 1s transition, whereby an electron from the second energy level of the atom fills the hole created by the incident electron ejecting one of the electrons from the ground state (as illustrated in Figure 8). This process emits the most intense, and thus favourable, variant of X-ray. X-rays arising from other, less favourable transitions are removed to produce a monochromatic, coherent beam that is then aimed at the sample. Incident X-rays are diffracted by the crystal lattice structure of the sample, with the altered phases of the X-ray radiation interfering either constructively to produce a stronger signal, or destructively to neutralise the signal; these are then picked up by a detector. The coherence of the diffracted X-rays is expressed by Bragg's Law:

$$n\lambda = 2d \sin\theta \tag{5}$$

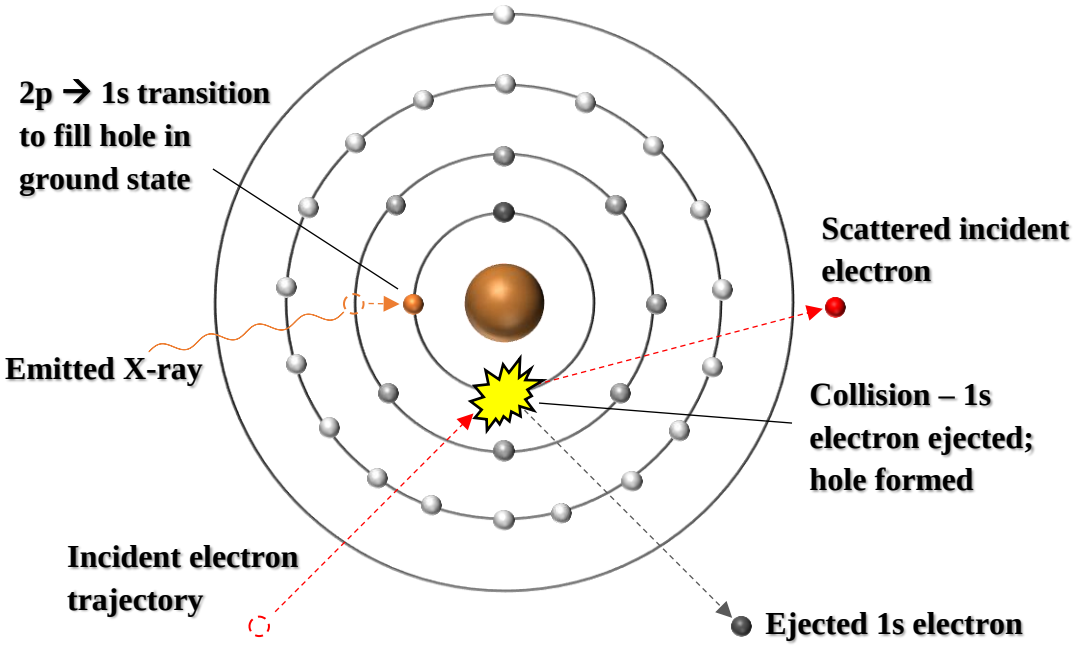

Figure 8: Illustration of the formation of X-rays in the X-ray tube of a diffractometer with a copper target, based on a 2p → 1s electron transition.

where n is an integer relating to the extra distance travelled by wave B relative to wave A in Figure 9; λ is the wavelength of the radiation; d is the distance between the atoms in the crystal structure; and θ is the angle of beam incidence. Ergo, maximum intensity of the diffracted signal is achieved only when n is an integer (Figure 9(b)); conversely, if n is 0.5, then the signal is completely cancelled out (Figure 9(c)). Either the sample or X-ray tube is rotated by a goniometer at an angle of θ, whilst the detector is rotated at an angle of 2θ [14].

The X-rays from a single crystal are diffracted in a conical pattern. However, powder samples have multiple, randomly-aligned crystal structures, resulting in a series of concentric cones being produced by the diffracted X-rays. As shown in Figure 10, a cross-section of the intensity of these concentric cones is plotted *vs.* the angle of beam incidence and compared to a set of standards to identify the materials present.

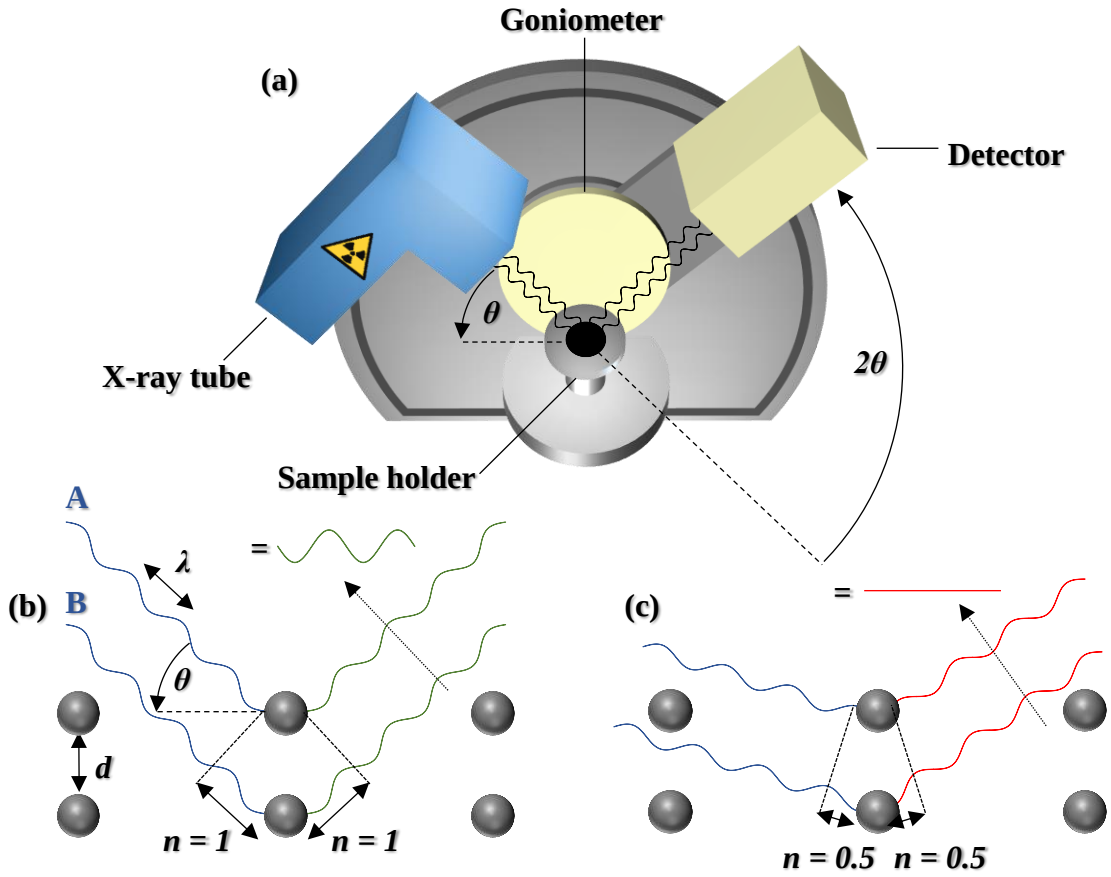

Figure 9: Schematic of an X-ray diffractometer (a), plus examples of constructive (b) and destructive (c) interference of X-rays that have been diffracted by the crystal lattice.

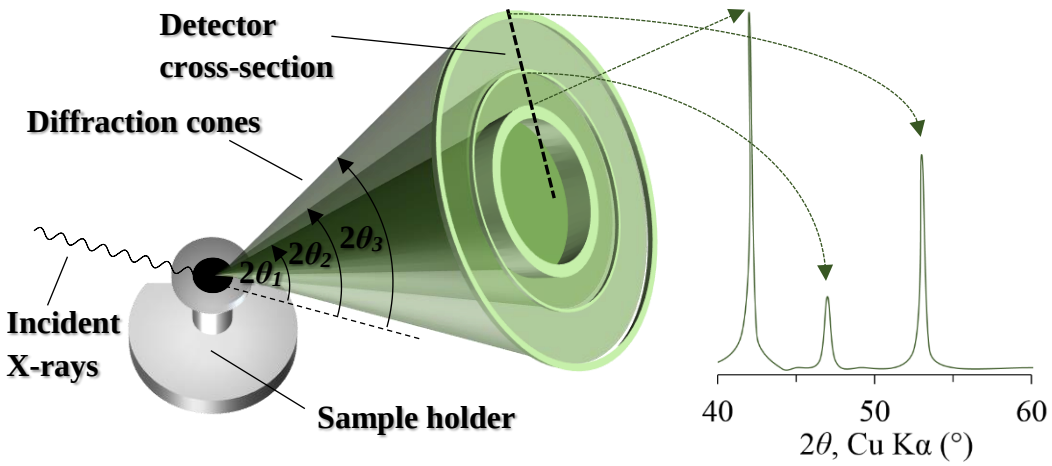

Figure 10: Illustration of the conical diffraction patterns formed by diffracted X-rays, and how these correlate to the peaks on an XRD plot.

XRD samples for this work were formerly conducted on a STOE and latterly on a Rigaku Smartlab, both of which had copper targets (X-ray wavelength 1.5418 Å, i.e. 1.5418×10^{-10} m). For the former, samples were packed into a capillary and sealed with silicone rubber. As such, the process was destructive, as it involved removal of material from the specimen. For the latter, samples were placed in the Rigaku's air-sensitive sample holder, thus allowing them to remain intact and undergo further cycling and/or analysis. All samples were prepared inside argon glove boxes to prevent atmospheric ingress. Diffraction patterns were collected between the angles of 10 ° and 90 °, although in most cases the diffraction peaks of interest were observed between 30 ° and 70 °. Whilst XRD is a powerful analytical technique, it must be backed up with other methods that are more capable detecting less crystalline materials [2].

2.6.3 Scanning electron microscopy (SEM) and energy-dispersive X-ray spectroscopy (EDX)

Important features in electrode samples can often be visually identified. These include lithium plating, structural cracking and the deposition of insoluble discharge salts, in addition to the

pore structure and morphology of the sample. However, the majority of these features cannot be seen with the naked eye. A scanning electron microscope (SEM) is a non-destructive imaging device that can achieve nanoscale magnification, far beyond the ≈ 1000× limits of optical microscopy, allowing these features to be easily identified.

An SEM consists of an electron beam source and detector inside a vacuum chamber, as illustrated in Figure 11. Two types of electron source exist: thermionic emission filaments and field emission guns. The former, typically made of either tungsten or lanthanum hexaboride (LaB_6), are heated to several thousand °C by passing a current through them, resulting in electrons being emitted from the tip. The latter induce quantum mechanical electron tunnelling from the tip using a powerful electric field.

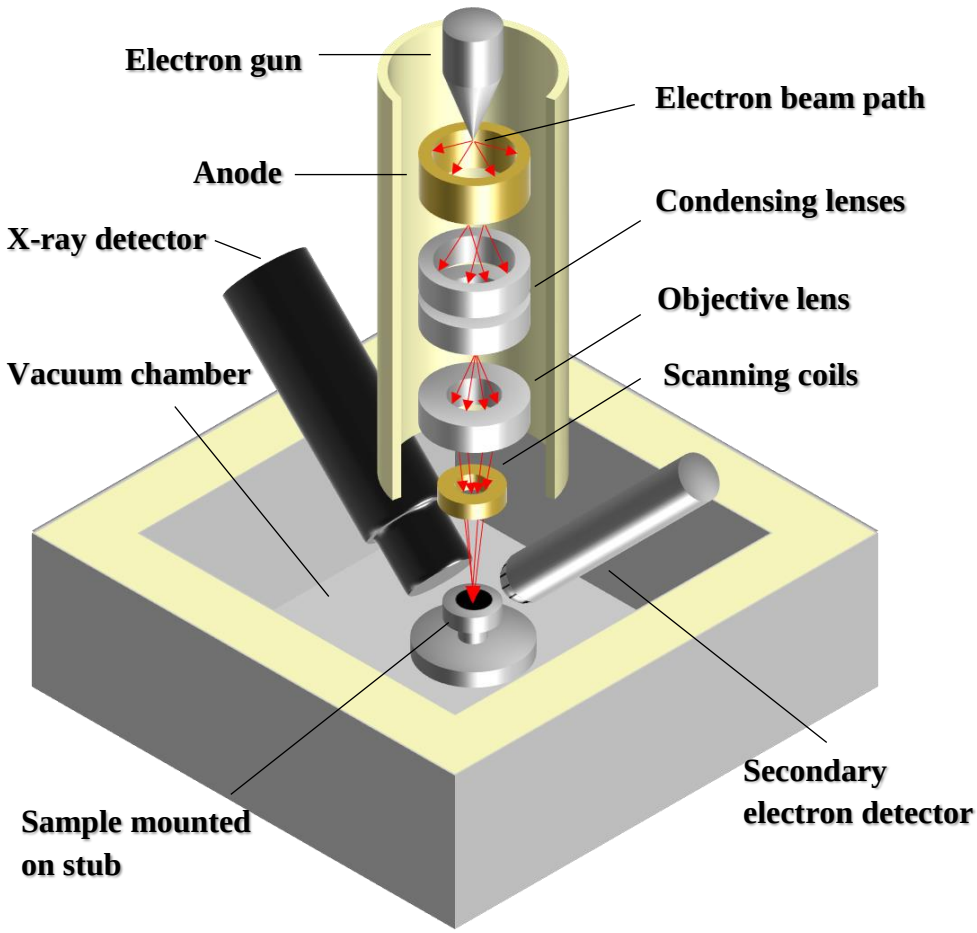

Figure 11: Schematic of a scanning electron microscope with EDX capability, showing the electron beam path (in red) from the electron gun to the sample.

During the SEM procedure, the sample is adhered to a sample holder using conductive copper tape and loaded into the vacuum chamber. Electrons from the source are accelerated across a potential difference and focussed into a fine point by electromagnetic condenser lenses before being aimed at the sample. Incident electrons "excite" an electron from an inner shell of an atom in the sample, ejecting it from the atom (as shown in Figure 8). The ejected electron collides with surrounding electrons from other atoms within a roughly teardrop-shaped volume of the structure (Figure 12), ejecting them and creating "secondary electrons," which have sufficiently low energies to allow them to be collected using a positive collector grid on a detector. The resultant signal is plotted on a two-dimensional graph [15]. The incident electron beam is then repositioned using scan coils to scan it across the sample surface. The "look angle" of the sample can be adjusted to give a better view of the 3D morphology of the sample. Information pertaining to the charge polarity of the sample may be obtained from secondary electrons, since their low energy means that their speed is easily influenced by the positive or

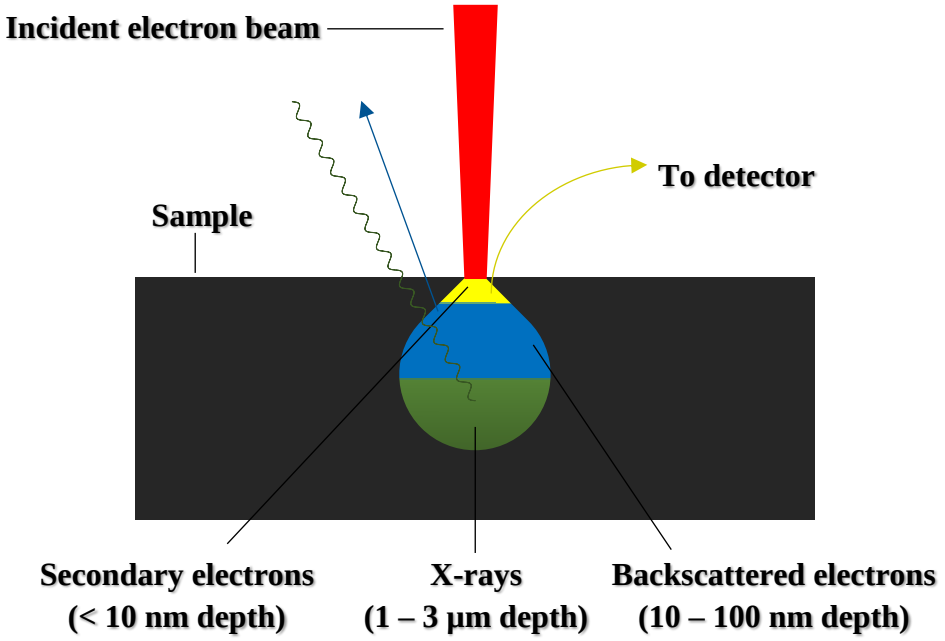

Figure 12: Cross-section of SEM sample showing the teardrop-shaped volume underneath the incident electron beam that yields data in the form of secondary electrons, backscattered electrons and X-rays. The depth of sample that these signals originate from are provided.

negative bias of the sample. As a result, negatively-charged regions appear brighter than positively-charged regions in an image generated from secondary electrons [15].

Secondary electrons, which originate from the region within approximately 10 nm directly beneath the incident beam, provide high-resolution data about the morphology of the sample. However, other signals from the SEM process, originating from deeper within the sample, may be utilised to identify its chemical composition. Backscattered electrons, which are high-energy electrons from the incident beam whose scattering pattern results in them being ejected from the sample on straight trajectories, may be detected using a detector mounted underneath the scanning coils. Information on chemical composition is provided by the greater contrast of electrons backscattered by atoms of a higher mass number, but resolution is low due to the larger volume from which these electrons originate (Figure 12) [15, 16]. Greater accuracy on chemical composition may be obtained using energy-dispersive X-ray spectroscopy (EDX). Ejected electrons create a "hole" in the atom's shell that is subsequently filled by an electron from an outer shell. The reduction in energy associated with the transition of an electron from a higher to a lower shell results in the emission of an X-ray, as shown in Figure 8. Each element has its own unique set of atomic shells and energies associated with the relaxation of an outer electron to a lower shell, and thus a unique intensity of X-ray radiation emitted during the process. The EDX detector can therefore determine the presence of a given element by the intensity of the radiation that it detects [16]. Once again, due to the area from which the X-rays originate being larger than the area of the incident electron beam (Figure 12), EDX resolution is lower than that of SEM.

SEM measurements for this study were conducted on Zeiss Merlin and EVO equipment. The former can achieve higher resolution and has both an air-sensitive sample holder and EDX capability.

2.6.4 Brunauer-Emmett-Teller surface area analysis (BET)

Some work in this thesis required the pore size of electrodes to be known in order to relate this parameter to the performance of a cell using a computational model (see Chapter 4). The pore size distribution may be calculated using a gas adsorption and desorption process called Brunauer-Emmett-Teller (BET) analysis.

A known mass of the sample material is inserted into the sample chamber of the BET analyser, which is then evacuated and filled with the pressurised working gas, namely nitrogen at 77 K. The nitrogen adsorbs onto the inner pore walls in distinct layers, i.e. multilayer absorption, followed by multilayer desorption upon evacuation (Figure 13). The adsorption and desorption

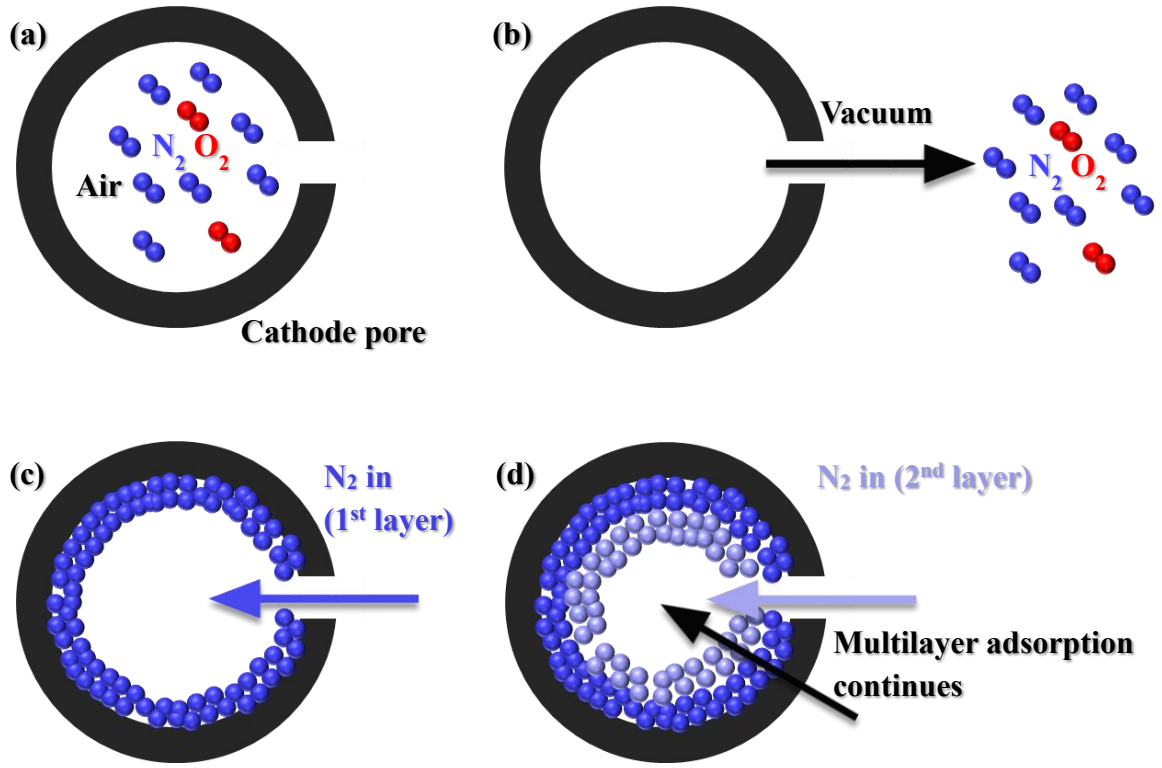

Figure 13: Simplified illustration of the BET multilayer adsorption process that occurs within the sample pores. Air-filled pores (a) are evacuated (b) and filled with nitrogen at 77 K (c), which absorbs on the inside of the pore walls in layers (d).

cumulative pore volume and differential pore area profiles are then calculated using the Barrett-Joyner-Halenda (BJH) method and plotted as a function of pore width in Å.

The BET theory upon which the above calculations are based is a multilayer extension of the Langmuir theory for the monolayer adsorption of a gas onto a surface. It assumes that the adsorption surface, in this case the inner pore walls of the electrode material, is nonporous and energetically uniform; that the constituent molecules of the surface act as adsorption sites for the first gas layer, and successive gas layers are adsorbed directly on top of the molecules of the underlying gas layers; that a new gas layer can be started before the underlying gas layer is complete; that the gas layers do not interact with each other; and that gas adsorbed in each layer is a constant amount at equilibrium pressure [17]. The resultant theory is expressed thus:

$$\frac{p}{v(p_0 - p)} = \frac{1}{v_m c} + \frac{c - 1}{v_m c}\frac{p}{p_0} \tag{6}$$

where p and p_0 are the equilibrium and saturation pressures of the gas layer, respectively; v and v_m are the volumes of gas presently absorbed by the gas layers and required to complete a gas layer, respectively; and c is a parameter related to the heat of absorption associated with the gas layers. The latter two can be obtained by plotting $p/v(p_0 - p)$ *vs.* p/p_0, which yields a straight line with an intercept of $1/v_m c$ and a gradient of $(c - 1)/v_m c$ [18]. The BET surface area of the sample can then be determined from the equation:

$$A_{BET} = v_m a_m N_A \tag{7}$$

where a_m is the molecular cross section, i.e. the area occupied by a single molecule in a gas layer; and N_A is the Avogadro constant. The aforementioned BJH method is used to indicate the pore size distribution of the material based on desorption of gas in the porous structure

during a stepped decrease in p/p_0. This method assumes that the pores are spherical and rigid [19].

BET measurements in this thesis were conducted on a Micromeritics TriStar II 3020 surface area and porosity analyser.

2.7 References

[1] M. Roberts, R. Younesi, W. Richardson, J. Liu, T. Gustafsson, J. Zhu and K. Edström, "Increased Cycling Efficiency of Lithium Anodes in Dimethyl Sulfoxide Electrolytes For Use in Li-O_2 Batteries," *ECS Electrochem. Lett.*, vol. 3, no. 6, pp. A62 - A65, 2014.

[2] Y. Chen, S. A. Freunberger, Z. Peng, F. Bardé and P. G. Bruce, "Li–O_2 Battery with a Dimethylformamide Electrolyte," *J. Am. Chem. Soc.*, vol. 134, no. 18, pp. 7952 - 7957, 2012.

[3] J. Read, "Ether-Based Electrolytes for the Lithium/Oxygen Organic Electrolyte Battery," *J. Electrochem. Soc.*, vol. 153, no. 1, pp. A96 - A100, 2006.

[4] A. Cedergren and S. Jonsson, "Progress in Karl Fischer Coulometry Using Diaphragm-Free Cells," *Anal. Chem.*, vol. 73, pp. 5611 - 5615, 2001.

[5] M. Lanz, C. D. Caro, K. Rüegg and A. D. Agostini, "Coulometric Karl Fischer Titration with a Diaphragm-Free Cell: Cell Design and Applications," *Food Chemistry*, vol. 96, pp. 431 – 435, 2006.

[6] Mettler-Toledo AG, Analytical. (April 2011). *Good Titration Practice in Karl Fischer Titration*, pp. 9 - 11. [Online]. Available: http://fr.mt.com/dam/LabDiv/Campaigns/TestingLabs2013/moisture/package/gtp-karl-fischer-EN.pdf. [Accessed 16 July 2015].

[7] S.-I. Pyun, H.-C. Shin, J.-W. Lee and J.-Y. Go, "Chapter 2: Electrochemical Methods," in *Electrochemistry of Insertion Materials for Hydrogen and Lithium*, Heidelberg, Springer, 2012, pp. 13 - 16.

[8] H. H. Girault, *Analytical and Physical Electrochemistry*, EPFL Press, 2004, p. 375.

[9] P. Zanello, *Inorganic Electrochemistry: Theory, Practice and Application*, The Royal Society of Chemistry, 2003, p. 133.

[10] P. Sun and M. V. Mirkin, "Kinetics of Electron-Transfer Reactions at Nanoelectrodes," *Anal. Chem.* , vol. 78, pp. 6526 - 6534, 2006.

[11] H. H. Girault, *Analytical and Physical Electrochemistry*, EPFL Press, 2004, pp. 301 - 305.

[12] A. J. Bard and L. R. Faulkner, *Electrochemical Methods: Fundamentals and Applications (2nd Edition)*, John Wiley & Sons, Inc, 2001, p. 335.

[13] Thermo Fisher Scientific. (2006). *Advantages of Fourier-Transform Near-Infrared Spectroscopy*. [Online]. Available: https://www.thermoscientific.com/content/dam/tfs/ATG/CAD/CAD%20Documents/Application%20%26%20Technical%20Notes/Bulk%20Weighing%20Monitoring%20and%20Sampling/Process%20Analysis%20and%20Control/AN50771_E%20FourierTransformNIR1206M_L.pdf. [Accessed 18 July 2015].

[14] A. A. Bunaciu, E. G. Udriştioiu and H. Y. Aboul-Enein, "X-Ray Diffraction: Instrumentation and Applications," *Critical Reviews in Analytical Chemistry,* vol. 45, pp. 289 – 299, 2015.

[15] Ludwig Reimer, *Scanning Electron Microscopy: Physics of Image Formation and Microanalysis*, Berlin: Springer-Verlag, 1985, pp. 1- 8.

[16] K. Vernon-Parry, "Scanning Electron Microscopy: an Introduction," *III-Vs Review*, vol. 13, no. 4, pp. 40 – 44, 2000.

[17] J. L. Figueiredo, M. M. Pereira and J. Faria, *Catalysis from Theory to Application: An Integrated Course*, Imprensa da Universidade de Coimbra, 2008, pp. 89 - 93.

[18] S. Brunauer, P. H. Emmett and E. Teller, "Adsorption of Gases in Multimolecular Layers," *J. Am. Chem. Soc.*, vol. 60, no. 2, pp. 309 – 319, 1938.

[19] J. Rouquerol, D. Avnir, C. W. Fairbridge, D. H. Everett, J. M. Haynes, N. Pernicone, J. D. F. Ramsay, K. S. W. Sing and a. K. K. Unger, "Recommendations for the Characterization of Porous Solids (Technical Report)," *Pure & Appl. Chem*, vol. 66, no. 8, pp. 1739 - 1758, 1994.

3 Instabilities of nitrile electrolytes for non-aqueous lithium-air cells

3.1 Introduction

As outlined in Chapter 1, the lithium-air cell is a promising candidate to supersede lithium-ion cells in portable applications, not least automotive traction batteries. Whilst Dahn *et al.* have rightly pointed out that the Tesla Model S has shown that Li-ion cells can power an EV for hundreds of miles on a single charge [1], Li-air cells are predicted to provide substantial gains in gravimetric energy density, whilst simultaneously cutting the cost of the traction battery per kWh capacity. However, Li-air cells have numerous hurdles to overcome prior to becoming commercially viable, not least poor solvent stability in non-aqueous systems, which has thus far typically lead to cell failure in under 10 cycles when using conventional carbon cathodes [2, 3, 4].

3.1.1 The search for a stable lithium-air electrolyte

The non-aqueous Li-air cell suffers from stability issues arising from the choice of electrolyte used. During cycling, solvent decomposition is encountered, which results in the formation of decomposition salts such as lithium carbonate, formate and acetate, rather than the desired Li_2O_2. These salts form a passivating layer on the cathode reaction sites, preventing the cell from cycling further, and require the cell to be polarised to upwards of 4 V upon charging, resulting in poor coulombic efficiency [5, 6]. All electrolytes that have been investigated so far have decomposed during cycling through at least one of two mechanisms: 1) attack by $O_2^{\bullet-}$ radicals and 2) electrochemical decomposition of the solvent in contact with Li_2O_2 upon

charging as the potential surpasses *circa* 3.5 V [7, 3, 8, 9, 10, 11]. Carbon electrodes, which are the most commonly-used cathodes in Li-air cells, have been shown to act as a catalyst in the latter process [5, 6]. This has led to research into alternative, carbon-free cathode materials that help to retain the stability of the electrolyte upon charging. Nanoporous gold and Ruthenium-coated Indium Tin Oxide (Ru/ITO) have both been shown to improve the cycle life of Li-air cells and reduce their charging overpotential *vs.* cells with Super P Li carbon cathodes, therefore improving their coulombic efficiency and minimising the exposure of the cells to high potentials that may cause the electrolyte to decompose [12, 13]. However, both gold and ITO are heavy and expensive and thus not practical for widespread use in portable applications. Additionally, in the nanoporous gold study, the pore structure of the cathode limited the specific capacity of the cathodes to *circa* 300 mAh g^{-1} [12]. Despite being unstable towards Li_2O_2 [5, 13], carbon remains a preferable cathode material due to its abundance, low cost and low gravimetric density. Therefore, there is still a need to find a non-aqueous electrolyte that is stable in contact with Li_2O_2 and $O_2^{\bullet-}$ radicals, in order to develop a Li-air cell chemistry that is both commercially viable and capable of withstanding hundreds of cycles with minimal capacity loss. As such, this study investigates the suitability of new electrolytes for use in Li-air cells with carbon cathodes.

3.1.2 Nitriles as an electrolyte for lithium-air cells

The nitriles considered in this study contain -C≡N functional groups and no oxygen. The -C≡N functional group is less polar and has a greater bond energy than the C-O and C=O bonds encountered in many solvents studied previously in Li-air cells, such as propylene carbonate (PC) and tetraethylene glycol dimethyl ether (TEGDME) [14]. Additionally, nitriles have been reported to exhibit higher oxidation potentials than other common Li-air solvents, such as PC and dimethyl sulfoxide (DMSO), during polarisation experiments [15, 16]. Therefore, nitriles

are predicted to exhibit improved stability in Li-air cells since they are less likely to oxidise during charging or be susceptible to nucleophilic attack from $O_2^{\bullet-}$ radicals than solvents that contain oxygen in their structure.

Several nitriles were available for this study, namely acetonitrile, adiponitrile, glutaronitrile, malononitrile and succinonitrile. The latter two nitriles were quickly disregarded due to being solid at room temperature and thus not providing sufficient ionic mobility for the discharge reaction to take place, as well as being difficult to purify using the standard distillation procedure outlined in Chapter 2. Acetonitrile has been studied previously and found to have high Li^+ conductivity and oxygen solubility. Its oxygen diffusion coefficient is twice that of TEGDME when used with a Li^+-based salt, which is advantageous when cycling a Li-air cell at higher rates [17]. Additionally, acetonitrile has shown superior stability to other common solvents in Li-air systems, exhibiting some of the smallest levels of parasitic electrochemistry upon charge and discharge (electron:O_2 consumption/evolution ratio close to 2 for both cases), stability towards Li_2O_2 and a higher oxidation potential than ethers [18, 19]. However, it is the most volatile nitrile considered here. Acetonitrile is regularly used in the lab as a cleaning solvent since it evaporates rapidly under vacuum, whereas heavier solvents do not evaporate even after an overnight exposure to vacuum. This property makes acetonitrile the least suited of the nitriles to practical Li-air applications, where the cells are not hermetically sealed units since the cathode is exposed to air. Admittedly, commercial non-hermitically sealed cell chemistries with heavier solvents, such as flooded NiCd cells, do require periodic topping up of electrolyte, but the issue is worsened with increasing solvent volatility. This was exemplified when acetonitrile evaporated from Swagelok cells during the solvent selection process for this study, resulting in the cells terminating early as their separators dried out. Attempts to increase the atmospheric content of acetonitrile prior to cycling by adding open

vials of the solvent to the glass Swagelok case failed to remedy this situation. Acetonitrile is also known to react with Li metal, further limiting its practicality as a Li-air solvent [20].

Adiponitrile and glutaronitrile (Figure 1), which have not been investigated as Li-air electrolytes before in the literature, are both liquid at room temperature and have sufficiently low volatility to limit evaporation during cycling. These factors would make these two solvents practical for use in commercial applications should they prove to be stable electrolytes. The promising electrochemical performance of acetonitrile in previous studies suggests that these two nitriles may yield the stability required to make a commercially viable Li-air cell. Therefore, they were subjected to cycling studies to assess their stability in Li-air cells.

3.2 Capacity retention of nitrile-based lithium-air cells

It is imperative that a Li-air secondary cell must be able to undergo hundreds of cycles with minimal capacity degradation in order to be commercially viable. Cells with nitrile electrolyte were subjected to five cycles to assess their discharge capacity and capacity retention at the early stages of cycling. Following this, cells were subjected to post-mortem analysis to ascertain the cause of any loss of capacity during cycling.

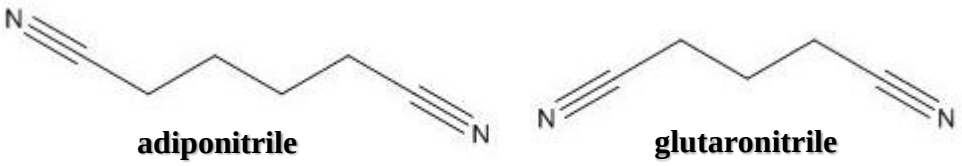

Figure 1: Structural formulae of adiponitrile and glutaronitrile, the two solvents that were considered in this study.

3.2.1 Preparation of cell components

Swagelok cells with precharged lithium iron phosphate (LFP) anodes, Super P Li carbon cathodes and Whatman glass microfiber separators were used in the cycling studies. The cells and their components were prepared as described in Chapter 2.

3.2.2 Preparation of electrolyte solution

All solvents were distilled and salts were dried prior to use in order to remove as much water as possible from the cells. Solvents were distilled using an iFischer LABODEST HMS 500 C distillation column as described in Chapter 2. All solvents considered in this chapter were distilled under vacuum to lower their boiling point. Distilled solvents were transferred to an MBraun argon glove box and stored in Schott DURAN bottles with freshly dried molecular sieves to remove any residual moisture. Karl Fischer Titration was used to verify water content; 5 ppm H_2O was found to be the practical limit of the drying process.

Salts were dried for 24 hours under vacuum in a Buchi oven prior to use. Due to the respective decomposition temperatures of each salt, lithium trifluoromethanesulfonate (Li triflate) was dried at 80 °C whilst lithium bistrifluoromethanesulfonimidate (LiTFSI) was dried at 90 °C, thus removing as much moisture as possible whilst preventing the decomposition of each salt. Electrolyte solutions were prepared with 0.5 M salt concentration.

3.2.3 Cell cycling procedure

Swagelok cells were placed inside a Memmert oven that maintained a constant temperature of 30 °C and had channel feedthroughs to a Maccor Series 4200 battery tester. The cells were galvanostatically cycled between 2 V and 4.5 V *vs.* Li/Li^+ (-1.5 V and 1 V *vs.* LFP) at

70 mA g^{-1} cathode active material for a predetermined number of discharges or full cycles, namely the first, second, third and fifth discharges and cycles. After cycling, the cells were returned to an argon glove box where the cathodes were removed, rinsed with anhydrous acetonitrile and dried under vacuum in the glove box antechamber for 30 minutes. They then underwent post-mortem analysis by XRD and FTIR spectroscopy to observe the accumulation and removal of discharge and decomposition products over a successive number of cycles.

3.2.4 Results and analysis

The first nitrile cells to be built were used to compare the impact of the chosen salt on the efficiency and reversibility of the cell. As shown in Figure 2, Li triflate yields a lower overpotential than LiTFSI and thus provides the more efficient cell chemistry. As such, it was selected for use in this study.

The cycling performance of adiponitrile and glutaronitrile cells are shown in Figure 3. Both cell chemistries exhibited substantial capacity loss upon cycling, with the glutaronitrile cells being the worst affected. The extent of the capacity loss is emphasised by the adiponitrile cell surpassing Nissan's definition of automotive traction battery failure, < 70 % of the original

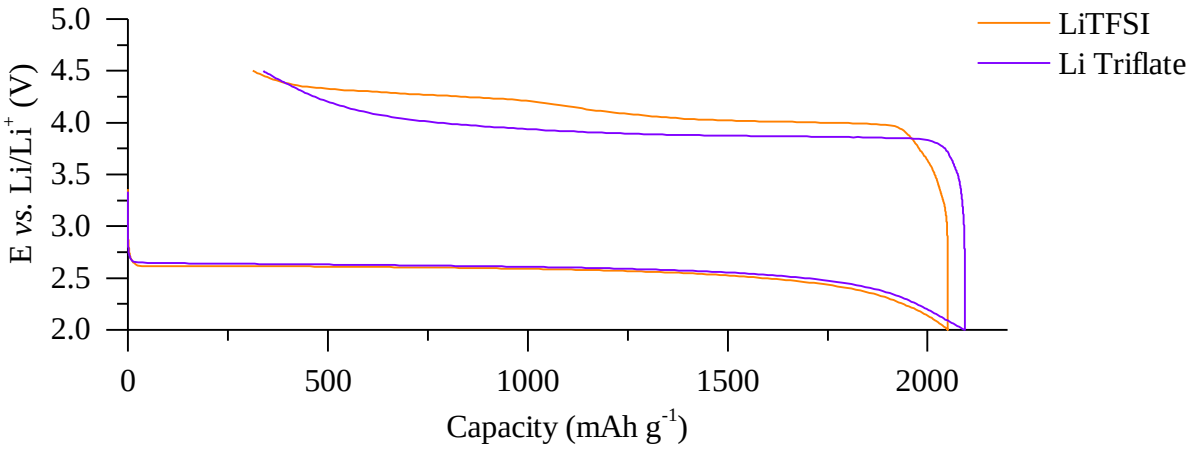

Figure 2: Comparison of the performance of adiponitrile cells using different lithium salts.

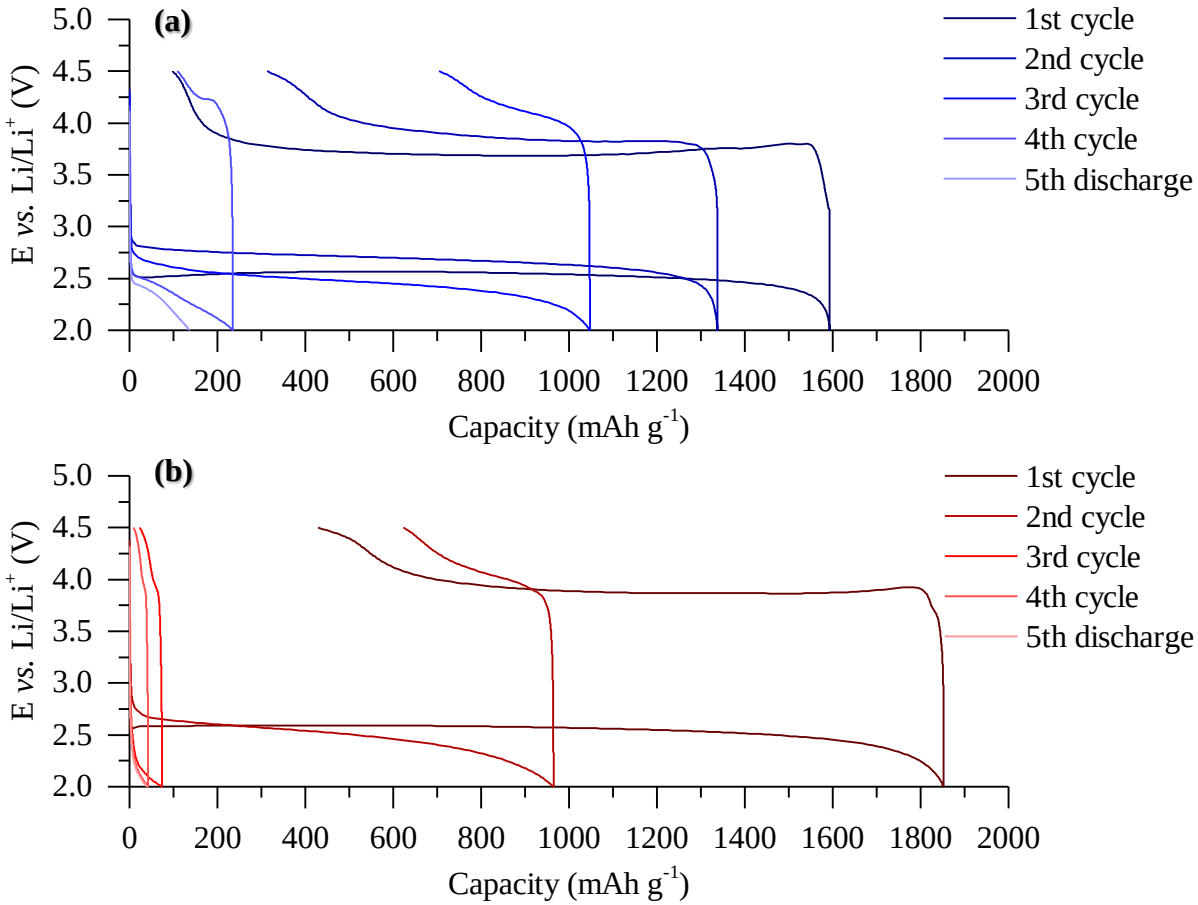

Figure 3: Cycling profiles for cells with adiponitrile (a) and glutaronitrile (b) based electrolytes.

capacity [20], by the third cycle, and the discharge capacity of the glutaronitrile cell nearly halving (48 % loss) between the first and second cycles. This is consistent with the rapid accumulation of a passivating layer of decomposition salts on the cathode reaction sites, thus causing the cell to fail.

XRD and FTIR were performed on cycled cathodes to observe the accumulation of discharge and decomposition products over a number of cycles. As shown in the XRD diffractogram for adiponitrile (Figure 4), Li_2O_2 is clearly visible after the first discharge, and is completely removed by the end of the first cycle. However, lithium hydroxide (LiOH), a decomposition product, is also visible after the second and third discharges, although it is not present in the patterns for the second and third cycles, indicating that it is oxidised. Lithium carbonate

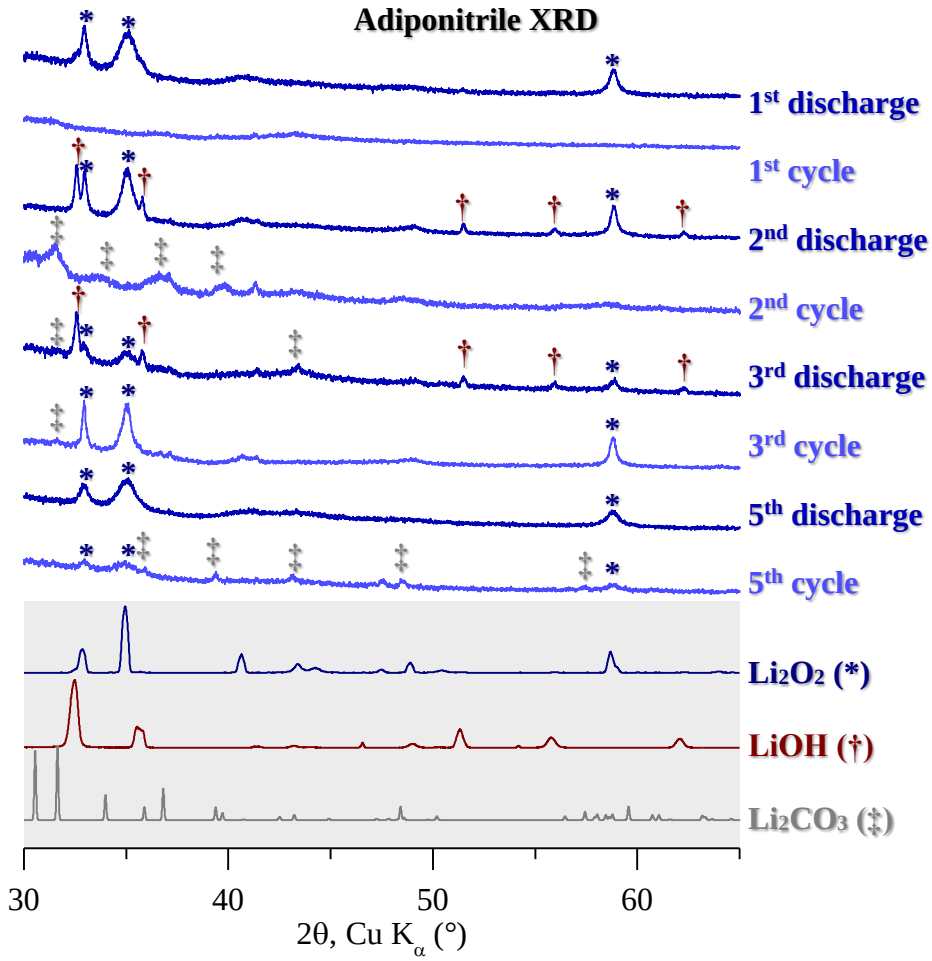

Figure 4: XRD diffractogram of Li-air cells with adiponitrile electrolyte at various stages of cycling. XRD standards are shown in the shaded region.

(Li_2CO_3) peaks appear at the end of the second cycle and are present in most of the subsequent patterns, which is to be expected due to the high oxidation potential of this compound. After the third discharge, the cell begins to fail, with the LiOH peaks being stronger than those of Li_2O_2. The cell fails to remove Li_2O_2 at the end of the third cycle and Li_2O_2 continues to accumulate thereafter. Interestingly, despite the cell having failed by the fifth discharge, there is no LiOH in the corresponding XRD pattern; a small amount of Li_2O_2 is visible, which is not removed upon charge and is accompanied by Li_2CO_3. FTIR spectra for adiponitrile (Figure 5) confirm the presence of LiOH from the second discharge onwards, with distictive peaks at 3670 cm^{-1} and 450 cm^{-1}. In contrast to the XRD data, the FTIR spectra indicate the presence of LiOH after charging. Since LiOH is known to oxidise at *circa* 3.32 V *vs.* Li/Li^+ [21], the

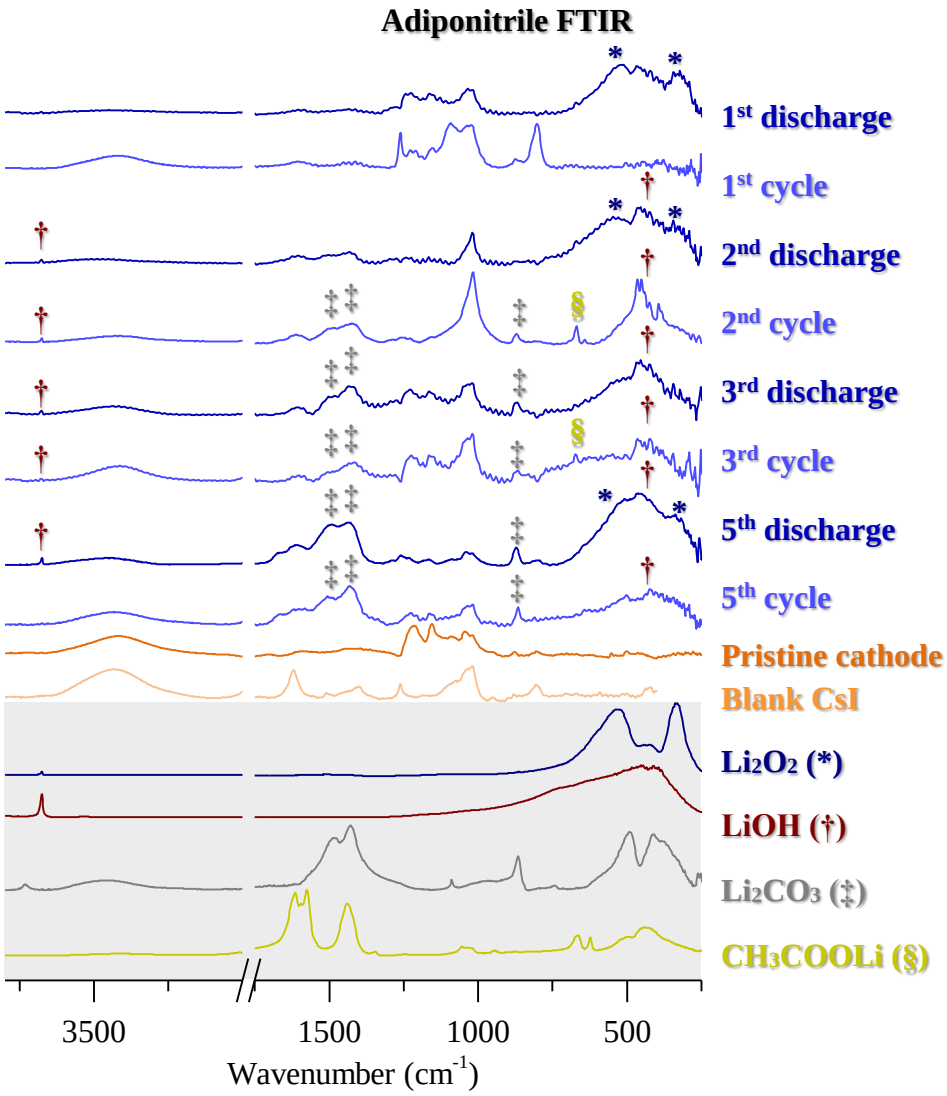

Figure 5: FTIR spectra of Li-air cells with adiponitrile electrolyte at various stages of cycling. FTIR standards are shown in the shaded region.

FTIR data indicates that the kinetics of the system have prevented all of the LiOH from oxidising. Additionally, peaks at 665 cm^{-1}, 865 cm^{-1}, 1430 cm^{-1} and 1480 cm^{-1} that may be attributed to Li_2CO_3 and Li acetate (CH_3COOLi) are visible from the second cycle, which are good indicators of electrolyte decompostion and thus the instability of these solvents in Li-air cells. The glutaronitrile cells exhibit a pronounced version of these events in the XRD patterns (Figure 6) with LiOH and Li_2CO_3 visible from the first discharge. LiOH is also present after every discharge in the FTIR spectra (Figure 7), with possible Li_2CO_3 and Li acetate peaks present from the first cycle, indicating accelerated degradation in comparison to adiponitrile.

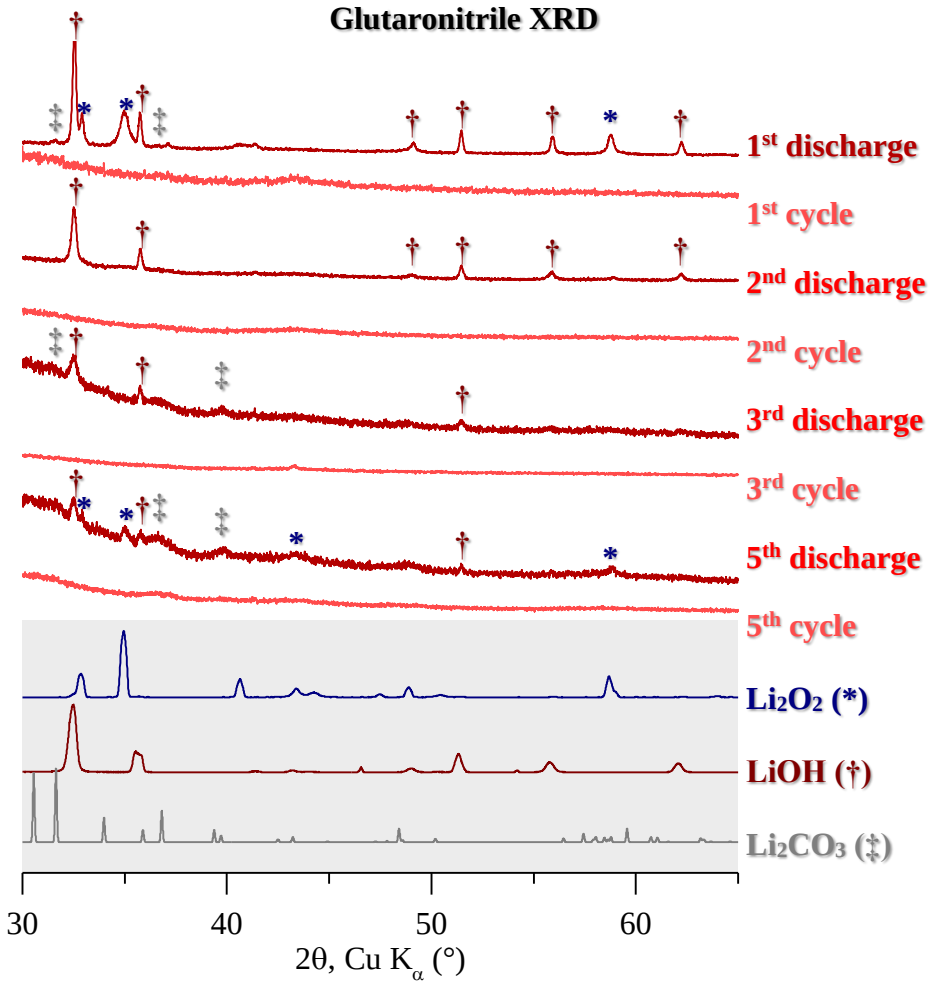

Figure 6: XRD diffractogram of Li-air cells with glutaronitrile electrolyte at various stages of cycling. XRD standards are shown in the shaded region.

3.3 Chemical stability of nitriles in contact with intermediate and discharge species

Initially, LiOH was thought to originate from the attack of Li_2O_2 through water ingress:

$$Li_2O_2 + 2H_2O \rightarrow 2LiOH + H_2O_2$$

This could happen through a number of routes, including insufficiently dried cell components, purging with impure O_2 or leaks in the Swagelok glass case. All of these avenues were thoroughly explored with rigorous new drying and distillation techniques, the addition of a

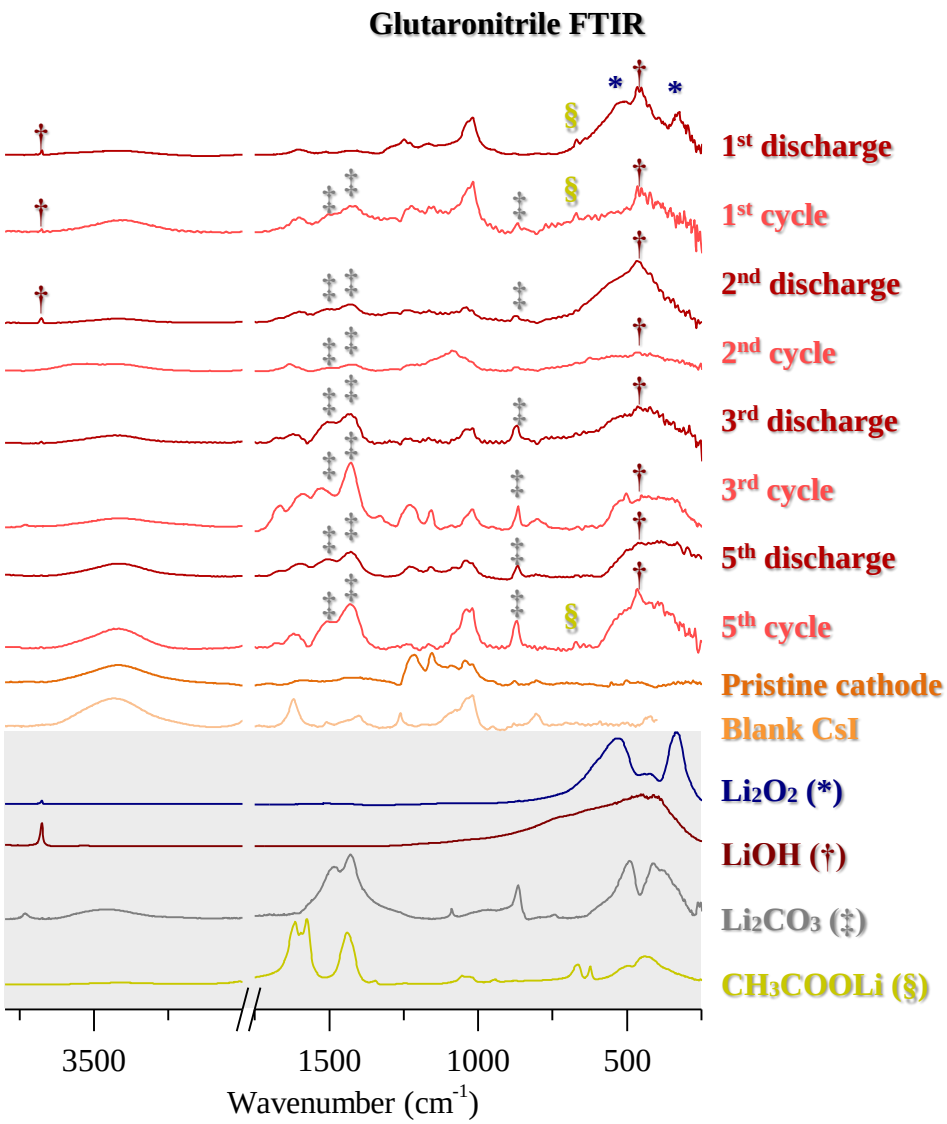

Figure 7: FTIR spectra of Li-air cells with glutaronitrile electrolyte at various stages of cycling. FTIR standards are shown in the shaded region.

drying column full of freshly dried molecular sieves to the O_2 purging equipment and leak checks on Swagelok glass cases. However, LiOH was still detected in nitrile cells. Recently, it has been reported that some electrolytes that have previously been considered stable in Li-air cells, are susceptible to attack from Li_2O_2. This causes the electrolyte to decompose and, in conjunction with $O_2^{\bullet-}$ radicals, converts Li_2O_2 into LiOH [18, 22]. Therefore, work was conducted to assess whether or not these mechanisms are also encountered in adiponitrile and glutaronitrile.

3.3.1 Chemical stability analysis procedure

To assess the chemical stability of nitriles in contact with Li_2O_2 and $O_2^{\bullet-}$ radicals, adiponitrile and glutaronitrile were each aged in vials with commercial Li_2O_2 powder in 1:100 powder:solvent molar ratio; commercial KO_2 powder (a stable source of $O_2^{\bullet-}$ radicals) in 1:100 molar ratio; and both Li_2O_2 and KO_2 powders in 1:1:100 molar ratio. Additionally, adiponitrile and glutaronitrile Swagelok cells of identical specification to those used in Section 3.2 were built and discharged once, and the cathodes rinsed in acetonitrile. These were then dried under vacuum and placed in vials of adiponitrile or glutaronitrile, with and without KO_2. The vials were left to age for one month, after which the solvents were analysed by FTIR to detect if they had decomposed. The cathodes and commercial powders were rinsed with acetonitrile four times, with the latter being centrifuged beforehand. They were then dried under vacuum overnight in a glove box antechamber before undergoing XRD and FTIR analysis to detect if Li_2O_2 had partially, or completely, reacted with the electrolyte and $O_2^{\bullet-}$ radicals and converted to LiOH.

3.3.2 Results and analysis

3.3.2.1 Stability of adiponitrile towards Li_2O_2 and KO_2

The XRD diffractogram for adiponitrile-aged cathodes with electrochemically deposited Li_2O_2 is provided in Figure 8. There is no change in the XRD pattern of electrochemically deposited Li_2O_2 when aged in adiponitrile only, thus indicating the stability of adiponitrile towards Li_2O_2 and vice versa. However, when superoxide is introduced in the form of KO_2, the distinctive XRD peaks of LiOH are visible at approximately 32.5 °, 35.9 °, 51.4 °, 55.9 ° and 62.2 °. These are faint in comparison to Li_2O_2 peaks after two days but strong after one month, after which

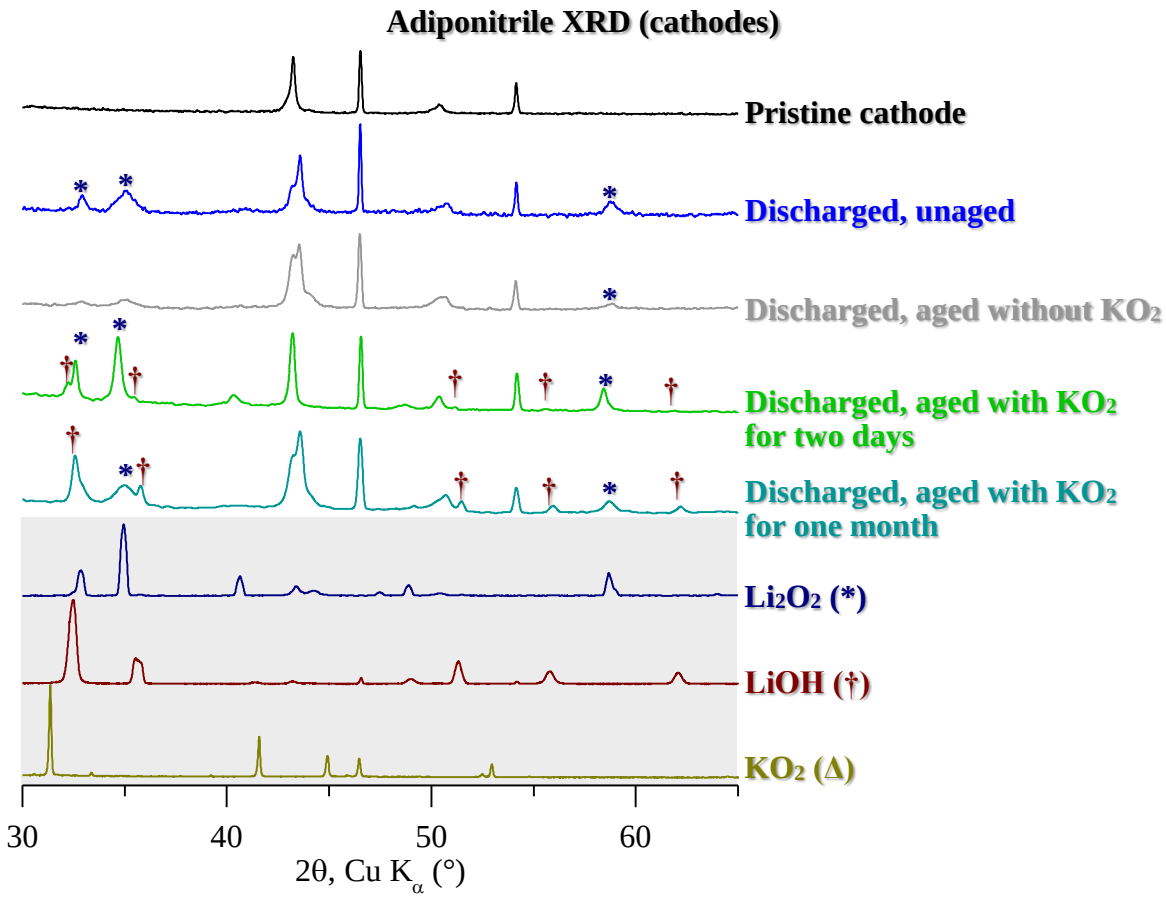

Figure 8: XRD diffractogram for discharged cathodes aged with and without KO_2 in adiponitrile for one month. XRD standards are shown in the shaded region.

the Li_2O_2 peaks have significantly reduced in height. This indicates that a side reaction takes place in cells with adiponitrile electrolyte that leads to the decomposition of Li_2O_2 to LiOH. These findings are reinforced by the FTIR spectra in Figure 9. There is a faint LiOH peak at 3670 cm^{-1} in the FTIR spectrum of the cathode that was aged with KO_2 for two days; the peak at 450 cm^{-1} may also be present, but is obscured by strong Li_2O_2 peaks. However, there are strong peaks at 3670 cm^{-1} and 450 cm^{-1} after one month of aging with KO_2 that positively identify the presence of LiOH. Clearly the time-dependent decomposition reaction occurs over a period of weeks rather than hours, but is still of cause for concern in a Li-air cell.

Figure 10 shows the XRD diffractogram for commercial Li_2O_2 powder aged in adiponitrile with and without KO_2. Again, there is no change to the peaks of Li_2O_2 when aged in

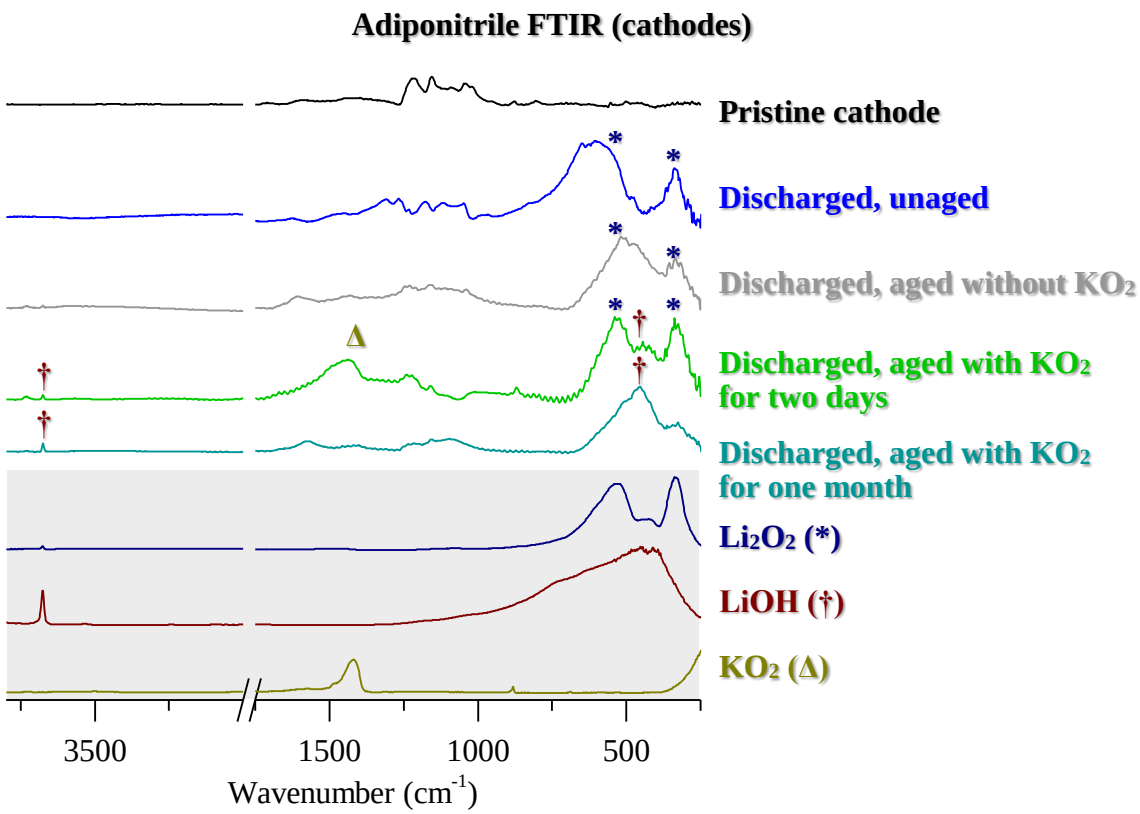

Figure 9: FTIR spectra for discharged cathodes aged with and without KO_2 in adiponitrile for one month. FTIR standards are shown in the shaded region.

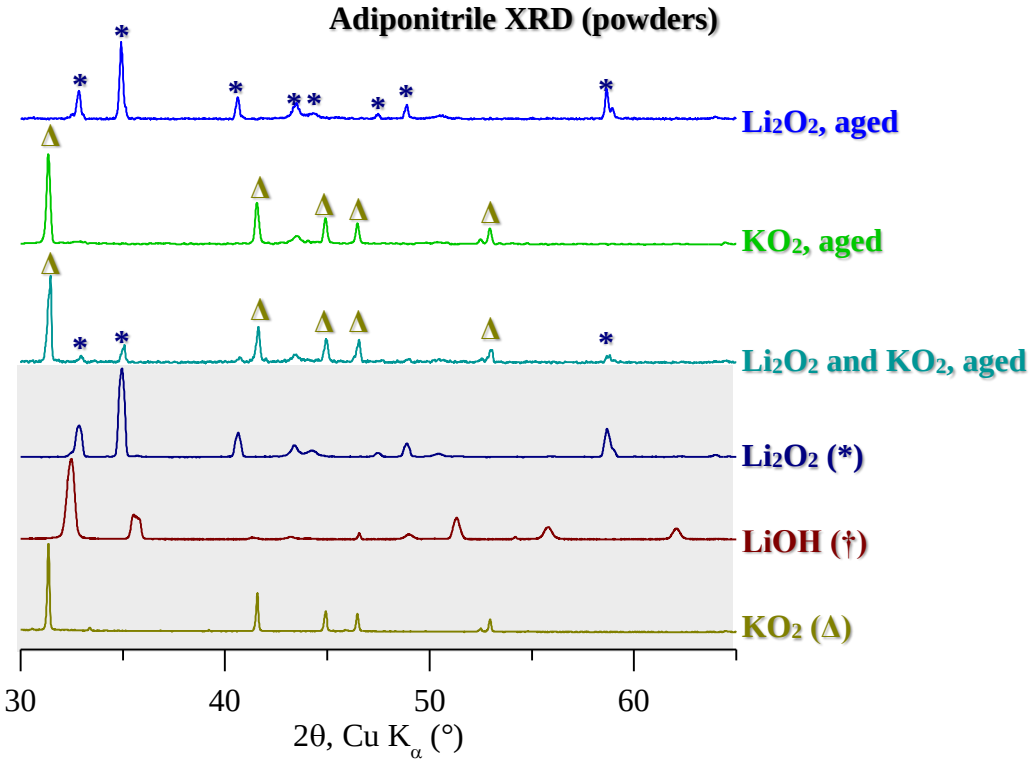

Figure 10: XRD diffractogram for commercial Li_2O_2 and KO_2 powders aged with adiponitrile for one month. XRD standards are shown in the shaded region.

adiponitrile without KO_2. However, there is a new peak for KO_2, when aged alone in adiponitrile, at 43.5 ° in the XRD pattern. This is close to one of the peaks for Li_2O_2 but not present in the XRD pattern of fresh KO_2, indicating that KO_2 reacts with adiponitrile to some extent. There is negligible difference to the Li_2O_2 peaks when aged with KO_2. The corresponding FTIR spectra (Figure 11) also show that KO_2 reacts with adiponitrile, with new peaks present at 2170 cm^{-1}, 1575 cm^{-1} and 1310 cm^{-1} in the FTIR spectrum, in addition to a broad, shallow peak covering the region between 1220 cm^{-1} and 960 cm^{-1}, all of which are not present in fresh KO_2. Additionally, there is a small LiOH peak at 3670 cm^{-1} in the FTIR spectrum for Li_2O_2 and KO_2 powders aged together, indicating that the Li_2O_2 has been decomposed by $O_2^{\bullet-}$ radicals, but to a lesser extent than electrochemically deposited Li_2O_2.

The difference in the stability of electrochemically deposited Li_2O_2 and commercial Li_2O_2 powder reflects the findings of earlier studies with DMSO and stems from the comparative lack of intermediate, highly-nucleophilic oxide species on the surface of commercial Li_2O_2 powder,

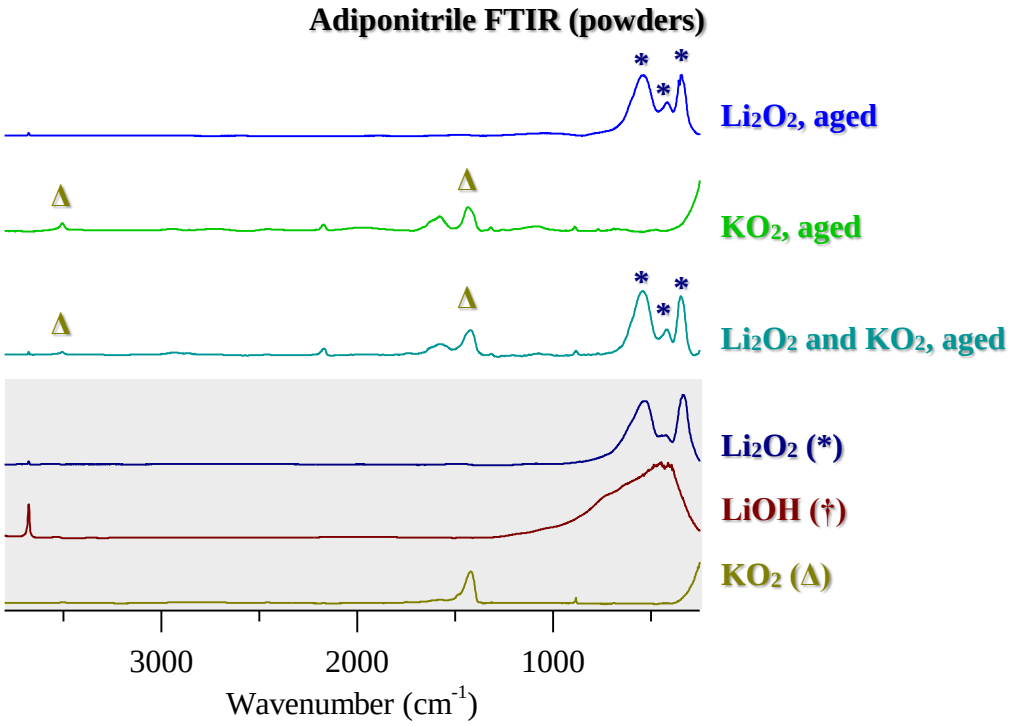

Figure 11: FTIR spectra for commercial Li_2O_2 and KO_2 powders aged with adiponitrile for one month. FTIR standards are shown in the shaded region.

coupled with its larger crystallite sizes [22]. This has a negative impact for real-world use, where cells with electrochemically deposited Li_2O_2 may be rested for prolonged periods of time, thus allowing $O_2^{\bullet-}$ radicals and the electrolyte to attack Li_2O_2 and decompose it to LiOH, which passivates the cathode reaction sites and prevents the cell from attaining its original discharge capacity.

From the data provided in Figures 8 - 11, it is not entirely clear if the decomposition of electrochemically deposited Li_2O_2 to LiOH is caused by $O_2^{\bullet-}$ radicals attacking Li_2O_2 directly, or by $O_2^{\bullet-}$ radicals attacking adiponitrile, which then forms by-products that react with Li_2O_2. Therefore, analysis of the adiponitrile solvent by FTIR is provided in Figure 12. Adiponitrile aged for one month with either electrochemically deposited Li_2O_2 or commercial Li_2O_2 powder was found to show no change to the FTIR spectrum, thus confirming that the electrolyte is

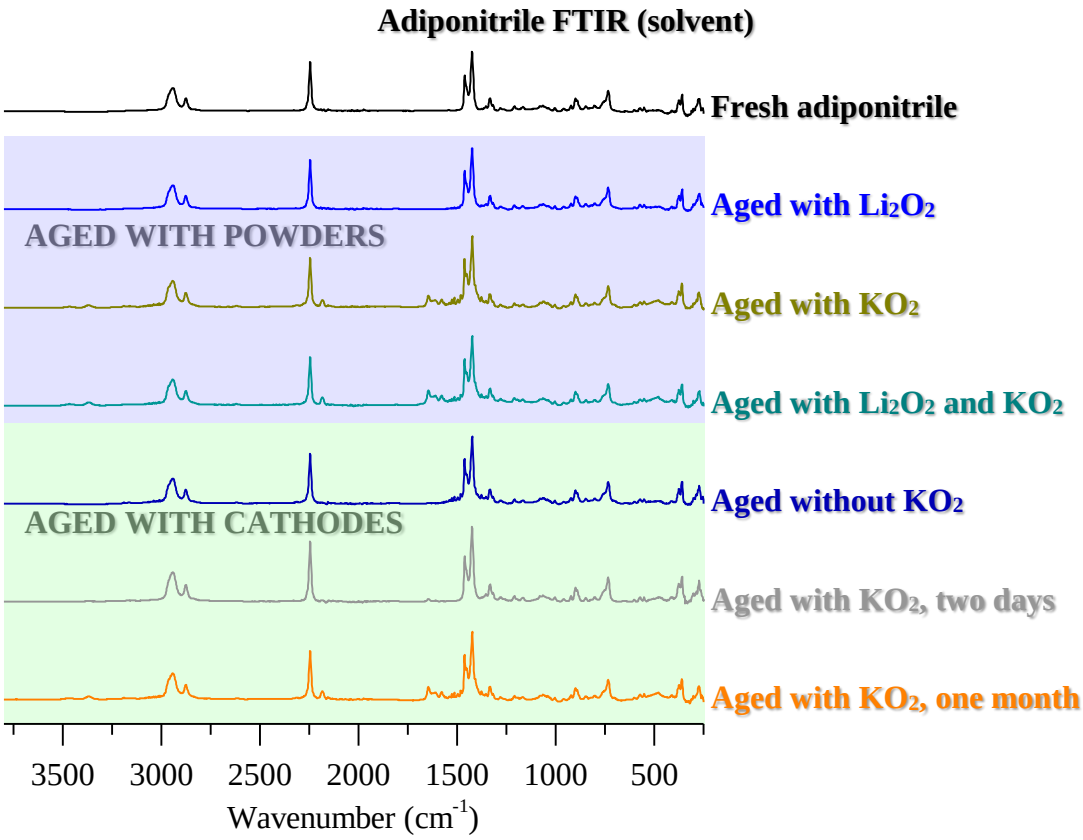

Figure 12: FTIR spectra for adiponitrile aged for one month with commercial Li_2O_2 and KO_2 powders and discharged Li-air cathodes.

stable towards Li_2O_2 in the absence of $O_2^{\bullet-}$ radicals. Adiponitrile that was aged for two days with a discharged cathode and KO_2 powder shows little difference in its FTIR spectrum compared to that of fresh adiponitrile, apart from a faint peak at 1645 cm^{-1}. However, all adiponitrile samples aged for one month with KO_2 powder show additional FTIR peaks at *circa* 2185 cm^{-1}, 1645 cm^{-1}, 1615 cm^{-1} and 1580 cm^{-1}, with two additional faint, broad peaks at 3470 cm^{-1} and 3370 cm^{-1}. This reveals that adiponitrile is susceptible to attack by $O_2^{\bullet-}$ radicals, causing it to decompose; these decomposition products then react with Li_2O_2 to form LiOH. Whilst the decomposition of adiponitrile in the presence of $O_2^{\bullet-}$ radicals does occur, the process is slow. Nonetheless, regardless of the stability of adiponitrile towards Li_2O_2, this solvent is not suitable for use in Li-air cells due to its failure to meet the criterion of being stable towards reduced O_2 intermediate species.

3.3.2.2 Stability of glutaronitrile towards Li_2O_2 and KO_2

The XRD diffractogram for discharged cathodes aged in glutaronitrile is shown in Figure 13. Cathodes from glutaronitrile cells show no Li_2O_2 immediately after discharge, with all of their discharge products clearly identified as LiOH. Consequently, there is no change to their XRD patterns when aged with or without KO_2, since the decomposition product has already formed. The same applies to the FTIR spectra for glutaronitrile provided in Figure 14. As such, the only indication of the stability of Li_2O_2 towards glutaronitrile may be obtained from the aging of commercial Li_2O_2 powder.

The XRD diffractogram for commercial Li_2O_2 powder aged in glutaronitrile with and without KO_2 is shown in Figure 15. New peaks at 46.8 ° and 54.4 ° may be seen the XRD pattern for Li_2O_2 powder aged in glutaronitrile. These new XRD peaks are close to the smallest peaks visible in the commercial LiOH pattern, although the larger LiOH peaks are not visible. This finding is supported by faint, broad new peaks at 1530 cm^{-1} and 1400 cm^{-1} in the corresponding

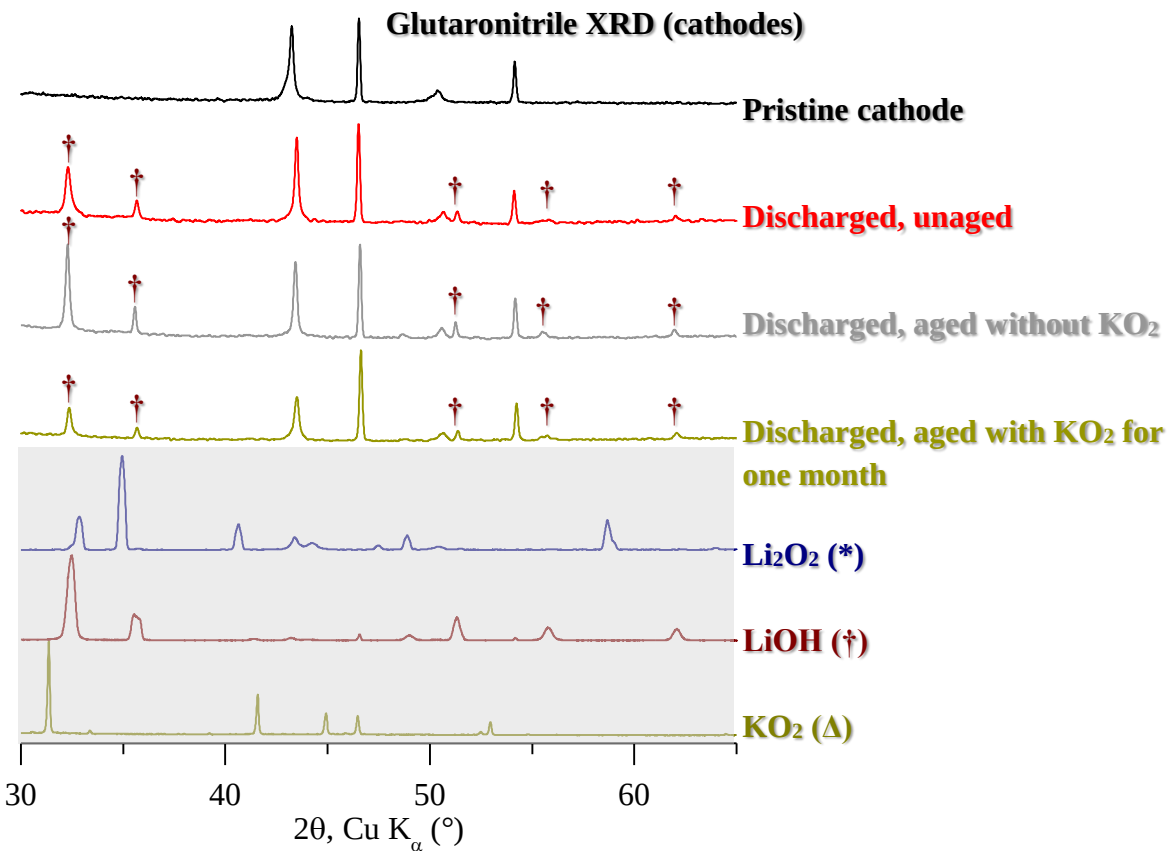

Figure 13: XRD patterns for discharged cathodes aged with and without KO_2 in glutaronitrile for one month. XRD standards are shown in the shaded region.

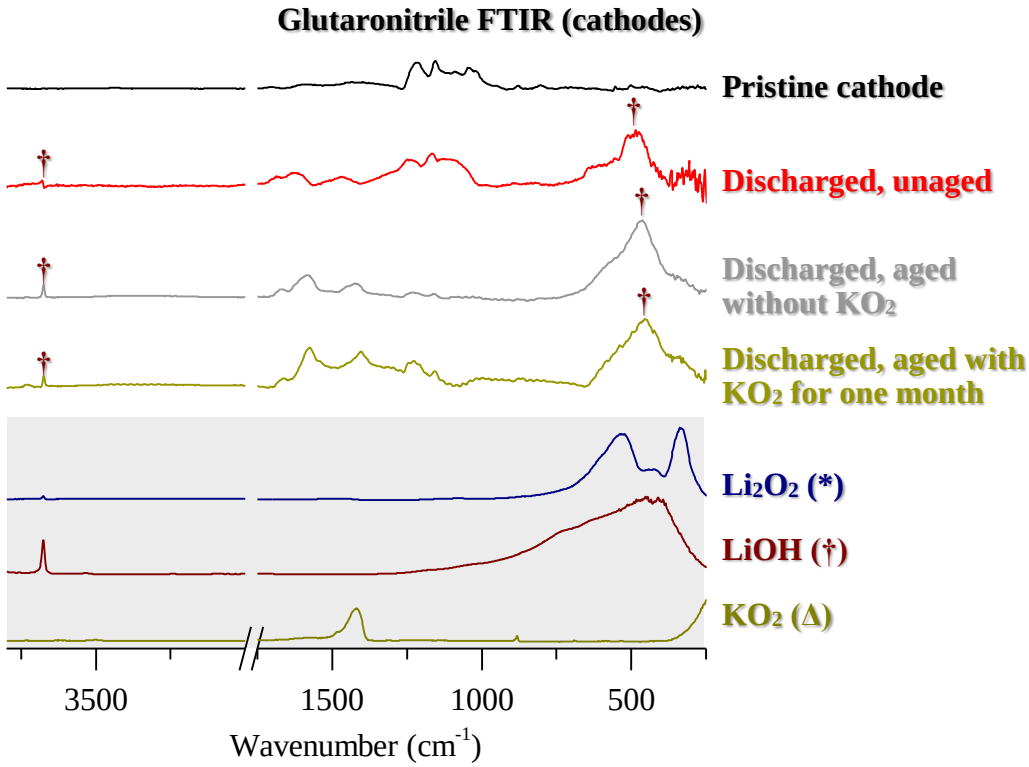

Figure 14: FTIR spectra for discharged cathodes aged with and without KO_2 in glutaronitrile for one month. FTIR standards are shown in the shaded region.

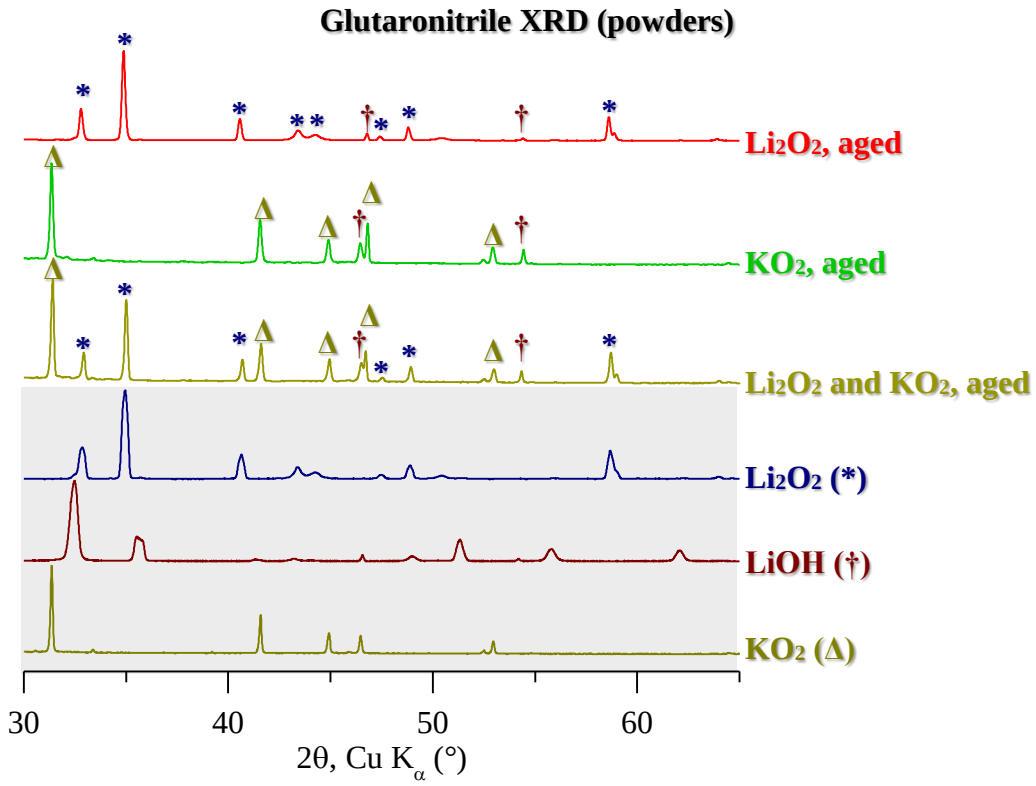

Figure 15: XRD diffractogram for commercial Li_2O_2 and KO_2 powders aged with glutaronitrile for one month. XRD standards are shown in the shaded region.

FTIR spectrum in Figure 16, which indicates that glutaronitrile attacks Li_2O_2 and decomposes it, possibly to LiOH, even in the absence of $O_2^{\bullet-}$ radicals, albeit at a slow rate. Additionally, the aforementioned LiOH peaks (46.8 ° and 54.4 °) appear in the XRD pattern for KO_2 after aging in glutaronitrile (Figure 15), and new peaks appear in the corresponding FTIR spectrum at 2930 cm^{-1}, 2170 cm^{-1} and 1580 cm^{-1} (Figure 16). The change in the structure of KO_2 is evidence that it reacts with glutaronitrile.

All peaks observed in the XRD pattern (Figure 15) and FTIR spectrum (Figure 16) for commercial Li_2O_2 and KO_2 powders aged together in glutaronitrile are a superimposition of those observed for each powder when aged independently. The decomposition peaks observed for Li_2O_2 aged alone in glutaronitrile in the same Figures are masked by the larger peaks of KO_2 in both analytical techniques. Nonetheless, there is no reduction in the height of the Li_2O_2 peaks, and no new LiOH peaks are visible. This indicates that the electrolyte is relatively stable

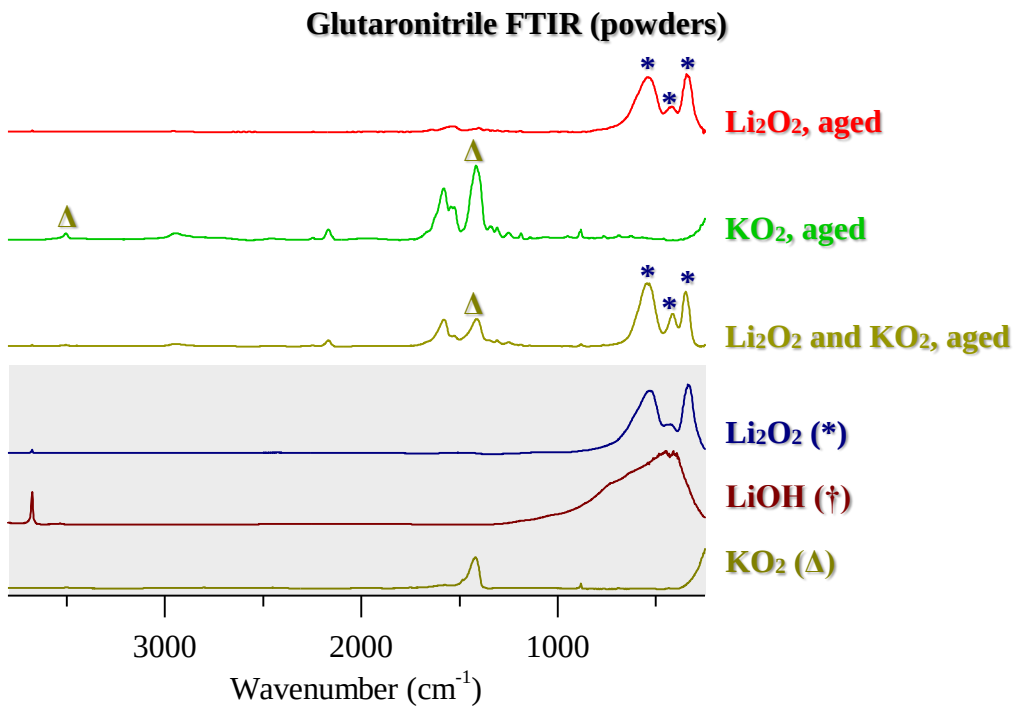

Figure 16: FTIR spectra for commercial Li_2O_2 and KO_2 powders aged with glutaronitrile for one month. FTIR standards are shown in the shaded region.

towards commercial Li_2O_2 powders when $O_2^{\bullet-}$ radicals are present, most likely due to their larger crystallite sizes as discussed earlier.

Solution FTIR was performed on glutaronitrile aged with identical salt and cathode sample combinations to adiponitrile in Section 3.3.2.1 in order to determine the method by which KO_2 reacts with glutaronitrile. Interestingly, glutaronitrile showed no discernible difference in its FTIR spectra when aged with commercial KO_2 or Li_2O_2 powders, or a discharged cathode (Figure 17). Given the new peaks observed in KO_2 powder when aged in glutaronitrile (Figures 15 and 16), this suggests that the products of the reaction between KO_2 and glutaronitrile are solid and therefore drop out of solution. The presence of $O_2^{\bullet-}$ radicals in KO_2 confirms that glutaronitrile is not stable in a Li-air system.

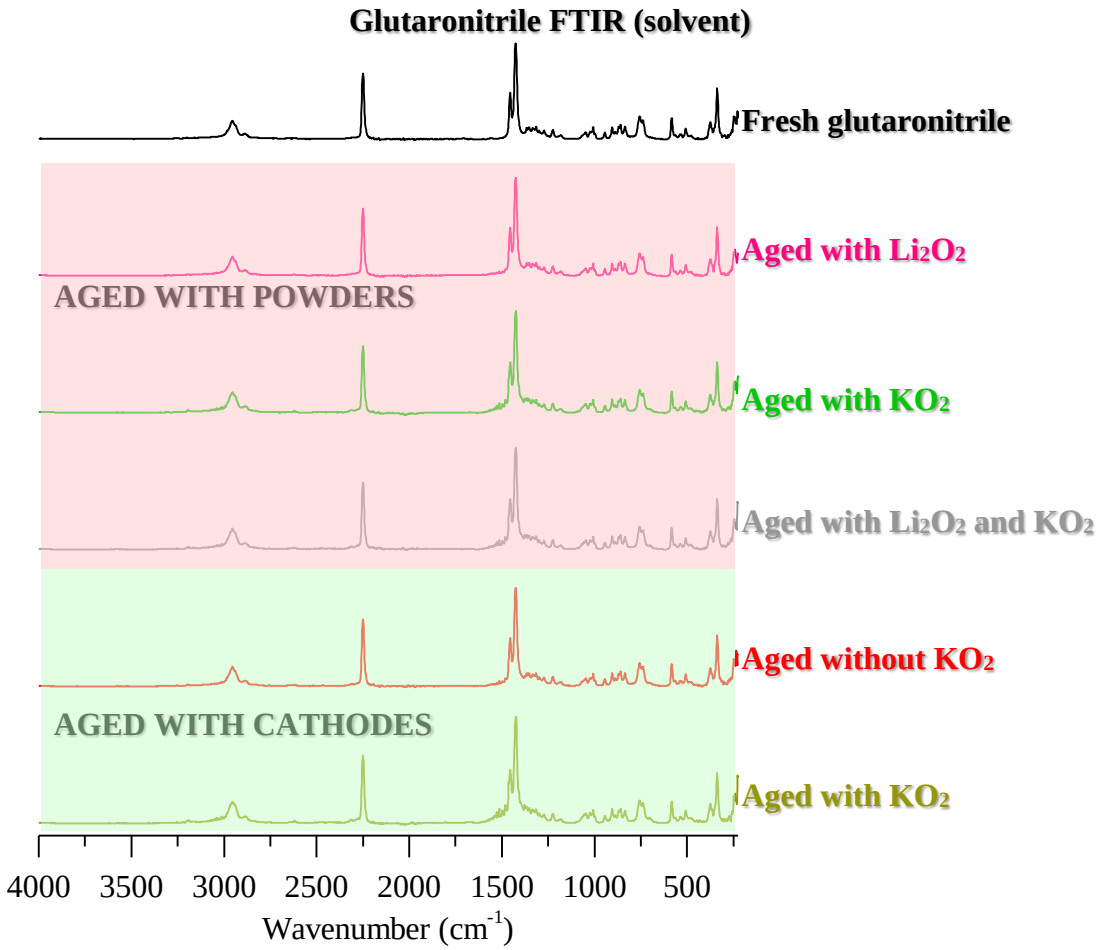

Figure 17: FTIR spectra for glutaronitrile aged for one month with commercial Li_2O_2 and KO_2 powders and discharged Li-air cathodes.

3.4 Electrochemical stability of nitriles within potential limits of Li-air cell cycling

Having established that adiponitrile and glutaronitrile are chemically unstable in the presence of $O_2^{\bullet-}$ radicals, facilitating the decomposition of electrochemically deposited Li_2O_2 to LiOH and passivating the reaction sites of the cathode, the electrochemical stability of the solvents was investigated to see if this also played a crucial role in the rapid failure of the Swagelok cells in Section 3.2. This involved finding the potentials at which each solvent begins to decompose through reduction and oxidation upon cycling, and comparing them to the

potentials at which the oxygen reduction reaction (ORR) and oxygen evolution reaction (OER) occur in that solvent. If the ORR or OER occur at potentials outwith the stability window of the solvent, then a Li-air cell employing that solvent in its electrolyte will be unstable and the electrolyte will decompose upon cycling.

3.4.1 Electrochemical stability analysis method

Each nitrile was mixed with 0.5 M Li triflate as before and pipetted into a five neck glass cell with a glassy carbon working electrode (WE), platinum counter electrode (CE) and precharged LFP reference electrode (RE). The RE was housed in a fritted container with 0.1 M lithium perchlorate ($LiClO_4$) and 1 M tetrabutylammonium perchlorate ($TBAClO_4$) in DMSO; the latter salt, and its tenfold increase in molarity over $LiClO_4$, helped to overcome the poor conductivity of the glass frit. Gas in/out bubblers were fitted to the remaining necks and used to saturate the electrolyte with nitrogen, thus creating an inert atmosphere and allowing the redox potentials of the electrolyte to be observed without being masked by the ORR and OER. Prior to cycling the cell, the potential of the RE was measured against Li foil in each nitrile and found to be +3 V *vs.* Li/Li^+ in both adiponitrile and glutaronitrile. The nitriles then underwent cyclic voltammetry at 100 mV s^{-1} within the same potential window as the Swagelok cells discussed in Section 3.2 (between 2 V and 4.5 V *vs.* Li/Li^+, i.e. -1 V and 1.5 V *vs.* the RE), thus simulating the potential window of a Li-air cell. The cell was then bubbled with O_2 and the process repeated to find the potentials at which the ORR and OER occur. DMSO, which is regarded as a relatively stable solvent in non-aqueous Li-air systems, underwent the same procedures for comparison. The potential of the RE *vs.* Li foil in DMSO was found to be +3.5 V, so the CV scan limits were adjusted to -1.5 V and 1 V *vs.* the RE accordingly.

3.4.2 Results and analysis

Figure 18 shows the CVs obtained for the two nitriles. As can be seen by the minimal increase in current on the cathodic potential sweep in a nitrogen atmosphere (Figure 18(a)), all solvents are stable down to 2 V *vs.* Li/Li^+. Upon reversing the potential sweep to 4.5 V, the current for DMSO is seen to increase from a steady plateau of *circa* 1 µA at 4 V up to 4 µA at 4.5 V, indicating the onset of electrolyte oxidation, albeit of a small magnitude. However, both nitriles start to decompose at potentials upwards of 3.5 V *vs.* Li/Li^+, with the process markedly

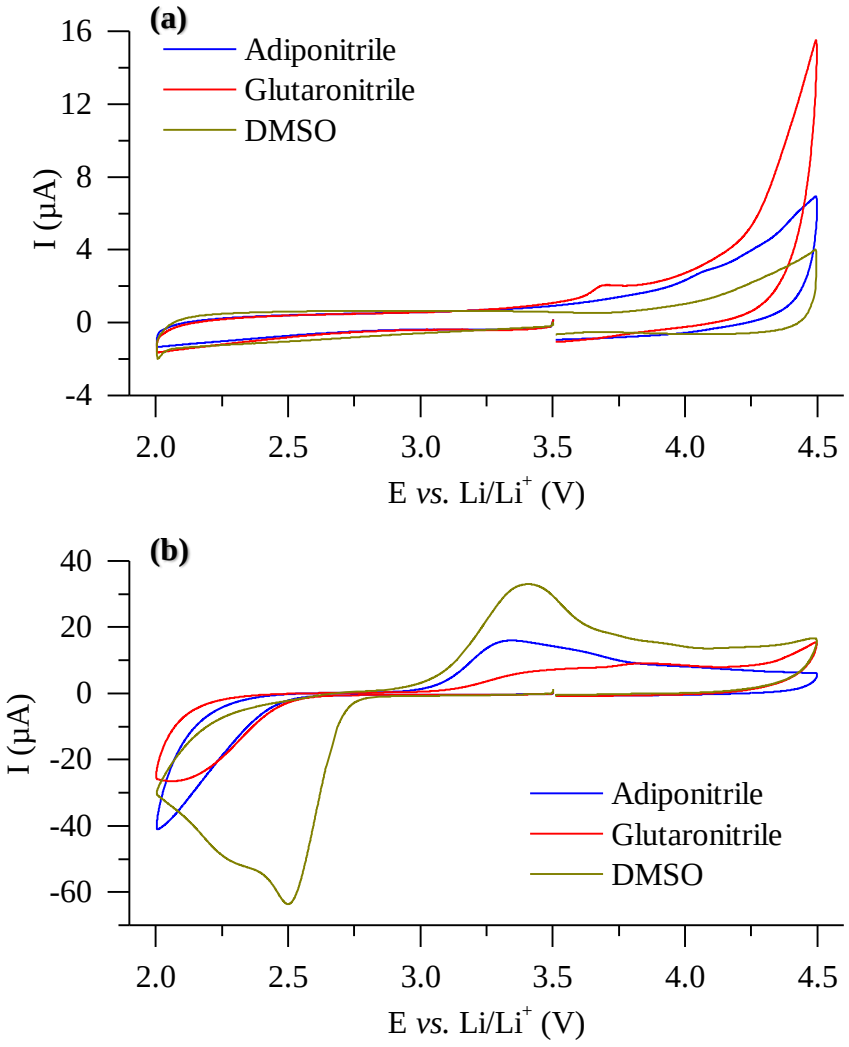

Figure 18: Cyclic voltammograms recorded in nitriles and DMSO containing 0.5 M Li triflate, cycled in the potential window of a Li-air cell, with N_2 atmosphere (a) and O_2 atmosphere (b).

accelerating beyond 4.2 V. Adiponitrile produces a current of 7 µA at 4.5 V, but glutaronitrile clearly undergoes the greater level of decomposition with a current of 15.5 µA. An oxidation peak is visible in the glutaronitrile plot at *circa* 3.7 V, which reveals a secondary reaction that is not encountered in the other solvents; no reduction peak is observed, indicating that this process is irreversible within the potential limits used in this study. Whilst the results for adiponitrile indicate that it is less stable than DMSO at the upper potential limit of the Swagelok Li-air cells, it is clear from Figure 18(a) that the level of decomposition that glutaronitrile undergoes at potentials of upwards of 4.2 V renders the latter nitrile particularly unsuitable for use in Li-air applications.

Figure 18(b) reveals the extent to which nitriles do not facilitate a sustainable, reversible ORR within the potential limits of a Li-air cell. DMSO is seen to support an ORR that commences at *circa* 2.8 V *vs.* Li/Li^+ and peaks at 2.5 V, with the OER commencing at *circa* 3 V. These values are comfortably within the potential limits of a Li-air cell and the decomposition limits of DMSO, and therefore indicate that DMSO is electrochemically capable of supporting multiple cycles in such a cell. The OER peak at 3.4 V does not produce as large a current as the ORR peak, but given that the formation and oxidation of Li_2O_2 are known to undertake different reaction mechanisms, this is to be expected [8, 23]. Indeed, the current plateau of *circa* 14 µA that follows the oxidation peak is indicative of the continued oxidation of Li_2O_2. Conversely, the current increase indicative of the onset of the ORR does not begin in adiponitrile or glutaronitrile until 2.5 V *vs.* Li/Li^+, and neither nitrile reaches the ORR peak within the potential window of a Li-air cell. Maximum reduction currents of 41 µA for adiponitrile and 26 µA for glutaronitrile are considerably smaller than the ORR peak of 64 µA measured for DMSO. Additionally, whilst the OER in adiponitrile commences at 3 V as for DMSO and peaks at *circa* 3.3 V, the magnitude of the peak is less than half of that of DMSO (16 µA *vs.* 33 µA). Considering that the ORR peak for adiponitrile is roughly two thirds of the

size of that of DMSO, this suggests a loss of efficiency upon charging, even factoring in the current plateau beyond 3.4 V. Conversely, when comparing the charge passed through each cell during the reduction and oxidation sweeps, the DMSO cell is found to have an efficiency of 78.7 %, but the adiponitrile cell has an efficiency of 99 %. However, when comparing Figures 18(a) and (b), it can be seen that approximately 50 % of the charge passed through the adiponitrile cell between 4 V and 4.5 V is due to electrolyte decomposition. As such, the formation and oxidation of Li_2O_2 is not as reversible in adiponitrile as it is in DMSO. Whilst the OER also occurs in glutaronitrile, it commences at 3.15 V, indicating that Li_2O_2 oxidation has a higher overpotential in glutaronitrile than the other solvents considered in this study, which results in poorer coulombic efficiency of the cell. Additionally, the OER is concentrated at higher potentials, with no current peak as for the other two solvents. The OER current plateau reaches parity with that of adiponitrile between 3.75 V and 4.25 V, followed by a rapid increase. Comparison with Figure 18(a) reveals that this rapid increase is due to solvent decomposition. Such is the extremity of this decomposition that a comparison of the charge passed through the cell during reduction and oxidation reveals that the total oxidation charge is greater than the reduction charge. This explains the significantly poorer performance of the glutaronitrile Swagelok cells in comparison to the adiponitrile cells encountered in Section 3.2. Overall, both nitriles are shown to be electrochemically unfavourable in Li-air systems, failing to reach the O_2 reduction peak before the lower potential limit of typical Li-air cells and undergoing excessive solvent decomposition at the potentials encountered upon charging.

3.5 Revised cycling procedures based on electrochemical stability of nitriles to enhance capacity retention

It can be seen from Figures 18(a) and (b) that most electrolyte decomposition occurs at potentials above 4.2 V *vs.* Li/Li^+. Therefore, new cycling parameters were applied to a number of Swagelok cells in an attempt to overcome this issue. One batch of cells was cycled between 2.4 V and 4.2 V *vs.* Li/Li^+ to prevent electrolyte decomposition, whilst another batch was capacity-limited to 1000 mAh g^{-1} Super P Li active cathode material, with no potential limits.

Figure 19 shows the result of the revised cycling procedures for adiponitrile. Rapid capacity loss is still exhibited by the cell cycled with a reduced potential window (Figure 19(a)). The

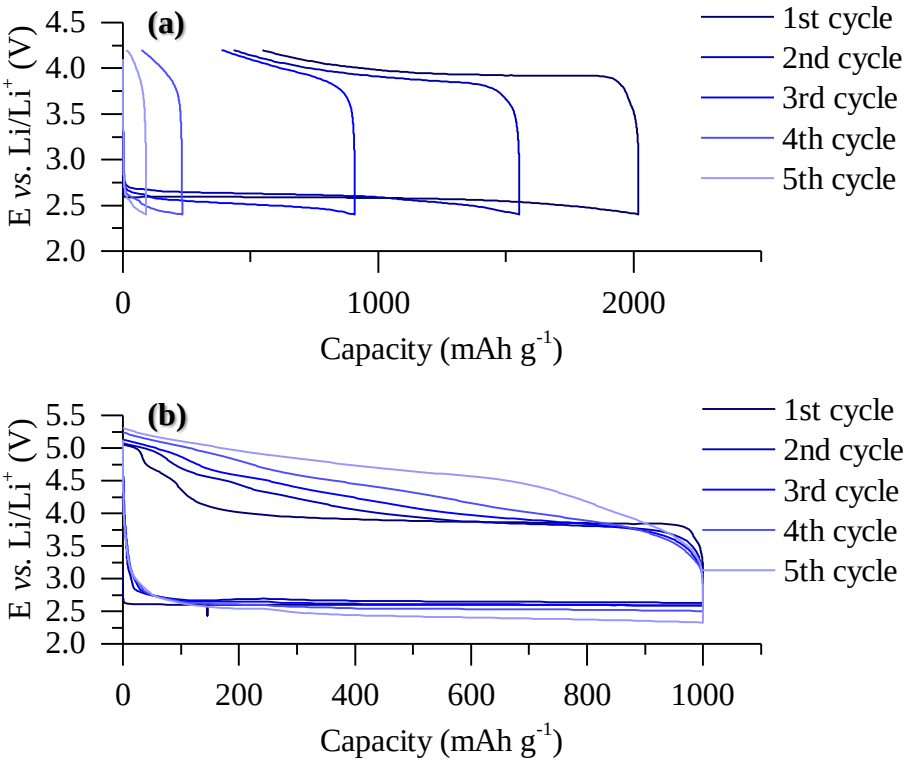

Figure 19: Cycling profiles for adiponitrile with limited potential window of 2.4 V to 4.2 V vs. Li/Li^+ (a) and limited discharge capacity of 1000 mAh g^{-1} Super P Li (b).

cell that was capacity-limited quickly polarised upon cycling (Figure 19(b)), with the charging overpotential increasing and discharge potential plateau decreasing on each successive cycle to the point that the cell has clearly failed. Glutaronitrile once again shows increased capacity fade under both cycling conditions (Figure 20). Therefore, whilst the original potential limits may have been partly responsible for the poor performance of both nitriles, it is apparent that these solvents will still decompose in a Li-air cell even if cycled with supposedly favourable cycling parameters.

3.6 Oxygen concentration and kinetics within nitrile electrolytes

Further electrochemistry was conducted on the nitriles to assess their oxygen diffusion coefficient, *D*, and concentration, *C*, in comparison to those of DMSO. The poor capacity

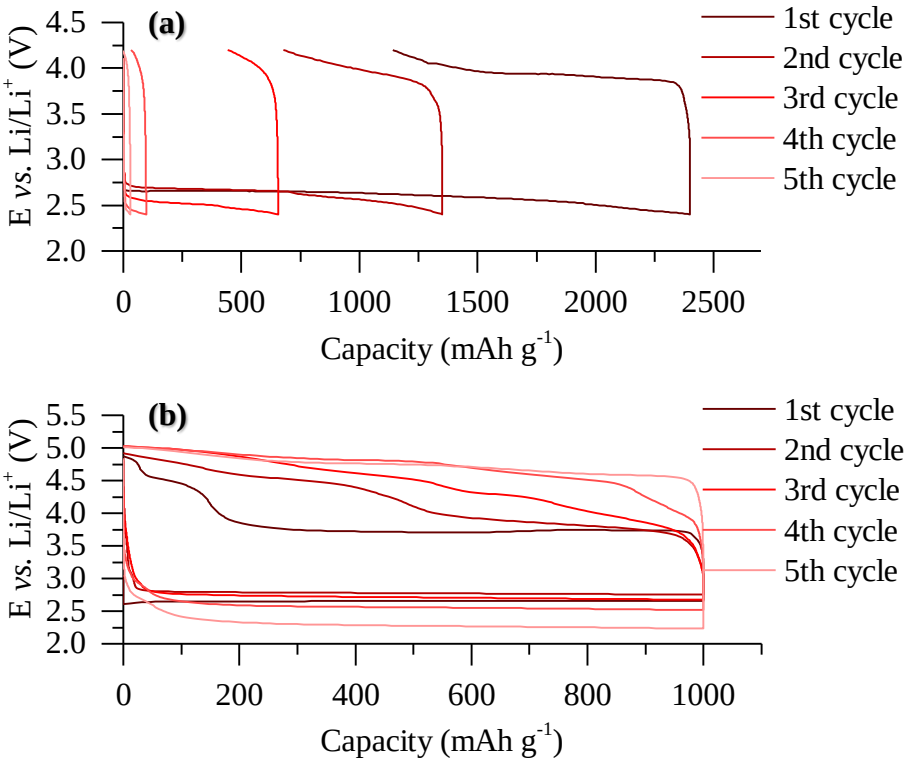

Figure 20: Cycling profiles for glutaronitrile with limited potential window of 2.4 V to 4.2 V vs. Li/Li$^+$ (a) and limited discharge capacity of 1000 mAh g^{-1}Super P Li (b).

retention of the nitrile cells suggests that the kinetics for oxygen within the cell are slow, causing LiO_2 intermediates to build up on the reaction sites of the cathode. These form a thick, passivating surface layer of Li_2O_2, which is then subsequently decomposed by $O_2^{\bullet-}$ radicals and the electrolyte to form decomposition salts. A low oxygen diffusion coefficient would indicate that this process is taking place due to the comparative difficulty faced by $O_2^{\bullet-}$ radicals trying to leave the reaction sites and drift into the electrolyte.

3.6.1 Determining oxygen concentration and diffusion coefficient in nitriles

Values for *C* and *D* were obtained using the Cottrell and ultramicroelectrode (UME) techniques outlined in Chapter 2, followed by simultaneously solving the equations of both, namely the Cottrell equation:

$$I_t = \frac{nFC\sqrt{D}A}{\sqrt{\pi t}} \quad (1)$$

and the equation for the steady-state current obtained using a UME:

$$I_{SS} = 4nFDCr \quad (2)$$

The rearrangement of each equation and subsequent calculations are explained in detail in Chapter 4.

In order to simultaneously solve Equations (1) and (2) for *C* and *D*, the limiting current, I_t, and steady-state current, I_{SS}, had to be obtained for adiponitrile and glutaronitrile. Firstly, each solvent was mixed with 0.1 M tetrabutylammonium bis-trifluoromethanesulfonimidate

(TBATFSI), a salt that produces reduction products that are soluble in organic solvents, unlike lithium-based salts that passivate the WE with Li_2O_2. Each electrolyte solution was pipetted into a five neck glass cell containing a glassy carbon WE, silver RE and platinum CE, plus oxygen in/out bubblers. The cell was saturated with oxygen before undergoing CV at 100 mV s^{-1} to find the oxidation and reduction peaks of the solvent. The chronoamperometry procedure to find I_t was then followed as described in Chapter 2. The UME procedure to find I_{SS} (Chapter 2) was then conducted at a scan rate of 10 mV s^{-1}, with a cathodic sweep to -1.5 V *vs.* the RE before cycling back to 0 V. Figures 21 and 22 show the resultant plots from the Cottrell and UME methods for adiponitrile and glutaronitrile, respectively; those of DMSO are shown in Figure 4 in Chapter 4.

3.6.2 Results and analysis

Table 1 contains the calculated oxygen concentration and diffusion coefficient of all of the solvents considered in this experiment. The measured value of *C* for DMSO is 0.27 mM lower than that reported in the literature [24, 25]. However, the salt used in the literature was tetraethylammonium chloride, as opposed to TBATFSI used in this study. This may explain, at least in part, the discrepancy in the measured and reported *C* values. The *D* value for DMSO compares favourably with the value of 3.23×10^{-9} m^2 s^{-1} reported in the literature [24]. Whilst adiponitrile and glutaronitrile contained more oxygen than DMSO, their diffusion coefficients are markedly lower. Consequently, in a Li-air cell, O_2 cannot diffuse as quickly into the

Solvent	***C* (mM)**	***D* (m^2 s^{-1})**	***CD***	$C\sqrt{D}$
Adiponitrile	3.48	1.33×10^{-9}	4.63×10^{-9}	1.27×10^{-4}
Glutaronitrile	3.00	1.42×10^{-9}	4.26×10^{-9}	1.13×10^{-4}
DMSO	1.83	3.16×10^{-9}	5.78×10^{-9}	1.03×10^{-4}

Table 1: Summary of the oxygen concentration C and diffusion coefficient D of nitrile electrolytes in comparison to DMSO.

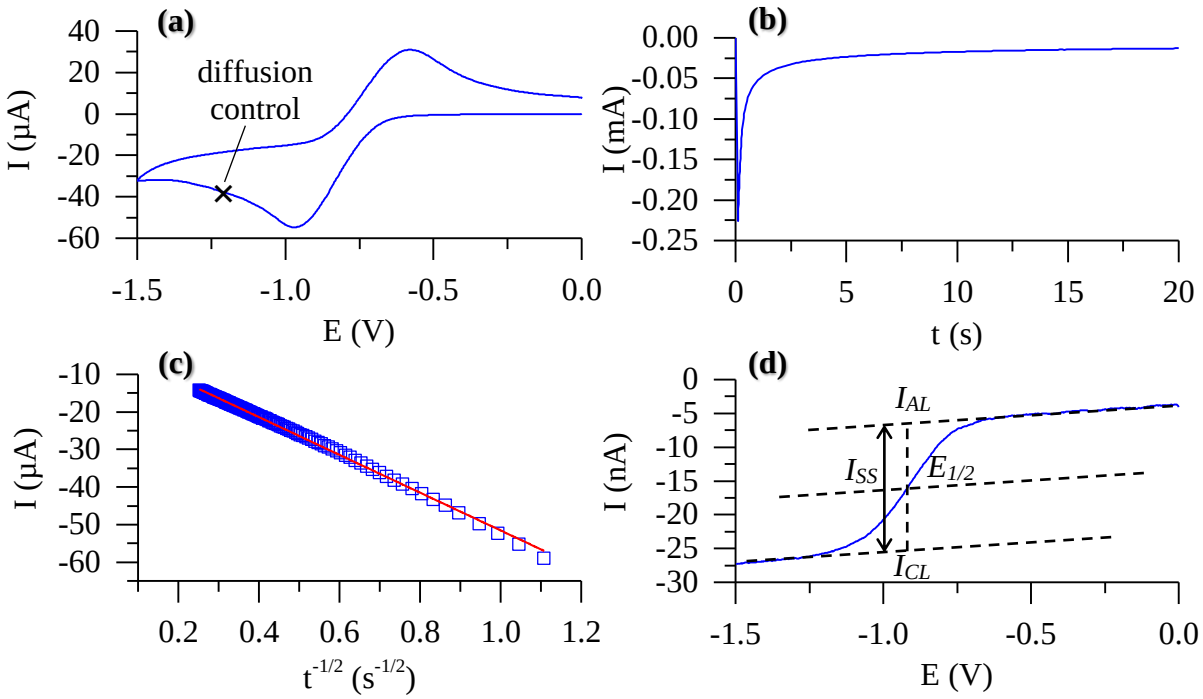

Figure 21: Electrochemical procedures to obtain the values required to calculate the oxygen concentration in, and diffusion coefficient of, adiponitrile. The CV (a), potential hold (b), Cottrell (c) and UME steady-state current (d) plots are shown.

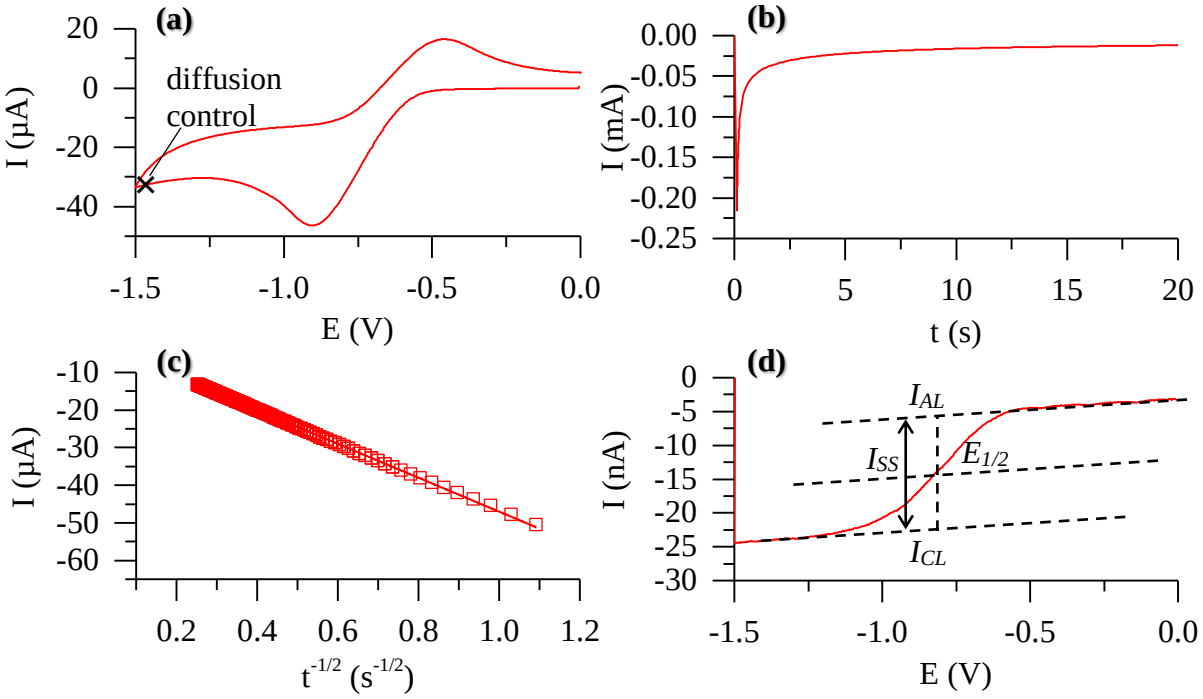

Figure 22: Electrochemical procedures to obtain the values required to calculate the oxygen concentration in, and diffusion coefficient of, glutaronitrile. The CV (a), potential hold (b), Cottrell (c) and UME steady-state current (d) plots are shown.

cathode in a nitrile electrolyte as with a DMSO electrolyte, increasing the likelihood of the accumulation of a passivating layer of Li_2O_2 close to the cathode surface rather than utilising as many of the available reaction sites as possible throughout the cathode. As expected due to its inferior cycling performance, glutaronitrile has a smaller oxygen concentration than adiponitrile, although it does have a similar diffusion coefficient. Conversely, one could argue that solvents with a higher bulk concentration of oxygen, but lower oxygen diffusion coefficient, would be more likely to suffer from poor capacity retention because of the large concentration of oxygen near the reaction sites combined with the restricted ability to drift into solution once it has been reduced to $O_2^{\bullet-}$, leading to the accumulation of intermediate species described in Section 3.6. However, in that case, adiponitrile would theoretically suffer from poorer capacity retention than glutaronitrile.

The influence of the concentration and diffusion coefficient of oxygen within each solvent on the performance of the cell is represented by the columns for *CD* and $C\sqrt{D}$, which represent the influence of *C* and *D* on the UME steady state current and the Cottrell limiting current, respectively. *CD* is greater in DMSO than in adiponitrile by 26.1 %, and greater than in glutaronitrile by 38.1 %, thus indicating DMSO-based UME cells are capable of sustaining a higher steady state current than nitrile cells. Conversely, $C\sqrt{D}$ is lower for DMSO than glutaronitrile by 9.1 %, and lower than adipontirile by 23.1 %. Whilst this margin is smaller than for *CD* values, this still represents poorer kinetics for DMSO cells than nitrile cells in this regard. The lower concentration of oxygen in DMSO will result in cells that use it as an electrolyte rapidly running out of O_2 within the vicinity of the electrode. The diffusion coefficient of oxygen is insufficient to compensate for the lack of O_2 near in comparison to nitrile cells. However, $C\sqrt{D}$ relates to the Cottrell equation, which applies to planar macroelectrodes undergoing chronoamperometry. In reality, Li-air cells are more likely to

undergo galvanostatic or variable load cycling in practical applications, so the findings of $C\sqrt{D}$ are less relevant for real cells. Furthermore, the porous carbon cathode is not planar, but a network of interconnected micro- and mesopores. As such, O_2 is more likely to diffuse to the reaction sites in a radial manner akin to that encountered in the UME cell. Therefore, the kinetics of the nitrile cells are less favourable than DMSO, with glutaronitrile having a lower *CD* value than adiponitrile, which is to be expected given its poorer performance in real Li-air cells.

3.7 Conclusions and further work

It is apparent from the cycling performance of adiponitrile and glutaronitrile that these solvents are not stable in a Li-air cell, even if the potential window and discharge capacity are restricted to aid cyclability as in previous studies [12]. LiOH and Li_2CO_3 were seen to form on the cathode of adiponitrile cells from the second cycle, and from the first cycle in glutaronitrile cells, confirming that the cathode was being passivated by decomposition products. The inability to sustain more than a handful of cycles renders these solvents unsuitable for commercial Li-air secondary cells.

Further analysis of the chemical stability of nitriles have shown that they are attacked by $O_2^{\bullet-}$ radicals, and in turn decompose electrochemically deposited Li_2O_2 to LiOH; the appearance of LiOH in cycled cathodes was previously believed to only occur in the presence of water. Given that this has also recently been observed in DMSO [22], this discovery represents an important understanding of the decomposition mechanisms of organic electrolytes in Li-air cells. It will be advantageous to test all previously studied solvents to see whether or not the same mechanism occurs upon aging in other electrolyte solutions; if there are any electrolytes that are resistant to this form of attack; and if there is a link between the structure or characteristics

of any $O_2^{\bullet-}$/Li_2O_2-resistant solvents. Additionally, all new solvents should be subjected to this study; even if they are able to sustain hundreds of cycles without rest, as per conventional Li-air cell testing, they will be impractical for real-life use if they can be decomposed by intermediate species and discharge products upon being rested in the discharged state for a prolonged period of time.

Electrochemical studies of both nitriles indicate that oxygen reduction and evolution reactions are not sustainable in nitriles due to poor oxygen kinetics, the excessively low potential of the ORR, the lack of an OER peak in glutaronitrile and significant electrolyte decomposition encountered at higher oxidation potentials. This results in the incomplete removal of Li_2O_2 and the formation of a variety of irreversible decomposition products. Whilst it is difficult to assert that the mechanisms observed in an electrochemical cell will translate directly into a real Li-air cell, the above observations suggest that a film of discharge and decomposition products will accumulate on the cathode pore walls of a real Li-air cell over successive cycles, blocking reaction sites and terminating the cell.

Regarding the reasoning behind the selection of nitriles for this study, the absence of oxygen from the structural formula of nitriles has clearly not prevented them from undergoing nucleophilic attack by $O_2^{\bullet-}$ radicals as had been hoped. Further solvents to be investigated must have strong bond energies and minimised polarity that allows the solvent to be resistant to nucleophilic attack whilst remaining sufficiently polar to be able to dissolve salts and thus form an electrolyte solution. A recently study has revealed an inverse linear relationship between the ability of common Li-air solvents to solvate the LiO_2 intermediate species and their ability to withstand nucleophilic attacks [26]. This explains the instability of DMSO when aged with a source of $O_2^{\bullet-}$ radicals by Kwabi *et al.* [22] and suggests that a solvent that is capable of yielding high levels of solution phase Li_2O_2 formation whilst resisting nucleophilic attack may need to be engineered in the laboratory. Alternatively, electrolyte solutions comprising

multiple solvents, chosen for their combined stability against attack from $O_2^{\bullet-}$ radicals and ability to solvate LiO_2, will have to be developed to enable reversible Li-air cells with sufficiently long cycle and calendar lives to make them commercially viable. Clearly, the nitriles are susceptible to nucleophilic attack, showing signs of decomposition within two days of exposure to $O_2^{\bullet-}$ radicals and significant levels of decomposition within one month.

If further studies fail to identify a liquid organic or ionic liquid electrolyte, or carefully selected electrolyte mixture thereof, that is stable towards intermediate species, discharge products and inexpensive, commercially viable cathode materials, then attention must turn to the development of solid-state electrolytes with high Li^+ conductivity. These would also have the advantage of negating any concerns about electrolyte evaporation during use in a non-hermetically sealed cell. Whilst the operating temperatures of such cells will be considerably lower than for molten salt battery packs, such as those used by Modec (see Chapter 1), the ability to operate in mild climates with minimal battery pack heating requirements is also desirable. The reduction and oxidation mechanisms of solid-state Li-air cells will also require investigation in order to determine if the cell decomposes during long-term cycling and, if so, how to mitigate this.

3.9 References

[1] J. C. Burns, A. Kassam, N. N. Sinha, L. E. Downie, L. Solnickova, B. M. Way and J. R. Dahn, "Predicting and Extending the Lifetime of Li-Ion Batteries," *J. Electrochem. Soc.*, vol. 160, no. 9, pp. A1451 - A1456, 2013.

[2] Y. Chen, S. A. Freunberger, Z. Peng, F. Bardé and P. G. Bruce, "Li−O_2 Battery with a Dimethylformamide Electrolyte," *J. Am. Chem. Soc.,* vol. 134, no. 18, pp. 7952 - 7957, 2012.

[3] S. A. Freunberger, Y. Chen, N. E. Drewett, L. J. Hardwick, F. Bardé and P. G. Bruce, "The Lithium–Oxygen Battery with Ether-Based Electrolytes," *Angew. Chem. Int. Ed.,* vol. 50, no. 37, pp. 8609 – 8613, 2011.

[4] J. Xiao, J. Hu, D. Wang, D. Hu, W. Xu, G. L. Graff, Z. Nie, J. Li and J.-G. Zhang, "Investigation of the Rechargeability of Li–O_2 Batteries in Non-Aqueous Electrolyte," *J. Power Sources,* vol. 196, no. 13, pp. 5674 – 5678, 2011.

[5] M. M. O. Thotiyl, S. A. Freunberger, Z. Peng and P. G. Bruce, "The Carbon Electrode in Nonaqueous Li–O_2 Cells," *J. Am. Chem. Soc.,* vol. 135, no. 1, pp. 494 – 500, 2013.

[6] M. M. O. Thotiyl, S. A. Freunberger, Z. Peng, Y. Chen, Z. Liu and P. G. Bruce, "A Stable Cathode for the Aprotic Li–O_2 Battery," *Nature Mater.,* vol. 12, pp. 1050 – 1056, 2013.

[7] B. D. McCloskey, A. Speidel, R. Scheffler, D. C. Miller, V. Viswanathan, J. S. Hummelshøj, J. K. Nørskov and A. C. Luntz, "Twin Problems of Interfacial Carbonate Formation in Nonaqueous Li–O_2 Batteries," *J. Phys. Chem. Lett.,* vol. 3, no. 8, pp. 997 – 1001, 2012.

[8] P. G. Bruce, S. A. Freunberger, L. J. Hardwick and J.-M. Tarascon, "Li–O_2 and Li–S Batteries with High Energy Storage," *Nature Mater.,* vol. 11, pp. 19 – 29, 2012.

[9] F. Mizuno, S. Nakanishi, Y. Kotani, S. Yokoishi and H. Iba, "Rechargeable Li-Air Batteries with Carbonate-Based Liquid Electrolytes," *Electrochemistry,* vol. 78, no. 5, pp. 403 - 405, 2010.

[10] N. Garcia-Araez and P. Novák, "Critical Aspects in the Development of Lithium–Air Batteries," *J. Sold State Electr.,* vol. 17, no. 7, pp. 1793 - 1807, 2013.

[11] G. Girishkumar, B. McCloskey, A. C. Luntz, S. Swanson and W. Wilcke, "Lithium−Air Battery: Promise and Challenges," *J. Phys. Chem. Lett.,* vol. 1, no. 14, pp. 2193–2203, 2010.

[12] Z. Peng, S. A. Freunberger, Y. Chen and P. G. Bruce, "A Reversible and Higher-Rate Li-O_2 Battery," *Science,* vol. 337, pp. 563 - 566, 2012.

[13] F. Li, D.-M. Tang, Y. Chen, D. Golberg, H. Kitaura, T. Zhang, A. Yamada and H. Zhou, "Ru/ITO: A Carbon-Free Cathode for Nonaqueous Li-O_2 Battery," *Nano Lett.,* vol. 13, pp. 4702 - 4707, 2013.

[14] S. S. Zumdahl and S. A. Zumdahl, "8.8: Covalent Bond Energies and Chemical Reactions," in *Chemistry, Ninth Edition,* Brooks Cole, 2014, pp. 373 - 375.

[15] M. Ue, K. Ida and S. Mori, "Electrochemical Properties of Organic Liquid Electrolytes Based on Quaternary Onium Salts for Electrical Double-Layer Capacitors," *J. Electrochem. Soc.,* vol. 141, no. 11, pp. 2989 - 2996, 1994.

[16] Y. Abu-Lebdeh and I. Davidson, "High-Voltage Electrolytes Based on Adiponitrile for Li-Ion Batteries," *J. Electrochem. Soc.,* vol. 156, no. 1, pp. A60 - A65, 2009.

[17] C. O. Laoire, S. Mukerjee, K. M. Abraham, E. J. Plichta and M. A. Hendrickson, "Influence of Nonaqueous Solvents on the Electrochemistry of Oxygen in the Rechargeable Lithium−Air Battery," *J. Phys. Chem. C,* vol. 114, no. 19, pp. 9178 – 9186, 2010.

[18] R. Younesi, P. Norby and T. Vegge, "A New Look at the Stability of Dimethyl Sulfoxide and Acetonitrile in Li-O_2 Batteries," *ECS Electrochem. Lett.*, vol. 3, no. 3, pp. A15 - A18, 2014.

[19] B. D. McCloskey, D. S. Bethune, R. M. Shelby, T. Mori, R. Scheffler, A. Speidel, M. Sherwood and A. C. Luntz, "Limitations in Rechargeability of Li-O_2 Batteries and Possible Origins," *J. Phys. Chem. Lett.*, vol. 3, no. 20, pp. 3043 - 3047, 2012.

[20] Nissan Great Britain. (2015). *Nissan LEAF Guarantees & Services*. [Online]. Available: http://www.nissan.co.uk/GB/en/vehicle/electric-vehicles/leaf/prices-and-equipment/services-warranty.html. [Accessed 04 September 2015].

[21] S. Wu, J. Tang, F. Li, X. Liu and H. Zhou, "Low Charge Overpotentials in Lithium–Oxygen Batteries Based on Tetraglyme Electrolytes with a Limited Amount of Water," *Chem. Commun.*, pp. 16860 - 16863, 2015.

[22] D. G. Kwabi, T. P. Batcho, C. V. Amanchukwu, N. Ortiz-Vitoriano, P. Hammond, C. V. Thompson and Y. Shao-Horn, "Chemical Instability of Dimethyl Sulfoxide in Lithium−Air Batteries," *J. Phys. Chem. Lett.*, vol. 5, pp. 2850 - 2856, 2014.

[23] L. J. Hardwick and P. G. Bruce, "The Pursuit of Rechargeable Non-Aqueous Lithium–Oxygen Battery Cathodes," *Curr. Opin. Solid St. M.*, vol. 16, pp. 178 - 185, 2012.

[24] D. T. Sawyer and J. L. R. Jr, "Electrochemistry of Oxygen and Superoxide Ion in Dimethylsulfoxide at Platinum, Gold and Mercury Electrodes," *J. Electroanal. Chem.*, vol. 12, pp. 90 - 101, 1966.

[25] J. Janata, *Principles of Chemical Sensors*, Springer, 2009, p. 234.

[26] A. Khetan, A. Luntz and V. Viswanathan, "Trade-Offs in Capacity and Rechargeability in Nonaqueous Li-O_2 Batteries: Solution-Driven Growth versus Nucleophilic Stability," *J. Phys. Chem. Lett.*, vol. 6, pp. 1254 - 1259, 2015.

4 Experimental verification of novel lithium-air multiscale computerised model

4.1 Introduction

Computer-simulated models of lithium-air cells can be used to predict the cycling mechanisms that occur for a given configuration of electrode materials and electrolyte solution. This allows solvents to be screened in order to assess the discharge capacity that they can yield within a cell under different parameters, such as current density, and thus indicate their viability as an electrolyte. Such a model can also be used to predict the optimum morphology of the cathode, including its pore size distribution, to facilitate maximum discharge capacity and cycle life [1].

As explained in Chapter 1, it has recently been discovered that Li_2O_2 may be formed *via* two different reaction mechanisms, namely surface layer growth and solution-phase formation. The occurrence of each mechanism depends on the donor number of the solvent used in the electrolyte solution, with higher donor numbers promoting the latter mechanism [2]. Since solution-phase Li_2O_2 formation is a recent discovery, most existing Li-air models predate this and therefore do not take this reaction into consideration. Others that do include both mechanisms assume that they cannot occur simultaneously at a given current density [3]. Furthermore, most of the previous models have been based on solvents that have relatively low donor numbers or that are now known to be unstable in Li-air cells, like propylene carbonate (PC) or dimethyl ether (DME). These solvents are less likely to exhibit solution-phase Li_2O_2 growth in the real cells, thus not allowing the accuracy of the models to be evaluated in the event that this is the dominant discharge mechanism [4, 5, 6, 7].

The first mathematical model to predict the discharge capacity of a Li-air cell assumed that cathode pores were cylindrical. It factored in current density, oxygen concentration in the electrolyte and cathode thickness to calculate the decrease in pore volume over time as a result of the formation of a layer of Li_2O_2 on the cathode pore walls. [4]. Whilst the predicted discharge capacity at atmospheric pressure of O_2 correlated well with experimental data for a current density of 0.05 mA cm^{-2}, there was an underestimation of 200 mAh g^{-1}, some 20 % of the capacity of the real cell, when this density was doubled. Additionally, the solvent used in the model was PC, which is unstable in Li-air cells and results in the formation of Li_2CO_3. However, this was not considered by the model, and neither was the passivation of active sites by discharge products. Later physical models incorporated Li_2CO_3 formation, and some considered cylindrical, spherical and linear deposition of discharge products, as well as the change in tortuosity of migration routes caused by these mechanisms over time. However, these models were based on cells cycled at low current densities and did not account for solution-phase Li_2O_2 growth [5, 6]. The influence of heat generation from the exothermic reactions taking place within the cell on cell performance was studied for the first time using a 2D non-isothermal model, but the effect of this was found to be negligible [7]. Furthermore, all of the above models only consider mechanisms occurring at the macroscale, thus neglecting mesoscale mechanisms such as oxygen transport in the electrolyte within the cathode pores as opposed to across the electrode as a whole [1].

Nimon *et al.* developed a model that accounted for the pore size distribution (PSD) of the cathode, which managed to closely map the shape of the discharge curve of real cells with dimethylformamide (DMF) electrolyte at low current densities (up to 2.5 A m^{-2}) and predict the discharge capacity within an error of as little as 5 % [8]. However, this model assumed that surface layer deposition of Li_2O_2 filled the entire volume of the smallest pores first, which contradicts many observations of toroidal Li_2O_2 particles with diameters of hundreds of

nanometres [9, 10, 11]. Bevarai *et al.* achieved a significant improvement upon this with their whole-cell model based on the same experimental data, with a close fit throughout the discharge curve at both 1 A m^{-2} and 2.5 A m^{-2} [12]. However, once again, the model only considered thin-film Li_2O_2 growth, whereas solution-phase Li_2O_2 growth would also be expected given that the solvent has a relatively high donor number of 26.6 kcal mol^{-1} [13].

If Li_2O_2 forms exclusively in solution-phase, this can increase the discharge capacity of a cell three-fold, and so the exclusion of this mechanism from previous models is likely to severely impact upon their accuracy [2]. Therefore, a new multiscale whole-cell model has been developed that can accurately predict the extent to which surface layer deposition and solution-phase growth of Li_2O_2 occurs in a cell based on its chemistry, and how this impacts on the discharge capacity of the cell, with the aim of being more representative of the true discharge curve of the cell than previous models [14]. This chapter discusses the verification procedure of the new model, which involved comparing its prediction of the discharge behaviour of fully-parameterised cells to the behaviour of real cells built and cycled to these specifications. A range of cell chemistries and cycling parameters were chosen, with each being more favourable towards either surface layer deposition or solution-phase growth of Li_2O_2. This allowed the accuracy with which the model could predict the extent of the occurrence of each mechanism to be determined.

4.2 Description of multiscale model

A multiscale model is a hierarchical algorithm that is capable of resolving several key interlinked spatially- and time-dependent mechanisms in a system, occurring at the mesoscale and macroscale, many of which may compete against each other. The aim of a multiscale model is to reduce the empirical assumptions made in multiphysics models, i.e. models that

consider many time-dependent mechanisms occurring in one spatial scale [15]. In the case of a Li-air cell during discharge, time-dependent factors include transport and consumption of oxygen in the electrolyte, the formation of Li_2O_2 and its subsequent passivation of reaction sites, and the potential of the cell [1]. The extent to which these factors occur is in turn influenced by spatially-dependent parameters, such as the PSD of the cathode, which has been proven to have greater influence over the discharge capacity of a cell than the total surface area of the cathode [1, 16, 17, 18]. However, it has been shown that the surface area of larger cathode pores can impact upon the discharge capacity of the cell, and so this must also be factored into the model [19].

The developed model, which is outlined in full in [14], is based on a porous carbon cathode of known thickness, area, PSD and porosity, which is split into 10 µm thick segments called bins. The model takes into account the "hall," the largest open area inside the porous cathode structure, defined as any void with greater than 125 nm radius, which is connected to smaller pores of successively decreasing size. These pores are classified numerically, with N = 1 representing the largest pore (Figure 1). It is assumed that the solution-phase nucleation of Li_2O_2 occurs in the hall, based on previous experimental observations of Li_2O_2 particles with diameters of several hundred nanometres [9, 10, 11]. Therefore, $O_2^{\bullet-}$ radicals must migrate

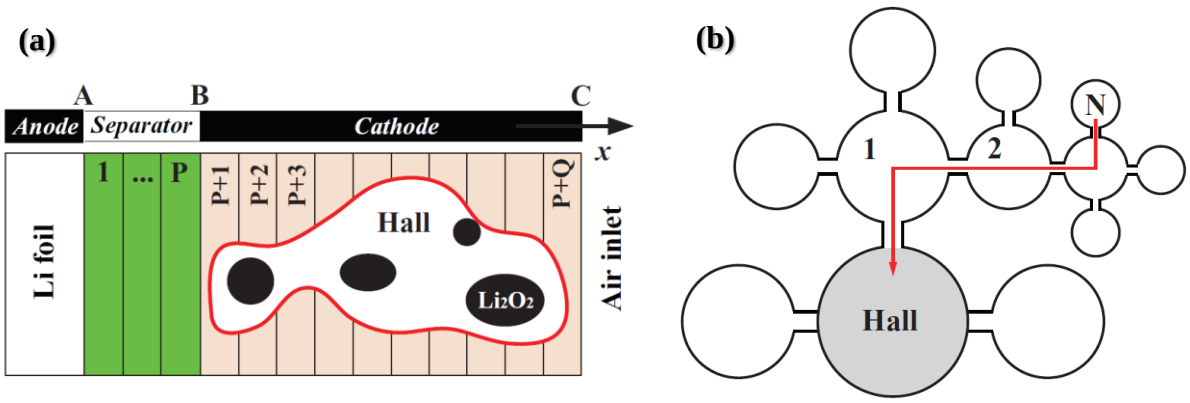

Figure 1: Illustration of the treatment of the cell structure by the model (a), showing the separator and cathode being split into bins and factoring in the hall in the cathode. The interconnecting pore structures leading off of the hall, denoted by increasing class numbers corresponding to decreasing pore radii, are illustrated in (b). Images from [14].

from the smaller pores to the hall in order for solution-phase nucleation to take place. This process has been modelled as an exponential function:

$$\chi(r) = \xi^{\frac{r_{max}-r}{r_{max}}} \tag{1}$$

where $\chi(r)$ is the escape function of a pore of radius r, and ξ is the escape probability. The latter defines the propensity of the $O_2^{\bullet-}$ radicals to migrate to a pore of larger diameter, as depicted in Figure 2, based on the donor number of the solvent and the discharge current of the cell. Since $\chi(r)$ is related to the likelihood of an $O_2^{\bullet-}$ radical forming Li_2O_2 in solution, it is assumed that all remaining $O_2^{\bullet-}$ radicals form Li_2O_2 on the cathode walls, such that:

$$O_2 + 2Li^+ + 2e^- \rightarrow \left[\frac{\chi(r)}{2-\chi(r)}\right] Li_2O_{2(sol-phase)} + 2\left[\frac{1-\chi(r)}{2-\chi(r)}\right] Li_2O_{2(surface)} \tag{2}$$

The value of ξ lies in the region of $0 \leq \xi \leq 1$, and is dependent on the donor number of the solvent and the discharge current of the cell. A high donor number encourages the $O_2^{\bullet-}$ radicals to detach from the pore wall and diffuse into the electrolyte, where two such molecules each react with Li^+ to form LiO_2 and then subsequently disproportionate to form Li_2O_2. This frees up reaction sites, allowing the discharge reaction to continue [2]. A lower discharge current

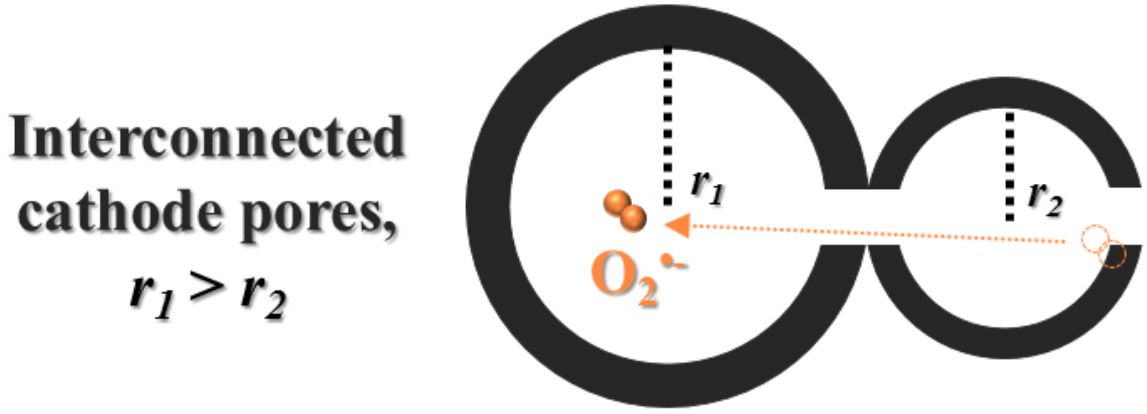

Figure 2: Illustration of the mechanism upon which the escape probability, ξ, is based.

gives $O_2^{\bullet-}$ more time to diffuse into the electrolyte due to the lower rate at which Li^+ ions migrate to the cathode surface and react with $O_2^{\bullet-}$ to form LiO_2 on the pore walls. In such scenarios, ξ tends to 1. Conversely, a low donor number hinders the ability of $O_2^{\bullet-}$ radicals to diffuse into the electrolyte, and a high discharge current results in a thick layer of LiO_2 intermediates forming on the pore walls before the $O_2^{\bullet-}$ radicals can detach from the reaction sites. Both of these conditions favour the surface layer growth of Li_2O_2, for which ξ tends to zero, as shown in Figure 3. It must be noted that surface layer Li_2O_2 growth is anticipated to passivate cathode reaction sites rather than completely clog pores, thus allowing the continued migration of $O_2^{\bullet-}$ radicals towards the hall [5]. Unlike some previous models by other groups, electron tunnelling through Li_2O_2 up to a maximum film thickness, at which the film becomes prohibitively insulating, is considered; this thickness is regarded as being in the region of 5 – 10 nm [20].

In order for oxygen transport within the cathode to be modelled, the concentration *C* and diffusion coefficient *D* of oxygen within the solvent in question must be known; the experimental procedure to obtain these values is outlined in Section 4.3.2. Oxygen transport is modelling using the formula:

$$\frac{\partial}{\partial t}[(1-s)\varepsilon_0 C] = \frac{\partial}{\partial x}\left[(1-s)^{1.5}{\varepsilon_0}^{1.5} D\left(\frac{\partial C}{\partial x}\right)\right] - \frac{a j_{Far}}{nF} \quad (3)$$

where ε_0 is the initial porosity; *a* is the specific surface area; j_{Far} is the Faradic current density; *n* is the number of electrons involved in the discharge reaction, which is 2 for Li-air; *F* is the Faraday constant and *s* is the saturation of the pore. The latter factors in the reduction in pore volume as the surface is passivated by Li_2O_2, and is calculated by the model, thus:

$$\varepsilon = (1-s)\varepsilon_0 \quad (4)$$

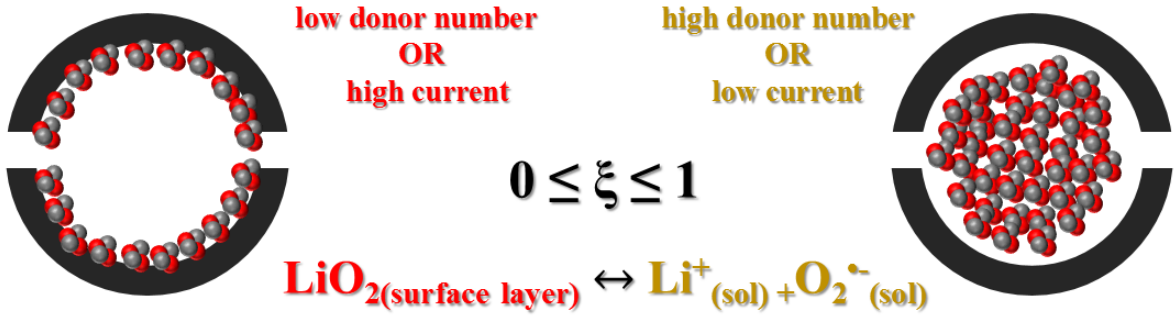

Figure 3: Illustration of the dependency of the escape probability ξ on the solvent donor number and discharge current of the cell.

where ε is the real-time porosity. Saturation is calculated by the model at bin level by monitoring the build-up of Li_2O_2 during discharge. The amount of Li_2O_2 produced, in conjunction with the known density of the discharge product, allows the saturation to be calculated thus:

$$s^{[i]}(t) = \frac{M_{Li_2O_2}}{\varepsilon_0 n F \rho_{Li_2O_2}} \int_0^t a^{[i]}(t') j_{Far}^{[i]}(t') dt' \tag{5}$$

where ρ and M represent the density and molar mass of Li_2O_2, respectively, and the superscript $[i]$ denotes the bin that is under consideration.

As the cell discharges, the active surface area of the pores is reduced by an increasing thickness of Li_2O_2 on the pore walls. This serves to reduce the volume of the pore, and thus the number of reaction sites, and also electrically passivates the pore walls. This is factored into the model using the following formula:

$$a_{[j]}^{[i]}(t) = \frac{A_{[j]}^{[i]}(t)}{V} = a_0 \left[\frac{r_{[j]} - \delta_{[j]}^{[i]}(t)}{r_{[j]}}\right]^2 \left\{\frac{1 - \mathrm{erf}\left[\delta_{[j]}^{[i]}(t) - 7\right]}{2}\right\} \times \left\{\frac{\alpha_0(r_{[j]})}{\sum_{j'} \alpha_0(r_{[j']})}\right\} \tag{6}$$

where $a_{[j]}^{[i]}(t)$ is the real-time specific surface area for pore class [j] bin [i]; $A_{[j]}^{[i]}(t)$ is the total active surface area in volume V; δ is the Li_2O_2 film thickness; a_0 is the initial specific surface area; α_0 is the surface area distribution function obtained from the PSD; and r is the pore radius. To calculate δ, it is noted that the Li_2O_2 film thickness is non-uniform and is dependent on the pore radius and thus the escape function (Equation (1)), whilst the Faradic current density is assumed to be uniformly distributed across all of the active surface area in a particular bin i according to the Butler-Volmer equation:

$$j_{Far} = nFkC\left\{\exp\left(-\frac{\beta F\eta}{RT}\right) - \exp\left(\frac{(1-\beta)F\eta}{RT}\right)\right\} \tag{7}$$

where k is the kinetic rate constant; β is the charge transfer coefficient; T is the temperature; R is the universal gas constant; and η is the Butler-Volmer overpotential. Therefore, the evolution of δ is calculated by the model using the formula:

$$\frac{d\delta_{[j]}^{[i]}(t)}{dt} = 10^9 \times \left(\frac{2M_{Li_2O_2}}{nF\rho_{Li_2O_2}}\right)\left[\frac{1-\chi(r_{[j]})}{2-\chi(r_{[j]})}\right] j_{Far}^{[i]}(t) \tag{8}$$

where 10^9 converts the units from m to nm.

Finally, to calculate the cell potential using the model, it is firstly acknowledged that the cathodic solid phase potential is uniform due to the high conductivity of the carbon materials, whilst the electrolyte phase potential undergoes minimal variation due to the low C-rate of Li-air cells. As such, the Butler-Volmer overpotential, η, is homogeneous, and can be determined from Equation (7) by summing the Faradic currents in all of the bins. By assuming that the charge transfer coefficient β of the cell is 0.5, and factoring in series resistance from the

electrolyte and anode overpotential, R_S, and resistance from the Li_2O_2 surface layer, R_{film}, the cell potential E is calculated using the formula:

$$E = E_0 - \frac{2RT}{F}\sinh^{-1}\left(\frac{J}{\sum_i 2na_i\Delta xFkC}\right) - JR_S - JR_{film} \quad (9)$$

where E_0 is the equilibrium cell voltage, defined as 2.86 V; R is the universal gas constant; T is the temperature; Δx represents the width of a bin (10 μm). R_{film} is approximated to:

$$R_{film} = \frac{\varrho\delta}{a_0\Delta x} \quad (10)$$

where the Li_2O_2 resistivity ϱ is fitted to the experimental discharge curves, along with R_S. The film thickness δ considered here is for the largest pores in the bin closest to the air inlet on the outer edge of the cathode. A block diagram of the model, highlighting the measured inputs, fitted parameters and modelled output, is provided in Figure 4.

It can be seen from Equation (3) that the model is linearly dependent on the concentration and diffusion coefficient of oxygen in the electrolyte; likewise for the former in the Butler-Volmer equation (7). These two values are obtained electrochemically (Section 4.3.2) using a potentiostat that can provide current and potential measurements to within a resolution of 76 fA and 5 μV, respectively. The former is six orders of magnitude smaller than the typical current magnitudes encountered in the obtaining of these values, thus ensuring negligible measurement error arising from the resolution of the apparatus. Dependency on the cathode porosity is multiplied to the power of 1.5 due to the Bruggeman-style correction in order to account for the porous structure of the cathode, thus placing emphasis on the use of a porosimeter to obtain an accurate value for this parameter. Equation (6) shows that the

simulation of real-time cathode surface area has linear dependencies on both the initial specific surface area and surface area distribution function, whilst Equation (10) indicates that the thin film resistance calculations have an inverse relationship with the former. Both of these values are obtained via BET analysis (Section 4.3.3).

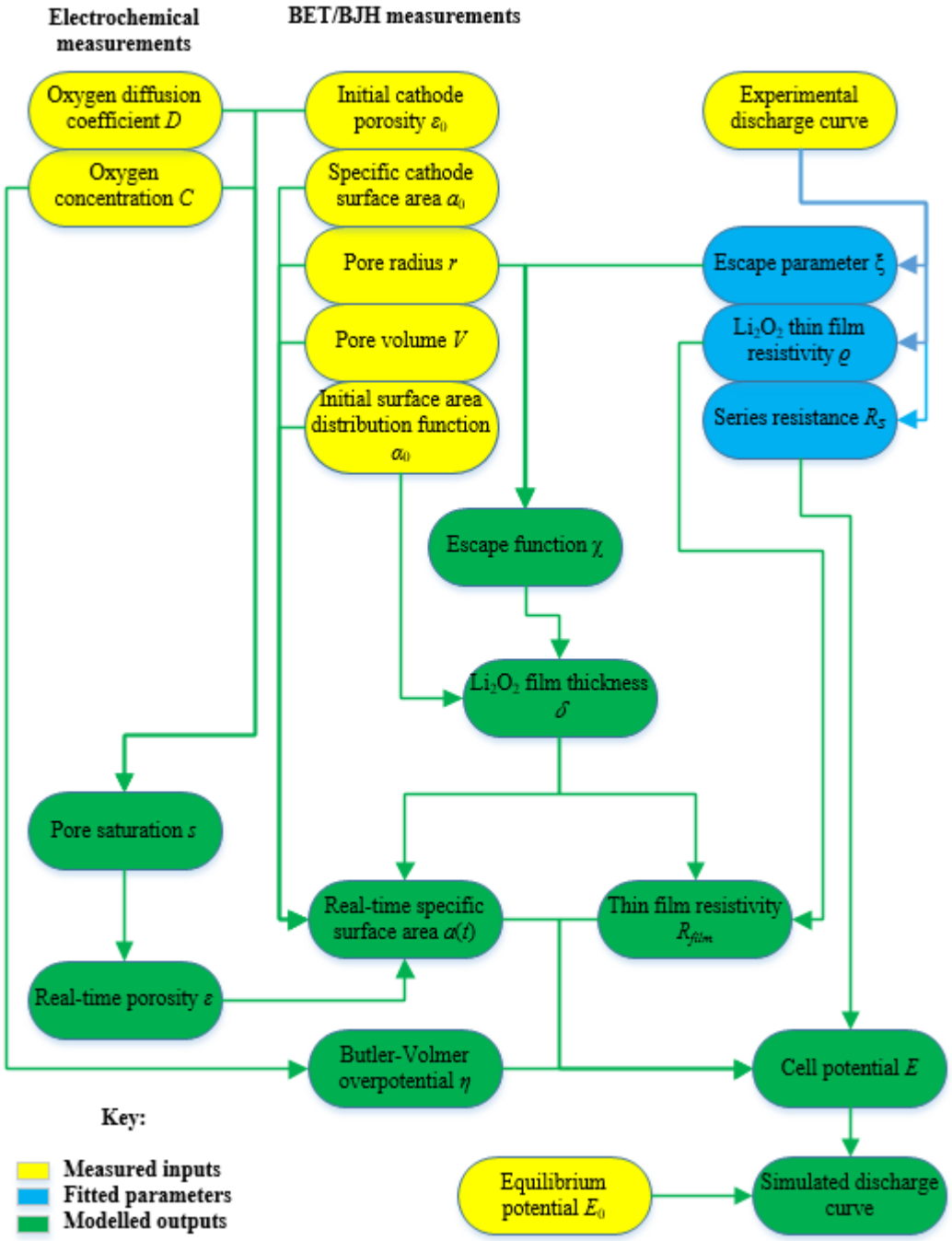

Figure 4: Block diagram of the Li-air model showing which parameters are fitted to, and what modelled output is calculated from, experimental data.

4.3 Discharging and parameterising real cells

The key new feature offered by the developed model is its ability to estimate the amount of surface layer deposition and solution-phase growth of Li_2O_2 that occurs in a cell based on its chemistry and the current density. Therefore, to test this aspect of the model, discharge data must be obtained from real, fully parameterised Li-air cells, employing solvents with different donor numbers that favour either surface layer or solution-phase Li_2O_2 growth. This data will then be juxtaposed against the predicted performance of those cells from the model. Dimethyl sulfoxide (DMSO) and tetraethylene glycol dimethyl ether (TEGDME) were chosen for this study due to the high donor number of the former (29.8 kcal mol^{-1}), which lends itself to the solution-phase discharge reaction, and the medium donor number of the latter (16.6 kcal mol^{-1}), which encourages a mixture of surface growth and solution-phase nucleation of Li_2O_2 to take place. The model also requires the thickness, specific surface area a_0 and pore size distribution (PSD) of the cathode, plus the bulk concentration C and diffusion coefficient D of oxygen in each solvent, to be known in advance, all of which must be obtained experimentally.

4.3.1 Cell cycling

Swagelok cell components were fabricated and assembled as described in Chapter 3. Each solvent was made into an electrolyte solution with 0.5 M lithium bis-trifluoromethanesulfonimidate (LiTFSI). The thickness of the cathodes and separators were measured with a calliper prior to assembly and found to be 100 µm and 840 µm, respectively. An average cathode area of 0.5 cm^2 was used in the corresponding model simulations, from which a cathode volume of 5×10^{-9} m^3 was obtained for the conversion of a_0 from m^2 g^{-1} to m^{-1}. Cells were discharged at one of three pre-determined current densities:

2 A m^{-2}, 4 A m^{-2} and 10 A m^{-2}, to compare the accuracy of the model under increasing loads and thus decreasing likelihood of solution-phase lithium peroxide formation. All measured parameters were applied to the model, in addition to the PSD (see Section 4.3.3). The model then simulated the first discharge of each cell at the aforementioned current densities.

4.3.2 Experimentally obtaining the oxygen diffusion coefficient and bulk concentration in the electrolytes

As explained in Chapter 2, the Cottrell equation can be used to calculate the values of oxygen concentration *C* and diffusion coefficient *D* in an electrolyte with respect to the time-dependent current I_t:

$$I_t = \frac{nFC\sqrt{D}A}{\sqrt{\pi t}} \tag{11}$$

The Cottrell equation requires the surface area of the working electrode (WE), *A*, to be known when calculating these parameters. Therefore, the surface area of the glassy carbon WE used for the proceeding experiments was measured in advance using cyclic voltammetry (CV) with a sweep rate of 10 mV s^{-1} as described in Chapter 2. The peak current I_P was found from the resultant plot to be 5.48 × 10^{-6} A. This was inserted into the Randles-Sevcik equation along with all known parameters (Equation (12)):

$$I_P = 2.69 \times 10^5 n^{\frac{3}{2}} C D^{\frac{1}{2}} v^{\frac{1}{2}} A \tag{12}$$

from which the surface area of the electrode was found to be 7.29 × 10^{-6} m^2.

The cell was then set up to obtain the time-dependent current, I_t, for O_2-saturated TEGDME with 0.5 M tetrabutylammonium bis-trifluoromethanesulfonimidate (TBATFSI), *via* the Cottrell method. Prior to running the experiments, the solvents were distilled as described in Chapter 2, whilst TBATFSI salt was dried at 80 °C for 24 hours under vacuum in a Buchi oven. TBATFSI was chosen because it has the same anion as the LiTFSI salt used for the Swagelok Li-air cells discharged as part of this study, but contains the molecular cation TBA. This cation is known to facilitate the reversible one-electron reduction of O_2, the products of which are soluble in organic electrolyte, unlike those of Li^+, which deposit on and passivate the surface of the WE.

The cell then underwent CV at 100 mV s^{-1} to identify the point at which the oxygen reduction reaction (ORR) takes place under diffusion control. As shown in Figure 5(a), this was found to be -1.6 V. This was used for the procedure to obtain the time-dependent current, I_t, *via* chronoamperometry (Figure 5(b)) as described in Chapter 2. The gradient, *m*, of the trendline for the resultant Cottrell plot (Figure 5(c)) was found to be 7.96×10^{-5} A. Given that *m* is equal to $I/t^{-1/2}$, this means that the Cottrell equation may be rewritten as:

$$m = \frac{nFC\sqrt{D}A}{\sqrt{\pi}} \tag{13}$$

As explained in Chapter 2, a further experiment must be conducted that allows *C* and *D* to be determined by simultaneously solving with another equation that considers these parameters. This can be achieved in a number of ways, which in turn affects the choice of the second simultaneous equation. The Rotating Disk Electrode (RDE) method, described in full in Chapter 2, was used in this study for TEGDME. Aside from swapping the WE for the RDE, all other cell components, electrolyte and working gas remained identical to the

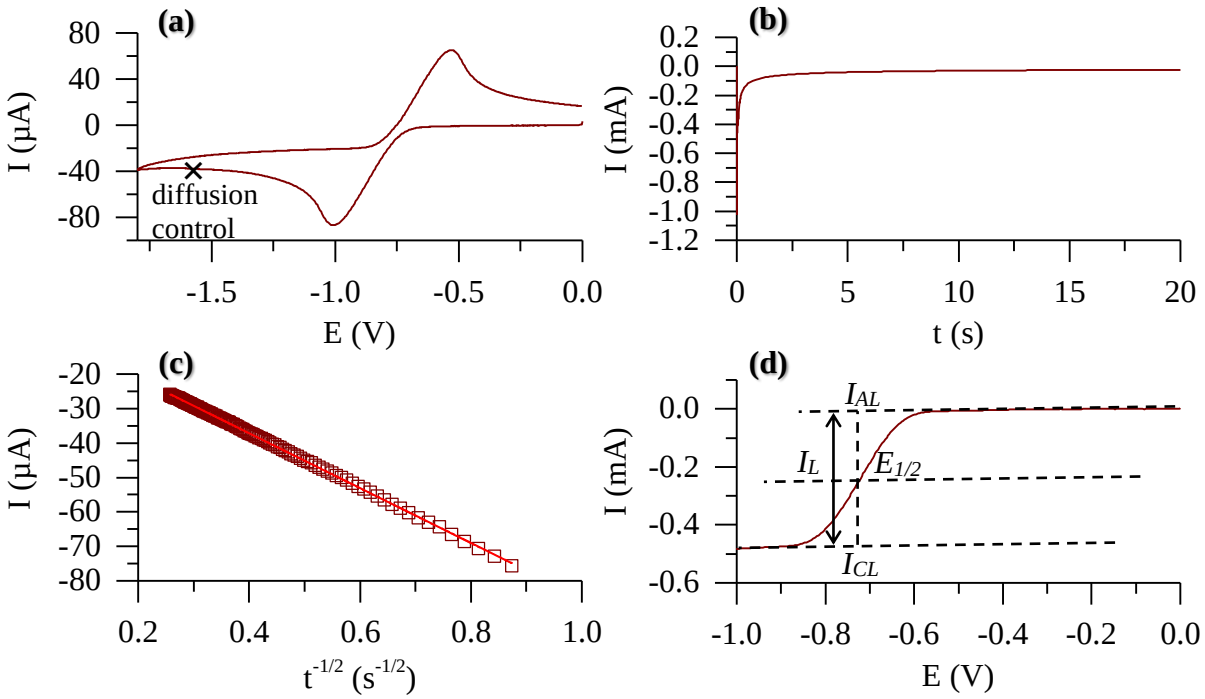

Figure 5: Electrochemical procedures to obtain the values required to calculate the oxygen diffusion coefficient of TEGDME. The CV (a), potential hold (b), Cottrell (c) and RDE (d) plots are shown.

chronoamperometry experiment. Wave analysis grids have been added to the plateaus of the RDE plot in Figure 5(d) to compensate for the resistance of the system when obtaining the Levich current; in a system with zero resistance, the plateaus either side of the current increase would be completely flat, thus allowing I_L to be read directly off of the plot. The top and bottom lines are based on the first and last 20 % of data points, respectively, and fitted by linear regression; the central line is the median between these linear regressions. A vertical intercept is drawn at $E_{1/2}$, which is the potential of the plot where it intercepts the median line. The values at which the vertical line intercepts the top and bottom linear regressions are the limiting anodic (I_{AL}) and cathodic (I_{CL}) currents, respectively. The Levich current is accurately determined by subtracting I_{AL} and I_{CL}, and is found to be 0.47 mA. This value is then substituted into the Levich equation:

$$I_L = 0.62nFAD^{\frac{2}{3}}\omega^{\frac{1}{2}}\nu^{-\frac{1}{6}}C \qquad (14)$$

A value of 4.1×10^{-6} m^2 s^{-1} was used for v, as obtained from the literature [21].

Equations (11) and (14) were then solved simultaneously for D by substituting the constants k_c for known values of the Cottrell equation and k_L for the known values of the Levich equation such that:

$$D = \left(\frac{I_L k_C}{k_L m}\right)^6 \tag{15}$$

from which D is found to be 1.06×10^{-9} m^2 s^{-1}. C may be calculated by substituting in D in Equations (11) or (14). Both equations confirm that C is 6.16 mM in TEGDME.

The procedure to obtain I_t for DMSO was identical to that of TEGDME. As shown in Figure 6(a), a potential of -1 V was found to correspond to the cell being under diffusion control during the CV. The cell was held at this potential (Figure 6(b)) and a plot of the resultant current *vs.* the inverse square root of time (Figure 6(c)) yielded a gradient of 4.08×10^{-5} A.

The ultramicroelectrode (UME) experiment (see Chapter 2) was used to provide the second set of values required to calculate C and D for DMSO. Firstly, the radius of the UME was calculated to be 1.02×10^{-8} m based on a steady-state current (I_{SS}) of 3.06×10^{-9} A extracted from the sigmoidal plot obtained from an anodic sweep of the electrode as described in Chapter 2.

The UME experiment was then conducted with DMSO at 10 mV s^{-1}, yielding an I_{SS} of 2.26×10^{-8} A (Figure 6(d)). By inserting this into the equation for the I_{SS} of the UME:

$$I_{SS} = 4nFDCr \tag{16}$$

And solving simultaneously for D with Equation (11) by substiting in the constant k_U for all known values of Equation (16) such that:

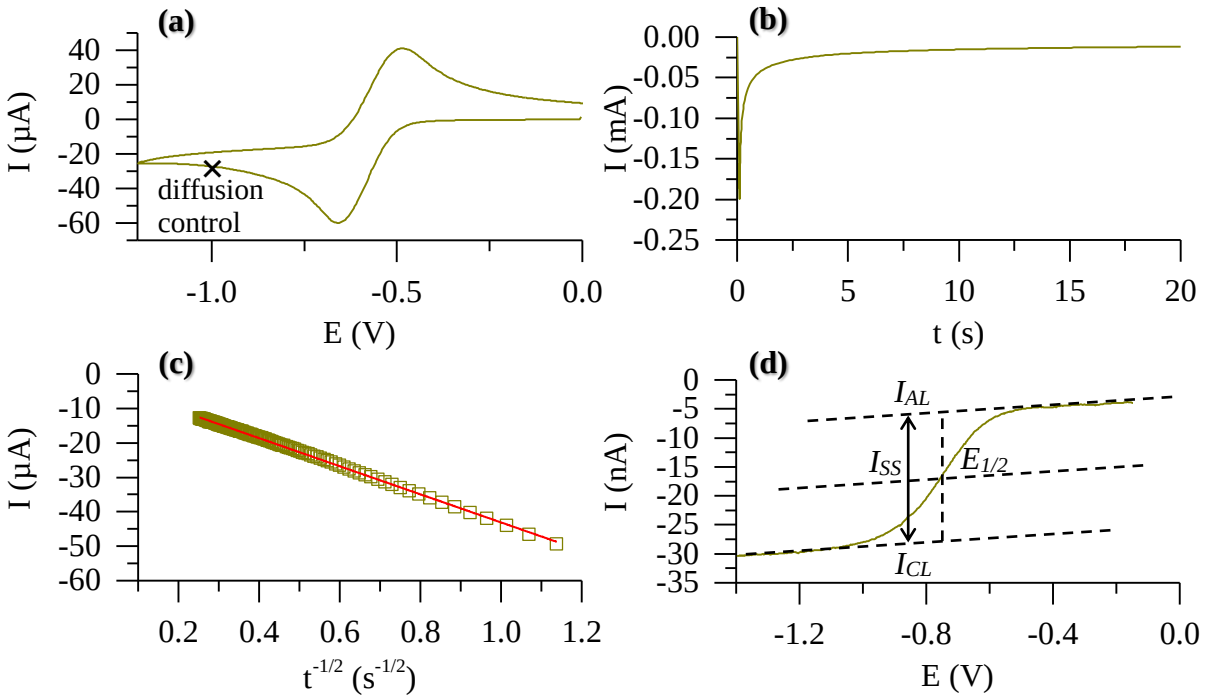

Figure 6: Electrochemical procedures to obtain the values required to calculate the oxygen diffusion coefficient of DMSO. The CV (a), potential hold (b), Cottrell (c) and UME steady-state current (d) plots are shown.

$$D = \left(\frac{I_{SS} k_C}{k_U m}\right)^2 \tag{17}$$

an oxygen diffusion coefficient of 3.16×10^{-9} m^2 s^{-1} was obtained for DMSO. C was then calculated to be 1.83 mM.

Although the initial bulk concentration of O_2 will be higher in cells with TEGDME electrolyte than in those with DMSO, the higher diffusion coefficient of DMSO will allow O_2 to migrate to the reaction sites faster than in TEGDME, thus sustaining a faster discharge reaction. It is also anticipated that the higher solvent donor number of DMSO will facilitate a greater proportion of solution-phase growth of Li_2O_2, which will free up reaction sites and allow greater discharge capacities to be achieved compared to solvents with lower donor numbers, especially at lower current densities. At higher current densities, discharge capacities for cells

using either electrolyte are expected to decrease due to the accumulation of intermediate species on the reaction sites.

4.3.3 Obtaining the pore size distribution (PSD)

The PSD of the cathode is required to factor the distribution of the total surface area, and thus reaction sites, across the various pore size classes into the model. This takes into account the number of pores of a given diameter, up to 150 nm, but excludes the hall as this is considered to be > 150 nm. The distribution of pore sizes will impact on the ability of $O_2^{\bullet-}$ radicals in solution to drift into successively larger pores and eventually reach the hall, without encountering blocked pathways due to excessive build-up of surface layer Li_2O_2.

The PSD of a known mass of cathode material was determined by Brunauer–Emmett–Teller (BET) analysis on a Micromeritics TriStar II 3020 surface area and porosity analyser using nitrogen at 77 K, as described in Chapter 2. The BJH desorption differential pore area profile of the cathode material is shown in Figure 7(a), which indicates that the majority of the pores have radii in the region of 2 – 3 nm. The cathode pore radius profile for the model (Figure 7(b)) was subsequently based on this. Assuming that pores are connected in linearly

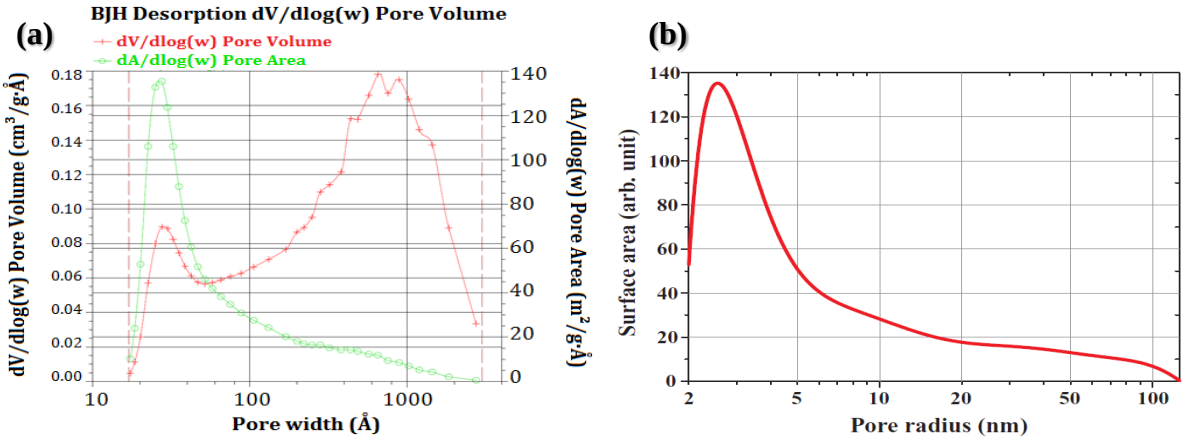

Figure 7: BJH differential pore area profile (a), upon which the pore radius profile for the cell model (b) is based.

ascending order of class from the hall (N = 1 → N = 2 → N = 3 *etc.*), where each increment in class number represents a decrease in pore radius, then several pores of the highest class number will be connected to each pore of the sequentially lower class. As such, the concentration of $O_2^{\bullet-}$ radicals in these lower class pores will be high during discharge.

A value of 66 $m^2\ g^{-1}$ for the specific surface area, a_0, of the Super P Li cathode was obtained from the BET summary report and converted to $1.98 \times 10^7\ m^{-1}$ by factoring in the density of the cathode based on its volume and the mass of Super P Li active material (1.5 mg).

4.4 Comparison of model and real cell cycling data

The above cathode and electrolyte parameters were input into the model, which then simulated cells discharging at the aforementioned current densities. As shown in Figure 8, the simulated cell performance at 2 A m^{-2} is in excellent agreement with the performance of the real cells for both electrolyte solutions used, yielding predicted capacities within *circa* 50 mAh g^{-1}, or 2.4 %, of real cells. This compares to a discretion of 200 mAh g^{-1}, or 20 % of capacity, in

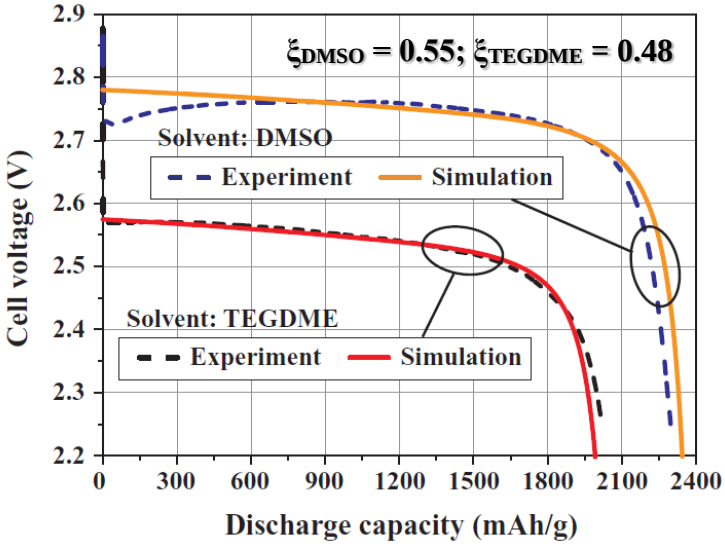

Figure 8: Discharge profiles for experimental and simulated cells based on TEGDME and DMSO electrolytes at 2 A m^{-2} active material. Values for the escape probability of $O_2^{\bullet-}$ are provided. All potentials are vs. Li/Li^+. Image reproduced from [14].

Sandhu's model [4] when simulating a current density of 1 A m^{-2}; an underestimation of specific capacity at 2 A cm^{-2} by 650 mAh g^{-1} (65 %) by the model developed by Andrei *et al.* [22]; and an underestimation of 5 % by the recently developed island-growth model by Jung *et al.* [23], all of which are compared to real cell data from Read [18] for cells with PC:DME electrolyte. Additionally, they are all one-dimensional models that do not factor in the solution-phase Li_2O_2 growth mechanism. The model developed by Chen *et al.*, which was based on a cell with TEGDME electrolyte but a carbon nanofiber cathode, overestimated the discharge capacity by 2.9 % (40 mAh g^{-1}) at the same current density considered here; it is worth noting that only cylindrical surface layer growth of Li_2O_2 was modelled by Chen [24]. Furthermore, our model managed to accurately simulate the exponential increase in resistance caused by the formation of a passivating layer of discharge products on the surface of the cathode pores, as evidenced by the sudden drop-off in potential towards the end of discharge. Conversely, the physical model of Albertus *et al.* [5] consistently estimated a shallower discharge curve than the comparable real cells despite factoring in changes in resistance observed on a flat glassy carbon electrode in an electrochemical cell. As predicted, the escape parameter ξ is higher for DMSO (0.55) than it is for TEGDME (0.48) since the former has a higher donor number and thus facilitates a greater proportion of solution-phase Li_2O_2 nucleation. The consequent decrease in passivation of available reaction sites allows for greater discharge capacity of the cell, both of which were simulated with great accuracy by our model. The discrepancy between the initial potentials of the experimental and simulated curves stems from the omission of the $t = 0$ case for the latter. As mentioned in Section 4.2, the model does take into account the equilibrium potential, E_0, of the cell, but since t = 0 has been omitted from the simulated curve, the cell potential immediately factors in the resistive losses occurred under load as described in Equation (9). The same applies for subsequent plots.

At 4 A m^{-2}, the model once again accurately simulates the discharge potential curve and capacity of the cell for both solvents (Figure 9), predicting discharge capacities to within 40 mAh g^{-1}, or 2.4 %, of the capacity of the real cell. The current density considered here is closest to the highest density considered by Sandhu *et al.* [4] for their whole cell model, which predicted a discharge capacity of approximately 120 mAh g^{-1}, or 42.9 %, less than the equivalent real cell at 5 A m^{-2}.

As discussed earlier, ξ decreases with increasing current since the $O_2^{\bullet-}$ radicals have less opportunity to drift away from the pore walls, thus leading to increased surface layer Li_2O_2 growth. Consequently, the values of ξ at this current density are reduced to 0.44 for DMSO and 0.4 for TEGDME, and the discharge capacities are reduced due to the faster termination of reaction sites.

Both discharge curves have lower potentials at 4 A m^{-2} than at 2 A m^{-2}. This can be explained using the Butler-Volmer equation, which relates the current to the overpotential of the cell (Equation (7)). As the current density is increased, the overpotential of the cell η also increases,

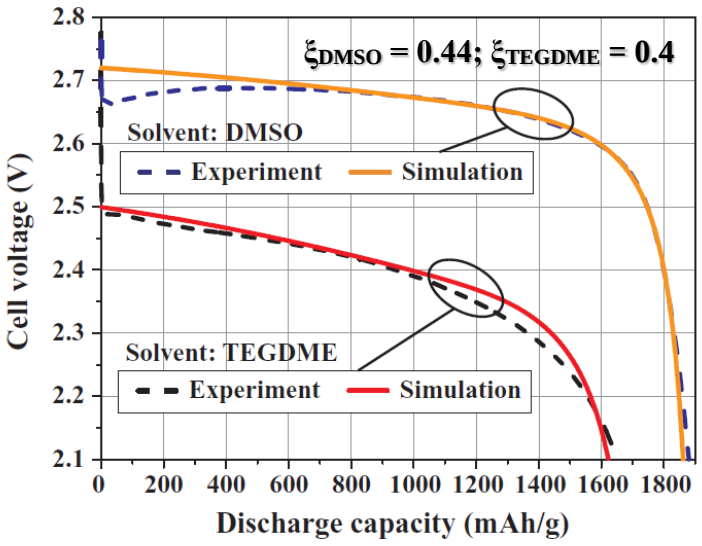

Figure 9: Discharge profiles for experimental and simulated cells based on TEGDME and DMSO electrolytes at 4 A m^{-2} active material. Values for the escape probability of $O_2^{\bullet-}$ are provided. All potentials are vs. Li/Li^+. Image reproduced from [14].

which serves to lower the potential of the cell. Additionally, as a thick surface layer of Li_2O_2 begins to form during discharge, the resistance of this passivating layer increases, as does the overpotential required to overcome it, which further reduces the cell potential.

The model failed to accurately simulate real cell performance at 10 A m^{-2}, as can be seen in Figure 10. Although the simulations started at the correct potentials and closely mapped the initial 30 % and 50 % of the real TEGDME and DMSO discharge curves, respectively, the model predicted that the DMSO cell would yield an 8 % greater capacity than was experimentally observed, and the TEGDME cell a 73 % improvement on the observed capacity. This was despite setting ξ to zero and thus assuming that 100 % of Li_2O_2 formed as a thin film on the reaction sites, with no solution-phase Li_2O_2 present in the cells. The failure of the real cells to meet or exceed the predicted discharge capacities indicates that Li_2O_2 must have formed exclusively as a surface layer in reality. However, it is clear from the discrepancy between the real and simulated results that the model has omitted at least one crucial parameter that becomes a limiting factor at higher current densities.

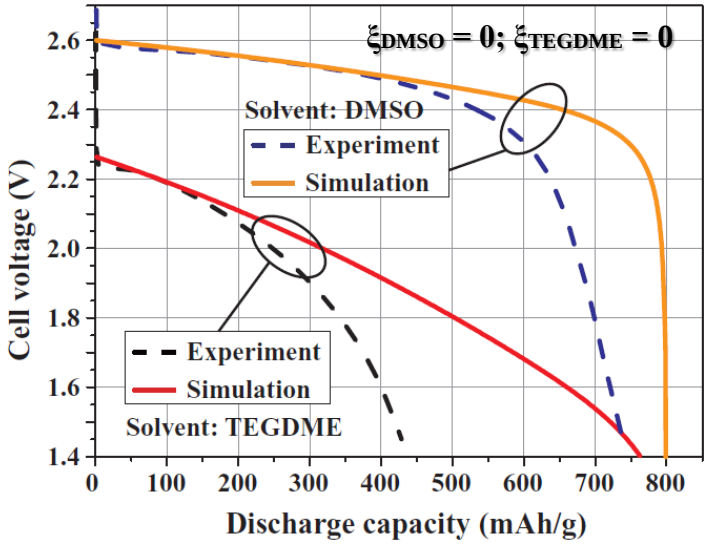

Figure 10: Discharge profiles for experimental and simulated cells based on TEGDME and DMSO electrolytes at 10 A m^{-2} active material. All potentials are vs. Li/Li^+. $\xi = 0$ for both solvents. Image reproduced from [14].

One such parameter is electrolyte decomposition mechanisms. Whilst minimal decomposition of the electrolyte would be expected upon the first discharge of a cell, the cells cycled at 10 A m^{-2} were deliberately cycled to the exceptionally low potential of 1.4 V *vs.* Li/Li^+. This was in order to compensate for the large overpotential arising from high resistance due to comparatively poor mass transport at high current densities. Lowering the potential this far could push the electrolytes beyond their stability window and cause them to be reduced to decomposition products, which will impact on the discharge mechanisms taking place in the cell. As such, we shall consider the data for discharge down to 2.0 V *vs.* Li/Li^+ as a safe lower potential limit at which no electrolyte reduction is expected to occur, as used by Read when discharging cells with Super P/PTFE cathodes and PC:DME electrolyte at current densities of up to 10 A m^{-2} [18]. In this case, the over-prediction of discharge capacities by the model is decreased to 28 % for TEGDME, but increased to 17 % for DMSO. Therefore, another important parameter must be missing from the model. This is thought to be the Li^+ diffusion coefficient since Li^+ has to travel a greater distance through the separator to reach the reaction sites than O_2; in the cell design used for this study, the minimum distance for the former is 840 µm compared to a maximum distance of 100 µm for the latter.

Read's data for cells with PC:DME electrolyte [18] was used by Andrei *et al.* to verify their own Li-air cell model, although their lower potential limit was 2.3 V *vs.* Li/Li^+ [22]. As shown in Figure 10, the overpotential of our cells with TEGDME electrolyte at 10 A m^{-2} resulted in their potentials dropping to 2.25 V immediately upon discharge, therefore ruling out the ability to use 2.3 V as the lower potential limit. However, the overpotential of cells with DMSO electrolyte is considerably lower and thus allows the 2.3 V cut-off to be used to compare our model to Andrei's [22].

Andrei's model [22] was found to underestimate the discharge capacity of Read's cell [18] by 100 %. Conversely, at 2.3 V, our developed multiscale model is found to overestimate the

discharge capacity of the cell by 25 %, thus representing a 4-fold increase in the accuracy of the model at high currents, when considering capacity only. It is worth noting that, whilst our model does not factor in Li^+ diffusion in the electrolyte, Andrei's model does, using the theory of concentrated solutions [22, 25]. These results suggest that a new multiscale model that considers both the Li^+ diffusion coefficient of the electrolyte and solution-phase growth of Li_2O_2 could yield further improvements in the accuracy with which the discharge capacity of cells can be predicted at high current densities.

4.5 Conclusions and further work

By taking into account the newly-discovered solution-phase Li_2O_2 growth mechanism, the lithium-air cell model created in this study is capable of predicting real cell discharge behaviour to a greater degree of accuracy than previous models, at low current densities. The solvent and cell component parameters required for the model are either readily available in the literature or may be measured in the lab. This will allow solvents to be rapidly screened for their suitability as an electrolyte for lithium-air cells, thus moving away from the trial and error approach that has dominated this field until recently [18, 26, 27, 28, 29, 30].

An additional feature of the model is that it can be used to reverse-engineer the optimum cathode structure for maximum capacity. This can be achieved by adjusting cathode parameters such as thickness, specific surface area/concentration of reaction sites and the pore radius profile, keeping all other cell and discharge parameters identical, and running a series of simulations until the maximum discharge capacity is observed. Maximising the porosity of the cathode at the air interface and minimising the extent to which the current collector impedes O_2 ingress are prime examples of methods by which to increase discharge capacity [7]. Once the optimum structure has been determined, it can then be fabricated from suitable materials in

the lab using the most appropriate procedure, such as 3D printing. Further reverse-engineering could be used to investigate ways to alleviate the oxygen transport limitations of the electrolyte, for example by increasing the O_2 partial pressure of the system or including gas injection infrastructure within the cathode; the advantages of overcoming O_2 transport limits have been demonstrated in the lab by Yang *et al.* [31], and using a physical model by Albertus *et al.* [5].

The primary limitation of the model is that it loses accuracy at high current densities. This is believed to be caused by not accounting for the Li^+ diffusion coefficient of the solvent. Whilst this had previously not been considered a limiting factor due to the greater initial concentration of Li^+ in the electrolyte compared to O_2 [20], it is known that the mobility of the Li^+ cation in an organic electrolyte is less than that of a typical anion owing to the stronger solvation and greater Stoke's radius of the former; this has already been identified as a rate-limiting factor of conventional Li-ion cells [32]. Work to rectify this will involve cataloguing the Li^+ diffusion coefficients of commonly-used solvents and adding a D_{Li+} function to the model. It is expected that, as the current density increases, it will reach a crossover point where D_{Li+} becomes more influential than the donor number in yielding greater capacity retention.

This study only considers the first discharge of a fresh Li-air cell. Once the above considerations have been factored into the model and accurate simulations can be achieved at high current densities, attention should shift to modelling the charging and subsequent cycling of the cell, as well as decomposition mechanisms encountered during cycling. The limitations of the present model will become increasingly apparent with unstable electrolyte and cathode combinations, which build up irreversible decomposition salts on the cathode over successive discharges rather than purely forming reversible Li_2O_2. Modelling these decomposition mechanisms will likely take considerable effort and will require verification by post-mortem analysis of real cells using XRD and FTIR; *in-situ* analysis using differential electrochemical mass spectrometry (DEMS) may also be beneficial.

4.6 References

[1] A. A. Franco and K.-H. Xue, "Carbon-Based Electrodes for Lithium Air Batteries: Scientific and Technological Challenges from a Modeling Perspective," *ECS J. Solid State Sci. Technol.*, vol. 2, no. 10, pp. M3084 - M3100, 2013.

[2] L. Johnson, C. Li, Z. Liu, Y. Chen, S. A. Freunberger, P. C. Ashok, B. B. Praveen, K. Dholakia, J.-M. Tarascon and P. G. Bruce, "The Role of LiO_2 Solubility in O_2 Reduction in Aprotic Solvents and its Consequences for Li–O_2 Batteries," *Nature Chemistry*, vol. 6, pp. 1091 – 1099, 2014.

[3] B. Horstmann, B. Gallant, R. Mitchell, W. G. Bessler, Y. Shao-Horn and M. Z. Bazant, "Rate-Dependent Morphology of Li_2O_2 Growth in Li–O_2 Batteries," *J. Phys. Chem. Lett.*, vol. 4, no. 24, pp. 4217 – 4222, 2013.

[4] S. Sandhu, J. Fellner and G. Brutchen, "Diffusion-Limited Model for a Lithium/Air Battery with an Organic Electrolyte," *J. Power Sources*, vol. 164, no. 1, pp. 365 – 371, 2007.

[5] P. Albertus, G. Girishkumar, B. McCloskey, R. S. Sánchez-Carrera, B. Kozinsky, J. Christensen and a. A. C. Luntz, "Identifying Capacity Limitations in the Li/Oxygen Battery Using Experiments and Modeling," *J. Electrochem. Soc.*, vol. 158, no. 3, pp. A343 - A351, 2011.

[6] Y. Wang, "Modeling Discharge Deposit Formation and its Effect on Lithium-Air Battery Performance," *Electrochim. Acta*, vol. 75, pp. 239 – 246, 2012.

[7] X. Li and A. Faghri, "Optimization of the Cathode Structure of Lithium-Air Batteries Based on a Two-Dimensional, Transient, Non-Isothermal Model," *J. Electrochem. Soc.*, vol. 159, no. 10, pp. A1747 - A1754, 2012.

[8] V. Y. Nimon, S. J. Visco, L. C. D. Jonghe, Y. M. Volfkovich and D. A. Bograchev, "Modeling and Experimental Study of Porous Carbon Cathodes in Li-O_2 Cells with Non-Aqueous Electrolyte," *ECS Electrochem. Lett.*, vol. 2, no. 4, pp. A33 - A35, 2013.

[9] R. R. Mitchell, B. M. Gallant, Y. Shao-Horn and C. V. Thompson, "Mechanisms of Morphological Evolution of Li_2O_2 Particles During Electrochemical Growth," *J. Phys. Chem. Lett.*, vol. 4, no. 7, pp. 1060 – 1064, 2013.

[10] Y.-C. Lu, D. G. Kwabi, K. P. C. Yao, J. R. Harding, J. Zhou, L. Zuin and Y. Shao-Horn, "The Discharge Rate Capability of Rechargeable Li–O_2 Batteries," *Energy Environ. Sci.*, vol. 4, pp. 2999 - 3007, 2011.

[11] D. Zhai, H.-H. Wang, J. Yang, K. C. Lau, K. Li, K. Amine and L. A. Curtiss, "Disproportionation in Li–O_2 Batteries Based on a Large Surface Area Carbon Cathode," *J. Am. Chem. Soc.*, vol. 135, no. 41, pp. 15364 – 15372, 2013.

[12] V. Bevara and P. Andrei, "Changing the Cathode Microstructure to Improve the Capacity of Li-Air Batteries: Theoretical Predictions," *J. Electrochem. Soc.*, vol. 161, no. 14, pp. A2068 - A2079, 2014.

[13] S. Sekhon, N. Arora and H. P. Singh, "Effect of Donor Number of Solvent on the Conductivity Behaviour of Nonaqueous Proton-Conducting Polymer Gel Electrolytes," *Solid State Ionics*, vol. 160, pp. 301 - 307, 2003.

[14] K.-H. Xue, E. McTurk, L. Johnson, P. G. Bruce and A. J. Franco, "A Comprehensive Model for Non-Aqueous Lithium Air Batteries Involving Different Reaction Mechanisms," *J. Electrochem. Soc.*, vol. 162, no. 4, pp. A614 - A621 , 2015.

[15] A. A. Franco, "Multiscale Modelling and Numerical Simulation of Rechargeable Lithium Ion Batteries: Concepts, Methods and Challenges," *RSC Adv.*, vol. 3, pp. 13027 - 13058, 2013.

[16] M. Mirzaeian and P. J. Hall, "Preparation of Controlled Porosity Carbon Aerogels for Energy Storage in Rechargeable Lithium Oxygen Batteries," *Electrochimica Acta,* vol. 54, no. 28, pp. 7444 – 7451, 2009.

[17] T. Kuboki, T. Okuyama, T. Ohsaki and N. Takami, "Lithium-Air Batteries using Hydrophobic Room Temperature Ionic Liquid Electrolyte," *J. Power Sources,* vol. 146, no. 1 - 2, pp. 766 – 769, 2005.

[18] J. Read, "Characterization of the Lithium/Oxygen Organic Electrolyte Battery," *J. Electrochem. Soc.*, vol. 149, no. 9, pp. A1190 - A1195, 2002.

[19] C. Tran, X.-Q. Yang and D. Qu, "Investigation of the Gas-Diffusion-Electrode used as Lithium/Air Cathode in Non-Aqueous Electrolyte and the Importance of Carbon Material Porosity," *J. Power Sources,* vol. 195, no. 7, pp. 2057 – 2063, 2010.

[20] K.-H. Xue, T.-K. Nguyen and A. A. Franco, "Impact of the Cathode Microstructure on the Discharge Performance of Lithium Air Batteries: A Multiscale Model," *J. Electrochem. Soc.*, vol. 161, no. 8, pp. E3028 - E3035, 2014.

[21] Merck Millipore. *Tetraethylene Glycol Dimethyl Ether Product Specification*. [Online]. Available: http://www.merckmillipore.com/GB/en/product/Tetraethylene-glycol-dimethyl-ether,MDA_CHEM-820959. [Accessed 06 September 2015].

[22] P. Andrei, J. P. Zheng, M. Hendrickson and E. J. Plichta, "Some Possible Approaches for Improving the Energy Density of Li-Air Batteries," *J. Electrochem. Soc.*, vol. 157, no. 12, pp. A1287 - A1295, 2010.

[23] C. Y. Jung, T. S. Zhao and L. An, "Modeling of Lithium-Oxygen Batteries with the Discharge Product Treated as a Discontinuous Deposit Layer," *J. Power Sources,* vol. 273, pp. 440 - 447, 2015.

[24] X. J. Chen, V. V. Bevara, P. Andrei, M. Hendrickson, E. J. Plichta and J. P. Zheng, "Combined Effects of Oxygen Diffusion and Electronic Resistance in Li-Air Batteries with Carbon Nanofiber Cathodes," *J. Electrochem. Soc.*, vol. 161, no. 12, pp. A1877 - A1883, 2014.

[25] J. Newman and K. E. Thomas-Alyea, *Electrochemical Systems, Third Edition*, Hoboken: John Wiley & Sons, 2004, pp. 297 – 314.

[26] J. Read, K. Mutolo, M. Ervin, W. Behl, J. Wolfenstine, A. Driedger and D. Foster, "Oxygen Transport Properties of Organic Electrolytes and Performance of Lithium/Oxygen Battery," *J. Electrochem. Soc.,* vol. 150, no. 10, pp. A1351 - A1356, 2003.

[27] J. Read, "Ether-Based Electrolytes for the Lithium/Oxygen Organic Electrolyte Battery," *J. Electrochem. Soc.*, vol. 153, no. 1, pp. A96 - A100, 2006.

[28] S. A. Freunberger, Y. Chen, N. E. Drewett, L. J. Hardwick, F. Bardé and P. G. Bruce, "The Lithium–Oxygen Battery with Ether-Based Electrolytes," *Angew. Chem. Int. Ed.*, vol. 50, no. 37, pp. 8609 – 8613, 2011.

[29] C. Ó. Laoire, S. Mukerjee, E. J. Plichta, M. A. Hendrickson and K. M. Abraham, "Rechargeable Lithium/TEGDME-$LiPF_6/O_2$ Battery," *J. Electrochem. Soc.*, vol. 158, no. 3, pp. A302 - A308, 2011.

[30] C. O. Laoire, S. Mukerjee and K. M. Abraham, "Influence of Nonaqueous Solvents on the Electrochemistry of Oxygen in the Rechargeable Lithium−Air Battery," *J. Phys. Chem. C*, vol. 114, no. 19, pp. 9178 – 9186, 2010.

[31] X.-h. Yang and Y.-y. Xia, "The Effect of Oxygen Pressures on the Electrochemical Profile of Lithium/Oxygen Battery," *J. Solid State Electr.*, vol. 14, no. 1, pp. 109 - 114, 2010.

[32] M. Winter, J. O. Besenhard, M. E. Spahr and P. Novák, "Insertion Electrode Materials for Rechargeable Lithium Batteries," *Adv. Mater.*, vol. 10, no. 10, pp. 725 - 763, 1998.

5 Modification of commercial lithium-ion pouch cells for long term degradation studies

5.1 Introduction

The role of the battery management system (BMS) in actively preventing lithium-ion cells from being subjected to abuse conditions, which can cause them to degrade or undergo thermal runaway, is crucial in order to maximise their cycle and calendar lives. This is particularly true for applications where the battery pack is one of the most expensive components of the product, such as in the automotive sector. As such, BMS technology found in electric vehicles is more advanced than that found in consumer electronics, with manufacturers regularly offering a warranty on the traction battery pack that covers a period of upwards of five years [1, 2, 3]. Conversely, in a typical laptop computer with a six-cell battery pack in a 3S2P formation (two parallel strings consisting of three cells each) and a crude BMS, the battery will fail within three years due to one of the strings being subjected to more abuse than the other; upon disassembly and testing, it is common to find that 50 % of the cells in a "dead" laptop battery still retain close to their original capacity [4]. Clearly, battery management has rapidly advanced in the automotive sector in comparison to consumer electronics.

Despite this notable progress, today's BMS algorithms and associated hardware, such as thermal management systems, are insufficient to meet both industry and consumer demands. As noted by Dahn *et al.*, whilst the Tesla Model S has demonstrated that conventional Li-ion cells may give an EV a range of hundreds of miles per charge, the cycle life of these cells

remains an area that is in need of improvement to satisfy the automotive sector [5]. Furthermore, the improper thermal management of the battery pack in the Mk1 Nissan LEAF has led to an increased rate of degradation in hot climates, and subsequent consumer backlash [6]. Therefore, there is a need to develop a BMS that can accurately model and predict the failure mechanisms of cells as they age, during a number of cycling conditions, and respond accordingly, e.g. by heating/cooling the pack or reducing the current drain on a particular cell or string thereof, in order to increase the lifespan of the battery pack.

In order to address this issue, an open circuit voltage (OCV) model has been developed that can determine the potential of each electrode from the full cell potential as the cell ages, or is subjected to abuse conditions, to within a root mean square error (RMSE) of 10 mV [7]. As outlined in Chapter 1, Li-ion cells undergo a large number of electrode-specific degradation mechanisms, which negatively impact on the capacity retention of the cell. These may be identified *via* the potential of each electrode, which will alter in the event of the onset of a particular failure mechanism; for example, anodic lithium plating may be observed by the potential of the anode dropping to 0 V *vs.* Li/Li^+. These deviations from the potential of a healthy electrode that has undergone an identical number of cycles can then be fed back to the BMS, which can use the predictive model to confirm that abuse conditions are taking place and then take evasive action. However, in commercial Li-ion cells, such electrode-specific measurements are not possible since the cells are two-electrode systems. Consequently, the only potential that may be obtained is that of the full cell, which equates to the difference between the cathode, or working electrode (WE), and the anode, also known as the counter electrode (CE).

In order to obtain the potential of each electrode in a commercial Li-ion cell *in situ*, a reference electrode (RE) must be inserted into the system, thus providing a stable potential against which that of the WE and CE may be measured independently of each other. Crucially, this procedure

must allow the RE to be brought into close contact with the electrodes in the cell without introducing contaminants such as air or water; without resulting in the removal of part of the active components of the cell, such as electrolyte loss *via* evaporation; and without altering the performance of the cell, such as by changing its internal resistance.

Previous work to insert an RE into commercial Li-ion cells has focussed on the cylindrical 18650 format. Whilst commendable progress has been made towards the creation of a modified 3-electrode commercial cell that is identical in performance to an unmodified cell, this work has often resulted in non-optimal conditions. Some work exposed the cell to a different electrolyte from that originally used in the cell. In addition to reducing the internal resistance of the cell through the increase in the volume of conductive medium between the electrodes, this can also alter the overpotential of the cell due to different side reactions, such as the formation of different materials on the SEI [5, 8, 9]. Complex and invasive drilling procedures used in the RE insertion process risk damaging the electrodes, creating internal short circuits and reducing cycle and calendar life [8, 10, 11]. Others positioned the RE some distance from the WE and CE, which risks a potential drop through the resistance of the electrolyte [9].

With the exception of Tesla, pouch cells are arguably more relevant than 18650 cells to traction battery packs for the automotive industry, not least Nissan, who use pouch cells in the LEAF [12]. Despite this, previous work to create 3-electrode pouch cells has involved fabricating bespoke cells in the lab, thus not facilitating a direct comparison with unmodified commercial Li-ion pouch cells [13, 14]. Therefore, this study set out to develop pouch cell modification techniques that meet the desired criteria outlined above, thus providing real electrode data obtained *in situ* that can be used to experimentally verify the developed OCV model. The accuracy of the *in situ* electrode potential data was assessed by comparing it to half-cells fabricated from electrode materials recovered from a pristine unmodified cell, whilst any

impact on cell performance was evaluated by comparing the discharge capacities of modified and unmodified full cells.

5.2 Experimental procedures

5.2.1 Full cell preparation

Kokam SLPB 533459H4 pouch cells were used for this study. These cells have 740 mAh capacity, conventional graphite anodes and cathode structure comprised of a blend of lithium nickel cobalt oxide (NCO) and lithium cobalt oxide (LCO), as determined by XRD and EDX (Appendix B.1), the methods for which are outlined in Chapter 2.

To improve safety, cells were discharged by CCCP (Constant Current followed by Constant Potential) to E_{min} as specified by the manufacturer's data sheet, and transferred to an argon glove box with H_2O and O_2 content of < 0.1 ppm prior to being modified [15].

5.2.2 Half-cell fabrication

Anode and cathode half-cells were fabricated as 2325 format coin cells (as described and illustrated in Chapter 2) using electrode materials recovered from a discharged full cell. The laminated aluminium pouch of the cell was cut open inside the glove box using a scalpel, and the winding of polymer separator membrane unwound to reveal the concertina-form electrode stack. One cathode and one anode sheet were removed from the cell, and disks of 15 mm diameter cut in them using a hole punch. These disks were then rinsed twice in dimethyl carbonate (DMC) to remove the electrolyte, and dried for 30 minutes at room temperature in the antechamber of the glove box.

Whilst the outer cathode sheets had one-sided substrates, all of the anode sheets were double-sided. This would result in an imbalance of active material between cathode and anode half-cells. Additionally, due to one side of anode active material being pressed up against the metal case of the coin cell, this would result in poorer electrical conductivity at the positive terminal and poorer ionic conductivity to the side of active material facing the case. Therefore, prior to cutting the anode sheet into disks, one side of active material was removed by wiping it with a tissue soaked in *N*-methyl-2-pyrollidone (NMP) to dissolve the binder.

All WEs were weighed prior to being assembled in a half-cell. The mass of active material was determined by subtracting the mass of bare 15 mm diameter disks of substrate (aluminium for the cathodes, copper for the anodes), again stripped of their active materials using NMP, from the weight of the WE. Half-cells were then assembled inside a coin cell with a 15 mm diameter Li foil CE and Whatman glass microfiber separator wetted with LP30 electrolyte (1 M $LiPF_6$ in 1:1 w:w ethylene carbonate (EC) and DMC, BASF).

5.2.3 "Patch" modification method

For the first full cell modification procedure, illustrated in Figure 1, insulated copper cables with banana plugs were soldered to the positive and negative terminals of a discharged pristine pouch cell prior to transferring it into the glove box. Once inside, a 5 mm incision was made in the laminated aluminium pouch of the cell at the end opposite to its existing terminals. The pouch was then peeled back to reveal the electrode stack underneath, encased in a winding of polymer separator. Insulating, adhesive-free polymer tape was used to cover the exposed aluminium edges of the pouch; both these and the peeled-back segments of pouch were held in place using adhesive tape. A lithium RE, in the form of a 2 cm^2 piece of foil, was then placed over the hole in the pouch, covering it entirely. This was topped with a smaller piece of copper

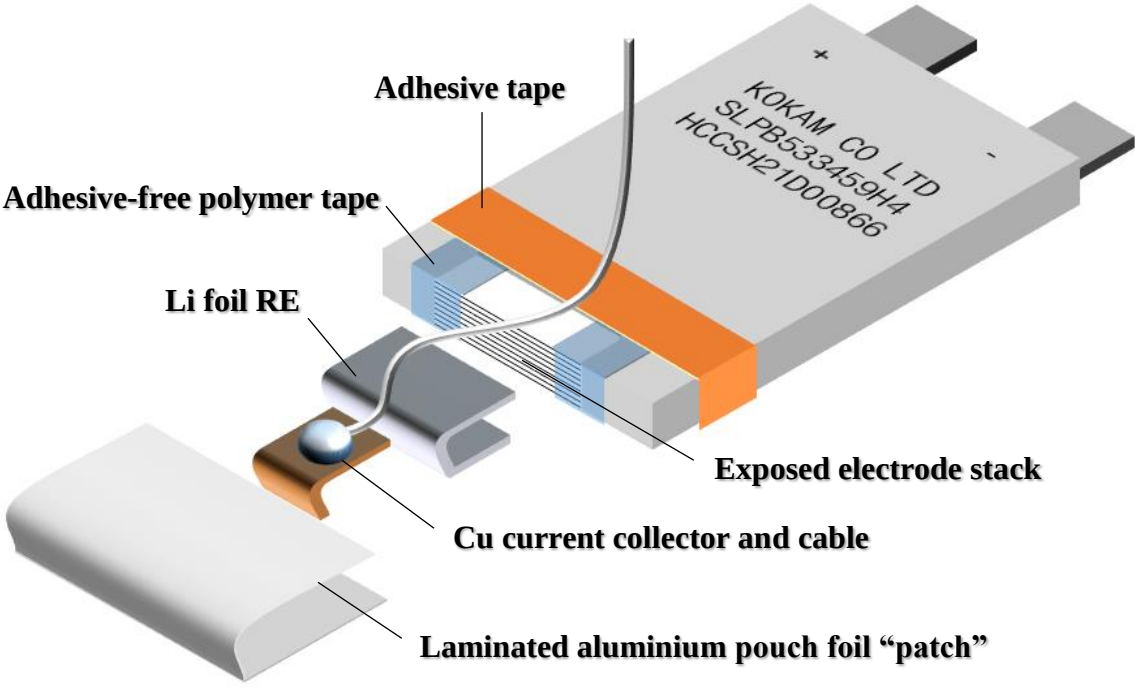

Figure 1: Exploded view of the "patch" modification procedure, prior to vacuum sealing in a large outer pouch.

current collector, which also had a wire with banana plug soldered to it, and then held in place using a large piece of laminated aluminium pouch foil and adhesive tape. The cell was then inserted into a large outer pouch with three sealed electrical feedthroughs for the electrodes. The outer pouch was then vacuum sealed using an Audionvac vacuum sealer.

5.2.4 "Wire" modification method

For the second modification technique, illustrated in Figure 2, the lithium RE was prepared in advance by electroplating a copper wire of 0.8 mm diameter inside a two neck glass flask in an argon glove box. The copper wire (WE) and a piece of lithium foil (CE) were immersed in commercial LP30 electrolyte. The cell then underwent linear voltammetry to -0.5 V to activate nucleation sites, followed by the application of a galvanostatic current of 10 mA cm^{-2} for

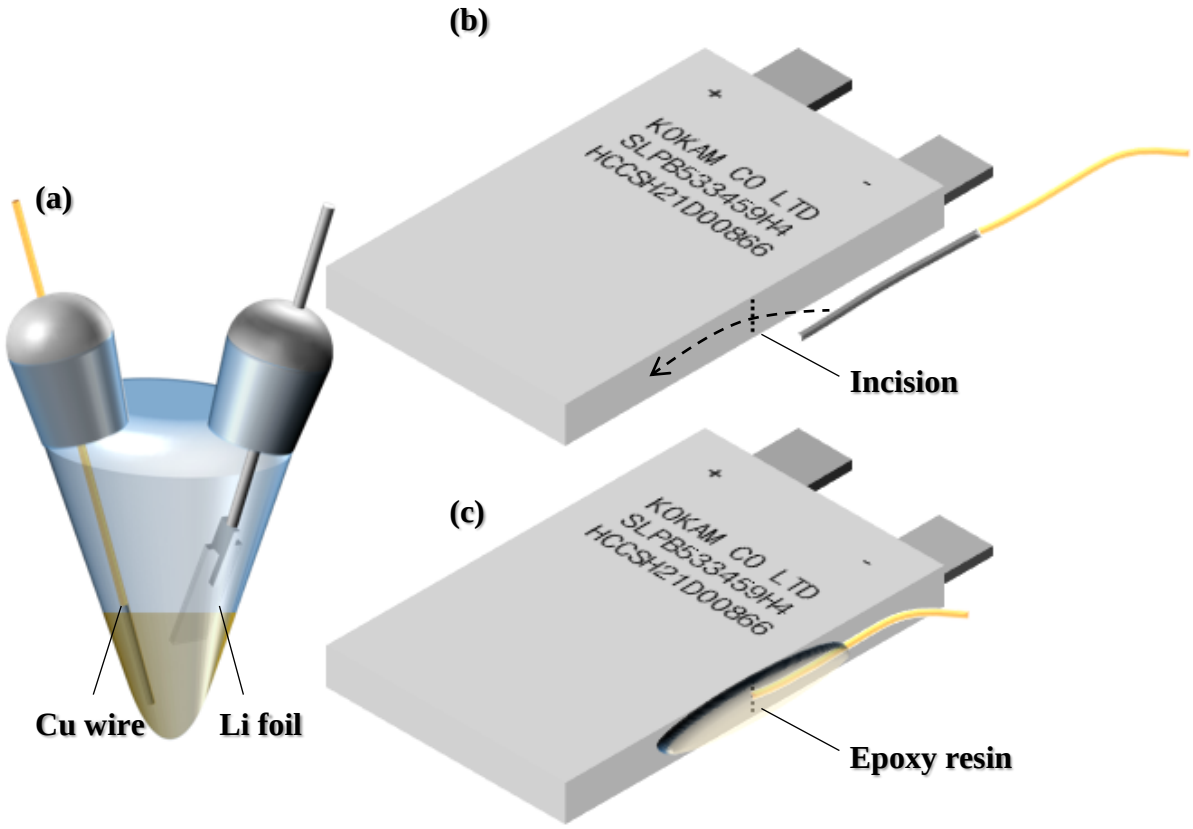

Figure 2: Illustration of the "wire" modification technique. Cu wire is electroplated with Li to form the RE (a) before inserting into an incision in the side of the pouch cell (b) and sealing with epoxy resin (c).

30 minutes to plate the wire with lithium. Once complete, the RE was rinsed twice with DMC and dried for 30 minutes at room temperature inside the antechamber of the glove box.

To modify the cell, a ceramic scalpel was used to create a 5 mm incision in the side of a discharged pristine cell, as shown in Figure 2(b), taking care not to puncture the polymer separator underneath. The lithium RE was inserted into the incision (Figure 2(c)), which was then sealed with fast-setting epoxy resin (Araldite) and left to dry overnight.

5.2.5 Cell cycling

Modified 3-electrode cells, unmodified full cells and half-cells were galvanostatically cycled at C/10 at room temperature (22 °C ± 2 °C) and 40 °C for twenty cycles using a Biologic VMP3

potentiostat and a Stuart S160 incubator. Due to time constraints, twenty cycles were deemed sufficient for this proof-of-concept stage, purely to demonstrate that the modification procedure yields the required data and has no impact on cell performance; cells would later be cycled for hundreds of cycles once a successful modification procedure had been developed. Groups of three cells were used for each modification procedure and each cycling temperature. E_{max} and E_{min} for modified and unmodified full cells were as specified by the manufacturer [15]. E_{max} and E_{min} for half-cells were determined by the initial results of 3-electrode cell cycling, whilst the current corresponding to C/10 was obtained from preliminary cycling of a test batch of half-cells. All cells were CCCP precharged to E_{max} prior to cycling.

5.2.6 Post-mortem analysis

Modified 3-electrode cells and unmodified full cells underwent SEM/EDX analysis to observe any difference in their structures that could arise from a negative impact of the modification procedures. Cells were discharged and transferred into an argon glove box, where they were cut open. Electrode sheets were removed and samples of approximately 1 cm^2 of material were cut from the edge opposite the positive and negative terminals (where the patch modification is performed) and the side of the cell (where the wire modification is performed), respectively. These were rinsed with DMC and dried as before, and analysed as described in Chapter 2.

5.3 Results and analysis

5.3.1 Capacity retention

Figure 3 shows the discharge profiles for patch- and wire-modified cells in comparison to unmodified cells on the 1st, 10th and 20th cycles at room temperature and 40 °C. On the first

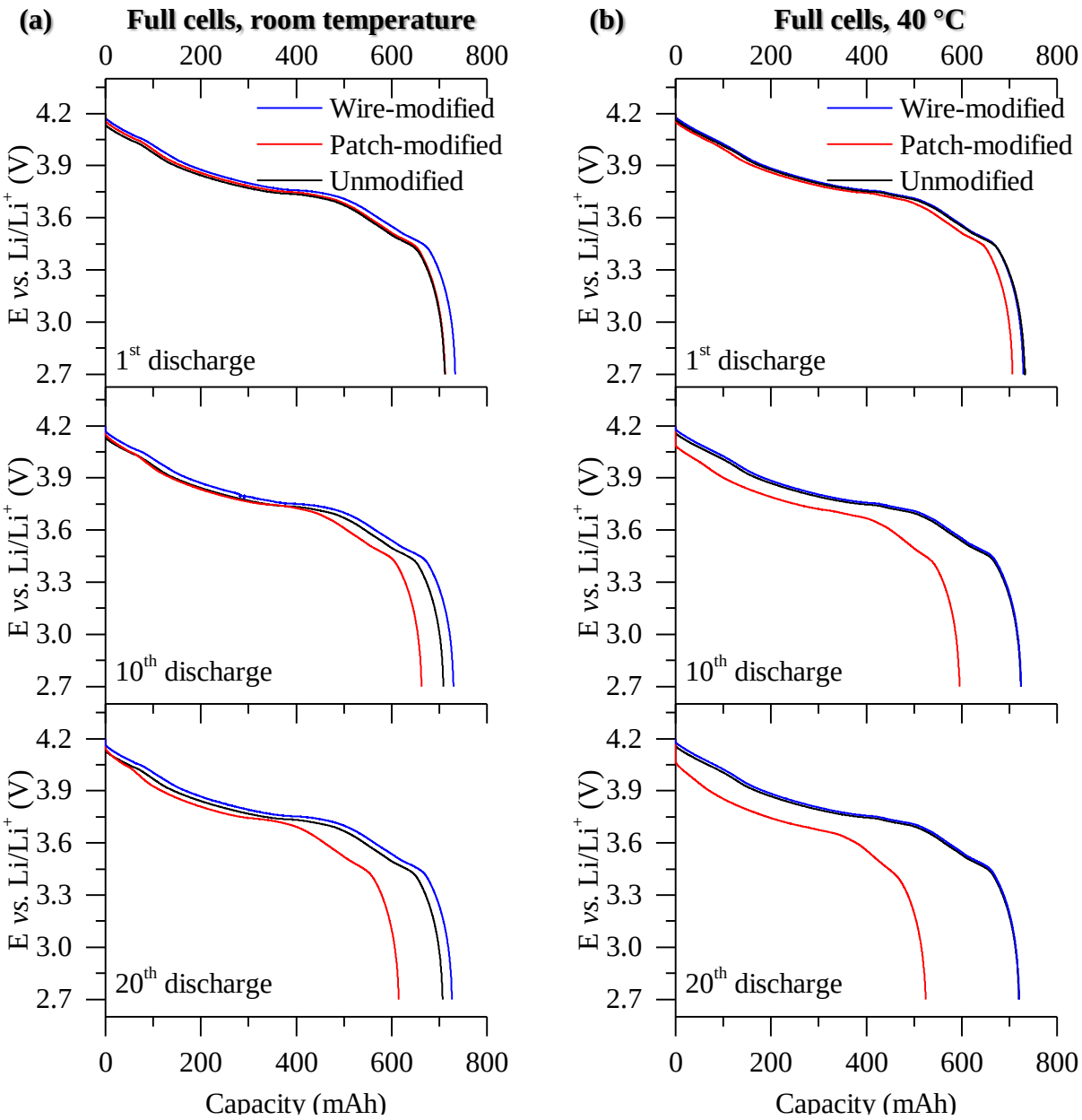

Figure 3: Potential profiles of the 1st, 10th and 20th discharge of unmodified, patch-modified and wire-modified cells at room temperature (a) and 40 °C (b).

discharge at both temperatures, both variants of modified cell achieve a discharge capacity that is within the standard deviation of the first discharge capacity of pristine Kokam cells. However, by the 10th discharge, the patch-modified cells have lost considerably more capacity than the wire-modified and unmodified cells; higher operating temperatures clearly exacerbate the issue. This trend continues at the 20th discharge, with the patch-modified cells encountering accelerated capacity loss in comparison to unmodified cells, whilst wire-modified cells closely

follow the capacity degradation trends of the unmodified cells. As seen in Table 1, the average capacity loss per cycle exhibited by unmodified and wire-modified cells are in excellent agreement with each other and well within the standard deviation of the groups of cells that were tested. Conversely, the capacity degradation per cycle for patch-modified cells is greater by an order of magnitude.

A number of reasons for the poor performance of patch-modified cells were explored, including evaporation of the electrolyte during vacuum sealing; alteration of the stack pressure of the electrode stack due to the invasive nature of the procedure; and parasitic reactions with the RE. Revisions were incorporated into the patch modification procedure in an attempt to resolve these issues. Firstly, cells were assembled at 8 mbar overpressure in the glove box, with minimal vacuum applied whilst cells were sealed in their outer pouches, to help to prevent the evaporation of the electrolyte. Secondly, cells were clamped between two thick pieces of Perspex to compensate for any change to the electrode stack pressure. Finally, an extra separator was added between the RE and the electrode stack to ensure no short circuits and to limit parasitic reactions. None of these procedures yielded any improvement in capacity retention. As such, the behaviour of patch-modified cells is not representative of unmodified cells, thus rendering them unsuitable for this study, whereas the wire modification procedure appears to have no impact on capacity degradation. Therefore, wire-modified cells were used for the continuation of this work.

Cell modification procedure	**Average capacity loss per cycle over 20 cycles (%)**	
	Room temperature	**40 °C**
Unmodified	0.07 ± 0.03	0.17 ± 0.07
Patch-modified	1.10 ± 0.42	1.12 ± 0.50
Wire-modified	0.11 ± 0.08	0.17 ± 0.14

Table 1: Average capacity loss, per cycle, over 20 cycles for each variant of modified and unmodified pouch cell.

5.3.2 Post-mortem analysis

Figure 4 shows SEM images of samples taken from the edge of anodes from pristine and cycled unmodified cells, along with the anode material from a cycled patch-modified cell. There is

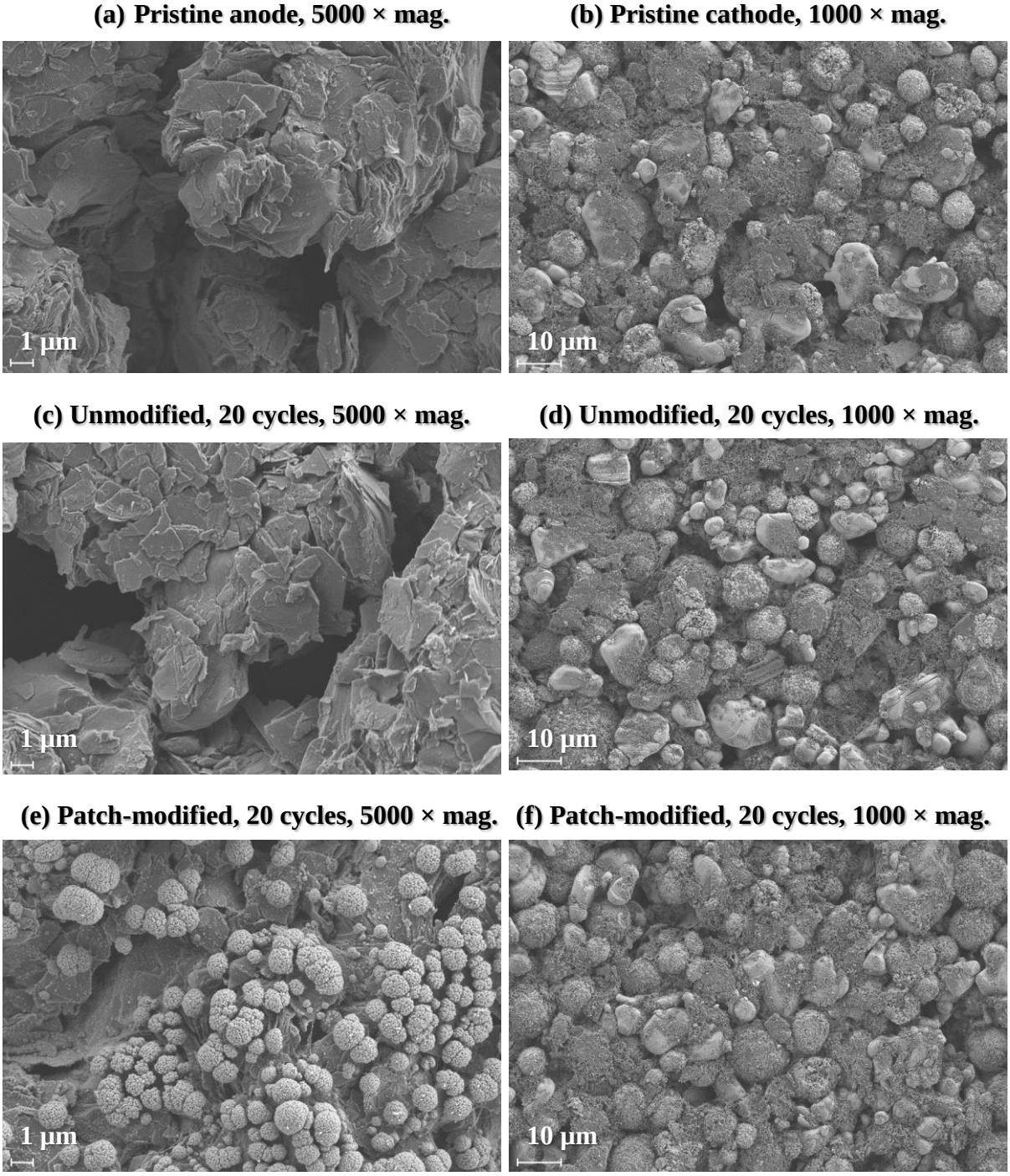

Figure 4: SEM images for the anodes and cathodes of a pristine cell (a,b) as well as unmodified (c,d) and patch-modified (e,f) cells after 20 cycles. Anodes are shown at 5000 × magnification whilst cathodes are shown at 1000 × magnification.

no visible difference between any of the cathodes. Likewise, there is no difference between the anodes of the pristine and unmodified cells. However, clusters of material have formed on the surface of the anode of the patch-modified cell. It is difficult to tell from SEM imagery alone what these clusters have been formed from. Therefore, EDX was performed on the sample, as shown in Figure 5. Unfortunately, EDX cannot detect lithium, but there is a clear presence of oxygen, unlike in pristine anodes, and a five-fold increase in the weight percentage (wt. %) of fluorine present *vs.* an uncycled anode. These elements are particularly prevalent in the clusters that are not present on the pristine anode. Fluorine likely originates from the electrode binder or the electrolyte salt. Phosphorous was also detected, suggesting that $LiPF_6$ was used as the salt, which is common in Li-ion cells [16, 17, 18]. However, oxygen should only be found in the cathode structure of this cell chemistry.

SEM and EDX were employed to identify any decomposition of the cathode structure of the patch-modified cell after cycling. There is no obvious difference in the SEM images of pristine cathodes (Figure 4 (b)) and those of cycled patch-modified cells (Figure 4(f)), which suggests that no cathodic decomposition has taken place. EDX analysis reports that the content of fluorine increased by 4.4 wt. % in the patch-modified sample (Appendix B.2). However, the EDX results must not be regarded as being highly accurate for three key reasons. Firstly, the cathode structure is mixed, which gives rise to the possibility of different ratios of heavy metal oxides in each sample due to the small area analysed by EDX. Secondly, the sample surface consists of numerous large particles rather than a flat surface, which results in X-rays being diffracted in random directions. Finally, the resolution of the data is not as high as with SEM, as illustrated in Figure 12 of Chapter 2. Consequently, changes in the chemical composition of these cathodes, as determined by EDX (Appendix B.2), are insufficient to suggest that cathodic decomposition has taken place, thus implying that the oxygen detected in the anode of the cycled patch-modified cell originated from elsewhere.

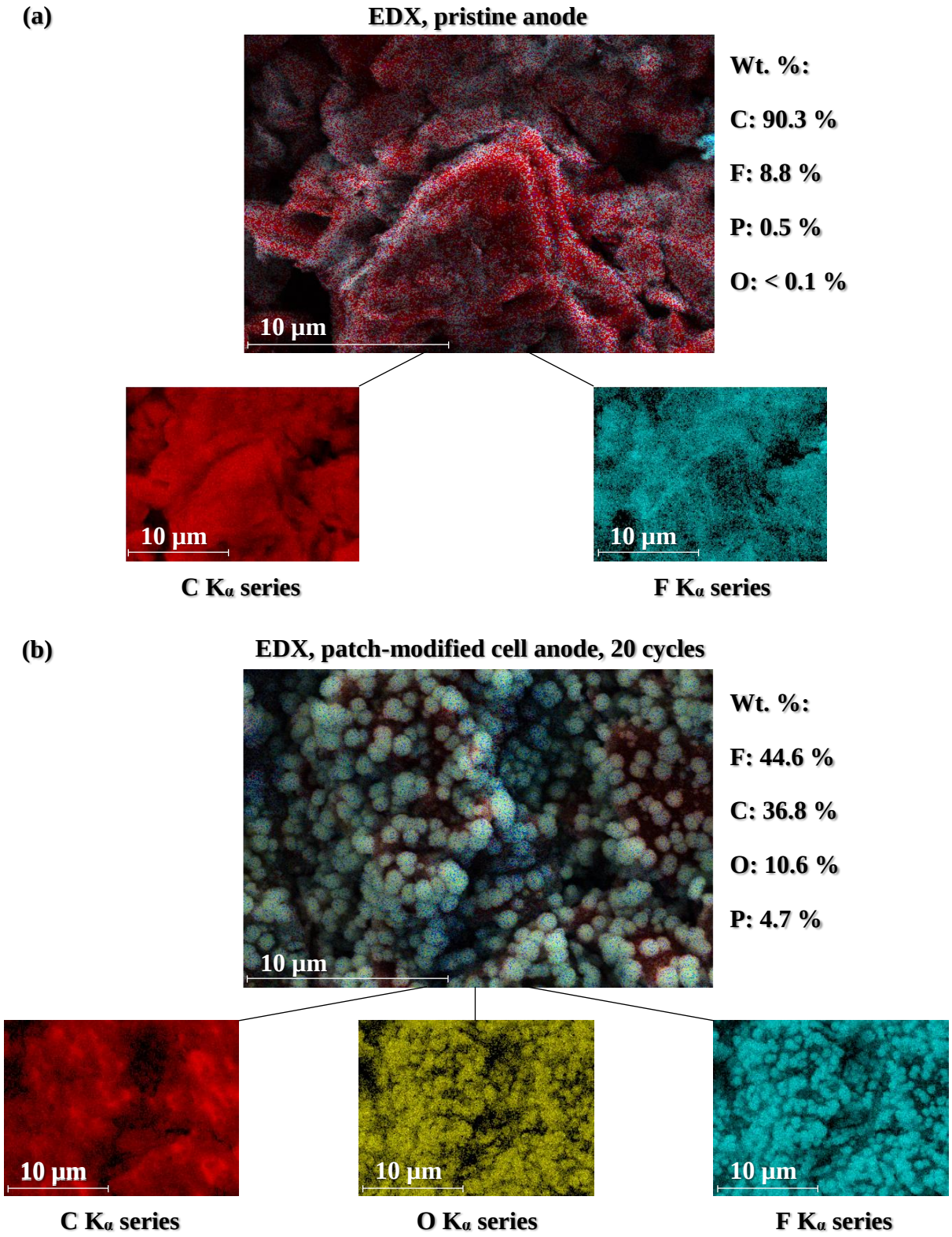

Figure 5: EDX colour maps for a pristine anode (a) and the anode of the cycled patch-modified cell shown in Figure 4(e), (b).

One possibility that may explain the source of oxygen in Figure 5(b) is the exposure of the sample to air whilst being transferred into the SEM vacuum chamber. It is thought that the

anode underwent a parasitic reaction with the RE during cycling, forming lithium deposits on its surface. These then reacted with oxygen from the air during transfer into the SEM, resulting in the oxygen-rich deposits seen in the EDX colour maps in Figure 5(b). This theory also explains why there is negligible oxygen present in the pristine anode in Figure 5(a), and the anode of an unmodified, cycled cell in Appendix B.3. This theory was tested by altering the patch modification procedure in an attempt to prevent such a parasitic reaction from taking place. An extra separator was added between the RE and the electrode stack, and extra adhesive-free polymer tape was applied to both sides of exposed aluminium edges of the pouch material that was in contact with the electrode stack.

Figure 6 shows the SEM image and EDX colour maps of the anode from a pouch cell with the revised patch modification procedure after 20 cycles. Despite the extra separator added between the RE and electrolyte, the anode is clearly covered by a film of deposits that are not present in the anode of the unmodified cell shown in Figure 4(c). EDX once again reveals high levels of fluorine, suggesting that the binder or electrolyte salt has been involved in a side reaction caused by the modification procedure, leading to the film of deposits on the anode surface. Blue specks in the EDX colour map are indicative of the K_α emissions of phosphorous. Oxygen is also a major component of the film, which could again be indicative of lithium that has oxidised during its exposure to air when being transferred into the SEM. Such a large amount of lithium is not expected in the anode of a discharged cell. This suggests that lithium plating has occurred, which would explain the uniform covering of the anode active material. The failure of the revisions to the patch modification procedure to prevent side reactions from taking place in modified cells makes the procedure unsuitable for this study. Furthermore, the cell lost an average of 1.29 % of its capacity per cycle over the 20 cycles, meaning that its capacity degradation was not representative of that of an unmodified cell.

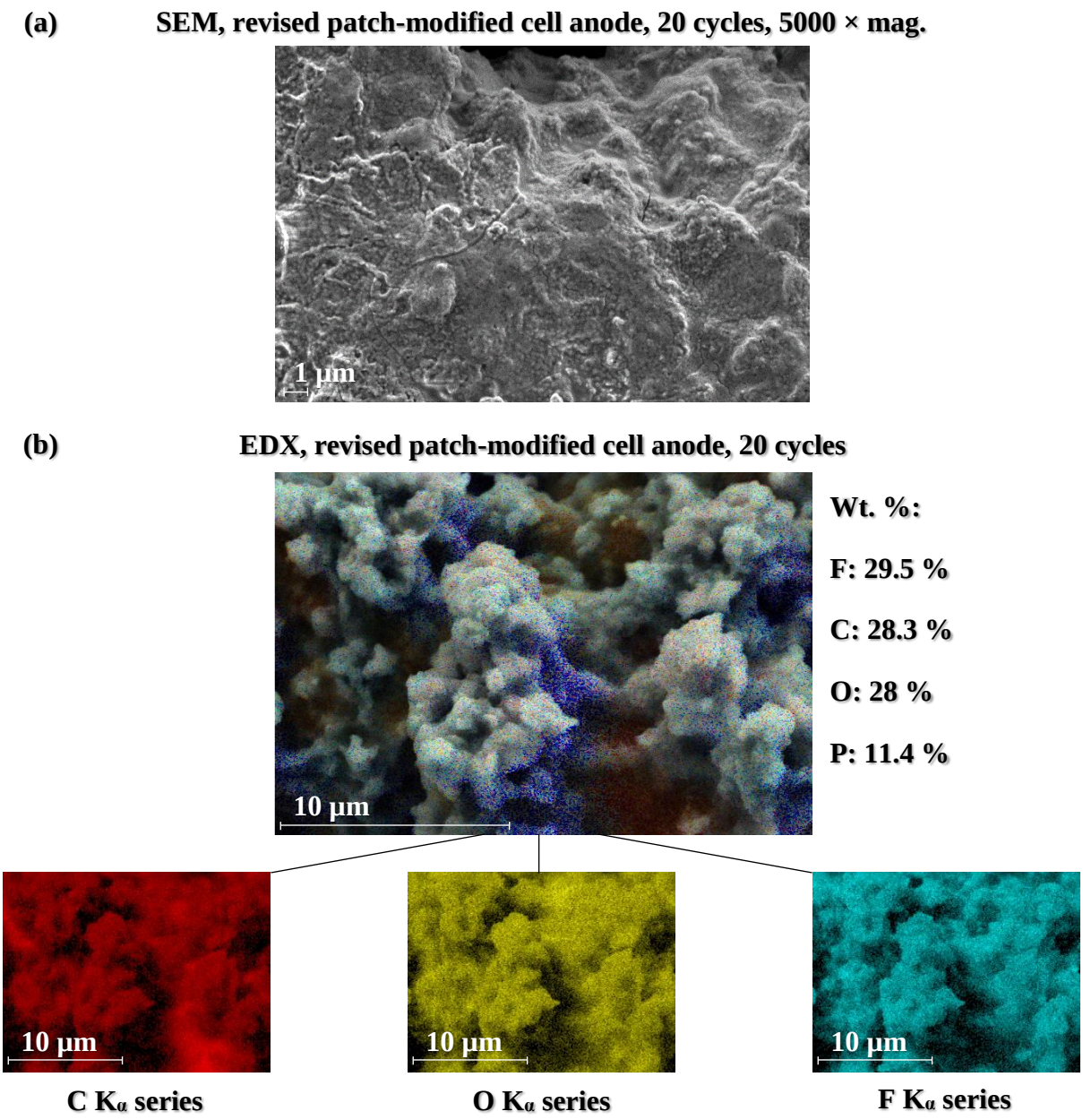

Figure 6: SEM image (a) and EDX colour maps (b) for the anode of a patch-modified cell that underwent the revised procedure with extra separators and insulation to prevent the parasitic reaction with the RE encountered in the anode shown in Figures 4(e) and 5(b). Blue specks denote K_α phosphorous emissions.

The SEM image and EDX colour maps for the anode from a wire-modified cell, cycled for 20 cycles, are shown in Figure 7. These were taken from the region of the anode that was adjacent to the incision made for the wire modification process. The SEM image shows no difference to the morphology of the anode in comparison to the unmodified, cycled cell in Figure 4(c), thus representing a marked improvement on all variants of the patch modification procedure.

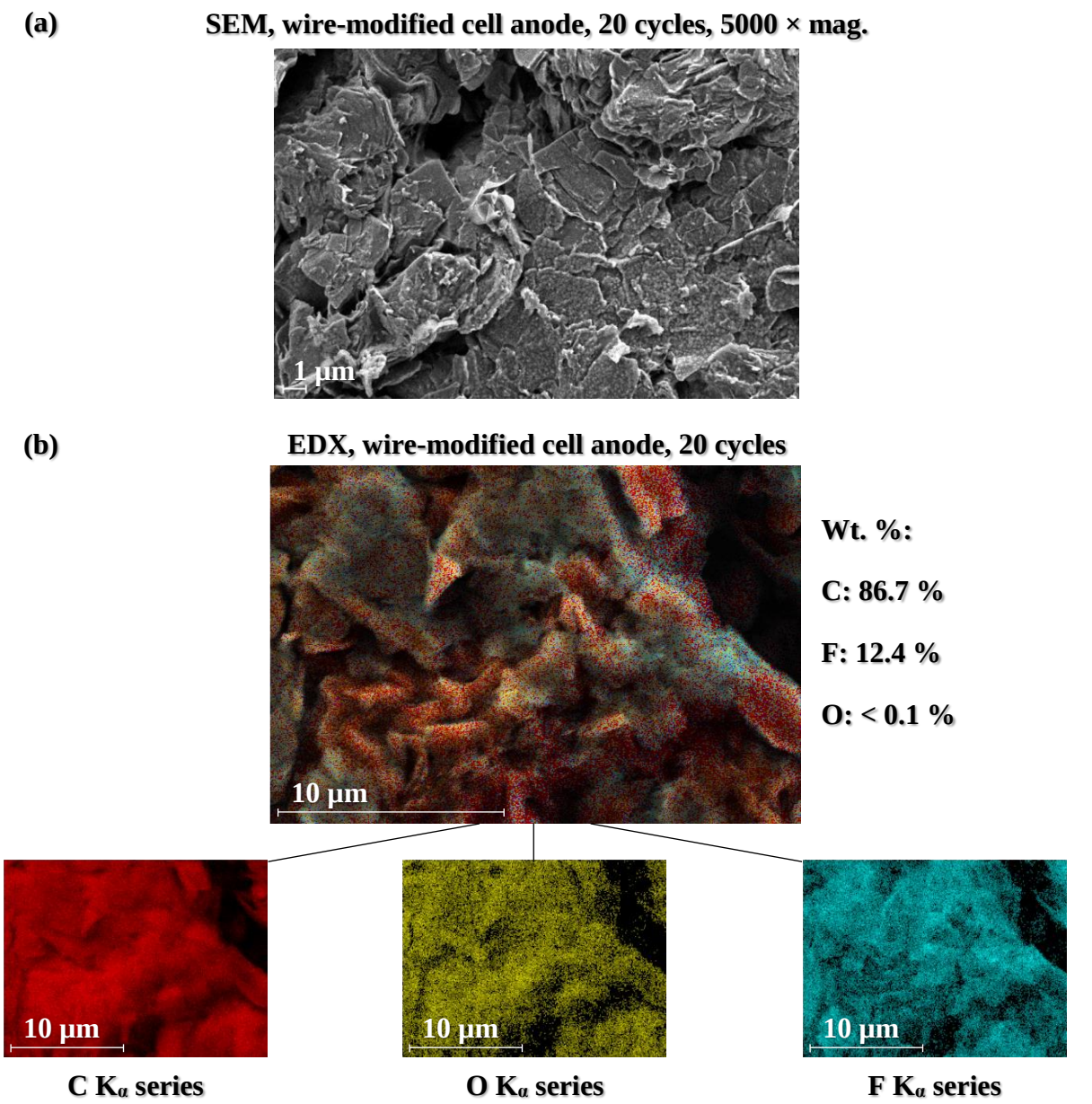

Figure 7: SEM image (a) and EDX colour maps (b) for the anode of a wire-modified cell.

Whilst the oxygen content appears moderate on the colour map, the actual content is negligible. The weight percentage of fluorine in comparison to carbon is slightly higher than that of a pristine anode (Figure 5(a)), but this represents a swing of 1.5 % towards fluorine compared to an unmodified cell that has undergone the same number of cycles (see Appendix B.3). Due to the rough morphology of the sample surface, which is not ideal for EDX analysis and results in irregular scattering of X-rays, it can be safely assumed that this discrepancy is within the margin of error for this sample type. From this, it can be determined that the wire modification

procedure does not induce side reactions within the cell during cycling. Therefore, the technique has no impact upon cell performance or cycling mechanisms in comparison to an unmodified cell, and is thus a reliable modification procedure with which to proceed in this study.

5.3.3 Electrode potential verification

Figure 8 shows the cathode potential profiles obtained from wire-modified cells in comparison to the potential profiles of cathode half-cells. Here, capacities have been converted to specific capacities to account for the significant differences in quantities of active material in each type of cell. Despite this, the specific capacity of the half-cells consistently falls short of that of the 3-electrode cells. This is likely due to differences in lithium loading or minor weighing errors, and can be easily accounted for by stretching the X-axis data of half-cell plots to fit those of the 3-electrode cells (see Appendix B.4). By doing this, the potential data from the 3-electrode cell cathodes and cathode half-cells are found to be in excellent agreement throughout the State of Charge (SoC) of the cell, with a maximum root mean square error (RMSE) of 5.72 mV between the plots (see Appendix B.4). Therefore, the cathode potential profile obtained from the 3-electrode cell is highly accurate.

The corresponding potential profiles for the anode half-cells and anode data from 3-electrode cells are shown in Figure 9. Note that the X-axis of the anode half-cells has been shifted with respect to the X-axis of the 3-electrode cells. As illustrated clearly in Figure 9(b), this is because the capacity of 3-electrode cells is cathode-limited, and thus the full capacity of the anode material is not exploited; this corresponds to the first 50 mAh g^{-1} active material of the anode half-cells, which is duly omitted from the plot. By adjusting the starting point of the X-axis

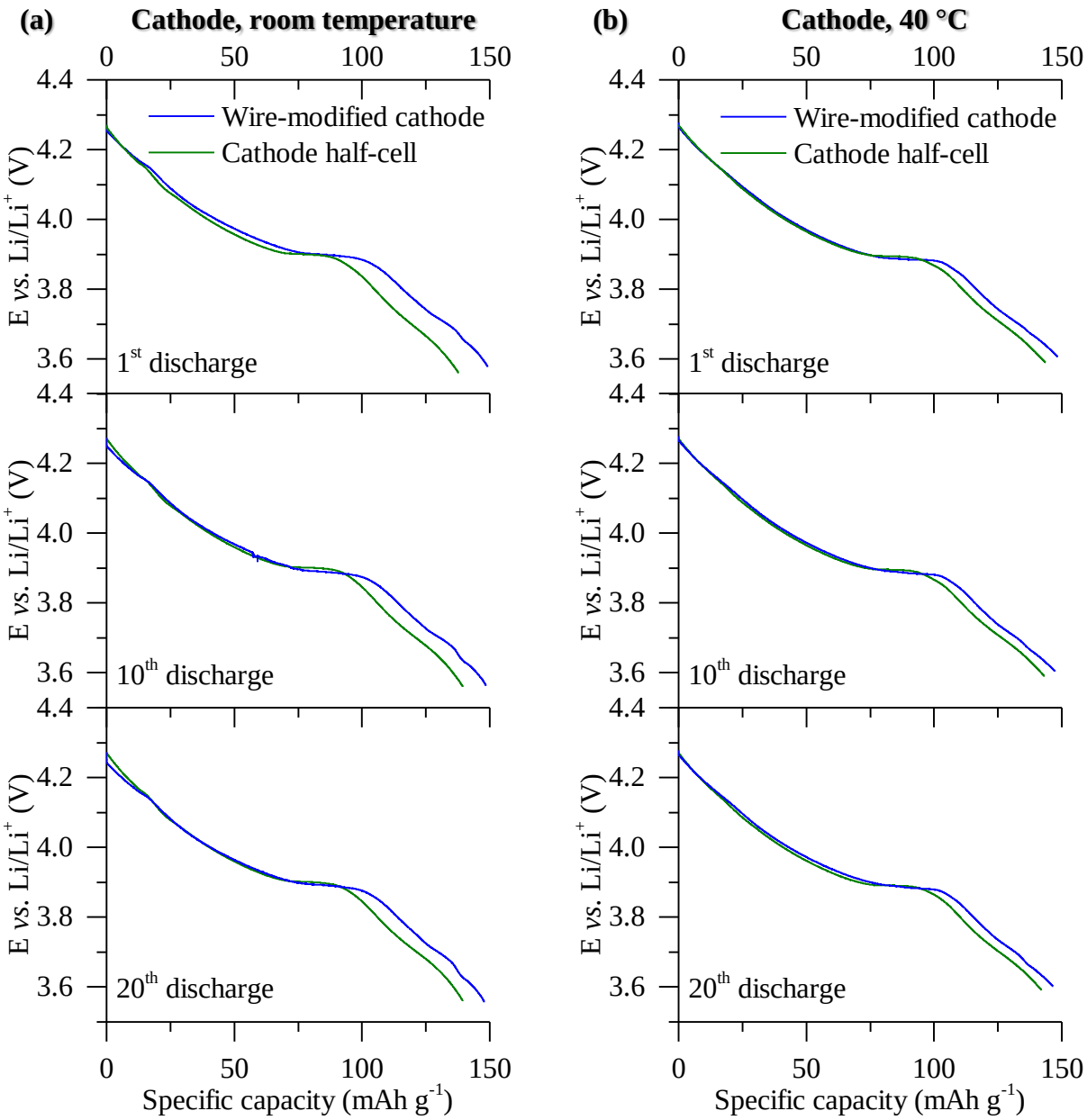

Figure 8: Potential profiles for the 1st, 10th and 20th discharge of cathode half-cells and the cathodes of wire-modified cells at room temperature (a) and 40 °C (b)

for the half-cells, it is found that the specific capacities and potential profiles of the 3-electrode cells and half-cells are in excellent agreement with each other.

In Figure 9(a), the anode half-cell X-axis is shifted so that 0 mAh g^{-1} corresponds to 15 mAh g^{-1} for the 3-electrode cell X-axis, which implies that the half-cell has less specific capacity than the 3-electrode cell at room temperature. All room temperature anode half-cells exhibited a lower specific capacity than anode half-cells that were cycled at 40 °C, whilst

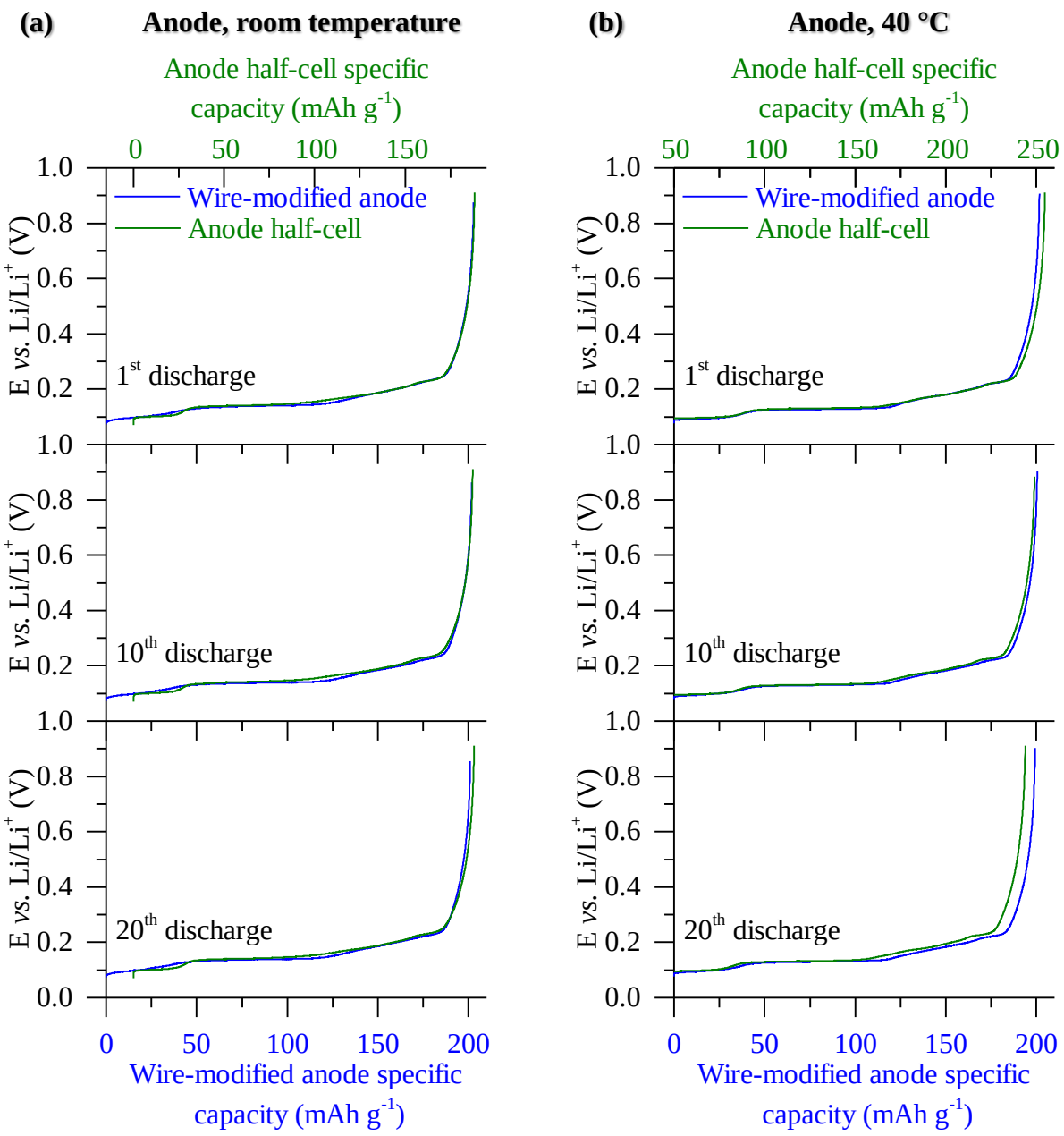

Figure 9: Potential profiles for the 1st, 10th and 20th discharge of anode half-cells and the anodes of wire-modified cells at room temperature (a) and 40 °C (b). Note that the X-axis of anode half-cells is shifted with respect to that of the 3-electrode cells to account for the cathode-limited capacity of the 3-electrode cells.

3-electrode cells cycled at room temperature and 40 °C achieved similar specific capacities. The 40 °C and room temperature anode half-cells were built in two separate batches, suggesting that a discrepancy during their fabrication may be to blame for their differing performance. Weighing errors of a sufficiently large magnitude to account for the full margin of error are unlikely due to the multiple weighing of each sample to ensure as accurate a reading as

possible, and the weighing of multiple bare substrates to obtain a reliable figure to subtract from the mass of the electrode to calculate the mass of active material. Another possibility is damage to the electrode during the removal of one side of active material from the double-sided substrate. NMP may have managed to seep underneath the tape holding the substrate down during this procedure, becoming absorbed by the underlying layer of active material and partially dissolving its binder. However, this would have an equal chance of affecting both batches of half-cells. One key difference between the two batches was the mechanical removal of the unwanted layer of active material. For 40 °C anode half-cells, this was achieved by applying NMP and wiping the dissolved binder and active material away using several tissues until the copper substrate was visible. This prevented the substrate from being stressed, bent or wrinkled, thus ensuring that the active material on the other side was not damaged. However, for room temperature half-cell batches, a spatula was also used to scrape the active material off after being soaked in NMP. Despite careful use of the spatula, this may have caused sufficient stress to the substrate to impair the active material on the other side, resulting in the comparatively poor cycling performance. As such, room temperature 3-electrode cell anode data plotted against 40 °C anode half-cells arguably yields a more representative comparison of performance than plotting *vs.* room-temperature anode half-cells as shown in Figure 9(a).

Further fitting of the X-axis data of each plot to yield common specific capacity values gives a maximum RMSE of 9.15 mV between the potentials of each data point; 5 mV for the more reliable 40 °C data in Figure 9(b) (see Appendix B.4). Therefore, the reliability of the RE has been confirmed for the anode, allowing the potential profile of each electrode in the cell to be accurately obtained over the 20 cycles considered in this study. Additionally, Figure 9(b) reveals that the first 50 mAh g^{-1} of capacity are not utilised in the anodes of the full cells. Consequently, assessing the cycling performance and capacity degradation of cell chemistries

using half-cells alone provides inaccurate results since the anode will have the ability to use more of its capacity than it would in a full cell, which will likely lead to an artificially large potential operating window and faster degradation of the active material. Also, the fabrication technique for half-cells using single-sided active material fabricated from a double-sided electrode can result in impaired performance due to the stress that the substrate is placed under during the fabrication process, and so the removal of the unwanted layer of active material must be achieved with caution.

5.4 Conclusions and further work

A 3-electrode modification procedure has been developed for commercial pouch cells that is able to provide the potential profiles for each electrode to within an accuracy of less than 10 mV RMSE [19]. The procedure allows the RE to be positioned as close to the electrode stack as possible without altering its mechanical or electrochemical properties, thus allowing the performance of the cell to remain unchanged in comparison to an unmodified cell; this has been verified over the first 20 cycles at C/10 at both room temperature and 40 °C. The sensitivity of commercial pouch cells to changes in stack pressure and electrolyte volume, and their vulnerability to internal short circuits and parasitic reactions, has been observed through the failed patch modification technique.

The modification procedure presented in this work is a useful tool with which to obtain real electrode potential profiles for the verification of Li-ion cell models that can predict the OCV of each electrode, and the full cell, over prolonged cycling and under various abuse conditions, such as the model created as part of the wider project surrounding this work. This model is based on cathode and anode sub-models derived from the Nernst equation and assumes four phase transitions during each discharge or charge. Having been calibrated using half-cell OCV

data obtained by GITT cycling (Section 2.4.3), the model is now able to map the OCV of each electrode of a 3-electrode pouch cell to within a maximum RMSE of 10 mV, using only the full cell potential as input data [7].

Work is currently underway to assess the ability of the model to predict electrode potentials under prolonged cycling and various abuse conditions. As mentioned earlier, each electrode in a Li-ion cell is vulnerable to a number of different degradation mechanisms, instigated by factors such as high current and extreme temperatures, each of which results in a change to the potential profile of the electrode. Wire-modified 3-electrode cells are presently undergoing tests designed to induce anodic lithium plating by cycling them at high C-rates at a temperature of -10 °C. Data from each electrode will be compared to the electrode potential profiles calculated by the model based on the full cell potential to assess the accuracy of the model under abuse conditions. Following this, the model will be tested under other abuse conditions in a similar manner. A logical progression of the work will be the application of the 3-electrode modification technique to other cell chemistries and larger format cells, such as those found in the Nissan LEAF, to test the flexibility of the modification technique and the model.

If the electrode potential profiles calculated by the model under abuse conditions are as accurate as the initial verification results, the model could be a powerful, yet computationally-simplistic addition to an automotive BMS. This would allow the BMS to use full cell potentials from commercial, unmodified 2-electrode cells to detect decomposition taking place at the electrodes and take evasive action, such as by reducing the maximum C-rate of a bank of cells or adjusting the thermal management system of the battery pack. The addition of look-up tables or a learning function to the algorithm would allow the BMS to predict the onset of degradation mechanisms or the impact of cycle or calendar aging, and adjust the treatment of the cell or bank accordingly. By gaining a greater understanding of the mechanisms occurring within commercial Li-ion cells, the 3-electrode pouch cell modification technique, coupled with the

developed model, will facilitate an increase in the lifespan of an automotive battery pack without any changes to the cell chemistry.

5.5 References

[1] Nissan Great Britain. (2015). *Nissan LEAF Guarantees & Services*. [Online]. Available: http://www.nissan.co.uk/GB/en/vehicle/electric-vehicles/leaf/prices-and-equipment/services-warranty.html. [Accessed 04 September 2015].

[2] BMW UK. (2015). *BMW i3 Aftersales Products and Services*. [Online]. Available: http://www.bmw.co.uk/en_GB/new-vehicles/bmw-i/i3/2013/iService.html. [Accessed 23 September 2015].

[3] Tesla Motors. (15 August 2014). *Infinite Mile Warranty*. [Online]. Available: http://www.teslamotors.com/en_GB/blog/infinite-mile-warranty. [Accessed 23 September 2015].

[4] C. R. Birkl, D. F. Frost, A. M. Bizeray, R. R. Richardson and D. A. Howey, "Modular Converter System for Low-Cost Off-grid Energy Storage Using Second Life Li-ion Batteries," in *IEEE GHTC*, Silicon Valley, CA, 2014.

[5] J. C. Burns, A. Kassam, N. N. Sinha, L. E. Downie, L. Solnickova, B. M. Way and J. R. Dahn, "Predicting and Extending the Lifetime of Li-Ion Batteries," *J. Electrochem. Soc.*, vol. 160, no. 9, pp. A1451 - A1456, 2013.

[6] J. L. Lurie, A. Sokolowski and T. Zohdy. (24 September 2012). *Klee v. Nissan N. Am., Inc. Case No. CV 12-08238 DDP (PJWx)*. [Online]. Available: http://www.courthousenews.com/2012/09/25/nissan.pdf. [Accessed 06 September 2015].

[7] C. R. Birkl, E. McTurk, M. R. Roberts, P. G. Bruce and D. A. Howey, “A Parametric Open Circuit Voltage Model for Lithium Ion Batteries,” *J. Electrochem. Soc.*, vol. 162, no. 12, pp. A2271 - A2280, 2015.

[8] J. R. Belt, D. M. Bernardi and V. Utgikar, “Development and Use of a Lithium-Metal Reference Electrode in Aging Studies of Lithium-Ion Batteries,” *J. Electrochem. Soc.*, vol. 161, no. 6, pp. A1116 - A1126, 2014.

[9] P. Liu, J. Wang, J. Hicks-Garner, E. Sherman, S. Soukiazian, M. Verbrugge, H. Tataria, J. Musser and P. Finamore, “Aging Mechanisms of $LiFePO_4$ Batteries Deduced by Electrochemical and Structural Analyses,” *J Electrochem. Soc.*, vol. 157, no. 4, pp. A499 - A507, 2010.

[10] W. Fang, O. J. Kwon and C.-Y. Wang, “Electrochemical-Thermal Modeling of Automotive Li-Ion Batteries and Experimental Validation Using a Three-Electrode Cell,” *Int. J. Energy Res,* vol. 34, no. 2, pp. 107 – 115, 2010.

[11] G. Nagasubramanian, “Two- and Three-Electrode Impedance Studies on 18650 Li-Ion Cells,” *J. Power Sources,* vol. 87, no. 1 - 2, pp. 226 - 229, 2000.

[12] B. Scrosati, J. Garche and W. Tillmetz, *Advances in Battery Technologies for Electric Vehicles*, Cambridge: Woodhead Publishing, 2015, p. 132.

[13] K. Wu, Y. Gao, X. Sun, S. Liu, N. Wu, H. Zhao and Y. Zhang, “Capacity Fading Mechanism of Large Scale $Li_4Ti_5O_{12}/LiCoO_2$ Battery,” in *ITEC Asia-Pacific 2014*, Beijing, 2014.

[14] T. R. Jow, J. Allen, M. Marx, K. Nechev, B. Deveney and S. Rickman, “Electrolytes, SEI and Charge Discharge Kinetics of Li-Ion Batteries,” *ECS Trans.,* vol. 25, no. 36, pp. 3 - 12, 2010.

[15] Kokam Co., Ltd. *Cell Specification Data SLPB 533459H4*. [Online]. Available: http://www.kokam.com/product/product_pdf/rc_070226/SLPB533459H4_740mAh_Grade.pdf. [Accessed 06 April 2015].

[16] V. A. Agubra and J. W. Fergus, “The Formation and Stability of the Solid Electrolyte Interface on the Graphite Anode,” *J. Power Sources,* vol. 268, pp. 153 - 162, 2014.

[17] B. Scrosati and J. Garche, “Lithium Batteries: Status, Prospects and Future,” *J. Power Sources,* vol. 195, pp. 2419 - 2430, 2010.

[18] S. S. Choi and H. S. Lim, “Factors That Affect Cycle-Life and Possible Degradation Mechanisms of a Li-Ion Cell Based on $LiCoO_2$,” *J. Power Sources,* vol. 111, no. 1, pp. 130 - 136, 2002.

[19] E. McTurk, C. R. Birkl, M. R. Roberts, D. A. Howey and P. G. Bruce, “Minimally Invasive Insertion of Reference Electrodes into Commercial Lithium-Ion Pouch Cells,” *ECS Electrochem. Lett.,* vol. 4, no. 12, pp. A145 - A147 , 2015.

6 Conclusions and outlook

Lithium-air cells undoubtedly hold a great deal of promise with regards to surpassing the requirements of the automotive industry in terms of specific energy and cost per kWh. However, in order to achieve commercial viability as a secondary cell, a stable electrolyte solution must be found that can satisfy the two key criteria of facilitating solution-phase growth of Li_2O_2 to yield the maximum possible discharge capacity, whilst resisting nucleophilic attack and subsequent decomposition. As seen in Chapter 3, this is not straightforward. The poor capacity retention of adiponitrile and glutaronitrile cells, coupled with the nucleophilic attack of these solvents by $O_2^{\bullet-}$ radicals, suggests that they are unsuitable for use in secondary lithium-air cells, adding to the list of unsuitable solvents including alkyl carbonates, ethers, formamides and dimethyl sulfoxide [1, 2, 3, 4, 5]. Recent publications have concluded that most, if not all, readily available organic solvents are unable to fulfil both of these key criteria simultaneously, and have suggested engineering a solution around the limitations of today's electrolytes. Avenues to explore include identifying or engineering solvent additives that prevent nucleophilic attack and promote the solution-phase growth of Li_2O_2; and selecting solvent mixtures that work in tandem to yield high discharge capacities and high stability towards intermediate discharge species and Li_2O_2 [6]. For the former option, the inclusion of H_2O in the electrolyte solution was recently investigated with respect to encouraging the solution-phase growth mechanism of Li_2O_2. The diameter of Li_2O_2 toroids was shown to increase with the content of H_2O in the organic electrolyte, with toroids reaching a diameter of 1 μm, and the discharge capacity of the cell reaching a plateau, when 4,000 ppm H_2O was present [7]. This suggests that solvent additives are a promising avenue to explore to find a stable and reversible Li-air cell chemistry.

Once a suitable electrolyte for a Li-air cell has been identified, attention must turn to the anode material. The Li-air studies conducted in this work featured precharged LFP anodes because pure Li anodes do not form a stable SEI layer in aprotic Li-air cells. A further concern regarding pure Li anodes has been their reactivity in the event of ingress of H_2O and CO_2 when cycling the cell in ambient air. However, recent studies have shown that these atmospheric compounds can be employed to form a stable SEI of inorganic compounds, namely Li_2CO_3 and LiF, on the surface of pure Li anodes in conjunction with $LiPF_6$ in a mixture of carbonate solvents that were previously ruled out for use in Li-air cells [1, 8, 9]. This process improves current distribution across the Li anode and reduces the surface area available for unwanted side reactions. It has been shown to increase the coulombic efficiency of a Li anode from circa 55 % in a system with no CO_2 and trace H_2O, to nearly 90 % in a system that had been briefly bubbled with ambient air and contained 35 ppm H_2O as well as 2.5×10^{-5} mol kg^{-1} CO_2. A further study, which prepared a Li anode with a Li_2CO_3 and Li_2O-based SEI by replacing $LiPF_6$ with $LiClO_4$, achieved a stable coulombic efficiency of 85 % in a DMSO-based electrolyte, which is more likely to achieve commercialisation than problematic carbonate-based electrolytes, up to an H_2O content within the electrolyte of 1,000 ppm [10]. Admittedly, such reactions are unwelcome on the cathode as they passivate reaction sites. Nonetheless, this discovery suggests that Li-air cells with high specific energy could be created by pre-treating Li anodes in ambient air as described above, then inserting them into a cell with a stable electrolyte and an O_2-selective membrane to prevent further such reactions from occurring at the cathode. As discussed above, additives based on the mechanism by which H_2O has been shown to increase solution-phase Li_2O_2 growth could be added to the electrolyte solution to yield even greater specific energy [7].

The model developed in Chapter 4 will prove useful in the search for an electrolyte and cathode combination that is capable of yielding the maximum possible capacity for a Li-air cell. By

factoring in the donor number of the solvent used in the electrolyte solution, the model confirmed that solution-phase Li_2O_2 growth does play a crucial role in the discharge capacity of a Li-air cell. This has been latterly verified by SEM images revealing the presence of Li_2O_2 toroids in cells with electrolytes that theoretically favour solution-phase formation of the discharge product. Additionally, the diameter of the toroids decreased for cells discharged at higher current densities, thus confirming the conclusion from our model that higher current densities hinder the solution-phase growth mechanism, which subsequently results in a decrease in discharge capacity [7]. The study in question also investigated the impact of H_2O content on the discharge mechanism of Li-air cells, and found that the inclusion of H_2O facilitates solution-phase growth at higher current rates than in cells that have anhydrous electrolyte solutions. Interestingly, H_2O did not react with Li_2O_2 to produce irreversible decomposition products like LiOH on account of its high logarithmic acid dissociation constant (pK_a), and thus weak acidity; previous studies have rigorously dried solvents and salts due to concerns that this reaction may occur [1, 2, 4]. However, H_2O did cause issues with the long-term cyclability of Li-air cells due to increased nucleophilic attack of the electrolyte by $O_2^{\bullet-}$ radicals in solution [7]. Nonetheless, further understanding of the mechanism by which H_2O allows the cell to discharge *via* the solution-phase Li_2O_2 growth method at higher current densities than previously possible could lead to the development of stable solvent additives that facilitate greater discharge capacities at higher current densities, without undergoing unwanted side reactions in the cell. This will simultaneously improve the specific energy of Li-air battery packs and yield higher peak currents for high performance applications, such as electric vehicles.

The Li-air model may be used to calculate the optimum pore radius distribution for a Li-air cell. This information can then be used to reverse-engineer cathodes with the most desirable pore structure. State-of-the-art 3D printers have a resolution, or voxel size, of 200 nm ×

200 nm × 600 nm. These could be used to create cathodes with a precise, binder-free pore network structure in the laboratory, with the option to subsequently chemically or electrochemically treat the cathode to produce nm-diameter pores within the structure. This would allow the optimum pore radius distribution determined by the model to be recreated in a real electrode. Admittedly, the expense of the equipment, the small printing area and the time taken to print a cathode structure presently limit such practice to proof-of-concept in the lab; writing areas are typically 100 mm × 100 mm, with 2 mm^3 structures taking 12 hours to print. Nonetheless, such work would represent a significant contribution towards understanding of the Li-air discharge mechanism.

Despite recent advances in cell chemistry and the understanding of reaction mechanisms, secondary metal-air cells remain in the research and development phase. In the case of Li-air, this is primarily due to their high capacity degradation over a small number of cycles when built using inexpensive materials such as carbon cathodes; high reversibility has only been achieved using commercially unfeasible materials like nanoporous gold cathodes [11]. In the interim, a solution for the automotive industry maybe found by engineering around the limitations of the cell chemistries. For example, APET developed a zinc-air battery that, whilst not able to recharge electrically, could be rejuvenated by exposing the oxidised zinc anodes to high temperatures. It was suggested that solar ovens could be used to facilitate zero-carbon motoring [12]. Similarly, Phinergy and Alcoa have jointly developed an aluminium-air battery pack that has been demonstrated in electric cars and boats, giving them a range of 1,000 miles and a navigation time of 25 hours, respectively [13, 14]. Incidentally, this verifies the feasibility of metal-air systems from an air flow rate perspective, as described in Chapter 1 and Appendix A. The Phinergy/Alcoa battery cannot be electrically recharged once the aluminium anode has been exhausted, so the electrodes must be removed, dried and reprocessed into aluminium [15]. Given the lack of battery swapping and servicing infrastructure in comparison

to EV charge points, the latter is being marketed as a range extender rather than the main traction battery pack, giving a one-shot increase in range for emergency scenarios. This is the logic behind Tesla's patent on a hybrid Li-ion/metal-air battery pack [16].

In terms of achieving commercial secondary Li-air cells, a recent study was conducted where the discharged cathode of a cell with TEGDME electrolyte was stripped of its insulating layer of Li_2O_2 using dilute sulfuric acid (0.5 M H_2SO_4), rinsed, dried and reassembled in the cell. The rejuvenated cell was able to attain the original discharge capacity of a fresh cell for ten cycles prior to exhibiting capacity fade [17]. Importantly, TEGDME was shown to exhibit a mixture of solution-phase and surface layer Li_2O_2 growth in Chapter 4, due to its mid-range donor number. At higher current densities, as encountered in automotive applications, surface layer Li_2O_2 growth was found to be the dominant factor in TEGDME. This is in excellent agreement with studies of the Li_2O_2 formation mechanism with other electrolytes of low- to mid-range donor numbers, which also concluded that such solvents are more resistant to nucleophilic attack by $O_2^{\bullet-}$ radicals [6]. Therefore, an interim solution for Li-air cells could be to use solvents that have high resistance to nucleophilic attack by $O_2^{\bullet-}$ radicals, but also favour the surface layer formation of Li_2O_2. These packs would then be serviced after each discharge, or every ten cycles in the case of the study by Shui *et al.* [17], by removing the cathodes and stripping their Li_2O_2 layers in H_2SO_4. Such a system would most likely rely on a battery swap station akin to those proposed by Tesla and Renault [18, 19], but with onsite servicing equipment replacing the grid-connected chargers. If this method proves to be scalable, the high energy density of Li-air cells, combined with the speed of battery swapping, would deliver range and "refuel" times equivalent to today's internal combustion engine-powered vehicles.

In the meantime, the parametric OCV model from Chapter 5 can be readily incorporated into the BMS of an EV to predict electrode-specific degradation mechanisms in Li-ion cells within the battery pack. Electrode-specific potential profiles, calculated by the model and verified by

3-electrode cells in the lab, can identify when the potential of each electrode reaches a region that causes, or indicates, damage. One such example is when the anode reaches a potential of 0 V *vs.* Li/Li^+ during rapid or low-temperature charging, resulting in Li plating. A BMS equipped with the developed OCV model will calculate that the anode has reached 0 V *vs.* Li/Li^+ and, combined with knowledge of the charging C-rate and input from thermal probes in the battery pack, reduce the C-rate or activate the battery heater accordingly. The low-temperature case highlights that the effectiveness of the BMS algorithm is limited by the available battery management hardware at its disposal, such as pack heaters. The development of this model allows the management of each string of cells to be given a more advanced approach beyond rudimentary protection against over-current and over/under-potential of the full cell, allowing abnormalities in the behaviour of an electrode to be detected prior to the full cell potential reaching E_{min} or E_{max}.

A further advantage of the OCV model is that it does not require 3-electrode cells to be incorporated into the vehicle. Electrode-specific potential profiles from the long-term degradation of 3-electrode cells can be obtained in the lab and used to calibrate the model, thus ensuring that no additional hardware costs are incurred. This represents a significant cost saving *vs*. setting up tooling to mass produce 3-electrode cells, plus further savings in the mass and complexity of the battery pack wiring loom and BMS hardware. The OCV model is therefore a simple BMS software modification that will help to extend the cycle and calendar lives of today's commercial Li-ion cells, bringing them closer to the 13.5 year average lifespan of a car in the UK [20]. Based on an estimated lifetime vehicle mileage of 106,650 miles extrapolated from the average annual vehicle mileage of 7,900 miles in the UK in 2014 [21], and the 100,000 mile battery warranty offered by BMW [22], the model could allow today's Li-ion cells to provide a greater mileage over their calendar life than they will be required to provide over the lifespan of the vehicle. Therefore, once properly integrated into a

BMS and calibrated using electrode data from the cells used in the battery pack, the model could make Li-ion battery packs that last as long as the vehicles that they power a reality.

6.1 References

[1] S. A. Freunberger, Y. Chen, Z. Peng, J. M. Griffin, L. J. Hardwick, F. Bardé, P. Novák and P. G. Bruce, "Reactions in the Rechargeable Lithium-O_2 Battery with Alkyl Carbonate Electrolytes," *J. Am. Chem. Soc.*, vol. 133, pp. 8040 - 8047, 2011.

[2] S. A. Freunberger, Y. Chen, N. E. Drewett, L. J. Hardwick, F. Bardé and P. G. Bruce, "The Lithium–Oxygen Battery with Ether-Based Electrolytes," *Angew. Chem. Int. Ed.*, vol. 50, no. 37, pp. 8609 – 8613, 2011.

[3] B. D. McCloskey, A. Speidel, R. Scheffler, D. C. Miller, V. Viswanathan, J. S. Hummelshøj, J. K. Nørskov and A. C. Luntz, "Twin Problems of Interfacial Carbonate Formation in Nonaqueous Li–O_2 Batteries," *J. Phys. Chem. Lett.*, vol. 3, no. 8, pp. 997 – 1001, 2012.

[4] Y. Chen, S. A. Freunberger, Z. Peng, F. Bardé and P. G. Bruce, "Li−O_2 Battery with a Dimethylformamide Electrolyte," *J. Am. Chem. Soc.*, vol. 134, no. 18, pp. 7952 - 7957, 2012.

[5] D. G. Kwabi, T. P. Batcho, C. V. Amanchukwu, N. Ortiz-Vitoriano, P. Hammond, C. V. Thompson and Y. Shao-Horn, "Chemical Instability of Dimethyl Sulfoxide in Lithium−Air Batteries," *J. Phys. Chem. Lett.*, vol. 5, pp. 2850 - 2856, 2014.

[6] A. Khetan, A. Luntz and V. Viswanathan, “Trade-Offs in Capacity and Rechargeability in Nonaqueous Li-O_2 Batteries: Solution-Driven Growth versus Nucleophilic Stability,” *J. Phys. Chem. Lett.,* vol. 6, pp. 1254 - 1259, 2015.

[7] N. B. Aetukuri, B. D. McCloskey, J. M. García, L. E. Krupp, V. Viswanathan and A. C. Luntz, “Solvating Additives Drive Solution-Mediated Electrochemistry and Enhance Toroid Growth in Non-Aqueous Li-O_2 Batteries,” *Nat. Chem.,* vol. 7, pp. 50 - 56, 2015.

[8] N. Togasaki, T. Momma and T. Osaka, “Enhancement Effect of Trace H_2O on the Charge–Discharge Cycling Performance of a Li Metal Anode,” *J. Power Sources,* vol. 261, pp. 23 – 27, 2014.

[9] F. Mizuno, S. Nakanishi, Y. Kotani, S. Yokoishi and H. Iba, “Rechargeable Li-Air Batteries with Carbonate-Based Liquid Electrolytes,” *Electrochemistry,* vol. 78, no. 5, pp. 403 - 405, 2010.

[10] N. Togasaki, T. Momma and T. Osaka, “Role of the Solid Electrolyte Interphase on a Li Metal Anode in a Dimethylsulfoxide-Based Electrolyte for a Lithium–Oxygen Battery,” *J. Power Sources,* vol. 294, pp. 588 – 592, 2015.

[11] Z. Peng, S. A. Freunberger, Y. Chen and P. G. Bruce, “A Reversible and Higher-Rate Li-O_2 Battery,” *Science,* vol. 337, pp. 563 - 566, 2012.

[12] C. Milton. (23 October 2009). *Electric Car Revolution? Zinc Batteries Powered By Sun And Air*. [Online]. Available: http://gas2.org/2009/10/23/electric-car-revolution-zinc-batteries-powered-by-sun-and-air/. [Accessed 15 October 2015].

[13] Alcoa inc. (5 February 2014). *Alcoa and Tech Company Phinergy to Develop, Commercialize Batteries that Run On Air and Aluminum*. [Online]. Available: https://www.alcoa.com/car_truck/en/news/releases/2014_02_05_Alcoa_and_Phinergy_to_Develop_and_Commercialize_Batteries.asp. [Accessed 15 October 2015].

[14] Alcoa inc. (26 August 2014). *Alcoa, Phinergy and Heig-VD University Demonstrate Electric Boat With Aluminum-Air Battery Range Extender at Lake Neuchâtel, Switzerland*. [Online]. Available: https://www.alcoa.com/car_truck/en/news/releases/2014_electric_boat.asp. [Accessed 15 October 2015].

[15] Phinergy. (13 March 2013). *Phinergy Drives Car by Metal, Air, and Water*. [Online]. Available: https://www.youtube.com/watch?v=k6kIJlgqezE. [Accessed 15 October 2015].

[16] Tesla Motors, "Electric Vehicle Extended Range Hybrid Battery Pack System". U.S. Patent US 20130187591 A1, 25 July 2013.

[17] J.-L. Shui, H.-H. Wang and D.-J. Liu, "Degradation and Revival of Li–O_2 Battery Cathode," *Electrochem. Commun.,* vol. 34, pp. 45 - 47, 2013.

[18] The Tesla Motors Team. (19 December 2014). *Battery Swap Pilot Program*. [Online]. Available: http://www.teslamotors.com/en_GB/blog/battery-swap-pilot-program. [Accessed 25 May 2015].

[19] Renault Press. (20 June 2011). *Renault and Better Place Partner in Australia to Launch Fluence Z.E. in 2012*. [Online]. Available: http://media.renault.com/global/en-gb/renaultgroup/Media/PressRelease.aspx?mediaid=28864. [Accessed 25 May 2015].

[20] The Society of Motor Manufacturers and Traders. (2014). *End of Life Vehicles*. [Online]. Available: http://www.smmt.co.uk/2014-sustainability/environmental-performance/end-life-vehicles/. [Accessed 15 October 2015].

[21] Department for Transport. (02 September 2015). *Table NTS0902: Annual Mileage of 4-Wheeled Cars by Fuel Type: England, Since 2002*. [Online]. Available: https://www.gov.uk/government/statistical-data-sets/nts09-vehicle-mileage-and-occupancy. [Accessed 15 October 2015].

[22] BMW UK. (2015). *BMW i3 Aftersales Products and Services*. [Online]. Available: http://www.bmw.co.uk/en_GB/new-vehicles/bmw-i/i3/2013/iService.html. [Accessed 23 September 2015].

Appendix A

A.1 Calculation of air flow rate for Li-air automotive battery pack

To calculate the air flow rate required to sustain the discharge reaction for an electric vehicle powered by Li-air cells, we shall base the calculations on a Nissan LEAF that has been retrofitted to Li-air with a design specification of a 500 mile range. The peak power of the motor is 80 kW and the nominal electricity consumption is 0.25 kWh per mile.

Therefore, the total energy contained in the battery pack is:

$$0.25 \text{ kW per mile} \times 500 \text{ mile range} = 125 \text{ kWh} \quad (1)$$

Assume a nominal Li-air cell voltage of 2.5 V.

Therefore, the total capacity of the battery pack is:

$$\frac{125 \text{ kWh}}{2.5 \text{ V}} = 50 \text{ kAh} = 50{,}000 \text{ Ah} = 180{,}000{,}000 \text{ C} \quad (2)$$

The charge of an electron is 1.6×10^{-19} C. The Li-air discharge reaction consumes two electrons per O_2 molecule. Therefore, the total number of O_2 molecules required to provide the full capacity of the battery pack is:

$$\frac{180{,}000{,}000 \text{ C}}{2 \times 1.6 \times 10^{-19} \text{ C}} = 5.63 \times 10^{26} \text{ O}_2 \text{ molecules} \quad (3)$$

Assume cathode stoichiometry of 5, equating to an O_2 utilisation of 20 %.

Therefore, the number of O_2 molecules required to be delivered to the Li-air battery pack is:

$$5 \times 5.63 \times 10^{26} = 2.81 \times 10^{27}\ \mathrm{O_2\ molecules} \tag{4}$$

Given the 80 kW peak power of the motor, the pack must be able to deliver the following number of O_2 molecules per second under maximum load:

$$\begin{aligned} &\frac{\text{Total } O_2 \text{ molecules delivered to pack}}{\left(\frac{\text{Total energy stored in pack}}{\text{Peak power of motor}}\right) \times 3600 \text{ seconds in an hour}} \\ &= \frac{2.81 \times 10^{27}\ \mathrm{O_2\ molecules}}{\left(\frac{125\ \mathrm{kWh}}{80\ \mathrm{kW}}\right) \times 3600 \text{ seconds in an hour}} \\ &= 5.0 \times 10^{23}\ \mathrm{O_2\ molecules\ per\ second} \end{aligned} \tag{5}$$

Now, the number of oxygen molecules in air must be considered. Take the volumetric oxygen content of air to be 20.95 %. Therefore, there is 0.21 m^3 of O_2 per cubic metre of air. Assume that oxygen behaves as an ideal gas. Therefore, the number of moles, *n*, of O_2 in a volume, *V*, of 0.21 m^3 at a temperature of 15 °C (*T* = 288.15 K) and atmospheric pressure (*p* = 101,325 Pa) is:

$$n = \frac{pV}{RT} = \frac{101{,}325 \times 0.21}{8.314 \times 288.15} = 8.86\ \text{moles of}\ \mathrm{O_2}\ \text{in 1 m}^3\ \text{air} \tag{6}$$

where *R* is the universal gas constant. Multiplying the above by Avogadro's number gives the total number of O_2 molecules per m^3 air as 5.34×10^{24} molecules.

The peak air flow rate required for the Li-air battery pack may now be calculated thus:

$$\frac{5.0 \times 10^{23}\ O_2 \text{ molecules per second}}{5.34 \times 10^{24}\ O_2 \text{ molecules per m}^3 \text{ air}} \times 1000 \text{ litres per m}^3 = 93.71 \text{ litres of air per second} \quad (7)$$

Based on the nominal electricity consumption of 0.25 kWh per mile and assuming an average speed of 30 mph, equating to 1/30 hour to travel one mile, the nominal power consumption is:

$$\frac{\text{nominal energy consumption per mile}}{\text{time taken to travel one mile (hours)}} = \frac{0.25 \text{ kWh per mile} \times 30}{1 \text{ hours}} = 7.5 \text{ kW} \quad (8)$$

The nominal air flow rate can then be calculated based on the peak air flow rate from (7):

$$93.71 \text{ litres per second} \times \frac{7.5 \text{ kW}}{80 \text{ kW}} = 8.79 \text{ litres per second} \quad (9)$$

The vehicle will require blowers to provide the peak air flow rate when the vehicle is stationary or travelling at low speeds. The blowers must ideally have a small form factor, the same voltage as the auxiliary or traction circuits, and low power consumption. A suitable example is the Orion ODB600PT-12HB, which has an air flow rate of 35 cubic feet per minute, which equates to 16.52 litres per second; a voltage of 12 V DC and current drain of 0.6 A, equating to a power drain of 7.2 W; and dimensions of 31.0 mm depth × 120.5 mm width × 120.5 mm height [1]. Since the peak air flow rate is 93.71 litres per second, six blowers are required, providing a total of 99.12 litres per second air flow. The six blowers have a combined power consumption of 43.2 W. Their small form factor allows them to be strategically located around the vehicle to optimise the air flow to the battery pack.

A.2 Calculation of onboard oxygen storage required for an oxygen-fed Li-O_2 automotive battery pack

From (4) in A.1, it can be seen that 2.81×10^{27} molecules of O_2 are required to be delivered to the Li-air battery pack over the course of a full discharge. To express this in moles, it is divided by Avogadro's number, i.e. 6.02×10^{23} molecules per mole of a substance. Therefore, the number of moles of O_2 that must be delivered to the Li-air battery pack is:

$$\frac{2.81 \times 10^{27}}{6.02 \times 10^{23}} = 4{,}670.27 \text{ moles of } O_2 \quad (10)$$

The molecular mass, *M*, of O_2 is 32 grams per mole. Therefore, the total mass, *m* of the required O_2 molecules is:

$$4{,}670.27 \text{ moles} \times 32 \text{ grams per mole} = 149{,}448.51 \text{ g} = 149.45 \text{ kg } O_2 \quad (11)$$

of which 20 %, or 29.89 kg, is used to complete the discharge reaction.

For onboard oxygen storage, assume the use of a pressurised container at a pressure, *p*, of 230 bar, or 23,000,000 Pa, at $T = 288.15$ K. Therefore, the total volume, *V*, of the compressed oxygen is:

$$V = \frac{mRT}{Mp} = \frac{149{,}448.51 \times 8.314 \times 288.15}{32 \times 23{,}000{,}000} = 0.49 \text{ m}^3 = 486.48 \text{ litres } O_2 \quad (12)$$

This equates to 110.43 m^3 of oxygen at atmospheric pressure (1 atm = 1.01 bar).

A.3 Calculation of quantity of soda lime required for an air-fed Li-air automotive battery pack

Reference [2] states that the Eureka fuel cell bus, which had a nominal power of 78 kW, required 500 kg of soda lime to operate at nominal load for 60 hours. From the nominal power and running time, this equates to 500 kg of soda lime in order for the pack to provide 4,680 kWh of energy. The Li-air Nissan LEAF example considered in this Appendix has a battery pack that contains 125 kWh of energy when fully charged. Therefore, the total mass of soda lime required for a full discharge is:

$$\frac{\text{Quantity of soda lime } \times \text{Energy in LEAF pack}}{\text{Energy yielded by Eureka bus pack}} = \frac{500 \text{ kg } \times 125 \text{ kWh}}{4{,}680 \text{ kWh}} \tag{13}$$

$$= 13.35 \text{ kg soda lime for full discharge of LEAF pack}$$

A.4 References

[1] Orion Fans, *ODB600PT Blower Series*, [Online]. Available: http://orionfans.com/products/dc-fans/item/odb600pt.html. [Accessed 13 May 2016].

[2] V. Ahuja, "CO_2 Removal from Air for Alkaline Fuel Cells Operating with Liquid Hydrogen," Ph.D. thesis, Dept. Mech. Eng., Univ. Canterbury, Christchurch, New Zealand, 1996, p. 10.

Appendix B

B.1 Identification of pouch cell cathode chemistry

X-ray diffraction (XRD) and energy-dispersive X-ray spectroscopy (EDX) were used to determine the cell chemistry of the Kokam pouch cells used in Chapter 5. When purchased from the supplier, the cells were believed to be lithium nickel manganese cobalt oxide (NMC) chemistry. However, XRD revealed additional peaks that were not attributed to NMC (Figure 1(a)). Comparison to a number of cell chemistry diffraction patterns revealed these to be lithium cobalt oxide (LCO) peaks (Figure 1(a)), indicating a blend of LCO and NMC.

Colour mapping *via* EDX revealed distinct cobalt-based and nickel-based heavy metal oxide particles in the cathode structure, but failed to detect manganese. Whilst EDX may occasionally attribute peaks to the wrong elements due to overlapping X-ray wavelengths [1], none of the elements detected by XRD could have been confused with manganese. As such, a number of additional XRD patterns of heavy metal oxides were compared to that of the cathode in order to identify the compound that had been mistakenly identified as NMC. The peaks of lithium nickel oxide (LNO) did not fully correspond to those that were not attributed to LCO. However, lithium nickel cobalt aluminium oxide (NCA) and lithium nickel cobalt oxide (NCO), which have similar diffraction patterns, both aligned well with the cathode sample.

EDX revealed that aluminium comprised 0.2 % of the cathode sample. However, the colour map for aluminium showed that it was reasonably evenly distributed around the sample, rather than concentrated in the same regions as nickel, which would have been indicative of NCA. The aluminium likely originates from the cathode current collector; similar concentrations of copper were found in EDX colour maps of anodes, which have copper current collectors. As

such, it was determined that the Kokam pouch cells have a cell chemistry based on a blend of LCO and NCO.

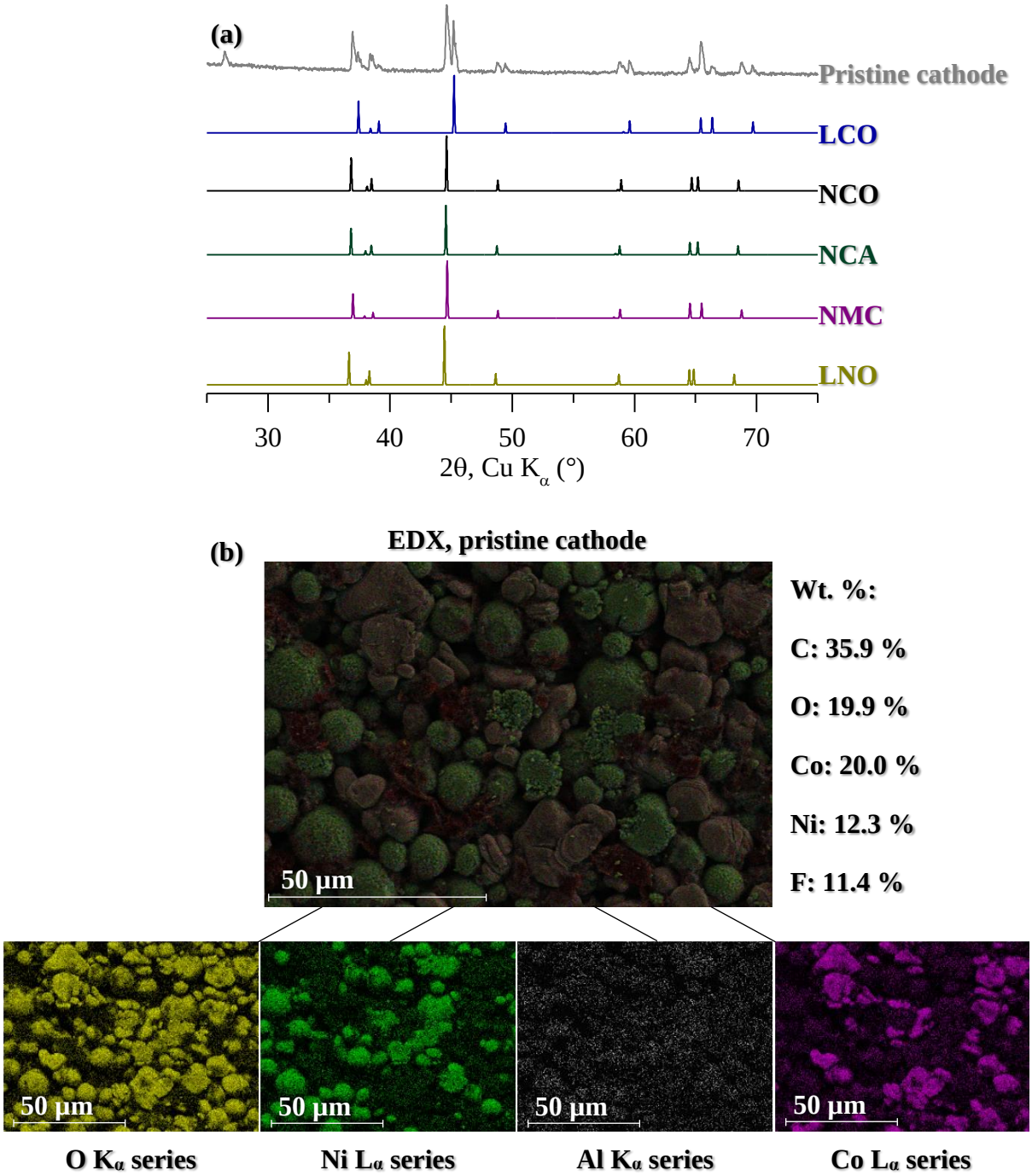

Figure 1: XRD diffractogram (a) and EDX colour maps (b) of a pristine Kokam pouch cell cathode, identifying the cell chemistry as a blend of LCO and NCO. Note the clusters of nickel-rich and cobalt-rich particles in the structure in (b). EDX is unable to detect lithium, so a lithium colour map is therefore not shown.

B.2 Table of chemical composition of cathode samples as determined by EDX

Cathode sample	Composition, wt. %				
	C	Co	O	Ni	F
Pristine	35.9	20.0	19.9	12.3	11.4
Unmodified, cycled	39.2	21.7	19.3	10.5	9.1
Patch-modified, cycled	30.5	22.1	20.6	10.1	15.8
Revised patch-modified, cycled	38.3	22.7	21.2	9.1	8.4
Wire-modified, cycled	39.5	18.0	18.6	10.8	12.5

Table 1: Chemical composition by wt. % of a pristine Kokam cathode in comparison to cathodes from cycled cells that have undergone patch or wire modifications. Due to the nature of the sample and the EDX process, any differences in composition are not sufficient to suggest significant change to the structure of the cathode.

B.3 EDX colour maps of unmodified, cycled anode

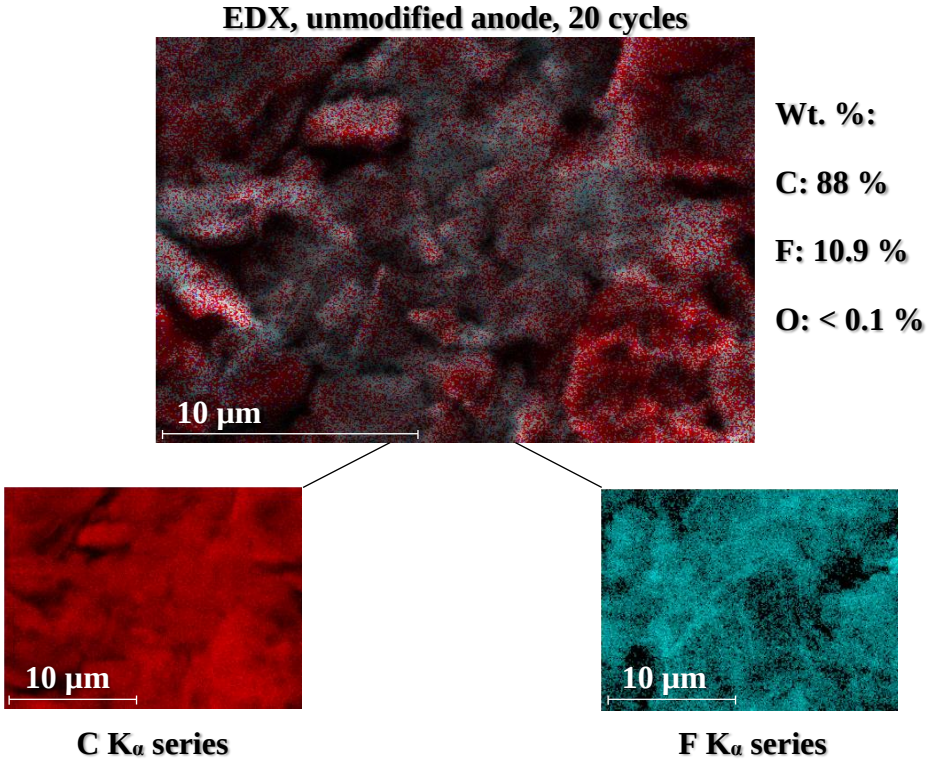

Figure 2: EDX colour maps for the anode of an unmodified pouch cell after 20 cycles.

B.4 RMSE data for potential profiles obtained from half-cells and 3-electrode cells

Discharge number	Cathode RMSE (mV)		Anode RMSE (mV)	
	Room temp.	40 °C	Room temp.	40 °C
1st	3.00	2.76	5.76	2.99
10th	5.38	2.99	8.55	3.92
20th	5.72	2.77	9.15	5.00

Table 2: RMSE values for the potential profiles of half-cells fitted with data obtained from wire-modified cells.

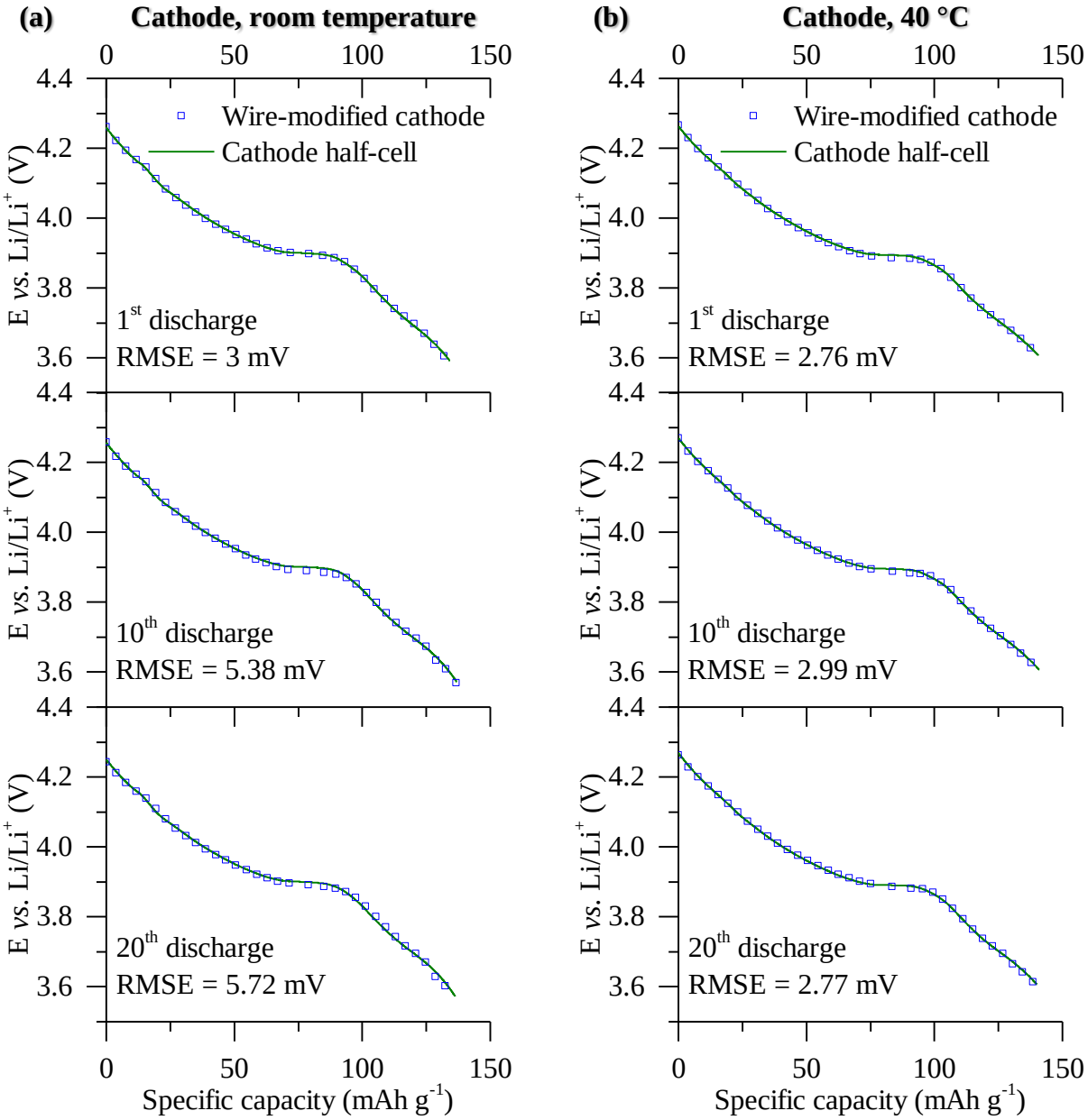

Figure 3: Fitted potential profiles for the 1st, 10th and 20th discharge of cathode half-cells and the cathodes of wire-modified cells at room temperature (a) and 40 °C (b), complete with RMSE values.

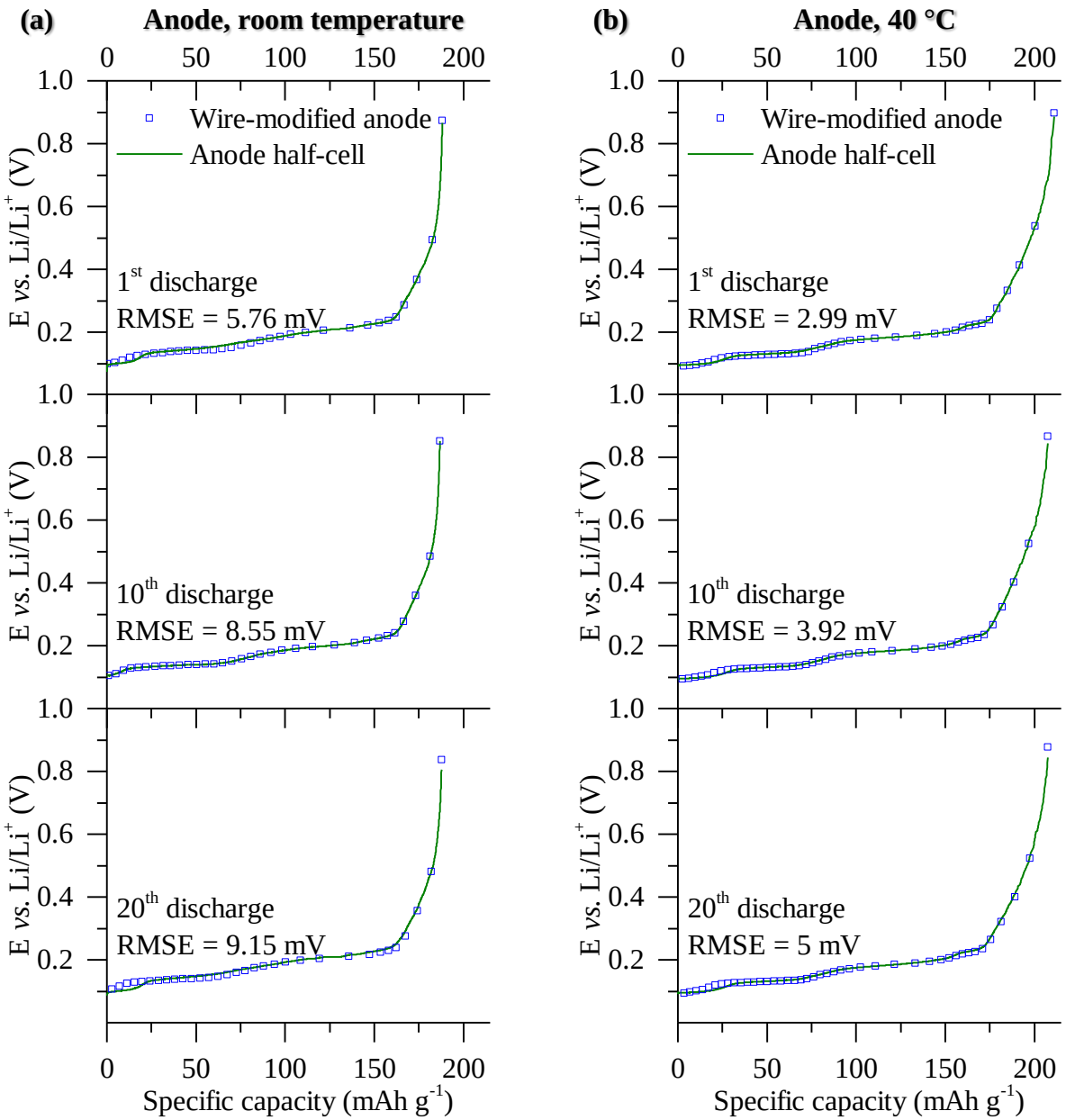

Figure 4: Fitted potential profiles for the 1st, 10th and 20th discharge of anode half-cells and the anodes of wire-modified cells at room temperature (a) and 40 °C (b), with RMSE values.

B.5 References

[1] J. Goodge. (14 June 2015). *Energy-Dispersive X-Ray Spectroscopy (EDS)*. [Online]. Available: http://serc.carleton.edu/research_education/geochemsheets/eds.html. [Accessed 01 October 2015].